A COMPARATIVE STUDY ON SEISMIC ANALYSIS METHODS AND THE RESPONSE OF SYSTEMS WITH CLASSICAL AND NONCLASSICAL DAMPING

A Thesis

presented to

the Faculty of California Polytechnic State University,

San Luis Obispo

In Partial Fulfillment

of the Requirements for the Degree

Master of Science in Civil and Environmental Engineering

by

Noah G. Bleichner

June 2020

COMMITTEE MEMBERSHIP

TITLE: A Comparative Study on Seismic Analysis Methods and the Response of Systems with Classical and Nonclassical Damping

AUTHOR: Noah G. Bleichner

DATE SUBMITTED: June 2020

COMMITTEE CHAIR: Eric Kasper, Ph.D.
Professor of Structural Engineering

COMMITTEE MEMBER: Garrett Hall, Ph.D.
Professor of Structural Engineering

COMMITTEE MEMBER: Mario Esola
Lecturer of Structural Engineering

ABSTRACT

A Comparative Study on Seismic Analysis Methods and the Response of Systems with Classical and Nonclassical Damping

Noah G. Bleichner

This thesis investigated the application of seismic analysis methods and the response of idealized shear frames subjected to seismic loading. To complete this research, a Design Basis Earthquake (DBE) for a project site in San Luis Obispo, CA, and five past earthquake records were considered. The DBE was produced per the American Society of Civil Engineers' *Minimum Design Loads for Buildings and Other Structures* (ASCE 7-10) and used for application of the Equivalent Lateral Force Procedure (ELFP) and Response Spectrum Analysis (RSA). When applying RSA, the modal peak responses were combined using the Absolute Sum (ABS), Square-Root-of-the-Sum-of-Squares (SRSS), and Complete Quadratic Combination (CQC) method.

MATLAB scripts were developed to produce several displacement, velocity, and acceleration spectrums for each earthquake. Moreover, MATLAB scripts were written to yield both analytical and numerical solutions for each system through application of Linear Time History Analysis (THA). To obtain analytical solutions, two implicit forms of the Newmark-beta Method were employed: the Average Acceleration Method and the Linear Acceleration Method.

To generate a comparison, the ELFP, RSA, and THA methods were applied to shear frames up to ten stories in height. The system parameters that impacted the accuracy of each method and the response of the systems were analyzed, including the effects of classical damping and nonclassical damping models. In addition to varying levels of Rayleigh damping, non-linear hysteric friction spring dampers (FSDs) were implemented into the systems. The design of the FSDs was based on target stiffness values, which were defined as portions of the system's lateral stiffness. To perform the required Nonlinear Time History Analysis (NTHA), a SAP2000 model was developed. The efficiencies of the FSDs at each target stiffness, with and without the addition of low levels of viscous modal damping are analyzed.

It was concluded that the ELFP should be supplemented by RSA when performing seismic response analysis. Regardless of system parameters, the ELFP yielded system responses 30% to 50% higher than RSA when combing responses with the SRSS or CQC method. When applying RSA, the ABS method produced inconsistent and inaccurate results, whereas the SRSS and CQC results were similar for regular, symmetric systems. Generally, the SRSS and CQC results were within 5% of the analytical solution yielded through THA. On the contrary, for irregular structures, the SRSS method significantly underestimated the response, and the CQC method was four to five times more accurate. Additionally, both the Average Acceleration Method and Linear

Acceleration Method yielded numerical solutions with errors typically below 1% when compared with the analytical solution.

When implemented into the systems, the FSDs proved to be most efficient when designed to have stiffnesses that were 50% of the lateral stiffness of each story. The addition of 1% modal damping to the FSDs resulted in quicker energy dissipation without significantly reducing the peak response of the system. At a stiffness of 50%, the FSDs reduced the displacement response by 40% to 60% when compared with 5% modal damping. Additionally, the FSDs at low stiffnesses exhibited the effects of negative lateral stiffness due to P-delta effects when the earthquake ground motions were too weak to induce sliding in the ring assemblies.

ACKNOWLEDGMENTS

I would like to express my deepest gratitude to my advisor, Professor Kasper. I'm extremely appreciative of the continual assistance you gave to me throughout this process. Your willingness to be my advisor provided me with a huge opportunity, allowing me to grow not only as a student, but also as a person. During this process, I was challenged to be creative, and I was pushed to learn and develop as an engineer in ways that wouldn't have been possible without your guidance. Writing this thesis was an invaluable experience for me, and for that reason I'm indebted to you. I sincerely thank you for the opportunity you gave me. Also, I would like to thank Professor Hall and Esola for your willingness to be on the thesis committee. Both of you played a critical role in my education and helped to make my time at Cal Poly a truly great experience.

TABLE OF CONTENTS

Page

LIST OF TABLES

LIST OF FIGURES

LIST OF NOMENCLATURE

ELFP	Equivalent Lateral Force Procedure
SDC	Seismic Design Category
DOF	Degree of Freedom
SDOF	Single Degree of Freedom
MDOF	Multiple Degrees of Freedom
FEA	Finite Element Analysis
FEM	Finite Element Method
RSA	Response Spectrum Analysis
ABS	Absolute Sum
SRSS	Square-Root-of-the-Sum-of-Squares
CQC	Complete Quadratic Combination
DBE	Design Basis Earthquake
THA	Linear Time History Analysis
NTHA	Nonlinear Time History Analysis
AAM	Average Acceleration Method
LAM	Linear Acceleration Method
PGA	Peak Ground Acceleration
PGV	Peak Ground Velocity
PGD	Peak Ground Displacement
FSDs	Friction Spring Dampers

1. Introduction

Recent major earthquakes have shown the need for adequate structural design in regions prone to seismic activity. Although structural and seismic engineering requirements are constantly improving, the yearly occurrence of high magnitude earthquakes continually brings to light the deficiencies of current seismic design standards. The purpose of this thesis is to develop recommendations for improving the performance of structural systems subject to earthquake ground motions. Throughout this research, two primary approaches are taken to better structures vulnerable to seismic activity. First, the accuracy of several seismic analysis methods – the Equivalent Lateral Force Procedure (ELFP), Response Spectrum Analysis (RSA), Time History Analysis (THA) – is analyzed. The seismic analysis methods are applied to a wide range of systems to develop an understanding of the limitations of each method, as well as the parameters that can improve or hinder their accuracy. Secondly, the impacts of damping on the response of a system are analyzed. In addition to classical damping models, this study researches the efficiency of nonclassical damping models through the application of Friction Spring Dampers (FSDs). In order to optimize the effects, an iterative approach is taken to designing and implementing the FSDs in each system. There is a need to study the effects of FSDs to not only improve their quality, but also to increase their prevalence in structural systems. To increase the level of understanding, the methods and approaches taken in this study are thoroughly detailed, and past research and literature are consistently referenced throughout this thesis.

1.1 Motivation

The occurrence of earthquakes in highly developed regions poses a serious danger to human life. In the twentieth century alone, over two million lives were lost due to earthquakes, with the average number of fatal earthquakes per year increasing through the century (Nichols & Beavers, 2008). In the first fifteen years of the twenty-first century alone, earthquakes have resulted in 800,000 deaths (Statista Research Department, 2016). Although improvements have been made to seismic analysis and design, structural collapse accounts for 75% of all earthquake related deaths (Coburn et al., 1992). Consequently, there is a continual need to research the effects of seismic events as they pertain to structural engineering.

2. Literature Review

The literature review herein focuses on the code provisions, theoretical development, and past work used to develop and conduct the research in this thesis. In addition to the references in this section, the subsequent chapters of this study utilize current literature to further detail and explain the applied methods and theories.

2.1 Code Provisions

In this study, the code requirements defined in the American Society of Civil Engineers' (AISC) *Minimum Design Loads for Buildings and Other Structures* (ASCE 7-10) are referenced. The criteria and provisions for applying the ELFP, RSA, and THA are found in Chapter 8, Chapter 9, and Chapter 16, respectively. Additionally, the National Earthquake Hazards Reduction Program's (NEHRP) *Recommended Seismic Provisions for New Buildings and Other Structures* (FEMA P-1050) are also referenced to further detail seismic requirements.

2.2 Theoretical Development

In order to correctly implement dynamic analysis, *An Introduction to Applied Structural Dynamics* (Kasper & Hall, 2018) is repeatedly referenced. This textbook provides equations, methods, and theory necessary for performing dynamic analysis on both single degree of freedom (SDOF) and multiple degree of freedom (MDOF), damped and undamped systems. Furthermore, *Dynamics of Structures: Theory and Applications to Earthquake Engineering* (Chopra 1995)

supplements the understanding and application of dynamic analysis in this thesis.

Moreover, *The Finite Element Method: Linear Static and Dynamic Finite Element Analysis* (Hughes, 2012) is referenced throughout this research. This textbook is used to apply finite element analysis (FEA) for the elastic analysis of the shear frames and to understand the differential equations necessary to solve for analytical and numerical solutions in THA. Hughes' provides numerous mathematical derivations and proofs which reveal the expected behavior and stability of each variation of the Newmark-beta numerical method, which are detailed and analyzed throughout this thesis.

2.3 Past Work

Past research has provided knowledge regarding the accuracy and applicability of various seismic analysis and numerical methods. *A Comparative Study of Equivalent Lateral Force Method and Response Spectrum Analysis in Seismic Design of Frames* (Shrestha, 2019) shows the ELFP yields conservative results for frames with heights above four-stories. In the study, *A Replacement for the SRSS Method in Seismic Analysis* (Wilson et al., 1981), the SRSS method considerably underestimates the response of three-dimensional structures with mass irregularities. Also, *Analysis Procedures for Performance Based Design* (Kelly & Chambers, 2000) suggests the application of THA for all performance-based designs, despite the relative complexity of the analysis. In *Stability and Accuracy of Newmark's Method* (Maghdid, 2002), the Newmark-beta method increases in accuracy for smaller beta values, but consequently

also results in only conditional stability of the solution. Additionally, *Stability of Average Acceleration Method for Structures with Nonlinear Damping* (Li et al., 2006) proves the stability of the Average Acceleration Method for SDOF systems with nonlinear damping using the velocity power function and MDOF systems with nonlinear damping by applying the virtual displacement theorem.

To develop an understanding of the FSDs, the findings of three key research studies are analyzed. First, *The Utility of Ring Springs in Seismic Isolation Systems* (Hill, 1995), defines equations for the stiffness properties and details the hysteric characteristics of the FSDs. Secondly, *Seismic Performance Evaluation of Low-Rise Steel Building Frames with Self-Centering Energy-Absorbing Rocking Cores* (Hu et al., 2019) provides a design procedure for the FSDs in Self-Centering Energy-Absorbing Rocking Core (SCENARIO) systems and shows that the FSDs successfully reduce the inter-story drifts and demolition patterns of the frames. Thirdly, in the thesis *Nonlinear Dynamic Analysis of a Single-Story Frame with Friction Spring Damper Using SAP2000* (Gurara, 2018), FSDs effectively reduce the inter-story drift and base shear of SDOF frames subjected to earthquake ground motions.

3. Static Seismic Analysis

Throughout the contents of this study, various methods of seismic analysis are performed on one-story, two-story, and three-story shear frames. Although the Modal Response Spectrum Analysis Method and Linear Response History Analysis Method are both accurate, dynamic methods of seismic analysis, the Equivalent Lateral Force Procedure (ELFP) outlined in ASCE 7-10 provides a simplified, static method for estimating seismic base shear forces. The results from the ELFP and various dynamic methods of analysis are compared at a later point in this work. Further explanation and a step-by-step example of the ELFP on a three-story shear frame are shown in this chapter.

3.1 Equivalent Lateral Force Procedure

The ELFP estimates the seismic forces by relating the total base shear and seismic weight of the structure through the seismic response coefficient. The governing equation of the ELFP is shown by Equation 3.1.

$$V = C_s W \qquad \text{(Equation 3.1)}$$

Where C_S represents the seismic response coefficient. The seismic response coefficient is dependent on various site-specific quantities, the importance factor of the structure, and the type of lateral force resisting system used.

In this study, the shear frames have floor heights of 11 feet, seismic floor weights of 100 kips, and seismic roof weights of 80 kips. Also, the geographic location of the three shear frames is chosen to be San Luis Obispo, CA 93407. In the case of a lateral force resisting system with an associated floor plan, the

seismic weights can be determined through the load combination equations defined in ASCE 7-10. Although in many cases the seismic weight is solely due to the dead load, ASCE 7-10 details the parameters and special inclusions to consider when calculating the seismic weight.

Once the seismic weights are determined, the next step in the ELFP for the three-story shear frame is to determine the Occupancy Category (Risk Category), which is then used to find the Importance Factor, I_e, associated with the structure. As outlined in ASCE 7-10, the Occupancy Category of a structure ranges from I to IV with Occupancy Category IV being designated for buildings with the greatest importance, such as hospitals or fire stations. Next, the site classification of the structure is determined, which references the soil or rock type at the site location. Conceptually, soft soils amplify earthquake waves, whereas stiff soils reduce earthquake waves. A three-story shear frame defined as a Risk Category II structure results in an Importance Factor of 1.0 and a Site Class D, representing stiff soil. Typically, Site Class D is assumed unless the authority having jurisdiction or geotechnical data confirms otherwise (NEHRP, 2015). In general, Site Class D is the most common soil type found in the United States.

The next step in the ELFP is to determine the site coefficients necessary for calculating the seismic response coefficient. The United States Geological Survey (USGS) website gives seismic design maps which can be utilized for determining specific site coefficients. In accordance with the requirements set forth by ASCE 7-10, a Risk Category II structure located in San Luis Obispo, CA 93407, results in the site parameters shown in Table 1 (Appendix A).

Table 1: Site Parameters – San Luis Obispo, CA

Type	Value	Description
S_S	1.121	MCE_R ground motion (for 0.2s period)
S_1	0.427	MCE_R ground motion (for 1.0s period)
S_{MS}	1.18	Site-modified spectral acceleration value
S_{M1}	0.672	Site-modified spectral acceleration value
S_{DS}	0.786	Numeric design value at 0.2s SA
S_{D1}	0.448	Numeric design value at 1.0s SA
SDS	D	Seismic Design Category
F_a	1.051	Site amplication factor at 0.2s
F_V	1.572	Site amplication factor at 1.0s
PGA	0.442	MCE_G peak ground acceleration

The site coefficients are determined with respect to the Design Basis Earthquake (DBE) and the Maximum Considered Event (MCE), which refers to an earthquake that is expected to occur once in every 500 years and 2500 years, respectively. Since the three-story shear frame is designed based on the DBE, the critical values for the design are S_{DS} and S_{D1}. S_{DS} and S_{D1} are the design spectral acceleration values at periods of 0.2 seconds and 1.0 seconds, respectively. With the S_{DS} and S_{D1} values, a Simplified Design Response Spectra can be developed in accordance with ASCE 7-10.

In addition to the site coefficients, the approximate fundamental period (T_a) is needed to determine the seismic response coefficient in Equation 3.1. As outlined in ASCE7-10, the approximate fundamental period of a structure can be determined with Equation 3.2.

$$T_a = C_t h_n^x \qquad \text{(Equation 3.2)}$$

Where C_t and x are both determined from Table 12.8-2 in ASCE 7-10, and h_n refers to the height of the building above the base. For a steel moment resisting frame, $C_t = 0.028$ and $x = 0.8$, which results in an approximate fundamental period of 0.459 seconds for the three-story shear frame.

Furthermore, ASCE 7-10 provides an addition equation for calculating the fundamental period of a structure, shown by Equation 3.2a below.

$$T_a = 0.1N \qquad \text{(Equation 3.2a)}$$

Where N refers to the number of stories above the base of the structure. ASCE 7-10 permits the use of Equation 3.2a as a replacement to Equation 3.2 for steel moment resisting frames that are less than 12 stories, with average story heights greater than 10 feet. For the three-story shear frame, Equation 3.2a results in an approximate fundamental period of 0.3 seconds. Despite the applicability of Equation 3.2a, an approximate fundamental period of 0.459 seconds is used for analysis of the three-story shear frame.

The final value necessary to determine the seismic response coefficient is the Response Modification Factor, R. The Response Modification Factor depends on the type of lateral force resisting system used. Table 12.2-1 in ASCE 7-10 defines the R value for each type of structural system. Conceptually, certain lateral force resisting systems perform better under seismic loads than others. In general, the more ductile the system, the better it performs. As a result, a higher R value correlates with a more ductile lateral force resisting system and therefore a lower seismic design force. An important consideration during design is the height limit for specific lateral force resisting systems with regards to the Seismic

Design Category (SDC) set forth by ASCE 7-10. As shown by Table 1, a site located in San Luis Obispo, CA, is in SDC D. According to ASCE 7-10 Table 12.2-1, the use of a steel ordinary moment resisting frame in SDC D is not permitted (NP), whereas the use of a steel intermediate moment resisting frame in SDC D is permitted (P) for structures less than 35 feet in height. Consequently, the three-story shear frame is categorized as a steel intermediate moment frame with an R value of 4.5. Although an in-depth design of the three-story shear frame is not the goal of this study, the use of an intermediate as opposed to an ordinary steel moment frame assumes that the frame and its connections are designed to be ductile and able to withstand significant inelastic deformation.

Next, the seismic response coefficient is determined in accordance with ASCE 7-10 through Equation 3.3.

$$C_s = \frac{S_{DS}}{(R/I)} \qquad \text{(Equation 3.3)}$$

As previously determined for the three-story shear frame the S_{DS}, R, and I value are 0.786, 4.5, and 1.0, respectively, which results in a C_s value of 0.175.

In addition to Equation 3.3, ASCE 7-10 establishes upper limits for the seismic response coefficient defined by Equations 3.3a and 3.3b, and a lower limit of 0.01 for the seismic response coefficient.

$$C_S = \frac{S_{D1}}{T(R/I)} \; for \; T \leq T_L \qquad \text{(Equation 3.3a)}$$

$$C_S = \frac{S_{D1}T_L}{T^2(R/I)} \; for \; T > T_L \qquad \text{(Equation 3.3b)}$$

Where T_L represents the long period transition period, which is determined from Figure 22-12 in ASCE7-10. For a structure site in San Luis Obispo, CA, the

T_L value is 8 seconds. The results of Equation 3.3a and 3.3b are 0.217 and 3.789, respectively, which means the C_S value obtained from Equation 3.3 governs. Also, it is important to note that if the S_1 value of the site is greater than or equal to 0.6g, ASCE 7-10 gives a supplemental lower bound equation for the seismic response coefficient.

The final step of the ELFP is to determine the total seismic base shear and vertically distribute the seismic forces at each story of the shear frame. In accordance with Equation 3.1, the calculated seismic weight and seismic response coefficient for the three-story shear frame result in a total seismic base shear of 49 kips. To vertically distribute the total seismic base shear along the height of the three-story shear frame, Equation 3.4 and Equation 3.5 are used.

$$C_{VX} = \frac{W_x h_x^k}{\Sigma_{i=1}^{n} W_i h_i^k} \qquad \text{(Equation 3.4)}$$

$$F_x = C_{vx} V \qquad \text{(Equation 3.5)}$$

Equation 3.4 and Equation 3.5 consider the seismic weight and height of each story in order to distribute the base shear into lateral shears at each level. In Equation 3.4, the value of k is dependent on the fundamental period of the structure. Since the fundamental period of the three-story shear frame is less than 0.5s, according to ASCE 7-10, k is equal to one.

The lateral story forces calculated through the ELFP for the one-story, two-story, and three-story are shown below in Figure 1, Figure 2, and Figure 3, respectively.

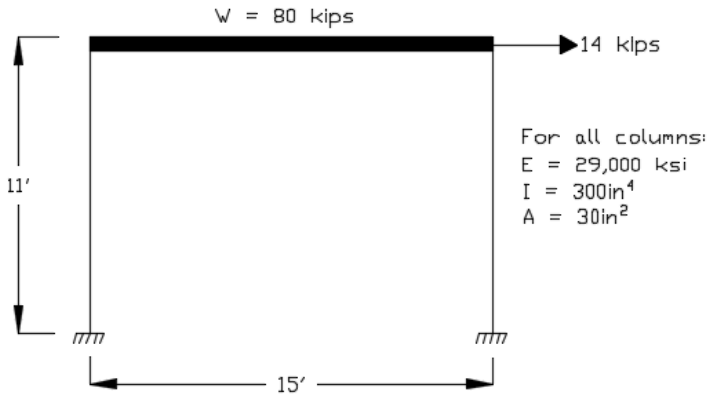

Figure 1: One-Story Shear Frame ELFP Results

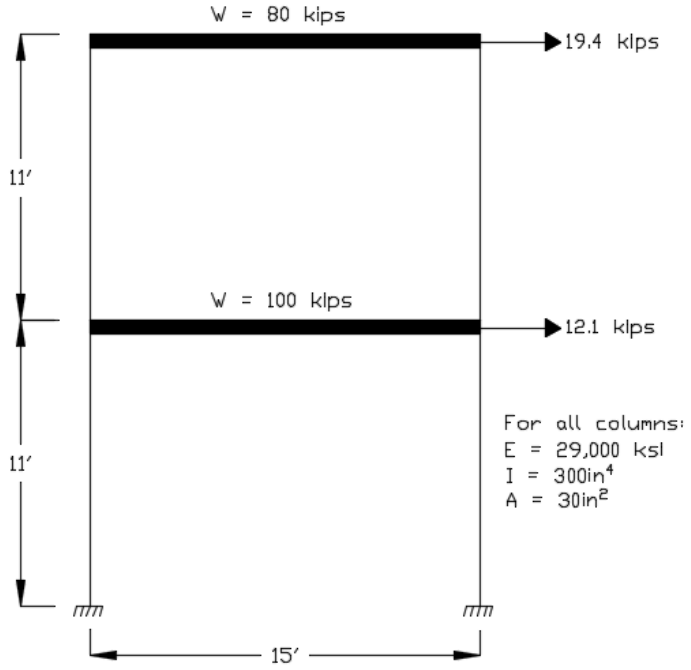

Figure 2: Two-Story Shear Frame ELFP Results

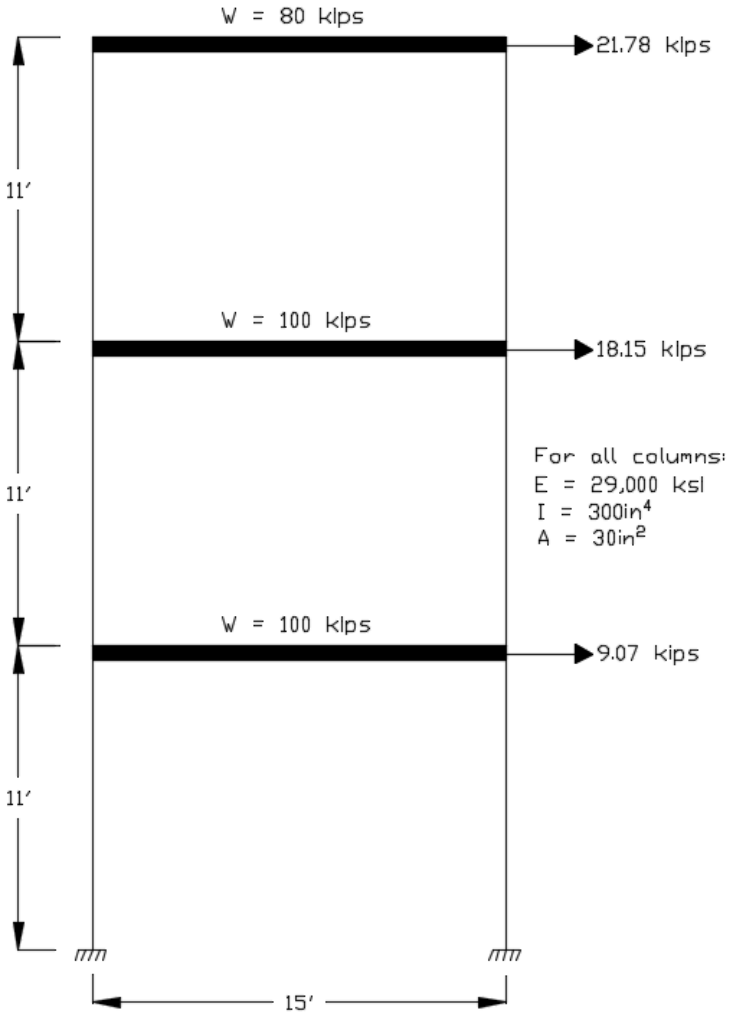

Figure 3: Three-Story Shear Frame ELFP Results

In the succeeding sections, matrix structural analysis is applied to the above shear frames to determine the lateral displacement response at each story. The displacement responses resulting from the ELFP are compared with the responses yielded by response spectrum analysis (RSA) in the subsequent chapters of this work.

3.2 Static Mechanics and Finite Element Analysis

To support the concepts of structural dynamics detailed in future chapters, a thorough understanding of static mechanics is necessary. Static Matrix Structural Analysis and Finite Element Analysis (FEA) provide many concepts applicable to structural dynamics problems. The following sections expand on static mechanics theory and serve as a stepping-stone for the dynamic analysis of the shear frames under earthquake excitations.

The main structural analysis method in matrix structural analysis stems from the direct stiffness method. The direct stiffness method uses linear elastic constitutive theory to determine the unknowns in statically indeterminate structures. The equation for Hooke's Law in one-dimension is shown below in Equation 3.6.

$$\sigma = E\varepsilon \qquad \text{(Equation 3.6)}$$

Hooke's Law in one-dimension relates the normal stress and strain of an element through the use of the Elastic Modulus, E. As shown in Equation 3.6, the Elastic Modulus is the result of dividing the stress by the strain. Shown below, Hooke's Law for the direct stiffness method is derived from Equation 3.6.

$$\sigma = E\varepsilon$$

$$\sigma = \frac{F}{A}, \varepsilon = \frac{\Delta L}{L}$$

$$\frac{F}{A} = \frac{\mathrm{E}\Delta L}{L}$$

$$\frac{F}{\Delta x} = \frac{EA}{L} = K$$

$$F = K\Delta x \qquad \text{(Equation 3.7)}$$

Although Equation 3.7 is derived from Hooke's Law in one-dimension, Equation 3.7 can also be written in matrix form as shown below in Equation 3.8

$$\{F\} = [K]\{u\} \qquad \text{(Equation 3.8)}$$

Equation 3.8 denotes linear elastic constitutive theory for multiple dimensions, and it is the governing equation behind the direct stiffness method. To solve for the unknowns in highly statically indeterminate structures, Equation 3.8 is applied to each element of the structure through the use of the Finite Element Method (FEM).

The Finite Element Method (FEM) uses partial differential equations and boundary conditions to obtain an approximate solution for the displacement at nodal points on an element. Despite the complex nature of the mathematics involved with Finite Element Analysis (FEA), the FEM is applicable for simple and complex structural and mechanical engineering problems.

For instance, consider a simple multi-member truss problem commonly seen in beginner engineering courses. At each element end, the pinned connections allow for the large truss to be broken into individual elements. The process of breaking the truss into a finite number of individual elements and analyzing the forces at each element node to solve the larger truss problem, is a simple example of FEA. Although the pinned connections of a truss result in solely axial member forces, the direct stiffness method implements the same concept to determine the unknown forces and displacements of elements that have higher degrees of freedom (DOFs). Despite the simplicity, understanding FEA for a truss problem gives a better groundwork for understanding more

complex engineering problems. For simple cases, FEA application is possible by hand, but as the complexity and number of active DOFs in the system increases, computer software is necessary. To obtain the values of the stiffness matrix for a beam element two derivations are detailed in the subsequent section.

3.3 Stiffness Coefficients

First, the stiffness coefficients can be derived through the principle of virtual work by applying a unit displacement at each DOF, while keeping the displacements and rotations at the other DOFs equal to zero. The element forces and rotations necessary to maintain the shape of the element under the unit displacement are referred to as the stiffness coefficients. For a beam element, the stiffness matrix is 4x4 to denote the shear displacements and rotations at each node. In order to derive the stiffness coefficients using the principle of virtual work, Bernuolli-Euler Beam Theory is applied to the beam element. It is important to note that linear beam theory relies on two assumptions: that plane sections remain plane and normal deformed rotations of the beam are small. Linear beam theory states that the moment divided by the moment of inertia and elastic modulus is equal to the second derivative of the displacement with respect to the distance along the length of the beam. A step-by-step derivation of the stiffness coefficients for a beam element using the Bernuolli-Euler Beam Theory for small deformations is shown in Appendix B.

Another method for determining the stiffness coefficients for a beam element is to utilize shape functions. A shape function is an interpolation function which gives a unique displacement function for each DOF of an element. The

use of shape functions allows for numerical integration, which is commonly used in FEA to simplify the analysis and produce approximate solutions to complex problems. The shape functions are dependent on the number of DOFs at each node of an element. For example, the shape functions for a truss element with one DOF (axial) at each node are determined through linear interpolation, whereas the shape functions for a beam element with two DOFs at each node (transverse and rotation) are determined through the use of Lagrange Polynomials. Since each beam element has four DOFs, four individual shape functions need to be formed to derive the stiffness coefficients. To derive the four shape functions for a beam element, the initial displacement function is cubic. A step-by-step derivation of the stiffness coefficients for a beam element using the FEM and shape functions is shown in Appendix C.

The method of virtual work and the use of shape functions to determine the stiffness coefficients for a two-dimensional beam element both result in the same stiffness matrix, which is shown in Equation 3.9 below.

$$k^e = \begin{bmatrix} \frac{12EI}{L^3} & \frac{6EI}{L^2} & -\frac{12EI}{L^3} & \frac{6EI}{L^2} \\ \frac{6EI}{L^2} & \frac{4EI}{L} & -\frac{6EI}{L^2} & \frac{2EI}{L} \\ -\frac{12EI}{L^3} & -\frac{6EI}{L^2} & \frac{12EI}{L^3} & -\frac{6EI}{L^2} \\ \frac{6EI}{L^2} & \frac{2EI}{L} & -\frac{6EI}{L^2} & \frac{4EI}{L} \end{bmatrix} \qquad \text{(Equation 3.9)}$$

In the case of a frame element, the stiffness matrix includes an axial degree of freedom at each node, resulting in three DOFs per node and a 6x6 element stiffness matrix. The previous derivations for the stiffness coefficients of a truss and beam element are combined to produce the stiffness matrix for a

frame element. The stiffness matrix for a frame element is shown in Equation 3.10 below.

$$k^e = \begin{bmatrix} \frac{EA}{L} & 0 & 0 & -\frac{EA}{L} & 0 & 0 \\ 0 & \frac{12EI}{L^3} & \frac{6EI}{L^2} & 0 & -\frac{12EI}{L^3} & \frac{6EI}{L^2} \\ 0 & \frac{6EI}{L^2} & \frac{4EI}{L} & 0 & -\frac{6EI}{L^2} & \frac{2EI}{L} \\ -\frac{EA}{L} & 0 & 0 & \frac{EA}{L} & 0 & 0 \\ 0 & -\frac{12EI}{L^3} & -\frac{6EI}{L^2} & 0 & \frac{12EI}{L^3} & -\frac{6EI}{L^2} \\ 0 & \frac{6EI}{L^2} & \frac{2EI}{L} & 0 & -\frac{6EI}{L^2} & \frac{4EI}{L} \end{bmatrix} \quad \text{(Equation 3.10)}$$

By definition, the beams in a shear frame are rigid, resulting in only a lateral DOF at each story level. As a result, the stiffness matrix of a shear frame has the same number of rows and columns as DOFs. Although the properties of a shear frame simplify the analysis, an element by element approach is still applicable and exemplified in the following section.

3.4 Matrix Structural Analysis

As referenced in the above sections, the stiffness coefficients were derived on an element-by-element basis in local coordinates. In order to determine the unknown displacements of a frame structure, each element is analyzed individually and transformed from the local element domain to the global element domain through vector calculus. Equation 3.11 shown below is used to transform the element stiffness matrix from local to global coordinates.

$$K_e = B_e^T k_e B_e \quad \text{(Equation 3.11)}$$

Where B_e represents the element transformation matrix. The element transformation matrix for a frame element is shown below in Equation 3.12.

$$B_e = \begin{bmatrix} cos\theta & sin\theta & 0 & 0 & 0 & 0 \\ -sin\theta & cos\theta & 0 & 0 & 0 & 0 \\ 0 & 0 & 1 & 0 & 0 & 0 \\ 0 & 0 & 0 & cos\theta & sin\theta & 0 \\ 0 & 0 & 0 & -sin\theta & cos\theta & 0 \\ 0 & 0 & 0 & 0 & 0 & 1 \end{bmatrix} \quad \text{(Equation 3.12)}$$

Through Equations 3.11 and 3.12, the element stiffness matrix is transformed from the local domain to the global domain. The transformation matrix uses sin and cos to relate the positions of each element in the structure. For example, consider the one-story shear frame in Figure 1, each element stiffness matrix in the local domain is determined through Equation 3.10, without accounting for the horizontal and vertical orientations of the beam and columns, respectively. Through the transformation matrix, the stiffness matrix of each individual element is transformed to the global domain in accordance with its position in the system. As a result, a global stiffness matrix is developed which represents the entire structure.

To exemplify the process of performing matrix structural analysis by hand, a step-by-step example for determining the lateral deflection of the one-story shear frame in Figure 1 is shown in Appendix D.

3.5 ELFP Results and Discussion

In combination with the hand-calculation shown in Appendix D, the lateral deflections at each story for the two-story and three-story shear frame shown in Figure 2 and Figure 3, respectively, are calculated using matrix structural analysis in MATLAB. The results for the lateral deflections of the three shear frames at each story are presented in Table 2.

Table 2: Lateral Deflections - ELFP

	Floor Level Deflections		
	U_1 (in.)	U_2 (in.)	U_3 (in.)
One-Story	0.1542	N/A	N/A
Two-Story	0.3470	0.5607	N/A
Three-Story	0.5398	0.9796	1.2195

Additionally, ASCE 7-10 defines requirements for the scaling of the lateral deflection values obtained from the ELFP. In accordance with ASCE 7-10 Section 12.8.6, for a structure in SDC D, the deflections calculated from elastic analysis must be scaled by the deflection amplification factor and importance factor of the structure. The scaling factor is shown by Equation 3.13 below.

$$\Delta = \frac{C_D u}{I_e} \qquad \text{(Equation 3.13)}$$

Where C_D is the deflection amplification factor, u is the calculated lateral deflection from elastic analysis, and I is the importance factor. Similar to the R factor determined earlier, the deflection amplification factor is dependent on the lateral force resisting system under analysis. For steel intermediate moment resisting frames, such as the one-story, two-story, and three-story shear frames, the C_D value is equal to four. Also, as previously determined, the importance factor of the three shear frames is equal to one. Applying Equation 3.13 to the lateral deflection values in Table 2 results in the design deflection values shown in Table 3 on the following page.

Table 3: Scaled Lateral Deflections - ELFP

	Design Floor Deflections		
	U_1 (in.)	U_2 (in.)	U_3 (in.)
One-Story	0.6168	N/A	N/A
Two-Story	1.3880	2.2428	N/A
Three-Story	2.1592	3.9184	4.8780

Lastly, Abaqus, a finite element analysis software, is used to visualize the unfactored deflected shapes of the three shear frames. The deflected shape for the one-story, two-story, and three-story shear frames subject to the lateral forces calculated using the ELFP are shown below in Figure 4, Figure 5, and Figure 6, respectively.

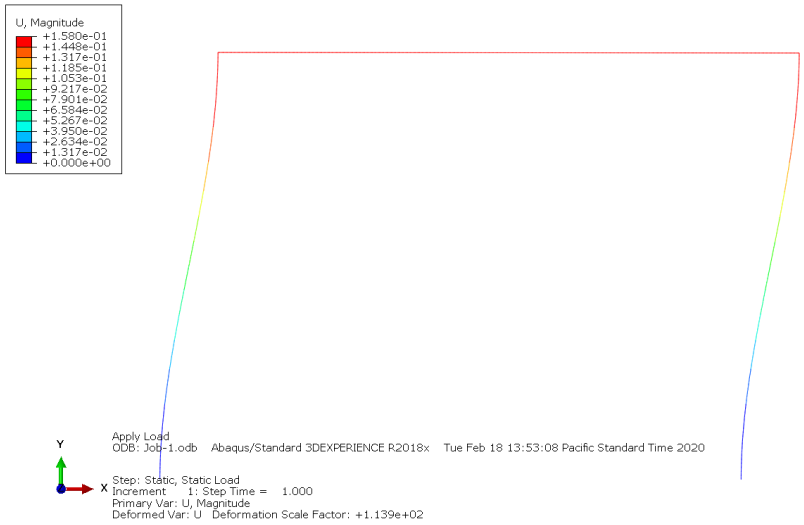

Figure 4: One-Story Shear Frame Deflected Shape - ELFP

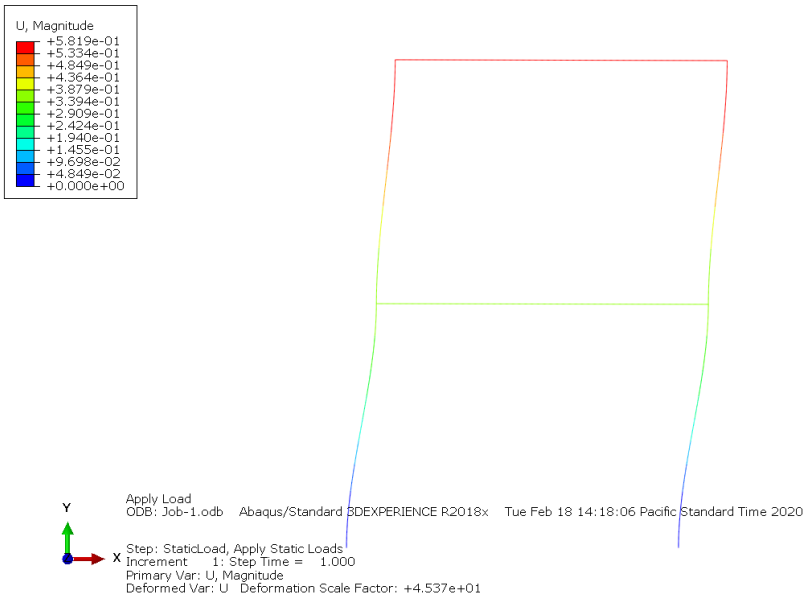

Figure 5: Two-Story Shear Frame Deflected Shape - ELFP

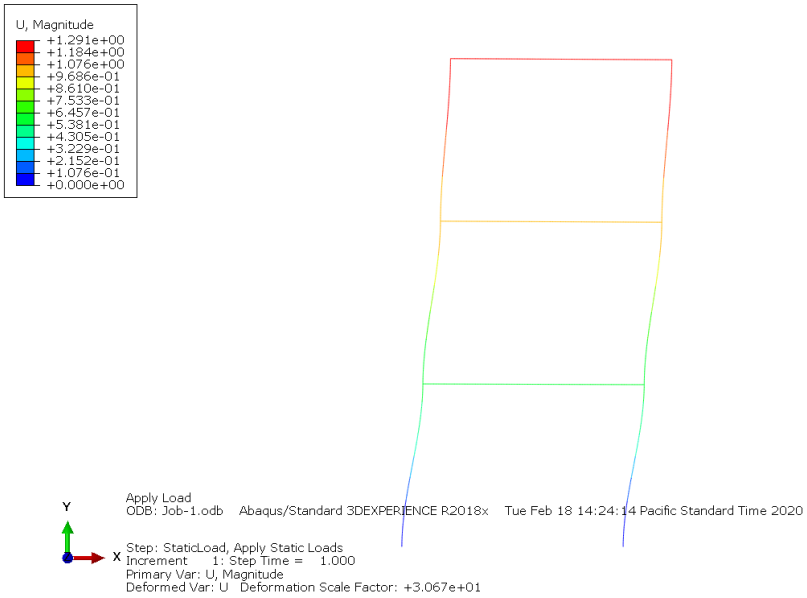

Figure 6: Three-Story Shear Frame Deflected Shape - ELFP

As shown in the above figures, the values for the displacements slightly vary from the results obtained from the exact MATLAB analysis. The slight discrepancies are due to the seed size and element type chosen in the Abaqus

model. Despite the differences, each Abaqus plot serves as a great visualization tool for understanding the behavior of the three shear frames under lateral loads.

3.6 Summary

The subsequent chapters in this study analyze the three shear frames using dynamic analysis. The principles of mechanics and the analysis methods detailed herein are applied throughout this study to determine the dynamic responses of the shear frames. Furthermore, the lateral forces and displacement values calculated through the ELFP and matrix structural analysis are compared with the results obtained from modal analysis in the subsequent chapters of this study.

4. Modal Response Spectrum Analysis

In this chapter, the principles of structural dynamics are introduced and applied to the one-story, two-story, and three-story shear frames. The results obtained throughout this chapter serve as a basis for applying time-history analysis (THA) to the shear frames. Although the ELFP serves as a code-based method for seismic design, it is important to consider the limitations of the ELFP. First, the ELFP attempts to simulate dynamic seismic loads through static lateral forces. Despite the fact that the ELFP produces displacements in the shear frames, horizontal ground accelerations are by nature dynamic and unpredictable. Secondly, the ELFP only considers the first natural frequency of vibration of the system. For most systems, the first natural frequency of vibration is the most impactful, but when considering systems with Multiple Degrees of Freedom (MDOF) such as the two-story and three-story shear frame, the natural frequencies of vibration for the higher DOFs impact the response. In a Single Degree of Freedom System (SDOF), the first and only fundamental period of vibration defines a system's response.

4.1 Dynamic Analysis

Structural dynamics applies the principles of structural analysis touched on in the previous chapter, to structures subject to time-dependent (dynamic) loads. A time-dependent load refers to any load that is a function of time. For example, earthquake ground accelerations, wind loads, or cars travelling across a bridge are all time-dependent loads. In areas of high seismicity, such as California, the dynamic responses of structures under earthquake ground

motions serve as a critical portion of a structure's design. Failure to perform dynamic analysis on a structure in California will increase the probability of its failure under dynamic loading.

Obviously, structural dynamics is very broad and carries many different engineering applications, so it is important to consider the type of system under analysis. Before beginning a dynamic analysis, it is important to consider whether the system is a SDOF or MDOF system, whether the system is damped or undamped, and what type of dynamic load is applied to the system.

First, as prefaced, the number of DOFs in the system governs the dynamic analysis performed on the system. Secondly, whether the system is damped or undamped defines the equation of motion used in the dynamic analysis. Realistically, every real-world physical system will have damping effects due to the connections and materials used, but in some analysis cases the effects of damping are ignored. Also, systems can include classical or nonclassical damping mechanisms. Although viscous damping is typically assumed, in the succeeding chapters of this work, friction spring dampers (FSDs) are detailed and included in the THA of the three shear frames. Thirdly, the process of dynamic analysis relies heavily on the type of dynamic loading applied to the system. For the three shear frames, the dynamic load is a result of horizontal earthquake ground accelerations, but if periodic loads, impulse loads, harmonic excitations, or free vibrations are applied, the process of dynamic analysis varies significantly. Additionally, the dynamic response of a system depends on the rate of the loading relative to the system frequencies.

The basis for the governing equation of motion used in structural dynamics derives from Newton's Second Law of Motion, which states force is equal to the product of mass and acceleration. To derive the governing equation of motion using Newton's Second Law of Motion, a free-body diagram (FBD) of a SDOF system is drawn and a simple summation of the forces is performed resulting in Equation 4.1.

$$m\ddot{u} + c\dot{u} + ku = p(t) \qquad \text{(Equation 4.1)}$$

Where mü is the mass multiplied by the acceleration, cu̇ is the damping coefficient multiplied by the velocity, ku is the stiffness multiplied by the displacement, and p(t) is the dynamic forcing function. Understanding how each product of Equation 4.1 effects the vibrations of a system is critical for dynamic analysis. A quick analysis of Equation 4.1 shows that each product results in consistent units allowing for them to be summed together. Equation 4.1 is also applicable for MDOF systems. The governing equation of motion in matrix notation is shown below in Equation 4.2.

$$M\ddot{u} + C\dot{u} + Ku = P(t) \qquad \text{(Equation 4.2)}$$

Where the mass, damping coefficients, and stiffness coefficients are matrices, and the forcing function is a vector. For the one-story shear frame, the scalar form of the governing equation shown in Equation 4.1 is applicable, but for the two-story and three-story shear frames, Equation 4.2 is necessary.

One of the primary goals of structural dynamics is to determine the natural frequencies and periods of vibration of the structure. The naturally period of vibration refers to the period that the system will oscillate at naturally due to its

stiffness and mass properties. From the natural frequency, the natural period of vibration can be calculated through Equation 4.3.

$$T_n = \frac{2\pi}{w_n} \qquad \text{(Equation 4.3)}$$

Where T_n is the natural period of vibration, and w_n is the natural frequency of vibration. In a SDOF system, the natural and fundamental period of vibration are the same, but for a MDOF system, the fundamental period of vibration refers to the largest natural period of vibration of the system.

Generally, a primary goal of seismic design is to prevent the structural system from oscillating at its natural period and vibrating at its natural frequency. If the dynamic loading function and the natural frequency of a structural system are in harmony, the oscillations will be amplified, resulting in a system that is in resonance. When a system is in resonance, the displacements and forces are at a maximum, significantly increasing the response. Consequently, systems in resonance are more likely to endure significant damages or even collapse under the dynamic loading. In order to calculate the natural frequency of vibration for a SDOF system, Equation 4.4 is used.

$$w_n = \sqrt{\frac{k}{m}} \qquad \text{(Equation 4.4)}$$

Where k is the stiffness of the system, and m is the mass of the system. The formerly derived stiffness coefficients are used to determine the stiffness of a system. Although the entire stiffness matrix for a frame element is derived in Chapter 3, only the stiffness coefficients for lateral or shear displacements are

applicable for shear frames. The hand calculations for the natural frequency and period of vibration for the SDOF system in Figure 7 are shown below.

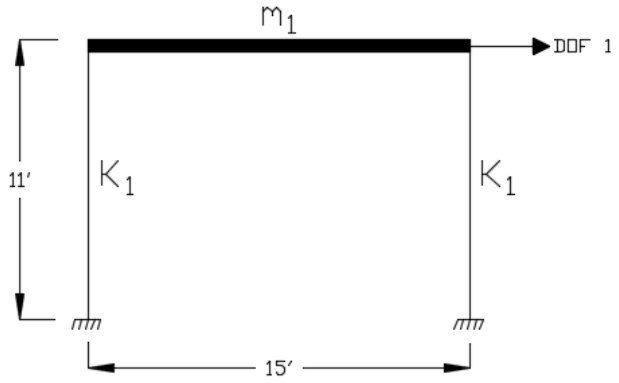

Figure 7: One-Story Shear Frame Dynamic Model

$$m_1 = \frac{W}{g} = \frac{80kips}{386.4\frac{in}{s^2}} = 0.20704\frac{kips}{in}s^2$$

$$K = 2K_1 = 2 * \frac{12EI}{L^3} = \frac{24(29000ksi)(300in^4)}{(132in)^3} = 90.78\frac{kips}{in}$$

$$w_n = \sqrt{\frac{k}{m}} = \sqrt{\frac{90.78\frac{kips}{in}}{0.20704\frac{kips}{in}s^2}} = 20.94\frac{rad}{s}$$

$$T_n = \frac{2\pi}{w_n} = \frac{2\pi}{20.94\frac{rad}{s}} = 0.3001s$$

For a MDOF system, the governing equation of motion for an undamped system in free vibration is used to derive Equation 4.5. Equation 4.5 is a generalized eigen value problem and relates the stiffness and mass matrices of the system with its matrix of mode shapes.

$$[K - w^2M]\phi = 0 \qquad \text{(Equation 4.5)}$$

Where K, M, and ϕ are the stiffness, mass, and mode shape matrices, respectively. To determine the natural frequencies of a MDOF system, properties of linear algebra are applied to Equation 4.5 (Goode & Annin, 2007). First, in order to solve Equation 4.5, each side of the equation must be multiplied by the inverse of $[K - w^2M]$ to separate the two matrices. Consider the case shown below in which $[K - w^2M]^{-1}$ is multiplied on each side of Equation 4.5.

$$[K - w^2M]^{-1}[K - w^2M]\phi = [K - w^2M]^{-1}0$$

$$\phi = [K - w^2M]^{-1}0$$

The result of multiplying each side by $[K - w^2M]^{-1}$ is a trivial solution, meaning a solution of only zeros. Obviously, a constant solution of all zeros for Equation 4.5 serves no purpose, which means the inverse of the matrix, $[K - w^2M]$, must not exist if Equation 4.5 is to produce a nontrivial solution. Recall from linear algebra that the inverse of a matrix does not exist if and only if the determinant of that matrix is equal to zero. Therefore, the determinant of $[K - w^2M]$ must be equal to zero in order for Equation 4.5 to yield a nontrivial solution.

By definition, the linear algebra proof used to obtain a nontrivial solution is an eigenvalue problem. The eigenvalues resulting from Equation 4.6 shown below are equal to the squared natural periods of vibration of the system. To conceptually understand the eigenvalue problem, the properties of Equation 4.5 and Equation 4.6 are analyzed. In both of the equations, the stiffness and mass matrices are known system properties; therefore, there are explicit values of each squared natural frequency that result in a nontrivial solution. The validity of

Equation 4.6 relies on the values of the squared natural frequencies, which by definition means they are eigenvalues. In Equation 4.6 shown below, the squared natural periods of vibration are substituted with a lambda (λ), which is commonly used in linear algebra to denote eigenvalues. Also, since the mass and stiffness matrices are symmetric, and the stiffness matrix is positive definite, the eigenvalues (λ) will be strictly positive.

$$det[K - \lambda M] = 0 \qquad \text{(Equation 4.6)}$$

In the cases of the MDOF two-story and three-story shear frame, Equation 4.6 is applicable. Figure 8, shown below, displays a model of the two-story shear frame, which is used for calculating the natural frequencies and periods of the system.

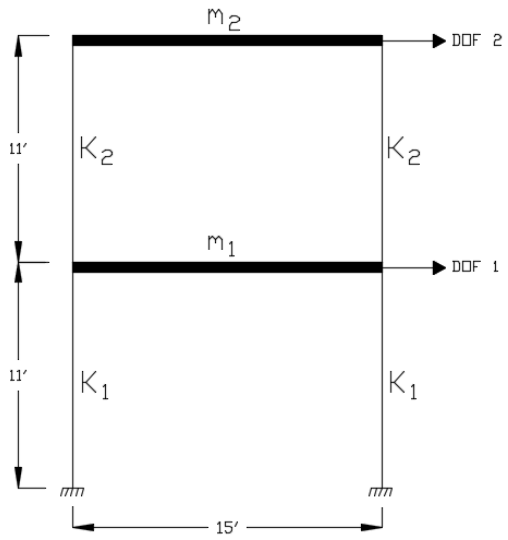

Figure 8: Two-Story Shear Frame Dynamic Model

In order to complete dynamic analysis on a MDOF system, a properly defined model is critical for maintaining consistency throughout the calculations. Without a defined model, the various stiffness and mass values, as well as the

responses at each DOF lack context. With reference to Figure 8, the hand calculations for determining the natural frequencies and periods of vibration for the two-story shear frame are shown below.

$$m_1 = \frac{W_1}{g} = \frac{100kips}{386.4\frac{in}{s^2}} = 0.25880\frac{kips}{in}s^2$$

$$m_2 = \frac{W_2}{g} = \frac{80kips}{386.4\frac{in}{s^2}} = 0.20704\frac{kips}{in}s^2$$

$$M = \begin{bmatrix} 0.25880 & 0 \\ 0 & 0.20704 \end{bmatrix}\frac{k}{in}s^2$$

$$K_1 = K_2 = \frac{12EI}{L^3} = \frac{12(29000ksi)(300in^4)}{(132in)^3} = 45.39\frac{k}{in}$$

$$K = \begin{bmatrix} 2K_1 + 2K_2 & -2K_1 \\ -2K_2 & 2K_2 \end{bmatrix} = \begin{bmatrix} 181.57 & -90.78 \\ -90.78 & 90.78 \end{bmatrix}\frac{k}{in}$$

$$\det[K - \lambda M] = 0$$

$$det\begin{bmatrix} 181.57 - \lambda 0.25880 & -90.78 \\ -90.78 & 90.78 - \lambda 0.20704 \end{bmatrix} = 0$$

$$Recall\text{: } \det(A) = |A| = \begin{vmatrix} a & b \\ c & d \end{vmatrix} = ad - cb$$

$$(181.57 - \lambda 0.25880)(90.78 - \lambda 0.20704) - (-90.78)^2 = 0$$

$$0.0536\lambda^2 - 61.087\lambda + 8241.73 = 0$$

$$\lambda_1 = 156.36,\ \lambda_2 = 983.70$$

$$w_{n1} = \sqrt{\lambda_1} = 12.51\frac{rad}{s}\ , w_{n2} = \sqrt{\lambda_2} = 31.36\frac{rad}{s}$$

$$T_{n1} = \frac{2\pi}{w_{n1}} = 0.5025s\ , T_{n2} = \frac{2\pi}{w_{n2}} = 0.2003s$$

For systems with high numbers of active DOFs, the application of numerical tools significantly reduces the computational effort of the eigen value

problem (Kasper & Hall, 2018). Thus, for the three-story shear frame, the natural periods and frequencies are calculated using MATLAB code. Figure 9, shown below, exhibits the model of the three-story shear frame. In addition to Figure 9, the results of the dynamic analysis are shown in Table 4.

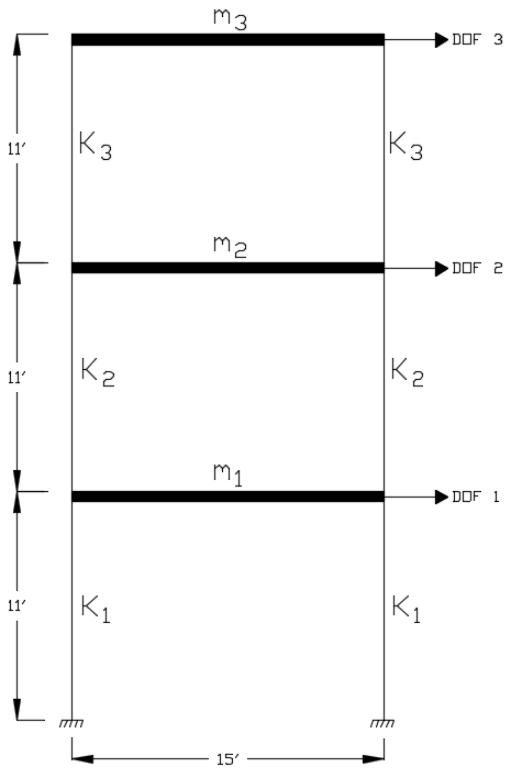

Figure 9: Three-Story Shear Frame Dynamic Model

Table 4: Three-Story Shear Frame Dynamic Results

	T_{n1} (s)	w_{n1} (rad/s)	T_{n2} (s)	w_{n2} (rad/s)	T_{n3} (s)	w_{n3} (rad/s)
One-Story	0.3001	20.94	N/A	N/A	N/A	N/A
Two-Story	0.5025	12.51	0.2003	31.36	N/A	N/A
Three-Story	0.7123	8.82	0.2584	24.32	0.1835	34.24

Once the natural frequencies and periods of vibration are calculated, the mode shapes or eigenvectors in Equation 4.5 are calculated. In modal analysis, the mode shapes represent the deformed shape of the system at each natural

frequency. Simply put, the mode shapes represent the natural deformation pattern of a system during free vibration. As evidenced in Equation 4.5, the mode shapes are dependent on the mass and stiffness properties of the system. When using Equation 4.5 to calculate the mode shapes, it is important to consider the rank-deficiency of the equation. As shown by the hand calculations for the two-story shear frame below, each mode shape calculation contains two equations, but both equations yield the exact same result. Consequently, Equation 4.5 is rank-deficient by one. One method for resolving the issue of rank-deficiency is to set the first value in each mode equal to one. Additionally, making the eigenvector a unit vector results in a solution, which is generally applied in MATLAB when solving the eigenvalue problem. The process of setting the first value equal to one simply normalizes the values of the mode shapes to a reference value of one. An example of how to calculate the mode shapes by hand for the two-story shear frame, shown in Figure 8, using Equation 4.5 is presented below.

$$[K-\lambda_i M]\begin{Bmatrix}\phi_{1i}\\ \phi_{2i}\end{Bmatrix}=\begin{bmatrix}181.57-\lambda_i 0.25880 & -90.78\\ -90.78 & 90.78-\lambda_i 0.20704\end{bmatrix}\begin{Bmatrix}\phi_{1i}\\ \phi_{2i}\end{Bmatrix}=\begin{Bmatrix}0\\ 0\end{Bmatrix}$$

$$1.\ First\ Mode\ Shape\colon \lambda_i = 156.36$$

$$\begin{bmatrix}181.57-(156.36)0.25880 & -90.78\\ -90.78 & 90.78-(156.36)0.20704\end{bmatrix}\begin{Bmatrix}\phi_{11}\\ \phi_{21}\end{Bmatrix}=\begin{Bmatrix}0\\ 0\end{Bmatrix}$$

$$\begin{bmatrix}141.10 & -90.78\\ -90.78 & 58.41\end{bmatrix}\begin{Bmatrix}\phi_{11}\\ \phi_{21}\end{Bmatrix}=\begin{Bmatrix}0\\ 0\end{Bmatrix}$$

$$141.10\phi_{11}-90.78\phi_{21}=0$$

$$-90.78\phi_{11}+58.41\phi_{21}=0$$

$$Normalize\ the\ equations\colon \phi_{11}=1$$

$$141.10 - 90.78\phi_{21} = 0 \rightarrow \ \phi_{21} = 1.554$$

$$-90.78 + 58.41\phi_{21} = 0 \rightarrow \ \phi_{21} = 1.554$$

$$\phi_1 = \begin{Bmatrix} \phi_{11} \\ \phi_{21} \end{Bmatrix} = \begin{Bmatrix} 1 \\ 1.554 \end{Bmatrix}$$

$$2.\ Second\ Mode\ Shape: \lambda_i = 983.70$$

$$\begin{bmatrix} 181.57 - (983.70)0.25880 & -90.78 \\ -90.78 & 90.78 - (983.70)0.20704 \end{bmatrix} \begin{Bmatrix} \phi_{12} \\ \phi_{22} \end{Bmatrix} = \begin{Bmatrix} 0 \\ 0 \end{Bmatrix}$$

$$\begin{bmatrix} -73.01 & -90.78 \\ -90.78 & -112.89 \end{bmatrix} \begin{Bmatrix} \phi_{12} \\ \phi_{22} \end{Bmatrix} = \begin{Bmatrix} 0 \\ 0 \end{Bmatrix}$$

$$-73.01\phi_{12} - 90.78\phi_{22} = 0$$

$$-90.78\phi_{12} - 112.89\phi_{22} = 0$$

$$Normalize\ the\ equations: \phi_{12} = 1$$

$$-73.01 - 90.78\phi_{22} = 0 \rightarrow \ \phi_{22} = 1.554$$

$$-90.78 - 112.89\phi_{22} = 0 \rightarrow \ \phi_{22} = 1.554$$

$$\phi_2 = \begin{Bmatrix} \phi_{12} \\ \phi_{22} \end{Bmatrix} = \begin{Bmatrix} 1 \\ -0.804 \end{Bmatrix}$$

$$\phi = \begin{bmatrix} 1 & 1 \\ 1.554 & -0.804 \end{bmatrix}$$

Once again, implementing MATLAB code significantly simplifies the computing process of calculating the mode shapes. The modes shapes of the two-story and three-story shear frame are calculated in MATLAB and shown in Table 5 on the following page.

Table 5: Matrix of Mode Shapes

	Matrix of Mode Shapes
Two-Story	$\phi = \begin{bmatrix} -1.1479 & -1.5957 \\ -1.7841 & 1.2834 \end{bmatrix}$
Three-Story	$\phi = \begin{bmatrix} -0.6993 & 1.4865 & -1.0794 \\ -1.2435 & 0.4671 & 1.4490 \\ -1.5119 & -1.3398 & -0.8656 \end{bmatrix}$

In Table 5, each column of the matrix represents a mode shape of the system. It is important to note the differences between the matrix of mode shapes produced from hand calculations and MATLAB. As previously stated, due to the rank-deficiency, the first value in each mode shape is normalized to one when calculating by hand. On the contrary, the MATLAB results are normalized in accordance with Equation 4.7 below.

$$1 = \sqrt{\phi_i^T M \phi_i} \qquad \text{(Equation 4.7)}$$

Where ϕ_i is the vector of mode shapes and M is the mass matrix. To understand the principle behind normalization, the results from MATLAB are normalized to one by dividing each column by the first value in the respective column. The process of normalizing the MATLAB results to one for the two-story shear frame is shown below.

$$\phi = \begin{bmatrix} -1.1479 & -1.5957 \\ -1.7841 & 1.2834 \end{bmatrix} \rightarrow \text{Matlab Results}$$

1. Divide the first mode shape by the first value in the column

$$\phi_1 = \begin{Bmatrix} \frac{-1.1479}{-1.1479} \\ \frac{-1.7841}{-1.1479} \end{Bmatrix} = \begin{Bmatrix} 1 \\ 1.554 \end{Bmatrix}$$

2. Divide the second mode shape by the first value in the column

$$\phi_2 = \begin{Bmatrix} \frac{-1.5957}{-1.5957} \\ \frac{1.2834}{-1.5957} \end{Bmatrix} = \begin{Bmatrix} 1 \\ -0.804 \end{Bmatrix}$$

From the calculation above, it is clear to see that normalizing the MATLAB results yields mode shapes that are identical with the mode shapes obtained through the hand calculations. Furthermore, Table 6 presents the normalized matrix of mode shapes for the two-story and three-story shear frame, which are used to determine the modal participation factors in the subsequent section.

Table 6: Normalized Matrix of Mode Shapes

	Normalized Matrix of Mode Shapes
Two-Story	$\phi = \begin{bmatrix} 1.000 & 1.000 \\ 1.554 & -0.804 \end{bmatrix}$
Three-Story	$\phi = \begin{bmatrix} 1.000 & 1.000 & 1.000 \\ 1.778 & 0.314 & -1.342 \\ 2.162 & -0.901 & 0.802 \end{bmatrix}$

4.2 Response Spectrum Analysis

Given the properties of the systems (I, E, T_n, ϕ_n), response spectrum analysis (RSA) is used to determine the maximum responses of each individual shear frame. In seismic design, it is common to use specific earthquake response spectrums, but in this study, a simplified design response spectrum is developed and applied to the shear frames. Section 11.4.5 of ASCE 7-10 provides a process for developing a simplified design response spectrum based

off of site-specific quantities. Figure 10, shown below, which was taking directly from ASCE 7-10, shows the parameters for creating a simplified design spectrum.

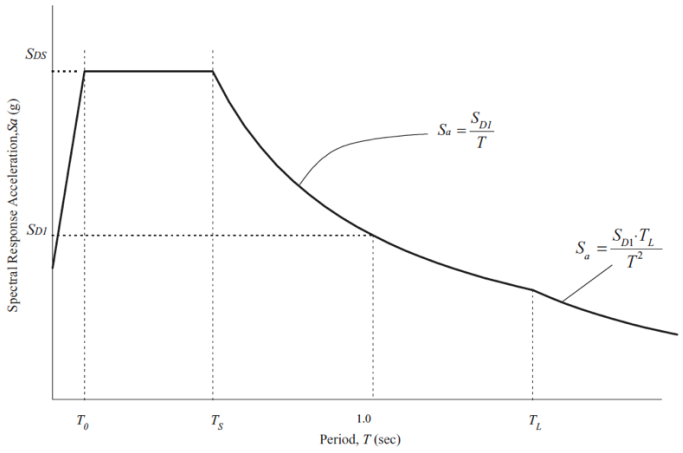

Figure 10: ASCE 7-10 Simplified Design Spectrum

(Source: ASCE 7-10)

In this study, the site-specific quantities for San Luis Obispo, CA, shown in Table 1 and Appendix A, are used to create a design response spectrum for the three shear frames. The design response spectrum for a site location in San Luis Obispo, CA is shown in Figure 11 below.

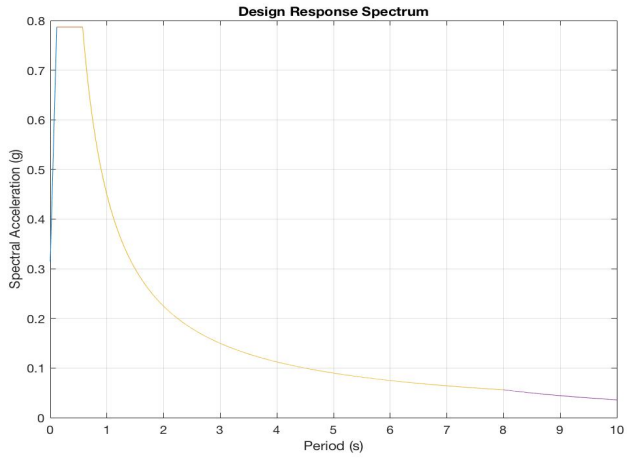

Figure 11: Simplified Design Spectrum – San Luis Obispo, CA 93407

The design response spectrum shown in Figure 11 is developed in MATLAB and adheres to the ASCE 7-10 standards shown in Figure 10. It is important to note that the site-specific quantities assume 5% damping. Now that the design response spectrum for San Luis Obispo, CA, is developed, the maximum displacement response is calculated for the shear frames. The simplified design response spectrum detailed in ASCE 7-10, and shown by Figure 10, is not applicable to all structures. In many cases, an exact response spectrum is required, but this is not the case for the shear frames analyzed herein.

It is important to consider that the equations for determining the displacement response through the design response spectrum use the pseudo spectral accelerations. Since the shear frames are considered to be undamped, the pseudo spectral accelerations are assumed to be the same as the spectral accelerations, which are used in Figure 11. In addition, it is important to note that determining the system responses from the pseudo spectral accelerations yields the most accurate results when compared with other factors such as velocity. To calculate the relative displacements from the design response spectrum, Equation 4.8 is applied.

$$PS_A = w^2 S_D \qquad \text{(Equation 4.8)}$$

Where PS_A is the pseudo spectral acceleration, w^2 is the squared natural period of vibration, and S_D is the relative displacement.

Due to the orthogonality of the modes of vibration, the simplified design response spectrum can be applied to SDOF and MDOF systems. For MDOF

systems, such as the two-story and three-story shear frames, the responses at each mode are calculated and then combined to produce a maximum displacement response. According to ASCE 7-10, the permitted modal combination methods are the Square-Root-of-Sum-of-Squares (SRSS) method, the Complete Quadratic Combination (CQC) method, and the modified Complete Quadratic Combination (CQC-4) method.

The governing formula for combining the modal responses using the SRSS and CQC methods is shown in Equation 4.9 below.

$$R_{MAX} = \sqrt{\sum_{i=1}^{n}\sum_{j=1}^{n}\rho_{ij}R_iR_j} \qquad \text{(Equation 4.9)}$$

Where R_{MAX} is the maximum modal response, ρ_{ij} is the modal correlation coefficient, which gives an indication of the interactions between modes i and j, and R_i and R_j are the spectral responses at modes i and j, respectively.

When combining the modal responses using the SRSS method, the correlation coefficient is either one, when i is equal to j, or zero, when i is not equal to j. The general formula for the SRSS method is shown in Equation 4.10 below.

$$R_{MAX} = \sqrt{\sum_{i=1}^{n}R_i^2} \qquad \text{(Equation 4.10)}$$

Furthermore, the maximum displacement response using the SRSS method is shown in Equation 4.11 on the following page.

$$|u|_{max} = \sqrt{\sum_{i=1}^{n} (|\phi_i \Gamma_i D_i|)^2} \qquad \text{(Equation 4.11)}$$

Where ϕ_i is the mode shape vector, Γ_i is the modal participation factor, and D_i is the maximum displacement response at mode i. The modal participation factor is a scalar quantity that shows the impact that each individual mode has on the dynamic response of a MDOF system. The larger the modal participation factor, the greater the impact the mode has on the system's response. For example, consider the SDOF one-story shear frame. Since there is only one mode of vibration, the single mode would be responsible for 100% of the system's response resulting in a modal participation factor of one. Equation 4.12 shows one of the many ways that the modal participation is calculated.

$$\Gamma_i = \frac{\phi_i^T P}{\mu_i} \qquad \text{(Equation 4.12)}$$

Where ϕ_i^T is the transpose of the normalized mode shape vector, P is the load distribution, and μ_i is the generalized mass. For a uniform horizontal ground motion, P is equal to M1, which is the mass matrix multiplied by a vector of all ones and represents a unit acceleration at each DOF. Conceptually, when a system is subject to ground motions, the lumped mass at each DOF acts laterally and is the driving force of a system's response. The numerator in Equation 4.12 is referred to as the generalized load. The generalized mass and generalized load refer to mass and stiffness matrices that are in modal coordinates. Equation 4.13 provides a method for transforming the mass matrix from physical to modal coordinates, resulting in the generalized mass.

$$\mu_i = \phi_i^T M \phi_i \qquad \text{(Equation 4.13)}$$

The process for obtaining the modal participation factors for the two-story shear frame is shown below.

$$\mu_1 = [1.000 \quad 1.554]\begin{bmatrix}0.25880 & 0\\ 0 & 0.20704\end{bmatrix}\begin{bmatrix}1.000\\ 1.554\end{bmatrix} = 0.75878$$

$$\mu_2 = [1.000 \quad -0.804]\begin{bmatrix}0.25880 & 0\\ 0 & 0.20704\end{bmatrix}\begin{bmatrix}1.000\\ -0.804\end{bmatrix} = 0.39263$$

$$P = M1 = \begin{bmatrix}0.25880 & 0\\ 0 & 0.20704\end{bmatrix}\begin{bmatrix}1\\ 1\end{bmatrix} = \begin{bmatrix}0.25880\\ 0.20704\end{bmatrix}$$

$$\phi_1^T P = [1.000 \quad 1.554]\begin{bmatrix}0.25880\\ 0.20704\end{bmatrix} = 0.58054$$

$$\phi_2^T P = [1.000 \quad -0.804]\begin{bmatrix}0.25880\\ 0.20704\end{bmatrix} = 0.09234$$

$$\Gamma_1 = \frac{\phi_1^T P}{\mu_1} = \frac{0.58054}{0.75878} = 0.7650$$

$$\Gamma_2 = \frac{\phi_2^T P}{\mu_2} = \frac{0.09234}{0.39263} = 0.2350$$

In addition to the two-story shear frame, the modal participation factors for the three-story shear frame are calculated using MATLAB code. The results for the modal participation factors for the two-story and three-story shear frames are shown below in Table 7.

Table 7: Modal Participation Factors

	Γ_1	Γ_2	Γ_3
Two-Story	0.7650	0.2350	N/A
Three-Story	0.5705	0.3392	0.0903

Lastly, to calculate the maximum displacement response using Equation 4.9, ASCE 7-10 Section 12.9.2 states that the values must be scaled in

accordance with the type of lateral force resisting system used. As detailed in Chapter 3, the shear frames are steel ordinary moment resisting frames with R = 4.5, I_e = 1.0, and C_d = 4.0.

In accordance with the design response spectrum in Figure 11, and the natural periods of vibration in Table 4, the spectral accelerations are individually determined for each mode of the one-story, two-story, and three-story shear frames. The spectral accelerations are found by simply inputting the natural periods of vibration into the design response spectrum in Figure 11 and finding the corresponding spectral acceleration values. The results of the spectral acceleration values are shown in Table 8.

Table 8: Spectral Accelerations

	T_{n1} (s)	S_{A1} (g)	T_{n2} (s)	S_{A2} (g)	T_{n3} (s)	S_{A3} (g)
One-Story	0.3001	0.787	N/A	N/A	N/A	N/A
Two-Story	0.5025	0.787	0.2003	0.787	N/A	N/A
Three-Story	0.7123	0.630	0.2584	0.787	0.1835	0.787

With the spectral accelerations in Table 8, the SRSS method is applied to the shear frames to determine the maximum displacement response at each DOF. The hand-calculations for the two-story shear frame using the SRSS method, along with the results, which are presented in Table 9, are shown on the following page.

$$S_{D1} = \frac{S_{A1}}{w_{n1}^2} = \frac{0.786g\left(386.4\frac{in}{s^2}\right)}{\left(12.51\frac{rad}{s}\right)^2} = 1.9431"$$

$$D_1 = S_{D1} * \frac{\frac{C_d}{I_e}}{\frac{R}{I_e}} = (1.9431") * \frac{\frac{4}{1}}{\frac{4.5}{1}} = 1.7272"$$

$$S_{D2} = \frac{S_{A2}}{w_{n2}^2} = \frac{0.786g\left(386.4\frac{in}{s^2}\right)}{\left(31.36\frac{rad}{s}\right)^2} = 0.3092"$$

$$D_2 = S_{D2} * \frac{\frac{C_d}{I_e}}{\frac{R}{I_e}} = (0.3092") * \frac{\frac{4}{1}}{\frac{4.5}{1}} = 0.2749"$$

$$|u|_{1MAX} = \sqrt{(\phi_{11}\Gamma_1 D_1)^2 + (\phi_{12}\Gamma_2 D_2)^2}$$

$$|u|_{1MAX} = \sqrt{(1.000 * 0.7650 * 1.7272)^2 + (1.000 * 0.2350 * 0.2749)^2}$$

$$|u|_{1MAX} = 1.3229"$$

$$|u|_{2MAX} = \sqrt{(\phi_{21}\Gamma_1 D_1)^2 + (\phi_{22}\Gamma_2 D_2)^2}$$

$$|u|_{2MAX} = \sqrt{(1.554 * 0.7650 * 1.7272)^2 + (-0.804 * 0.2350 * 0.2749)^2}$$

$$|u|_{2MAX} = 2.0543"$$

Table 9: Displacement Response – SRSS

	$u_{1(max)}$ (in.)	$u_{2(max)}$ (in.)	$U_{3(max)}$ (in.)
One-Story	0.6168	N/A	N/A
Two-Story	1.3229	2.0543	N/A
Three-Story	1.5872	2.8172	3.4308

In the SRSS hand-calculations for the two-story shear frame, the maximum displacement response is specific to each mode or DOF, but the u_{MAX} variable in Equation 4.11 does not have a subscript to denote the maximum response of each specific DOF. Although the notation in Equation 4.11 is adequate because ϕ_i and u are vectors, Equation 4.14 better illustrates how the SRSS method yields individual responses at each DOF.

$$\begin{Bmatrix} |u_1|_{MAX} \\ |u_2|_{MAX} \end{Bmatrix} = \sqrt{\sum_{i=1}^{n} (|\phi_i \Gamma_i D_i|)^2} = \sqrt{\left(\begin{Bmatrix} \phi_{11} \\ \phi_{21} \end{Bmatrix} \Gamma_1 D_1 \right)^2 + \left(\begin{Bmatrix} \phi_{12} \\ \phi_{22} \end{Bmatrix} \Gamma_2 D_2 \right)^2} \quad \text{(Equation 4.14)}$$

In general, for SDOF systems, the modal combination methods are unnecessary. For example, the modal participation factor and mode shape vector are both equal to one for the one-story shear frame, which results in a maximum displacement that is equal to the maximum displacement response of the singular mode. Although unnecessary, the modal combination methods are self-consistent, and still yield the correct answer if applied to a SDOF system.

In addition to the SRSS method, other modal combination methods, such as the Complete Quadratic Combination (CQC) method, are used to determine the maximum modal response. Unlike the SRSS method, which assumes values of one or zero, the CQC method calculates the correlation coefficients through Equation 4.15 below (Wilson et al., 1981).

$$\rho_{ij} = \frac{8\sqrt{\zeta_n \zeta_m}(\zeta_n + r\zeta_m) r^{1.5}}{(1 - r^2)^2 + 4\zeta_n \zeta_m r(1 + r)^2 + 4(\zeta_n^2 + \zeta_m^2) r^2} \quad \text{(Equation 4.15)}$$

Where ρ_{ij} is the correlation coefficient between modes i and j, ζ_n is the damping coefficient for mode n, ζ_m is the damping coefficient for mode m, and r is equal to w_j divided by w_i. Furthermore, Equation 4.15 reduces to Equation 4.16 for systems with constant damping.

$$\rho_{ij} = \frac{8\zeta^2(1 + r) r^{1.5}}{(1 - r^2)^2 + 4\zeta^2 r(1 + r)^2} \quad \text{(Equation 4.16)}$$

Typically, when the natural frequencies of a system are well-spaced, the correlation coefficients are small. For example, consider Figure 12, which shows

the relationship between the correlation coefficient and the ratio of natural frequencies (Chopra, 1995).

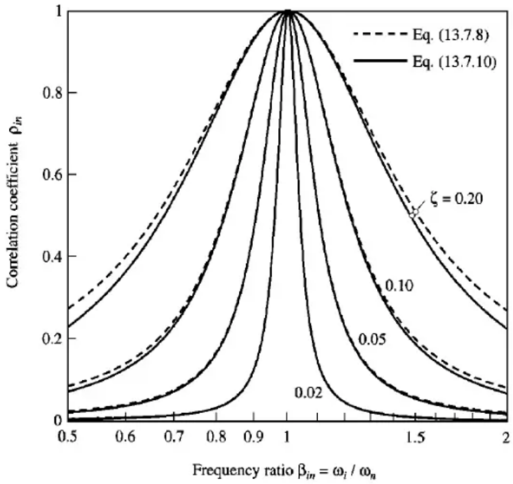

Figure 12: CQC Method Correlation Coefficient Relationship

(Source: Chopra 1995)

In Figure 12, the correlation coefficients are denoted as ρ_{in} and β_{in}, respectively, where i and n are the modes. As shown, the correlation coefficients are relatively small unless the ratio of the natural frequencies is high. For 5% damping, a natural frequency ratio of 75% still yields a correlation coefficient less than 0.2. Consequently, when the natural frequency ratios are small, the interaction between modes is small, and the CQC method essentially reduces to the SRSS method. On the contrary, when the natural frequencies are closely spaced, such as in three-dimensional structures or irregular structures, the correlation coefficient amplifies, and the CQC method yields better results.

Now, using Equation 4.9 in combination with Equation 4.16, the hand-calculations for the two-story shear frame using the CQC method, along with the results, which are presented in Table 10, are shown below.

$$r_{11} = \frac{w_{1n}}{w_{1n}} = \frac{12.51\frac{rad}{s}}{12.51\frac{rad}{s}} = 1$$

$$r_{12} = \frac{w_{2n}}{w_{1n}} = \frac{31.36\frac{rad}{s}}{12.51\frac{rad}{s}} = 2.5068$$

$$r_{21} = \frac{w_{1n}}{w_{2n}} = \frac{12.51\frac{rad}{s}}{31.36\frac{rad}{s}} = 0.3989$$

$$r_{22} = \frac{w_{2n}}{w_{2n}} = \frac{31.36\frac{rad}{s}}{31.36\frac{rad}{s}} = 1$$

$$\rho_{11} = \rho_{22} = \frac{8(0.05)^2(1+1)1^{1.5}}{(1-1^2)^2 + 4(0.05)^2(1)(1+1)^2} = 1$$

$$\rho_{12} = \frac{8(0.05)^2(1+2.5068)2.5068^{1.5}}{(1-2.5068^2)^2 + 4(0.05)^2(2.5068)(1+2.5068)^2} = 0.00985$$

$$\rho_{21} = \frac{8(0.05)^2(1+0.3989)0.3989^{1.5}}{(1-0.3989^2)^2 + 4(0.05)^2(0.3989)(1+0.3989)^2} = 0.00985$$

$$R_{11} = \phi_{11}\Gamma_1 D_1 = (1.000)(0.7650)(1.7272) = 1.32131"$$

$$R_{12} = \phi_{12}\Gamma_2 D_2 = (1.000)(0.2350)(0.2749) = 0.06459"$$

$$R_{21} = \phi_{21}\Gamma_1 D_1 = (1.554)(0.7650)(1.7272) = 2.05344"$$

$$R_{22} = \phi_{22}\Gamma_2 D_2 = (-0.804)(0.2350)(0.2749) = -0.05193"$$

$$u_{MAX} = \sqrt{\begin{Bmatrix}\rho_{11}R_{11}R_{11} + \rho_{12}R_{11}R_{12} + \rho_{21}R_{12}R_{11} + \rho_{22}R_{12}R_{12} \\ \rho_{11}R_{21}R_{21} + \rho_{12}R_{21}R_{22} + \rho_{21}R_{22}R_{21} + \rho_{22}R_{22}R_{22}\end{Bmatrix}} = \begin{Bmatrix}1.3236" \\ 2.0538"\end{Bmatrix}$$

$$|u|_{1MAX} = 1.3236"$$

$$|u|_{2MAX} = 2.0538"$$

Table 10: Displacement Response - CQC

	$u_{1(max)}$ (in.)	$u_{2(max)}$ (in.)	$U_{3(max)}$ (in.)
One-Story	0.6168	N/A	N/A
Two-Story	1.3236	2.0538	N/A
Three-Story	1.5882	2.1874	3.4300

Similar to the SRSS method, the maximum response variable in Equation 4.9, R_{max}, for the CQC method does not have a subscript to denote the maximum response at each DOF. Although Equation 4.9 is adequate, Equation 4.17 better clarifies how the CQC method yields the maximum responses at each DOF.

$$R_{\alpha_{MAX}} = \sqrt{\sum_{i=1}^{n}\sum_{j=1}^{n}\rho_{ij}R_{\alpha i}R_{\alpha j}} \qquad \text{(Equation 4.17)}$$

Where α refers to the DOF at which the response occurs. Equation 4.17 is derived from the hand-calculations of the two-story shear frame using the CQC method. Through analysis of the individual components of the summation for the response at each DOF, Equation 4.17 was developed to better illustrate the relationship between the modes, i and j, and the DOF, α, which is not shown by Equation 4.9.

Lastly, although not permitted by ASCE 7-10, the Absolute Sum (ABS) method is used to combine the modal responses. The general formula for the ABS method is shown below in Equation 4.18.

$$R_{MAX} = \sum_{i=1}^{n}|R_i| \qquad \text{(Equation 4.18)}$$

The ABS method assumes that the peak responses at each mode are positive and occur at the same time. Generally, the ABS method results in the highest peak total response. The results of the ABS method are shown below in Table 11.

Table 11: Displacement Response - ABS

	$u_{1(max)}$ (in.)	$u_{2(max)}$ (in.)	$U_{3(max)}$ (in.)
One-Story	0.6168	N/A	N/A
Two-Story	1.3859	2.1056	N/A
Three-Story	1.7049	2.8640	3.5376

4.3 RSA Results and Discussion

First, the maximum modal displacement responses obtained from the SRSS, CQC, and ABS method are compared. The percent difference of the CQC and ABS results when compared with the SRSS results for the two-story and three-story shear frame are shown on the following page in Table 12 and Table 13, respectively.

Table 12: Two-Story Modal Combination Results

	SRSS	CQC	ABS	CQC Diff.	ABS Diff.
u_1	1.3229”	1.3236”	1.3859”	0.0529%	4.7623%
u_2	2.0543”	2.0538”	2.1056”	0.0243%	2.4972%

Table 13: Three-Story Modal Combination Results

	SRSS	CQC	ABS	CQC Diff.	ABS Diff.
u_1	1.5872”	1.5882”	1.7049”	0.0630%	7.4156%
u_2	2.8172”	2.8174”	2.8640”	0.0071%	1.6612%
u_3	3.4308”	3.4300”	3.5376”	0.0233%	3.1130%

For both the two-story and three-story shear frame, the SRSS and CQC results are extremely similar and vary by less than a percent for the response at each DOF. The similarity in response between the two methods is due to the well-spaced modes of the shear frames. As mentioned previously, the CQC method essentially reduces to the SRSS method when the ratios of the fundamental frequencies are small.

As expected, the ABS method yields the highest peak response at each DOF. Although the peak responses are higher, the ABS method results are still within 10% of the SRSS results. Furthermore, the average difference between the ABS and SRSS results increases for the three-story shear frame. In the subsequent chapters of this study, analysis is performed to further analyze the impacts of frame height on the accuracy of the modal combination methods.

Secondly, the results of the ELFP and RSA are compared. The percent difference of the SRSS, CQC, and ABS results when compared with the ELFP results for the two-story and three-story shear frame are shown in Table 14 and Table 15, respectively.

Table 14: Two-Story ELFP and RSA Comparison

	SRSS Diff.	**CQC Diff.**	**ABS Diff.**
$\mathbf{u_1}$	4.6902%	4.6398%	0.1513%
$\mathbf{u_2}$	8.4047%	8.4270%	6.1174%

Table 15: Three-Story ELFP and RSA Comparison

	SRSS Diff.	**CQC Diff.**	**ABS Diff.**
$\mathbf{u_1}$	26.4913%	26.4450%	21.0402%
$\mathbf{u_2}$	28.1033%	28.0982%	26.9089%
$\mathbf{u_3}$	29.6679%	29.6843%	27.4785%

In every instance, the ELFP yields larger displacement responses than RSA. For the two-story shear frame, the difference between each modal combination method and the ELFP are below 10%. Furthermore, the response for the first DOF yielded by the ABS method closely resembles the ELFP. For the three-story shear frame, regardless of combination method, the ELFP yields displacement responses that are 20% than RSA. As a whole, the ELFP results in the most conservative displacement response.

Lastly, it is interesting to consider the effects of using modal analysis to calculate the first natural period as opposed to Equation 3.2 given by ASCE 7-10, which is used to approximate the fundamental period in the ELFP. Table 16 compares the first natural period of vibration for the three shear frames when calculated using dynamic analysis as opposed to Equation 3.2.

Table 16: Fundamental Period Comparison – ELFP and RSA

	ELFP T_{n1} (s)	**Dynamic T_{n1} (s)**	**Percent Difference**
One-Story	0.1907	0.3001	36.45%
Two-Story	0.3220	0.5025	35.92%
Three-Story	0.4592	0.7123	35.53%

In each case, the ELFP produces a first natural period of vibration that is over 35% less than the natural period calculated through dynamic analysis. To show the effects of the smaller period, the ELFP is used to analyze the three-story shear frame using the natural period calculated through dynamic analysis. For the three-story shear frame, dynamic analysis resulted in a first natural period of 0.7123 seconds, whereas for the same shear frame, Equation 3.2 produces a first natural period of 0.4592 seconds. If 0.7123 seconds replaces the

approximate fundamental period in the ELFP, the design base shear decreases. The reason for this decrease is due to the upper limit of the seismic response coefficient shown by Equation 3.3a. Since Equation 3.3a yields a seismic response coefficient value of 0.1401, Equation 3.3a governs. Consequently, the smaller response coefficient reduces the total base shear. The deflection results obtained from the ELFP when using a natural period of 0.7123 seconds are shown in Table 17 below. Also, the percent difference of the SRSS, CQC, and ABS results when compared with the ELFP results when using a fundamental period of 0.7123 seconds are shown in Table 18.

Table 17: ELFP Results – T_n = 0.7123s

U_1	1.7512”
U_2	3.2412”
U_3	4.1088”

Table 18: Three-Story ELFP and RSA Comparison - T_n = 0.7123s

	SRSS Diff.	**CQC Diff.**	**ABS Diff.**
u_1	9.3650%	9.3079%	2.6439%
u_2	13.0816%	13.0754%	11.6377%
u_3	16.5012%	16.5206%	13.9019%

Interestingly, even with the reduced seismic response coefficient due to the larger fundamental period, the ELFP deflection results for the three-story shear frame are still larger than the RSA results. Although larger, when using the period calculated through dynamic analysis, the ELFP yields responses that more closely resemble the RSA results.

In conclusion, the ELFP yields more conservative results than RSA for the two-story and three-story shear frame. Additionally, the SRSS and CQC methods

result in very similar results. The results obtained through RSA are compared with the results of the THA performed in the subsequent chapter of this thesis.

5. Linear Time History Analysis

In the previous chapters, static and dynamic analysis methods were used to perform seismic analysis on the shear frames. In both static and dynamic methods of seismic analysis, the seismic forces imposed on a system are estimated. Although the methods covered thus far are effective, the unpredictable nature of earthquake ground motions makes it nearly impossible to determine the exact response of a system. In THA, the acceleration records from past earthquakes are used to determine the analytical response of a system. Even though every earthquake in history is unique, past earthquake records can indicate the acceleration records of future earthquakes. In this chapter, THA is used to determine the response of each shear frame and compared with the results obtained through dynamic analysis.

5.1 Earthquake Ground Motions

In order to obtain past earthquake ground motion records, various databases can be accessed online through organizations such as COSMOS and PEER. Each organization provides different earthquake records, as well as different tools for analysis. In this chapter, MATLAB code is written and used for analysis of the ground motions obtained from COSMOS and PEER.

Typically, the ground motion records for a specific earthquake include two horizontal and one vertical acceleration record. For each of the earthquakes used in this chapter, the two horizontal acceleration records are given perpendicular to one another, and each horizontal record is given in degrees with respect to the cardinal directions. In many cases, the record is labeled as 00, 90, 180, 270, and

360, indicating that the acceleration records were recorded parallel with either the North-South (N-S) or East-West (E-W) cardinal directions. For example, the acceleration records for the El Centro Earthquake on 5/18/1940 give two horizontal components, 00 and 90, referring to the N-S and E-W directions, respectively. On the other hand, the Kern County Earthquake on 7/21/1952 gives the horizontal components, 21 and 111. In this case, the accelerations were recorded 21 degrees east of north and 111 degrees west of south. Although the direction of the accelerations may impact the sign of the maximum response, the main interest is the absolute value of the response. For this reason, as long as the horizontal components are perpendicular to one another, accurate THA can be performed. The vertical component of the ground motion record is commonly denoted as UP.

In addition, the earthquake accelerations can be either corrected or uncorrected. If uncorrected, the accelerations are the exact recording of the seismograph at the time of the earthquake. Although uncorrected data can be useful, the reading of the seismograph can be impacted by vibrations not caused by the earthquake, such as noise or the seismograph itself. Through analysis, the uncorrected reading is corrected to represent solely the vibrations caused by the earthquake.

Even though the purpose of this chapter is not to design the shear frames, it is important to consider the scaling of the acceleration records. For every record, the location of the seismograph reading plays a role on the acceleration

recordings. To exemplify this idea, the earthquake ground motion records from the Northridge Earthquake are taken from two different station locations.

Each of the earthquakes chosen for THA analysis in this chapter occurred in California. Table 19 shown below summarizes each earthquake recording. In addition, Table 20 denotes the damages caused by each of the five earthquakes.

Table 19: Earthquake Ground Motion Records

Earthquake	Station	Hypocenter Distance	Magnitude
El Centro 5/18/1940	El Centro, CA Station Array #9	12.2 km	M_W = 6.9 M_L = 7.1
Kern County 7/21/1952	Taft, CA USGS Sta. 1095	36.2 km	M_W = 7.3 M_L = 7.5
San Luis Obispo 11/22/1952	San Luis Obispo, CA USGS, Sta. 1083	70.3 km	M_W = 6.0 M_L = 6.2
Loma Prieta 10/17/1989	Corralitos, CA CSMIP Sta. 57007	2.8 km	M_W = 6.9 M_L = 7.1
Northridge (1) 1/17/1994	Los Angeles, CA USC Sta. 5303	12.9 km	M_W = 6.7 M_L = 6.9
Northridge (2) 1/17/1994	Tarzana, CA Cedar Hill Nursery A	16.7 km	M_W = 6.7 M_L = 6.9

Table 20: Earthquake Damages

Earthquake	Approximate Damage	Human Deaths	Human Injuries
Imperial Valley (1940)	$6,000,000	9	20
Kern County (1952)	$60,000,000	12	200
San Luis Obispo (1952)	0	0	0
Loma Prieta (1989)	$6,000,000,000	63	3,800
Northridge (1994)	$25,000,000,000	57	9,000

As shown above, each of the California earthquakes used for analysis had magnitudes larger than or equal to 6.0. Per USGS, any earthquake with a magnitude greater than 6.0 “may be destructive in highly populated areas,” which

is an important point to consider. The only earthquake shown above that didn't result in monetary damages or human deaths was the San Luis Obispo Earthquake in 1952. The main reason for this was the location of the epicenter. Unlike the other earthquakes, the San Luis Obispo earthquake occurred in Cambria, CA, a lowly populated town on the central coast of California. For this reason, the San Luis Obispo Earthquake is rarely studied. On the other hand, the Loma Prieta and Northridge Earthquakes had devastating impacts due to their proximity to San Francisco and Los Angeles, respectively. Although the consequences of the earthquakes vary, it is still interesting to analyze the differences in Peak Ground Acceleration (PGA). With the scaled acceleration records obtained from COSMOS for the earthquakes shown in Table 19, the accelerograms are created in MATLAB. The accelerograms for each direction of the 1994 Northridge Earthquake, recorded by USC Sta. 53003, are shown in the figures below. The remaining accelerograms are presented in Appendix E.

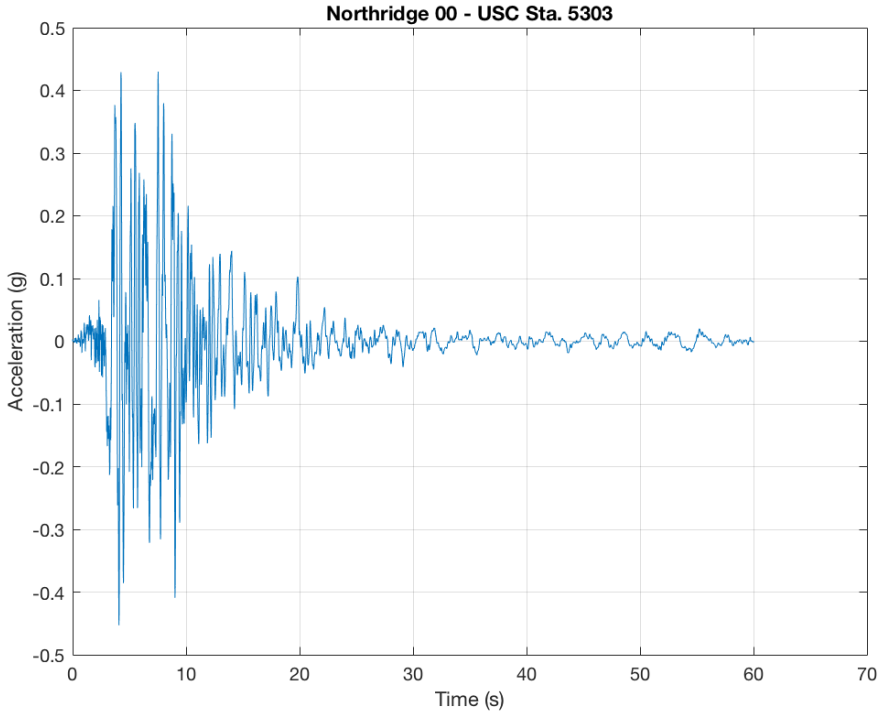

Figure 13: Northridge EQ 00 – USC Sta. 5303 (PGA = -0.4529g)

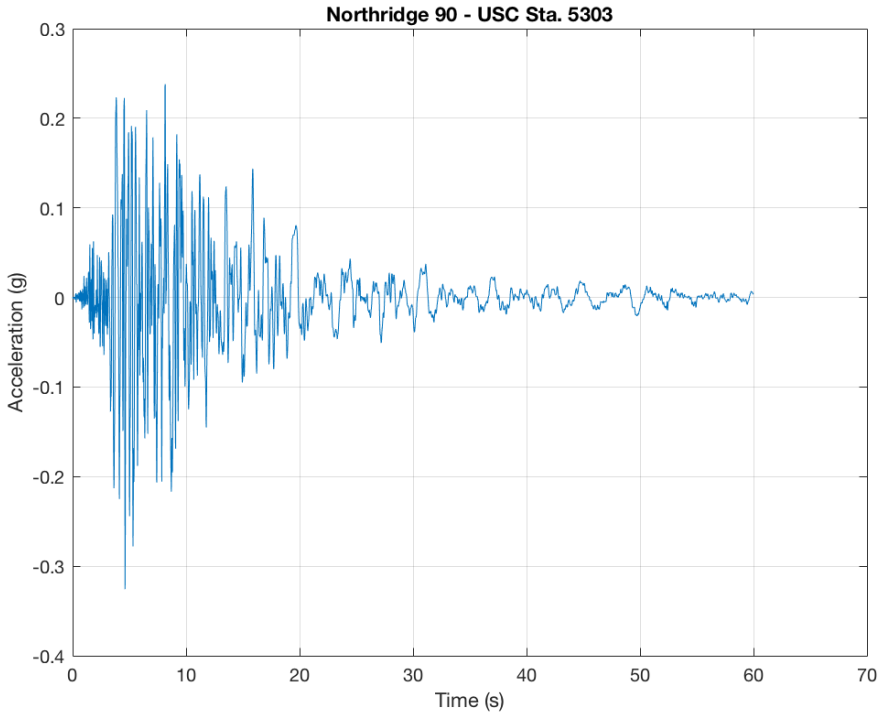

Figure 14: Northridge EQ 90 – USC Sta. 5303 (PGA = -0.3257g)

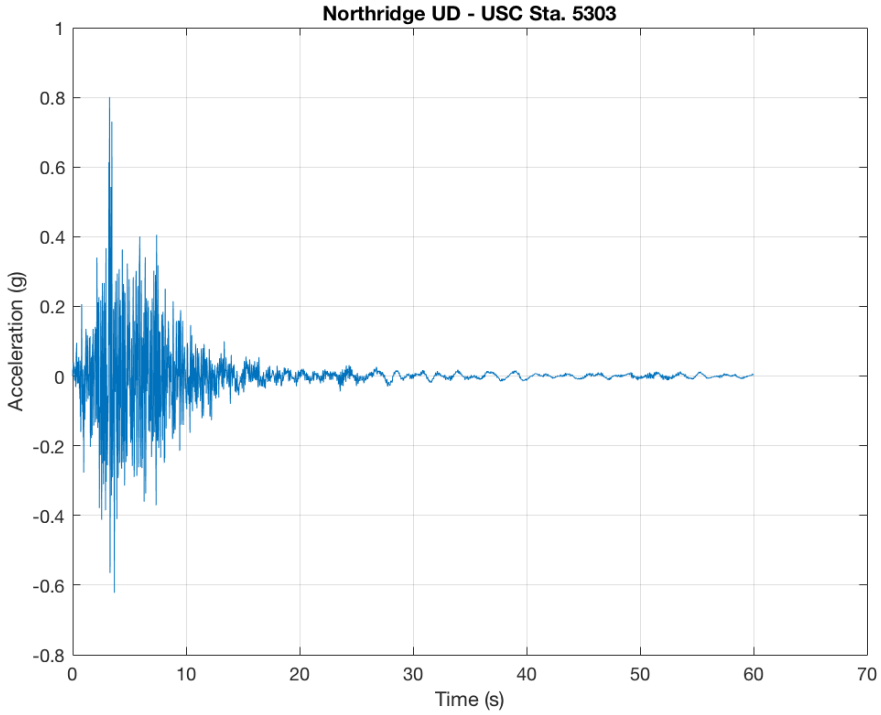

Figure 15: Northridge EQ UD – USC Sta. 5303 (PGA = 0.8005g)

5.2 Time History Analysis Methods

As mentioned previously, the purpose of this chapter is to develop displacement time histories for the one-story, two-story, and three-story shear frame under past earthquake ground motions. Even though it produces the analytical solutions for the maximum displacements of the shear frames, due to its complexity, the THA in this chapter is only feasible to perform with MATLAB. Although MATLAB code is generated and used, it is still critical to understand the principles of THA.

In order to perform THA, the governing equation of motion shown in Chapter 4 is expanded to include the presence of time-dependent loads. Despite the fact that the modal analysis shown in Chapter 4 produces natural periods and frequencies that have units of time, the generalized eigenvalue problem

considers an at-rest system in free vibration. In THA, initial displacement and velocity conditions are present, resulting in a different form of the governing equation of motion. Through the use of the governing equations of motion for damped and undamped systems, as well as the Euler relation, the following equations are derived.

$$u(t) = u_o cosw_n t + \frac{\dot{u}_o}{w_n} sinw_n t \qquad \text{(Equation 5.1)}$$

$$u(t) = e^{-\xi w_n t}(u_o cosw_D t + \frac{\dot{u}_o + \xi w_n t}{w_D} sinw_D t) \qquad \text{(Equation 5.2)}$$

Where u_o is the initial displacement and $\dot{u}_0$ is the initial velocity. Although the derivation of Equation 5.1 and Equation 5.2 is not shown, plenty of literature is available on the topic (Kasper and Hall, 2018).

The two equations shown above represent the steady state response of a system with initial velocities and displacements. To understand the incorporation of the initial displacements and velocities, it is important to consider how THA uses the acceleration records of past earthquakes to obtain the response of a system. Each acceleration value is given with respect to a time or time-step. Typically, the time-steps range between 0.005 seconds and 0.02 seconds. For each of the six ground motion records shown in Table 19, the time-step is 0.02 seconds. In other words, throughout the duration of each earthquake, an acceleration value is given at an interval of 0.02 seconds. Conceptually, whether the time-steps are small or large, linear interpolation can be assumed between the values at each time-step. Consider one of the earthquake records shown in Table 19 with a time-step of 0.02 seconds. At a time of 0.00 seconds, the system

is at rest and the linear interpolation between 0.00 seconds and 0.02 seconds would not include the presence of an initial displacement or initial velocity. Now consider the next time-step between 0.02 seconds and 0.04 seconds. During the first time-step, the system incurred a specific displacement and velocity which now must be included to determine the response of the system during the second time-step. This process repeats itself for the entire duration of the earthquake record.

In addition to the steady-state response, the transient response of the system under the ground motion accelerations must be included. For a system subject to earthquake ground motions, the accelerations act as arbitrary forcing functions by base excitation. Unlike a harmonic forcing function, determining the response of a system due to the periodic ground motion accelerations requires integration, which inevitably increases the complexity. For the response of linear systems subject to arbitrary time-varying loads, Duhamel's integral is used.

$$u(t) = \frac{1}{mw_D}\int_0^t p(\tau)e^{-\xi w_n(t-\tau)}sinw_D(t-\tau)d\tau \qquad \text{(Equation 5.3)}$$

Duhamel's integral for an undamped SDOF system can be obtained by simply replacing the damped natural frequency, w_D, with the natural frequency of vibration w_n, and setting the damping ratio to zero in Equation 5.3. Equation 5.3 can be combined with Equation 5.2 to produce the total response of a damped SDOF system subject to initial displacements, velocities, and arbitrary time-varying loads.

$$u(t) = e^{-\xi w_n t}(u_o cos w_D t + \frac{u_o + \xi w_n t}{w_D} sin w_D t + \frac{1}{m w_D}\int_0^t p(\tau) e^{-\xi w_n (t-\tau)} sin w_D (t-\tau) d\tau \quad \text{(Equation 5.4)}$$

Since it is applicable to any type of arbitrary loading, it is useful to consider Equation 5.4 for a system subject to earthquake ground accelerations. Consider a sample ground acceleration shown in Figure 16.

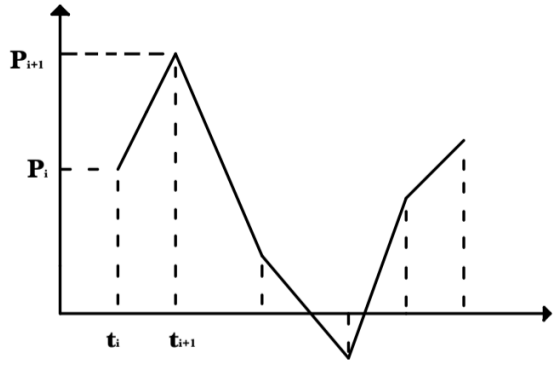

Figure 16: Typical Acceleration Record

Figure 16 replicates a typical earthquake acceleration record that can be found in *An Introduction to Applied Structural Dynamics* (Kasper & Hall, 2018). For the first line in Figure 16, the transient response is characterized by two arbitrary loads. First, at t_i, a constant arbitrary load, P_i, is applied. Secondly, from P_i to P_{i+1}, a sloped arbitrary load is applied. For the first case, the forcing function in Duhamel's integral, is simply replaced with the constant force P_i. On the other hand, the forcing function for the sloped portion is dependent on time. The two arbitrary loading conditions along with the effects of the initial conditions are used to define the response of the system at each time-step. The following equations show the results of Duhamel's integral for the two loading conditions.

$$u(t)_{constant} = \frac{P_i}{k} - \frac{P_i}{k} e^{-\xi w_n t}(cosw_D t + \frac{\xi}{\sqrt{1-\xi^2}} sinw_D t) \quad \text{(Equation 5.5)}$$

$$u(t)_{sloped} = \frac{P_i}{k}\left(t - \frac{2\xi}{w_n}\right) + \frac{P_i}{k}\left(\frac{2\xi}{w_n}\right) e^{-\xi w_n t} cosw_D t + \frac{P_i}{k}(2\xi^2 - 1)\frac{1}{w_D} e^{-\xi w_n t} sinw_D t$$

(Equation 5.6)

Although Duhamel's integral can be solved for ground motions, it is still important to consider the complexity of solving for the analytical solution. For example, consider Duhamel's integral for the constant initial load, P_i. Even with a constant force, Duhamel's integral requires integration by parts, and for the sloped portion where the arbitrary load is dependent on time, Duhamel's integral is even more complex. Despite the complexity, Equations 5.5 and 5.6 replace Duhamel's integral in Equation 5.4, resulting in a further simplified equation for the total response.

Finally, due to the use of a constant time interval, the equation for the total displacement response can be written in recursive form as shown below.

$$u_{i+1} = A_1 u_i + A_2 u_i + A_3 P_i + A_4 P_{i+1} \quad \text{(Equation 5.7)}$$

$$u_{i+1} = B_1 u_i + B_2 u_i + B_3 P_i + B_4 P_{i+1} \quad \text{(Equation 5.8)}$$

Recursive form is used to define sequences in such a way that the next term in the sequence is defined by the previous term in the sequence. In accordance with the definition, the A_n and B_n values are all constants in which the value of A_1 is dependent on the value of B_1, and the value A_2 is dependent on the value of B_2, etc. Although not shown in this chapter, the constant values A_n and B_n can be calculated, resulting in an analytical solution for the displacement response of linear systems with damping coefficients less than one. Obviously,

producing an analytical solution for the displacement time history of a system requires significant effort.

To simplify the process, numerical solutions of the displacement time history can often replace the analytical solution. In general, numerical analysis attempts to simplify complex problems through approximations, in turn resulting in a numerical or approximate solution. In the case of numerical solutions, it is always important to ensure that the solution is accurate enough to replace the analytical solution. Although there are plenty of avenues for obtaining a numerical solution for the displacement time history of a system subject to earthquake excitations, the Newmark-beta Method is applied in this chapter to produce numerical solutions.

The Newmark-beta Method takes a multi-step approach when solving for the response history of a system. A multi-step approach takes progressive steps and uses the information from previous steps to gain efficiency in solving for a solution. The Newmark-beta method defines the displacement and velocity responses of a system through the following two equations.

$$u_{i+1} = u_i + \Delta t u_i + (\Delta t)^2 \left(\frac{1}{2} - \beta\right) u_i + \beta (\Delta t)^2 u_{i+1} \quad \text{(Equation 5.9)}$$

$$u_{i+1} = u_i + (1 - \gamma)\Delta t u_i + \gamma \Delta t u_{i+1} \quad \text{(Equation 5.10)}$$

The values for beta and gamma in the above equations are chosen parameters. The stability and accuracy of the Newmark-beta Method is completely reliant on the selection of beta and gamma. In terms of the Newmark-beta Method, instability results in a divergent solution, whereas stability refers to the fact that the chosen parameters do not significantly hinder the accuracy of

the solution at any given time step. Stability can be achieved through a variety of beta and gamma values and combinations, but the use of beta=1/4 and gamma=1/2 results in an unconditionally stable solution. In general, 2beta > gamma> ½ results in stable solutions for linear structural dynamics applications, no matter the time step. Although this relationship results in stability, the overall accuracy of the solution is still important. Even if beta and gamma are chosen to ensure stability, the most accurate solution is not always achieved through parameters that guarantee stability. In general, the number one goal of the Newmark-beta Method is to achieve solutions that are the most accurate and in turn stable, so it is important to not confine the values of beta and gamma to stability. All in all, the accuracy of the Newmark-beta Method relies heavily on the size of the time step. Obviously, as the time step gets smaller, the results of the Newmark-beta method will converge with the analytical solution, essentially mimicking integration.

In this chapter, the Newmark-beta Method is used to produce numerical solutions, but it is important to consider the following relationships that the Newmark-beta Method has with other numerical methods.

1. If beta=1/4 and gamma=1/2 the Newmark-beta Method is identical to the Average Acceleration Method (AAM).
2. If beta=1/6 and gamma=1/2 the Newmark-beta Method is identical to the Linear Acceleration Method (LAM).
3. If beta=0 and gamma=1/2 the Newmark-beta Method is identical to the Central Difference Method.

Throughout the rest of this chapter, analytical and numerical solutions are obtained through THA using MATLAB, which shows the relative accuracy of various beta and gamma parameters, as well as the numerical solutions in general.

5.3 Displacement Time History

Using the acceleration records and accelerograms in Section 5.1, the displacement time histories of specific systems can be developed. As proved by the equations in Section 5.2, the displacement time history of a SDOF system solely relies on the natural period of vibration and the damping ratio. For each of the earthquakes detailed earlier in this chapter, various periods and damping ratios were used to develop displacement time history graphs. Although each earthquake is analyzed, only the displacement time histories for the Northridge Earthquake (USC Sta. 5303) are shown in this chapter. The Loma Prieta Earthquake (CSMIP Sta. 57007) displacement time histories are shown in Appendix F.

First, displacement time histories are produced using natural periods of 0.30, 0.50, 1.00, 2.50, and 5.00 seconds. For each of the values, a uniform damping ratio of 0.05 (5%) is used in order to exemplify the impact that the natural period has on the displacement response of a system. The displacement time histories for the Northridge Earthquake are shown for each period in the figures below. Also, Table 21 tabulates the maximum response at each natural period value for the five earthquakes.

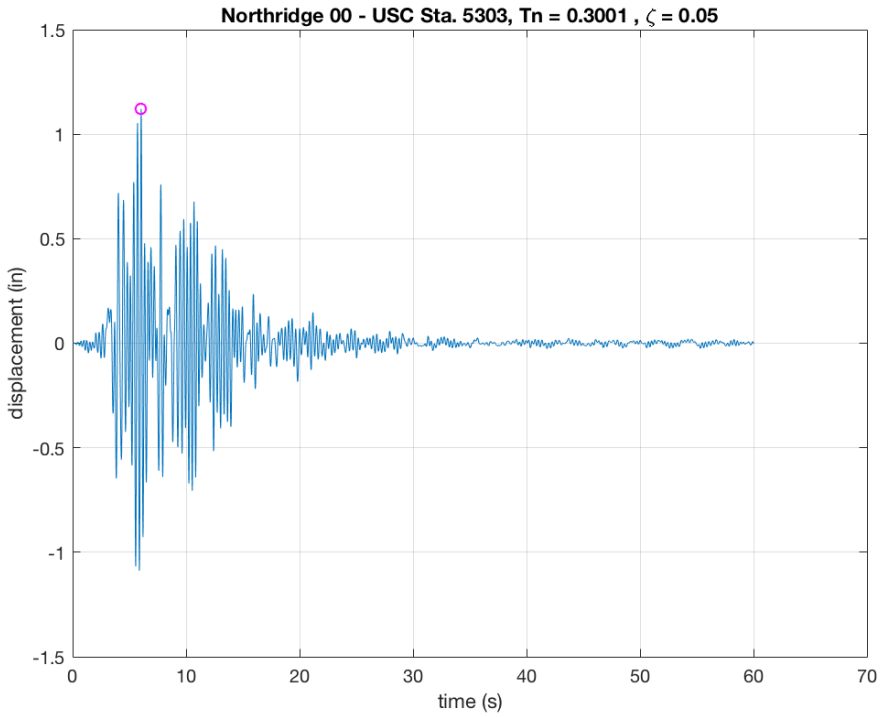

Figure 17: Northridge 00 (T_n = 0.3001s) Displacement Time History

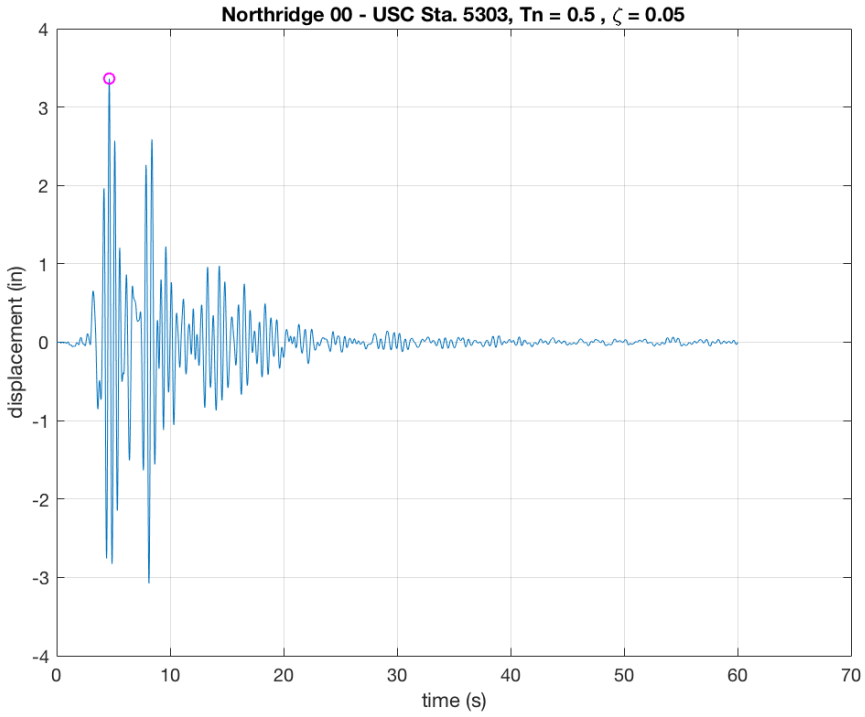

Figure 18: Northridge 00 (T_n = 0.50s) Displacement Time History

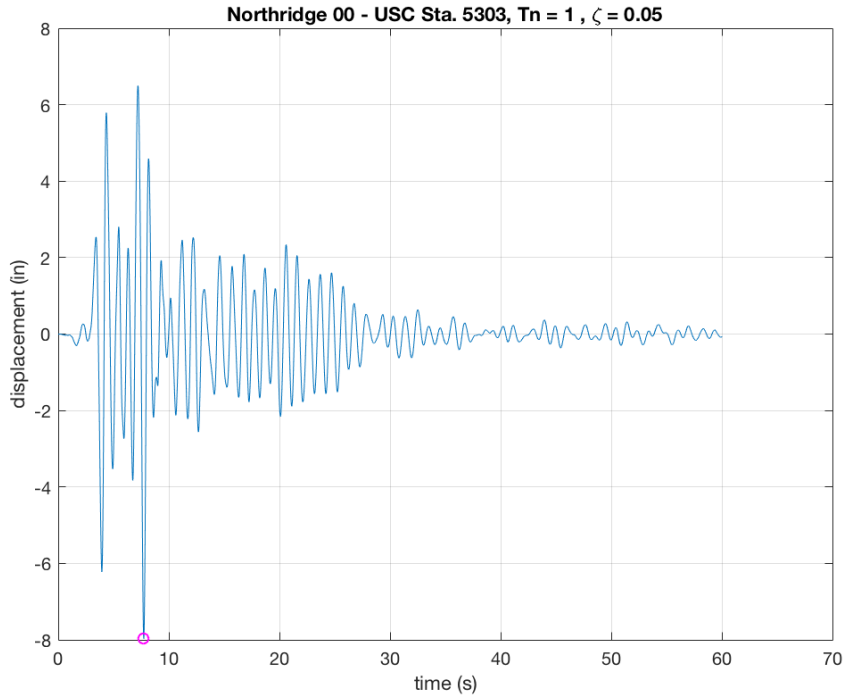

Figure 19: Northridge 00 (T_n = 1.00s) Displacement Time History

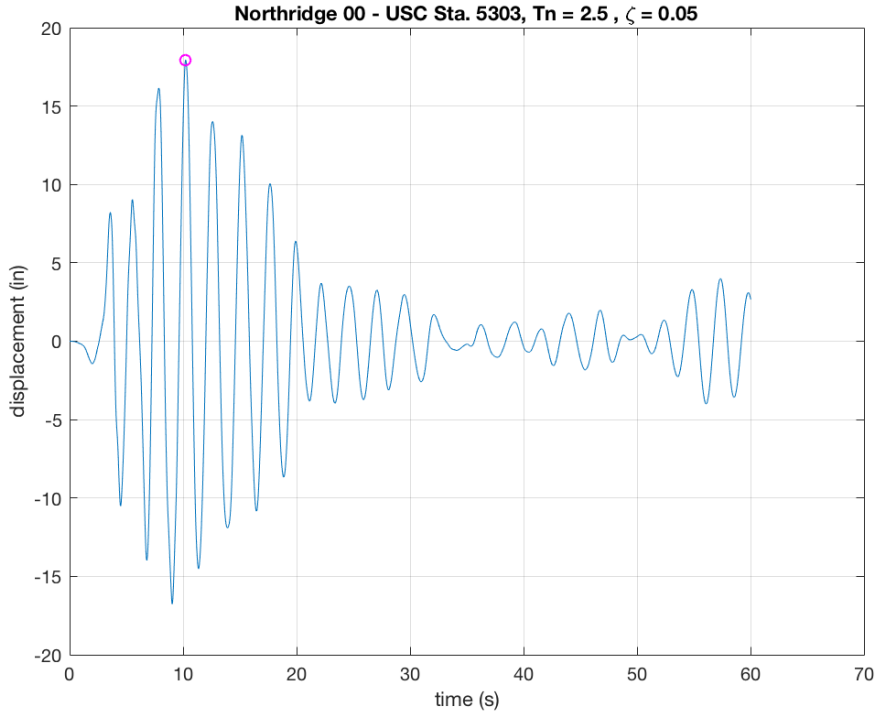

Figure 20: Northridge 00 (T_n = 2.50s) Displacement Time History

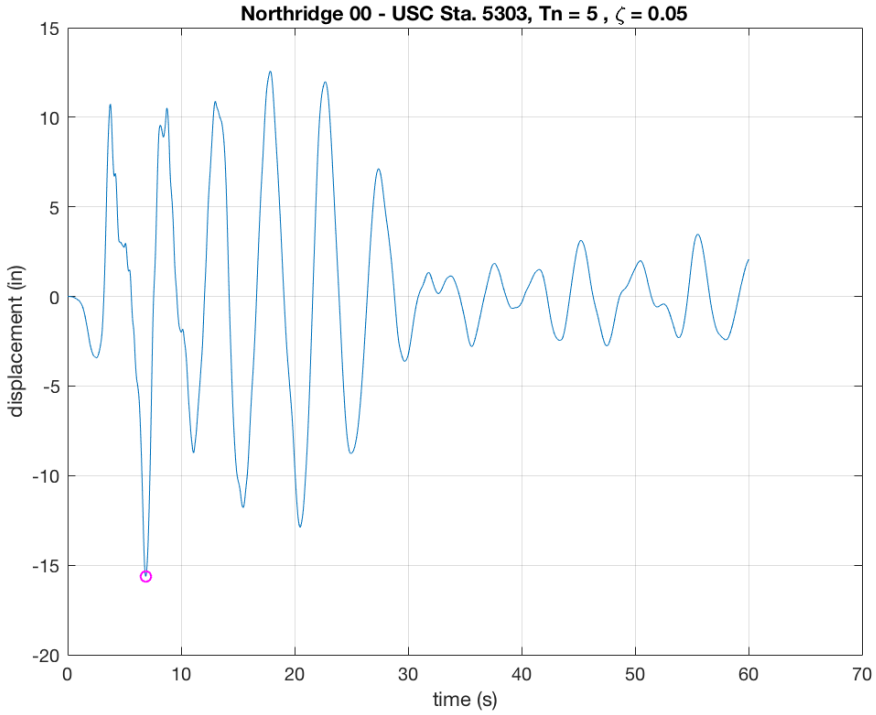

Figure 21: Northridge 00 (T_n = 5.00s) Displacement Time History

Table 21: Maximum Response at Varying Natural Periods

Damping Ratio (ξ) = 0.05 (5%)			
Earthquake	**T_n (s)**	**U_{MAX} (in.)**	**Time (s)**
El Centro 00	0.30	0.623	2.62
	0.50	2.016	2.40
	1.00	5.033	4.40
	2.50	10.803	5.72
	5.00	7.347	28.84
Kern County 111	0.30	0.353	6.64
	0.50	0.845	6.76
	1.00	1.552	3.94
	2.50	3.528	4.94
	5.00	6.313	41.00
SLO 324	0.30	0.114	2.56
	0.50	0.182	2.30
	1.00	0.588	9.78
	2.50	0.568	24.64
	5.00	0.502	15.62
Loma Prieta 00	0.30	1.874	3.12
	0.50	3.456	2.76
	1.00	3.802	3.04
	2.50	7.545	7.08
	5.00	6.335	6.40
Northridge 00	0.30	1.121	6.04
	0.50	3.363	4.64
	1.00	7.973	7.74
	2.50	17.94	10.22
	5.00	15.63	6.88

From the figures and results above, two major relationships between the displacement time history and natural period can be drawn. First, as shown in the figures, no matter the earthquake, a system has a tendency to vibrate at its natural period. Secondly, as shown in Table 21, the maximum displacement response of the system increases with the period in the range of 0.30 to 2.50 seconds for all of the earthquakes except the San Luis Obispo Earthquake, but

decreases between the periods of 2.50 and 5.00 seconds. From this, it can be concluded that the displacement response of a system increases with the period for small periods, but at a certain point, this relationship no longer holds true. Although it is not a definitive relationship, a majority of systems, including the one-story, two-story, and three-story shear frame have natural periods well below 2.50 seconds.

The next point of analysis is the effect of the damping ratio on the displacement time history of the system. In this case scenario, the natural period is held constant at 0.30 seconds, which is the natural period for the SDOF one-story shear frame calculated in Chapter 3. With a constant period of 0.30 seconds, the displacement time histories for each earthquake are developed with damping ratios of 0.00, 0.025, 0.050, 0.075, and 0.1000. Once again, the displacement time histories for the Northridge Earthquake are shown in the figures on the subsequent pages, followed by Table 22 which tabulates the maximum response for each value of the damping ratio for the five earthquakes. The displacement time histories for the Loma Prieta Earthquake are shown in Appendix G.

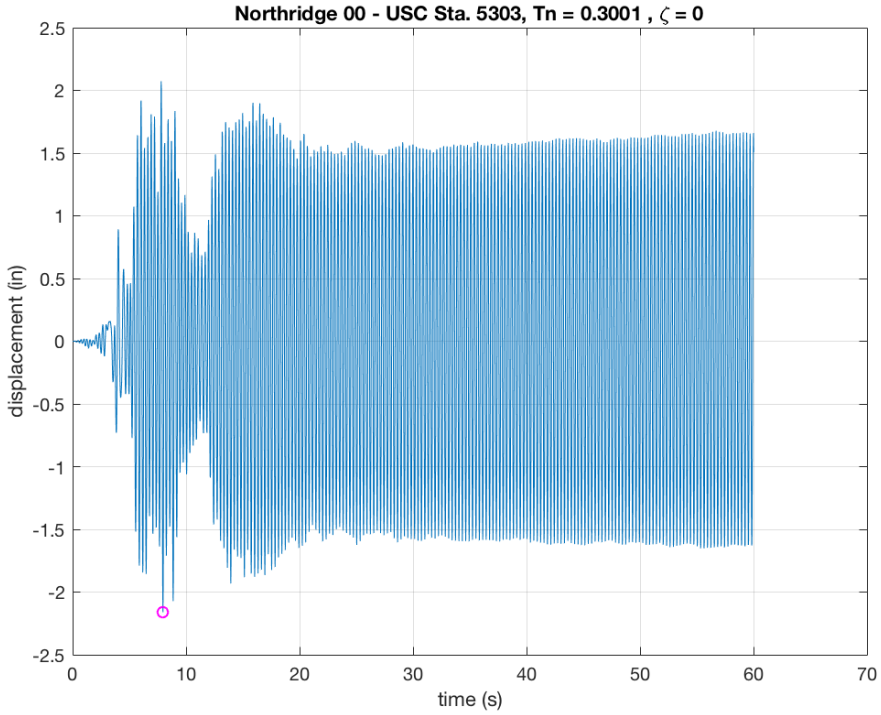

Figure 22: Northridge 00 ($\xi = 0.00$) Displacement Time History

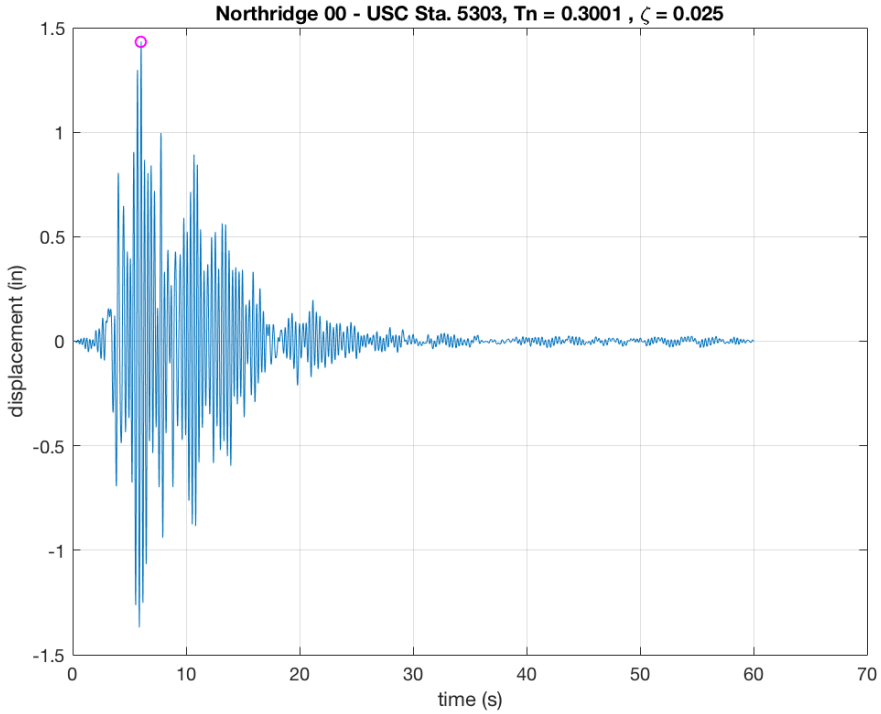

Figure 23: Northridge 00 ($\xi = 0.025$) Displacement Time History

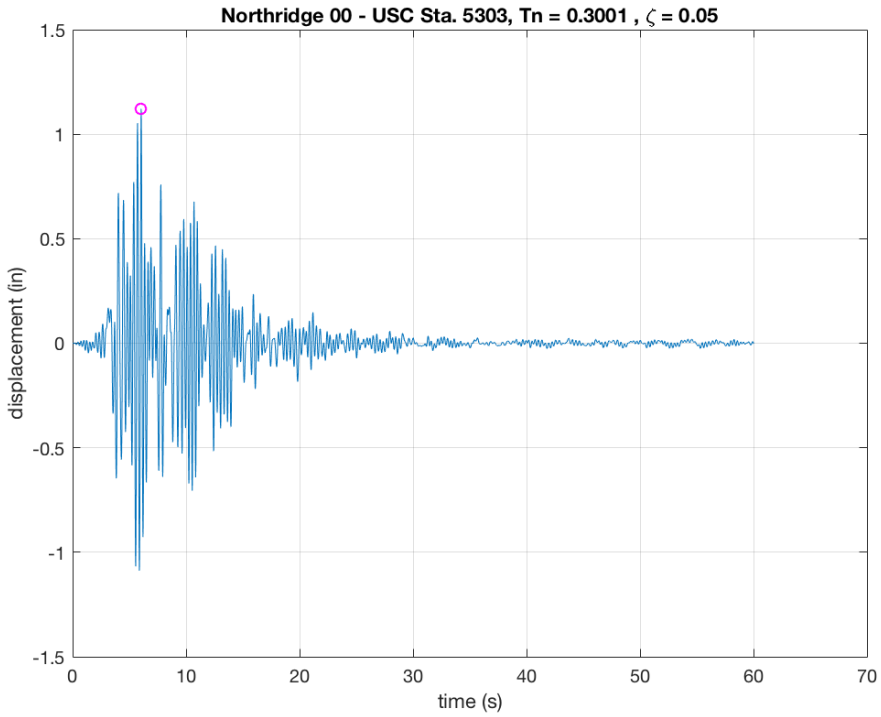

Figure 24: Northridge 00 ($\xi = 0.050$) Displacement Time History

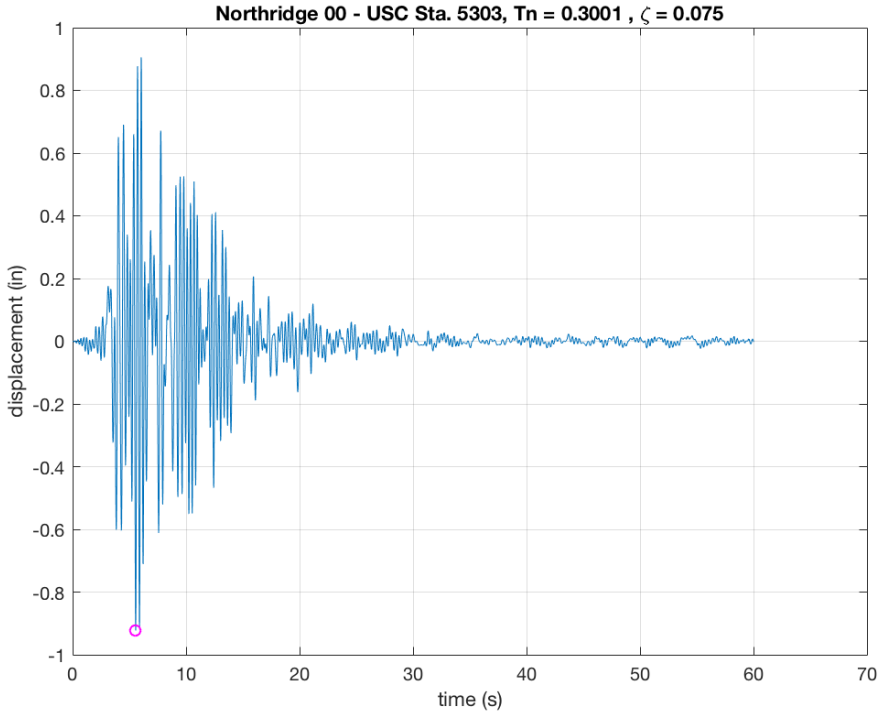

Figure 25: Northridge 00 ($\xi = 0.075$) Displacement Time History

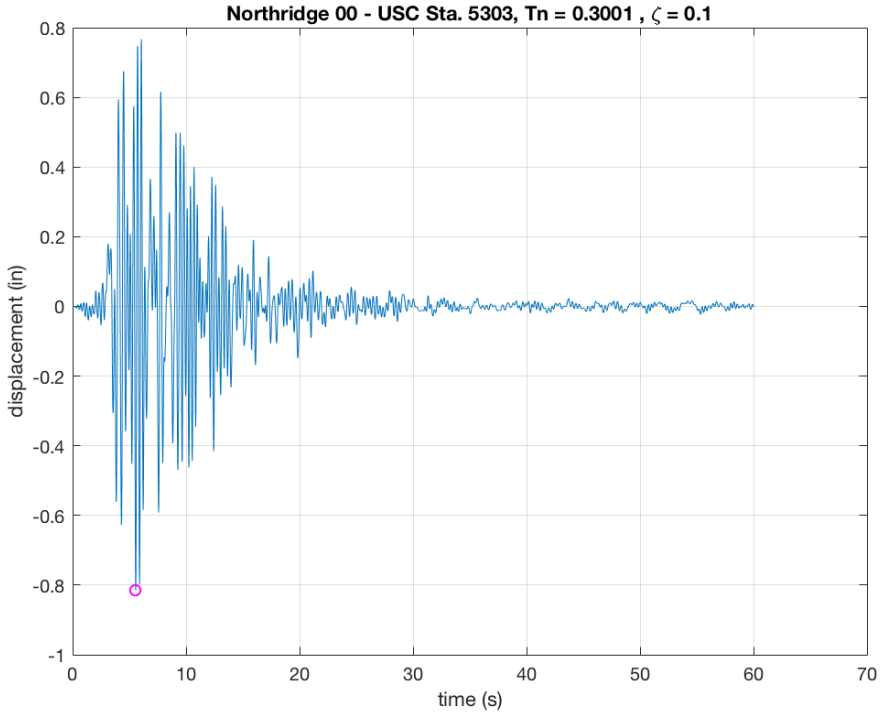

Figure 26: Northridge 00 ($\xi = 0.100$) Displacement Time History

Table 22: Maximum Response at Varying Damping Ratios

Natural Period (T_n) = 0.30s			
Earthquake	ξ	**U_{MAX} (in.)**	**Time (s)**
El Centro 00	0.00	1.848	30.36
	0.025	0.726	2.62
	0.050	0.623	2.62
	0.075	0.534	2.62
	0.100	0.462	2.32
Kern County 111	0.00	1.366	12.76
	0.025	0.471	6.62
	0.050	0.353	6.64
	0.075	0.312	6.64
	0.100	0.285	6.64
SLO 324	0.00	0.287	30.32
	0.025	0.154	3.00
	0.050	0.114	2.56
	0.075	0.0974	1.68
	0.100	0.0889	1.68
Loma Prieta 00	0.00	2.791	3.26
	0.025	2.262	3.26
	0.050	1.874	3.12
	0.075	1.610	3.12
	0.100	1.393	3.12
Northridge 00	0.00	2.160	7.96
	0.025	1.434	6.04
	0.050	1.121	6.04
	0.075	0.923	5.56
	0.100	0.816	5.56

From the figures and results above, it is clear to see the relationship between the displacement response and damping ratio. As the damping ratio increases, the maximum response of the system decreases. Conceptually, this relationship makes sense. A higher damping ratio indicates that a higher percentage of the energy is dissipated, inevitably resulting in a lessened response. An interesting point of analysis is the change in the maximum

response as the damping ratio is increased. As the results in Table 22 show, the increase in damping ratio does decrease the maximum response, but the relationship is not necessarily linear. Figure 27 below plots the damping ratio versus the maximum displacement response.

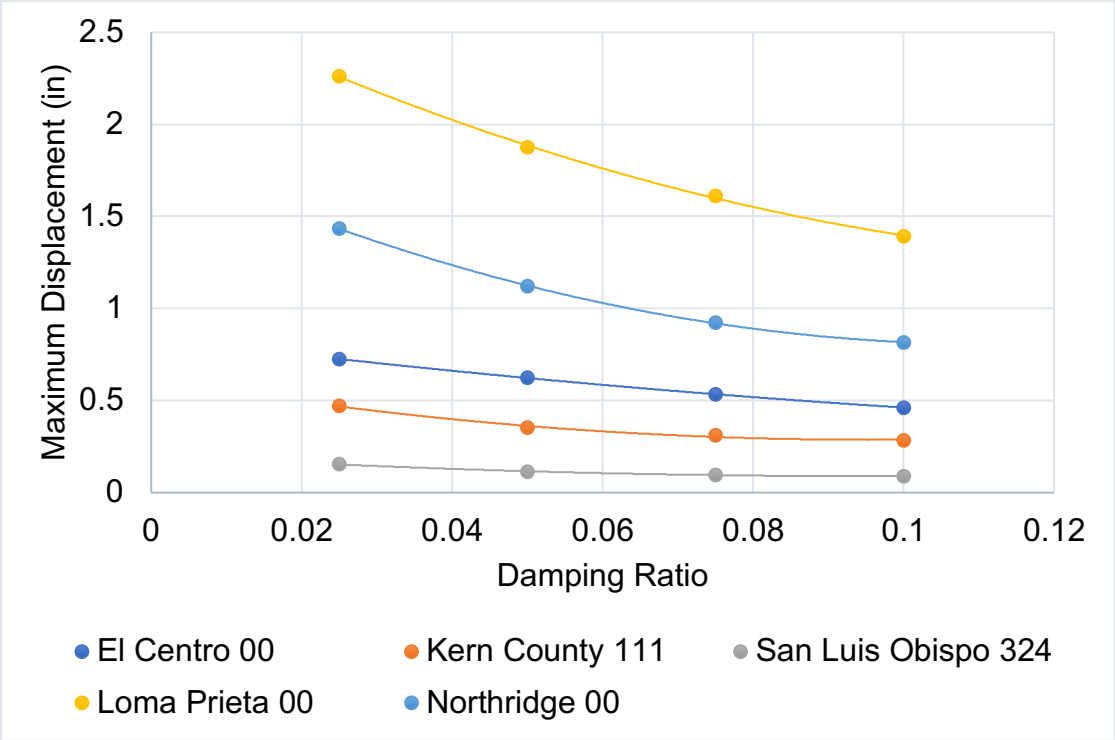

Figure 27: Damping Ratio versus Maximum Displacement Response

Although Figure 27 appears to show a somewhat linear relationship between the increase in the damping ratio and the decrease in the maximum displacement response, it is clear that there is curvature in the trendlines. Using the best fit line for each earthquake in Figure 27, the most accurate characterization of the relationship is a second order polynomial (parabola). In addition to the analytical response, the AAM ($\beta=1/2, \gamma=1/4$) and LAM ($\beta=1/2, \gamma=1/6$) are used to determine the maximum response of systems with the various natural periods and damping ratios. The displacement time history

graphs of the Loma Prieta and Northridge Earthquakes using the AAM and LAM at the five periods with a 5% damping ratio and the five damping ratios with a period of 0.30 seconds are developed. The displacement time histories using the AAM and LAM are presented in Appendix H and Appendix I, respectively. Also, Table 23 and Table 24 on the subsequent pages tabulate the maximum displacement responses for the five earthquakes using the numerical methods, along with the percent difference with the analytical maximum displacement response.

As shown in the figures in Appendix H and I, the Average Acceleration Method (AAM) and the Linear Acceleration Method (LAM) both produced displacement time histories very similar to the analytical analysis case. When analyzing Table 23 and Table 24 there is no consistent correlation between the damping ratio, natural period, and accuracy of the numerical solution. Although a direct relationship isn't formed, the average percent error for each analysis shows the overall accuracy of each method. If the five earthquakes are analyzed together, the AAM and LAM result in average percent errors of 0.195% and 0.291% for varying periods and 0.827% and 0.546% for varying damping ratios, respectively. Even though approaching the five earthquakes as a whole shows the AAM being more accurate for varying periods and the LAM more accurate for varying damping ratios, the earthquakes should be analyzed one by one to compare the general accuracy of the numerical methods. Outliers such as the El Centro 00 case without damping can significantly skew the data when analyzing the earthquakes together.

Table 23: Numerical Max Displacement Response with Varying Damping

Natural Period (T_n) = 0.30s						
Earthquake	ξ	**U_{MAX} (in.)**	**U_{MAX} (in.) AAM**	**% Difference**	**U_{MAX} (in.) LAM**	**% Difference**
El Centro 00	0.00	1.848	1.707	7.630	1.777	3.842
	0.025	0.726	0.727	0.152	0.727	0.165
	0.050	0.623	0.623	0.016	0.623	0.016
	0.075	0.534	0.534	0.037	0.534	0.019
	0.100	0.462	0.466	0.909	0.467	1.017
Kern County 111	0.00	1.366	1.351	1.105	1.358	0.586
	0.025	0.471	0.473	0.446	0.472	0.255
	0.050	0.353	0.358	1.303	0.357	1.133
	0.075	0.312	0.312	0.032	0.312	0.096
	0.100	0.285	0.285	0.105	0.285	0.070
SLO 324	0.00	0.287	0.280	2.441	0.283	1.220
	0.025	0.154	0.155	0.975	0.153	0.325
	0.050	0.114	0.115	0.701	0.115	0.858
	0.075	0.0974	0.098	0.670	0.098	0.886
	0.100	0.0889	0.089	0.045	0.089	0.068
Loma Prieta 00	0.00	2.791	2.808	0.609	2.808	0.609
	0.025	2.262	2.281	0.858	2.283	0.946
	0.050	1.874	1.872	0.107	1.873	0.053
	0.075	1.610	1.608	0.112	1.610	0.025
	0.100	1.393	1.391	0.129	1.393	0.036
Northridge 00	0.00	2.160	2.136	1.102	2.149	0.509
	0.025	1.434	1.443	0.621	1.441	0.488
	0.050	1.121	1.126	0.410	1.124	0.268
	0.075	0.923	0.923	0.065	0.923	0.065
	0.100	0.816	0.817	0.094	0.817	0.089

Table 24: Numerical Max Displacement Response with Varying Period

Damping Ratio (ξ) = 0.05 (5%)						
Earthquake	ξ	**U_{MAX} (in.)**	**U_{MAX} (in.) AAM**	**% Difference**	**U_{MAX} (in.) LAM**	**% Difference**
El Centro 00	0.30	0.623	0.623	0.016	0.623	0.016
	0.50	2.016	2.031	0.729	2.031	0.749
	1.00	5.033	5.040	0.135	5.040	0.145
	2.50	10.803	10.804	0.009	10.805	0.019
	5.00	7.347	7.348	0.014	7.348	0.015
Kern County 111	0.30	0.353	0.358	1.303	0.357	1.133
	0.50	0.845	0.844	0.083	0.845	0.032
	1.00	1.552	1.553	0.077	1.554	0.097
	2.50	3.528	3.531	0.077	3.531	0.082
	5.00	6.313	6.341	0.002	6.314	0.003
SLO 324	0.30	0.114	0.115	0.701	0.115	0.858
	0.50	0.182	0.184	0.840	0.184	0.956
	1.00	0.588	0.587	0.003	0.588	0.009
	2.50	0.568	0.569	0.040	0.569	0.042
	5.00	0.502	0.502	0.000	0.502	0.002
Loma Prieta 00	0.30	1.874	1.872	0.107	1.873	0.053
	0.50	3.456	3.453	0.087	3.546	2.601
	1.00	3.802	3.800	0.055	3.801	0.024
	2.50	7.545	7.545	0.007	7.545	0.001
	5.00	6.335	6.336	0.021	6.336	0.022
Northridge 00	0.30	1.121	1.126	0.410	1.124	0.268
	0.50	3.363	3.359	0.119	3.361	0.054
	1.00	7.973	7.976	0.038	7.978	0.058
	2.50	17.94	17.940	0.000	17.945	0.028
	5.00	15.63	15.630	0.000	15.629	0.006

In order to show the accuracy of each method for each earthquake, Table 25 shows the average percent error of each case. As shown in Table 25, the average percent error for the LAM when the period is kept constant is more accurate for each earthquake case when compared with the AAM. On the other hand, with a constant damping ratio, the AAM produces more accurate results for

the El Centro, San Luis Obispo, and Loma Prieta Earthquakes. All in all, besides the El Centro Earthquake with constant damping, the average percent error is under one percent for all of the analysis cases. For the El Centro Earthquake, the relatively larger percent error can be attributed to the undamped case. Later in this chapter, the comparisons drawn in this section can be used to estimate the accuracy of the numerical methods for the three shear frames with varying periods and damping ratios.

Table 25: Average Percent Difference of Numerical Methods

	Average Percent Error			
Earthquake	**Constant Damping (0.050)**		**Constant Period (0.30s)**	
El Centro 00	AAM	0.181%	AAM	1.749%
	LAM	0.189%	LAM	1.102%
Kern County 111	AAM	0.308%	AAM	0.598%
	LAM	0.269%	LAM	0.428%
San Luis Obispo 324	AAM	0.317%	AAM	0.966%
	LAM	0.373%	LAM	0.671%
Loma Prieta 00	AAM	0.055%	AAM	0.363%
	LAM	0.540%	LAM	0.334%
Northridge 00	AAM	0.113%	AAM	0.458%
	LAM	0.083%	LAM	0.284%

5.4 Analytical Response Spectrum Analysis

Although the individual analyses of each earthquake in Section 5.3 led to maximum displacements for each earthquake for systems with various natural periods and damping ratios, developing specific displacement, velocity, and acceleration time histories for every case scenario is not ideal. In order to simplify this process, analytical response spectrums can be created for each earthquake. Similar to the simplified design response spectrum developed using ASCE 7-10

for a site in San Luis Obispo, CA, 93407 in Chapter 4, an analytical response spectrum plots the maximum response with respect to the natural period of vibration. Since the maximum response of a system is reliant solely on the natural period and damping ratio, response spectrums are an efficient way to study the impacts of specific earthquake ground motions on a wide range of systems.

Consider the simplified design response spectrum in Chapter 4. Through the use of the Design Basis Earthquake (DBE) the simplified design response spectrum is developed, and in turn the maximum displacement response for each shear frame was calculated. In the case of THA, specific earthquakes are analyzed, allowing for the development of analytical response spectrums. In general, the pseudo-acceleration (PSa), pseudo-velocity (PSv), and spectral (maximum) displacement response spectrums are of particular importance when studying the effects of specific earthquake ground motions. In each response spectrum case, the spectrums show the maximum response of a SDOF system for each natural period, and through the orthogonality of the modes, the spectrums can be applied to MDOF systems to determine their maximum response.

First, consider the development of PSa spectrums for each of the five earthquakes outlined in this chapter. As previously mentioned, the forces induced on a structure are a result of the horizontal ground accelerations resulting from earthquakes. The PSa response spectrums for the five earthquakes with various damping ratios are developed through the use of MATLAB code. The PSa

response spectrum for the Northridge Earthquake is shown by Figure 28 below, and the remaining PSa spectrums are displayed in Appendix J.

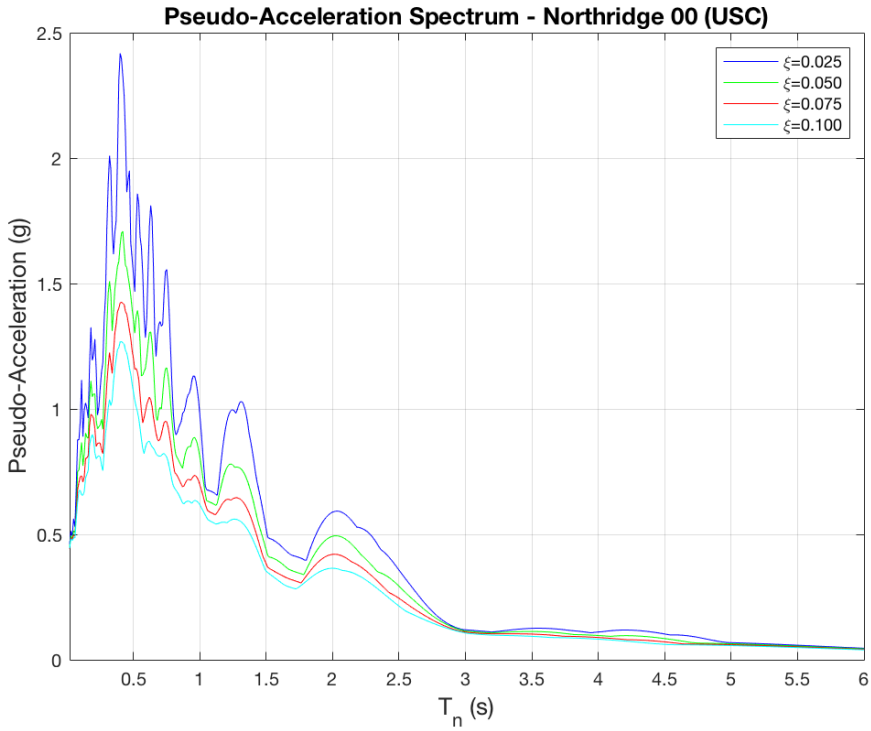

Figure 28: Pseudo-Acceleration Spectrum – Northridge 00 (USC Sta. 5303)

Secondly, consider the development of the PSv spectrums for the five earthquakes. The PSv spectrums are useful for determining the kinetic energy of a wide range of systems with respect to their natural period. When considering the governing equation of motion, a PSv spectrum shows the effects of damping on the dissipation of the kinetic energy in systems subject to dynamic loading. The PSa and PSv are related through Equation 5.11 shown below.

$$PSa = w_n PSv \qquad \text{(Equation 5.11)}$$

Through the relationship shown in Equation 5.11, the PSv spectrums for the five earthquakes with various damping ratios are developed in MATLAB. The

PSv response spectrum for the Northridge Earthquake is shown by Figure 29 below, and the remaining PSv spectrums are displayed in Appendix K.

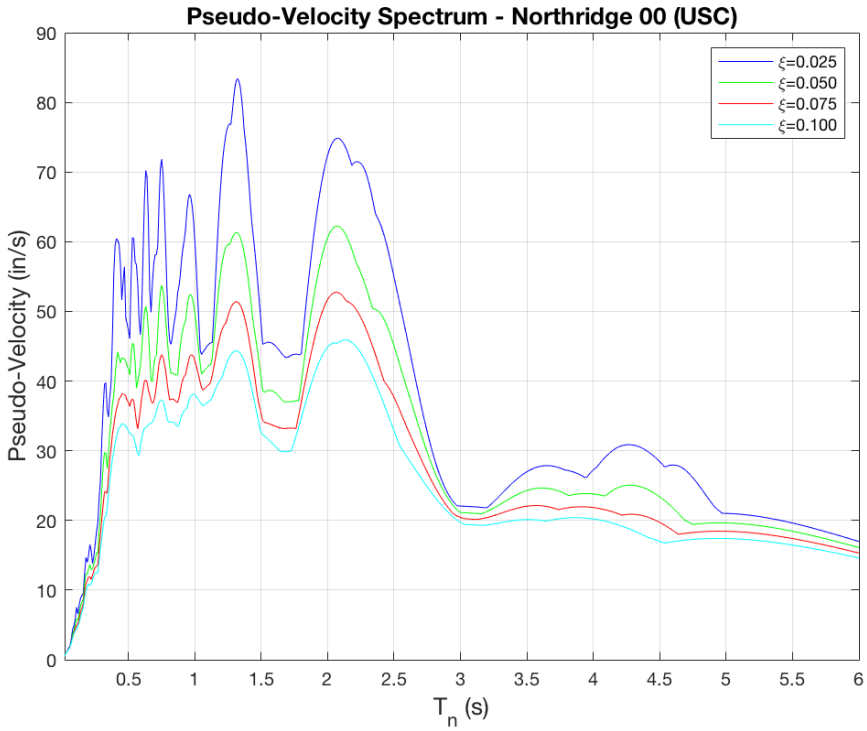

Figure 29: Pseudo-Velocity Spectrum – Northridge 00 (USC Sta. 5303)

Finally, the spectral displacement response spectrum for the five earthquakes can be created either through the PSa spectrums and Equation 4.8 or the PSv spectrums and Equation 5.12 shown below.

$$PSv = w_n Sd \qquad \text{(Equation 5.12)}$$

Using Equation 5.12, the maximum displacement response spectrums for the five earthquakes with various damping ratios are developed in MATLAB. The spectral displacement response spectrum for the Northridge Earthquake is shown by Figure 30 below, and the remaining spectral displacement spectrums are displayed in Appendix L.

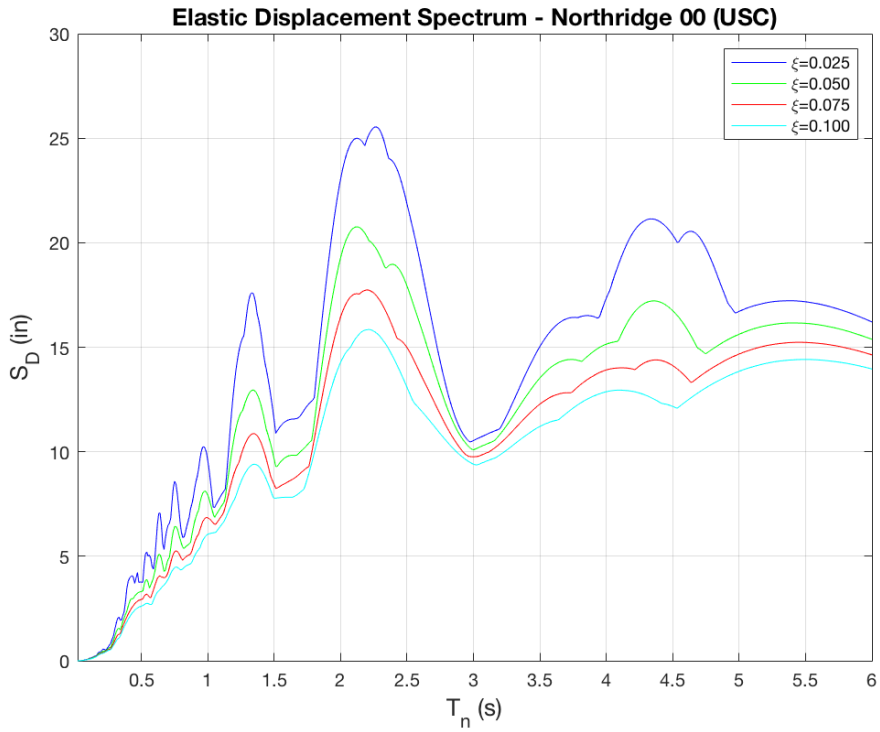

Figure 30: Max Displacement Spectrum – Northridge 00 (USC Sta. 5303)

For the response spectrums shown above, the maximum response at each natural period and damping ratio is identical to the maximum response produced for each individual analytical analysis case in Section 5.3. When considering the effects of the natural periods and damping ratios on the maximum response, the same connections are drawn as in Section 5.3. First, each response spectrum shows that a higher damping ratio results in a lessened response, whether it is pseudo-acceleration, pseudo-velocity, or displacement. Next, the displacement spectrums for each earthquake show how at small periods the maximum displacement increases with the natural period, but at a certain point the maximum displacement response no longer increases with the period. For instance, consider the maximum displacement spectrum for the Northridge earthquake shown in Figure 30. For period between 0 and 1.35

seconds, the maximum displacement response increases with the period, but after periods of 1.35 seconds the relationship no longer holds true. For each level of damping, a system with a natural period of 1.35 seconds will have a maximum displacement response that is a few inches larger than the maximum displacement response of a system with a natural period of 1.5 seconds. Obviously, the relationship between the natural period and the maximum displacement response is entirely dependent on the earthquake under analysis.

In the next section of this chapter, the response spectrums for the five earthquakes are used to determine the maximum displacement responses of the MDOF shear frames using various modal combination methods, and the results are compared with the analytical and numerical solutions. Although the response spectrums shown above and in the appendices are used for analysis, the principle behind PSa and PSv spectrums can be exemplified by comparing them with the spectral acceleration (Sa) and velocity (Sv) spectrums, respectively. As briefly noted in Chapter 4, for systems with low damping ratios, the pseudo values are assumed to be the same as the spectral values for acceleration and velocity, allowing Equation 5.11 and 5.12 to be used to relate the various response spectrums. Obviously, using the equations above significantly simplifies the process of developing the response spectrums and allows for the complex integration to be avoided. In general, most civil engineering structures have damping ratios less than 20% which allows for the pseudo spectrums to be used. In order to compare the PSa and Sa values with one another, the two acceleration responses for the Northridge earthquake at 5% damping are shown

in Figure 31 below. Additionally, the PSa and Sa spectrums for the Northridge Earthquake at 2.5%, 7.5%, and 10% damping are shown in Appendix M.

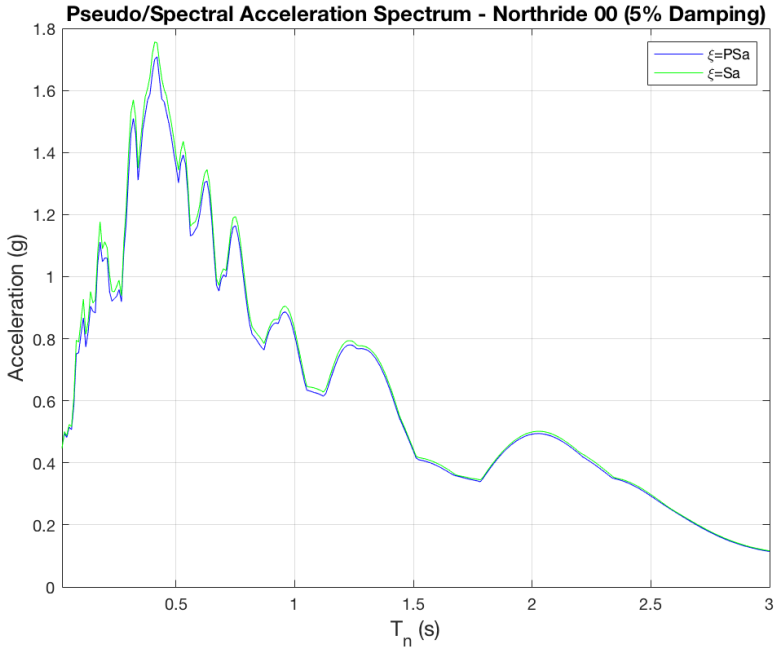

Figure 31: PSa and Sa (5% Damping) – Northridge 00 (USC Sta. 5303)

As shown by Figure 31 and the figure in Appendix M, as the damping ratio increases, the error of the pseudo-acceleration spectrums also increases. For the 2.5% damping case, the two accelerations are nearly identical, whereas for the 10% damping case, the error between the two spectrums is more noticeable. Furthermore, this relationship is exemplified in Figure 32 by plotting the ratio of the PSa divided by the Sa for periods ranging between 0 and 20 seconds.

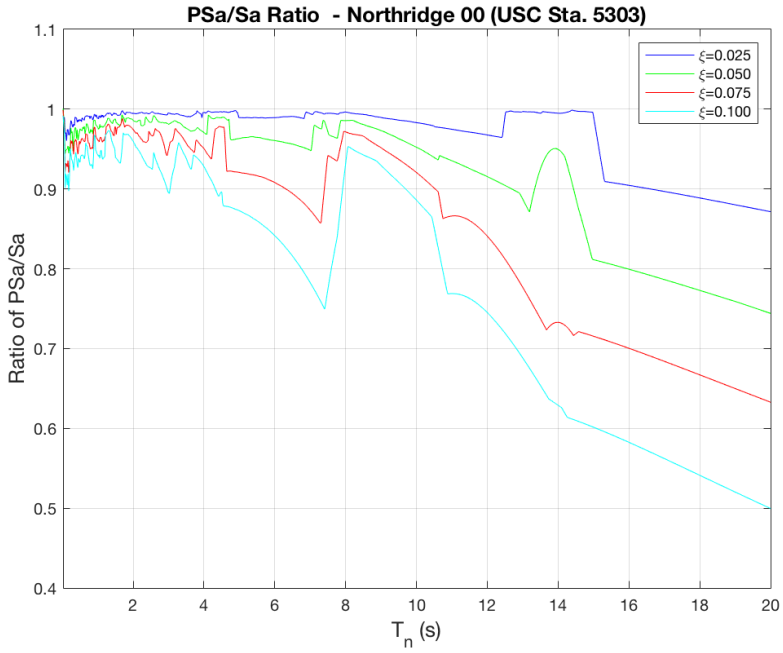

Figure 32: PSa/Sa Ratio – Northridge 00 (USC Sta. 5303)

Figure 32 further shows how the increase in damping ratio decreases the accuracy of the PSa values. For long periods (14 seconds and above), the PSa values are much less accurate, and increasing the damping ratio by 2.5% amplifies the inaccuracy by over 10%.

To further study the general trends of PSa response spectrums, the PSa values can be normalized by the peak ground acceleration (PGA). By normalizing the PSa spectrum, the acceleration response caused by earthquake ground motions is shown regardless of the specific PGA. The normalized pseudo-acceleration response spectrums are shown in the figures below for the Loma Prieta and Northridge earthquakes.

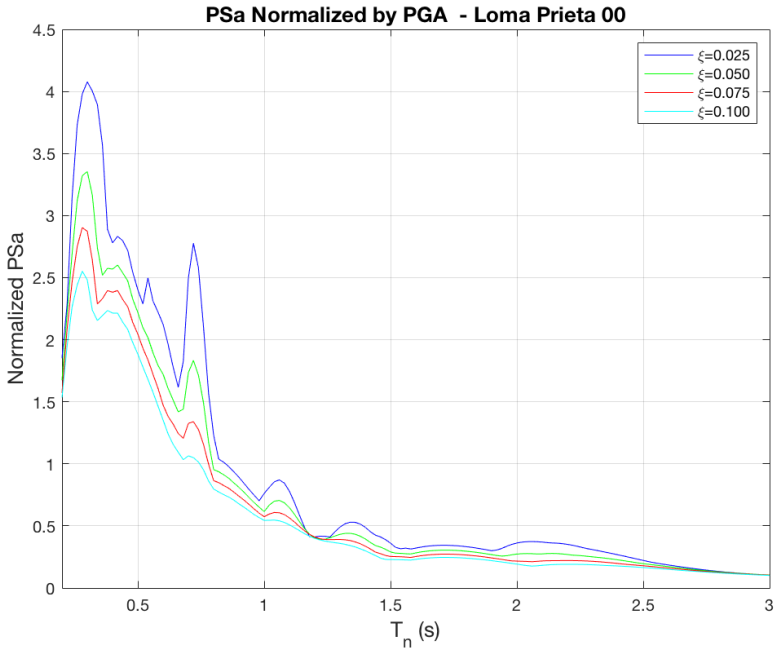

Figure 33: PSa Spectrum Normalized to PGA – Loma Prieta 00

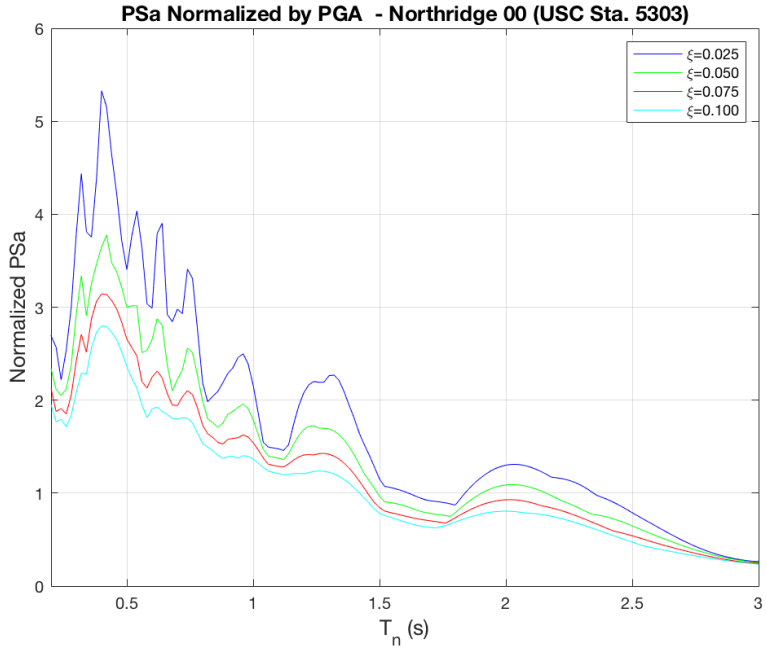

Figure 34: PSa Spectrum Normalized to PGA – Northridge 00 (USC Sta.)

Although the normalized spectrums are still unique to the specific earthquake, similar trends between the two spectrums can be established. In

both cases, the peak PSa value occurs at a natural period that is less than 0.5 seconds. After the peak, the PSa values trend downwards. At periods greater than 2 seconds, the values decrease directly with an increase in the natural period and the level of damping has a lessened effect. At periods greater than 3 seconds, the PSa values are nearly identical regardless of the damping ratio.

Similarly, the PSv spectrums can also be normalized by the peak ground velocity (PGV). Although effective, the normalized PSv spectrums are more difficult to establish trends for when compared with the normalized PSa spectrums. For this reason, the normalized PSv spectrums for the five earthquakes are developed. The normalized PSv spectrums for the Loma Prieta and Northridge Earthquakes are shown below in Figure 35 and 36, respectively.

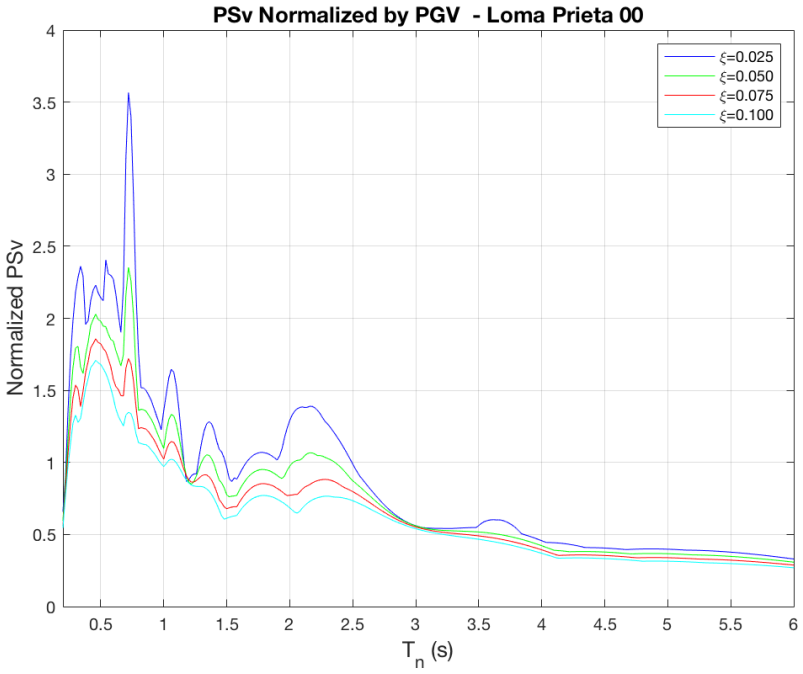

Figure 35: PSv Spectrum Normalized to PGV – Loma Prieta 00

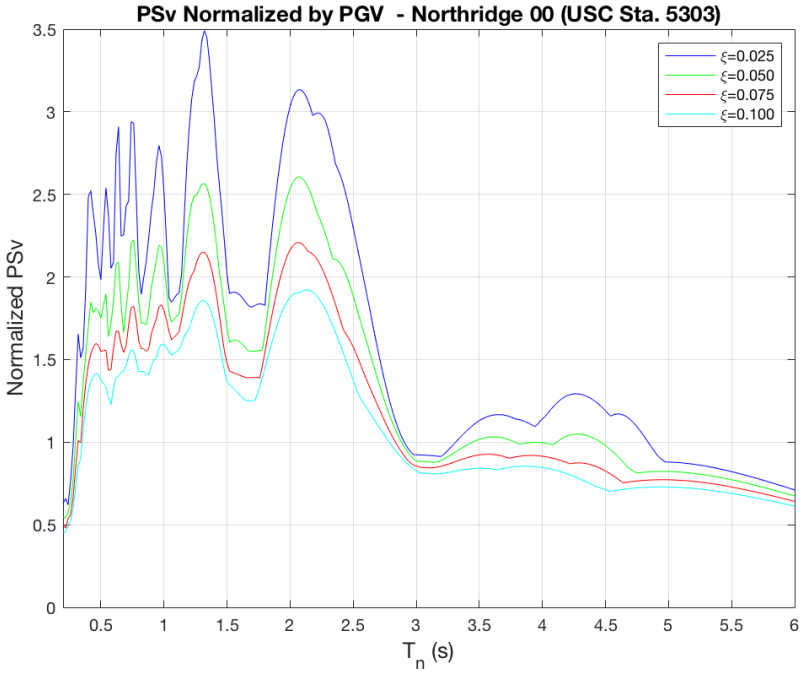

Figure 36: PSv Spectrum Normalized to PGV – Northridge 00 (USC Sta.)

The normalized PSv spectrums for the remaining earthquakes are presented in Appendix N. Evidenced by the figures, the PSv spectrums are more dependent on the specific earthquake under analysis. Despite this, all five of the earthquakes have peak PSv values that occur at periods less than 2 seconds. Although this trend can be established, a 2 second range is not as precise as the 0.5 second range shown by the normalized PSa spectrums. Another more obvious trend shown by the normalized spectrums is that at higher periods, the PSv values decrease with an increase in natural period.

Lastly, from the normalized PSa and PSv spectrums a relationship between the peak PSa values and PGA and peak PSv values and PGV can be developed. Although a sample size of five earthquakes is too small to establish a definitive relationship, through research, design spectrums have been developed that attempt to characterize the elastic response of systems subject to any

earthquake ground motion. Through the analysis of a large number of earthquakes, a generic elastic design spectrum can be developed, which can then be scaled to the PGA and PGV values of specific earthquakes and used in structural design. Although not covered in this thesis, generic elastic design spectrums are useful tools that can further simplify the process of seismic analysis.

5.5 Response Analysis of MDOF Shear Frames

In conjunction with the previous chapters, the three systems of interest are the one-story, two-story, and three-story shear frame. Through the application of THA, the analytical maximum displacement response for each shear frame due to the five earthquake ground motions is determined. For each earthquake and shear frame, damping ratios of 0.025, 0.050, 0.075, and 0.10 are applied for analysis. The analytical solutions for each shear frame, earthquake, and damping ratio are then compared with the results obtained from the Absolute Sum (ABS), Square-Root-of-the-Sum-of-Squares (SRSS), and Complete Quadratic Combination (CQC) modal combination methods. The analytical displacement response spectrums for each earthquake developed in Section 5.4 are used for each modal combination method in this section. In the subsequent section, Section 5.6, the analytical maximum displacement responses are compared with the results obtained from the modal combination methods when the numerical displacement response spectrums are used.

An important consideration is the fact that the one-story shear frame is a SDOF system. In Section 5.3, the analytical and numerical displacement time

histories were developed for a SDOF system with a natural period of 0.3001s. For this reason, the analysis completed in Section 5.3 represents the response of the one-story shear frame for each earthquake and damping ratio. Obviously, for SDOF systems, modal combination methods are not necessary, making the primary focus of this section and Section 5.6 the MDOF two-story and three-story shear frame.

First, the analytical maximum displacement responses resulting from the five earthquake ground motions are determined for the two-story shear frame. From the analytical response spectrums developed in Section 5.4, the maximum displacement at each natural period of the two-story shear frame is found and shown in Table 26 below.

Table 26: Maximum Displacement Response for Two-Story Shear Frame

U_{1MAX} (in) for T_{n1} = 0.5025s					
(ξ)	**El Centro**	**Kern**	**SLO**	**Loma Prieta**	**Northridge**
0	2.9186	2.4828	0.2295	5.5881	4.4235
0.025	2.4219	0.9033	0.2008	3.7572	3.8230
0.050	2.0474	0.8489	0.1847	3.4680	3.3663
0.075	1.8694	0.7856	0.1705	3.1923	2.9768
0.100	1.7185	0.7193	0.1590	2.9379	2.6479
U_{2MAX} (in) for T_{n2} = 0.2003s					
(ξ)	**El Centro**	**Kern**	**SLO**	**Loma Prieta**	**Northridge**
0	0.6283	0.5047	0.1477	0.4649	0.6335
0.025	0.3277	0.2111	0.0825	0.4128	0.4749
0.050	0.2551	0.1644	0.0605	0.3910	0.4142
0.075	0.2251	0.1343	0.0485	0.3786	0.3845
0.100	0.2055	0.1170	0.0411	0.3692	0.3531

Next, MATLAB code is developed to find the displacement time history at each DOF of the two-story shear frame when it is subject to the five earthquake ground motions.

The first earthquake ground motion applied to the two-story shear frame is the Imperial Valley – El Centro Earthquake which took place on 5/18/1940. The ground motion was recorded by Station Array #9 in the 00 (N-S) direction. The record shows a PGA of 0.348 g, a PGV of 13.169 inches per second, and a PGD of 4.278 inches. Figure 37 below shows the analytical displacement history for each DOF and a damping of 5%. In addition to Figure 37, the analytical displacement histories for the El Centro Earthquake at 2.5%, 7.5%, and 10% damping are shown in Appendix O.

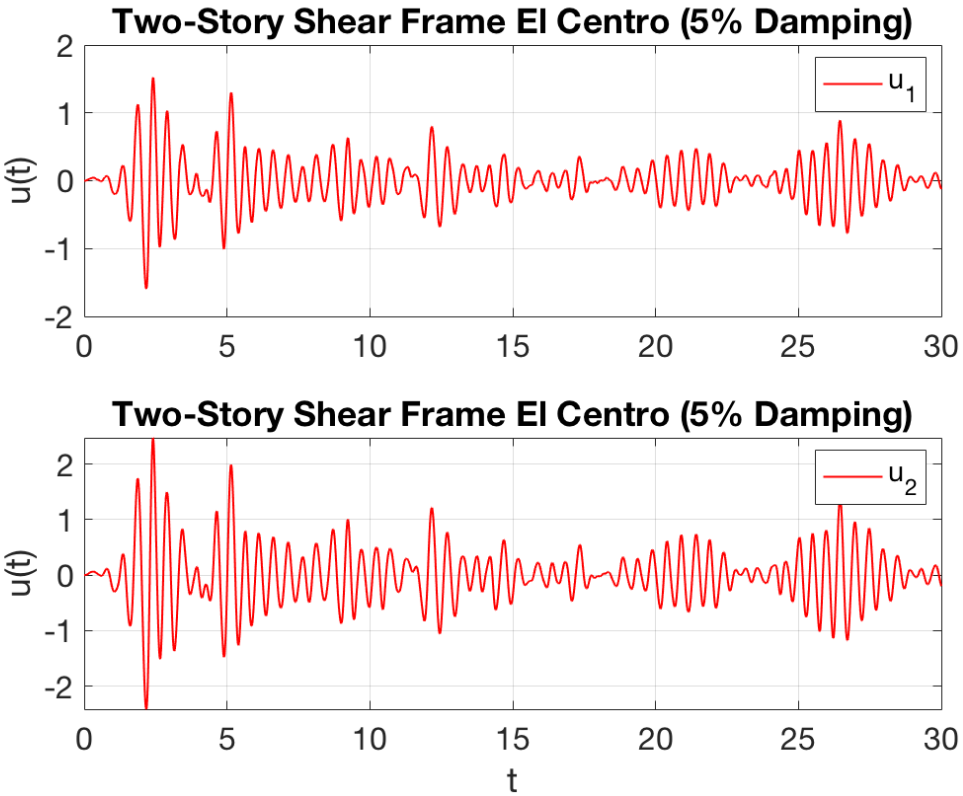

Figure 37: Two-Story El Centro 00 Displacement History (ξ = 0.05)

The analytical maximum displacement response at each DOF for the El Centro 00 ground motion is now compared with the SRSS, CQC, and ABS methods shown below in Table 27, Table 28, and Table 29, respectively.

Table 27: Two-Story El Centro 00 SRSS Method

El Centro 00 SRSS Method Maximum Displacement Response						
(ξ)	**U_{1MAX} Analytical**	**U_{2MAX} Analytical**	**U_{1MAX} SRSS**	**U_1 Error SRSS**	**U_{2MAX} SRSS**	**U_2 Error SRSS**
0.025	1.8128”	2.9506”	1.8544”	0.0229	2.8803”	0.0238
0.050	1.5939”	2.4746”	1.5674”	0.0167	2.4348”	0.0161
0.075	1.4582”	2.2008”	1.4311”	0.0186	2.2231”	0.0101
0.100	1.3469”	2.0252”	1.3155”	0.0233	2.0437”	0.0091

Table 28: Two-Story El Centro 00 CQC Method

El Centro 00 CQC Method Maximum Displacement Response						
(ξ)	**U_{1MAX} Analytical**	**U_{2MAX} Analytical**	**U_{1MAX} CQC**	**U_1 Error CQC**	**U_{2MAX} CQC**	**U_2 Error CQC**
0.025	1.8128”	2.9506”	1.8541”	0.0228	2.8805”	0.0238
0.050	1.5939”	2.4746”	1.5668”	0.0171	2.4354”	0.0159
0.075	1.4582”	2.2008”	1.4298”	0.0195	2.2248”	0.0106
0.100	1.3469”	2.0252”	1.3135”	0.0248	2.0453”	0.0099

Table 29: Two-Story El Centro 00 ABS Method

El Centro 00 ABS Method Maximum Displacement Response						
(ξ)	**U_{1MAX} Analytical**	**U_{2MAX} Analytical**	**U_{1MAX} ABS**	**U_1 Error ABS**	**U_{2MAX} ABS**	**U_2 Error ABS**
0.025	1.8128”	2.9506”	1.9298”	0.0645	2.9416”	0.0030
0.050	1.5939”	2.4746”	1.6262”	0.0202	2.4826”	0.0032
0.075	1.4582”	2.2008”	1.4830”	0.0170	2.2653”	0.0293
0.100	1.3469”	2.0252”	1.3629”	0.0119	2.0821”	0.0281

The second earthquake ground motion applied to the two-story shear frame is the Kern County Earthquake which took place on 7/21/1952. The ground motion was recorded by USGS Station 1095 in the 111 (S69E) direction. The record shows a PGA of 0.179 g, a PGV of 6.974 inches per second, and a PGD of 3.603 inches. Figure 38 below shows the analytical displacement history for each DOF and a damping of 5%. In addition to Figure 38, the analytical displacement histories for the Kern County Earthquake at 2.5%, 7.5%, and 10% damping are shown in Appendix P.

Figure 38: Two-Story Kern County 111 Displacement History (ξ = 0.05)

The analytical maximum displacement response at each DOF for the Kern County 111 ground motion is now compared with the SRSS, CQC, and ABS methods shown below in Table 30, Table 31, and Table 32, respectively.

Table 30: Two-Story Kern County 111 SRSS Method

Kern County 111 SRSS Method Maximum Displacement Response						
(ξ)	**U_{1MAX} Analytical**	**U_{2MAX} Analytical**	**U_{1MAX} SRSS**	**U_1 Error SRSS**	**U_{2MAX} SRSS**	**U_2 Error SRSS**
0.025	0.7021”	1.0752”	0.6930”	0.0130	1.0748”	0.0003
0.050	0.6533”	1.0041”	0.6506”	0.0042	1.0098”	0.0057
0.075	0.6010”	0.9273”	0.6018”	0.0013	0.9344”	0.0077
0.100	0.5555”	0.8574”	0.5510”	0.0081	0.8556”	0.0021

Table 31: Two-Story Kern County 111 CQC Method

Kern County 111 CQC Method Maximum Displacement Response						
(ξ)	**U_{1MAX} Analytical**	**U_{2MAX} Analytical**	**U_{1MAX} CQC**	**U_1 Error CQC**	**U_{2MAX} CQC**	**U_2 Error CQC**
0.025	0.7021”	1.0752”	0.6928”	0.0132	1.0749”	0.0002
0.050	0.6533”	1.0041”	0.6510”	0.0035	1.0095”	0.0054
0.075	0.6010”	0.9273”	0.6026”	0.0026	0.9338”	0.0071
0.100	0.5555”	0.8574”	0.5221”	0.0060	0.8546”	0.0032

Table 32: Two-Story Kern County 111 ABS Method

Kern County 111 ABS Method Maximum Displacement Response						
(ξ)	**U_{1MAX} Analytical**	**U_{2MAX} Analytical**	**U_{1MAX} ABS**	**U_1 Error ABS**	**U_{2MAX} ABS**	**U_2 Error ABS**
0.025	0.7021”	1.0752”	0.7430”	0.0582	1.1158”	0.0378
0.050	0.6533”	1.0041”	0.6880”	0.0532	1.0404”	0.0362
0.075	0.6010”	0.9273”	0.6326”	0.0524	0.9595”	0.0347
0.100	0.5555”	0.8574”	0.5778”	0.0401	0.8774”	0.0233

The third earthquake ground motion applied to the two-story shear frame is the San Luis Obispo Earthquake which took place on 11/22/1952. The ground motion was recorded by USGS Station 1083 in the 324 (N36W) direction. The record shows a PGA of 0.054 g, a PGV of 1.322 inches per second, and a PGD of 0.315 inches. Figure 39 below shows the analytical displacement history for each DOF and a damping of 5%. In addition to Figure 39, the analytical displacement histories for the San Luis Obispo Earthquake at 2.5%, 7.5%, and 10% damping are shown in Appendix Q.

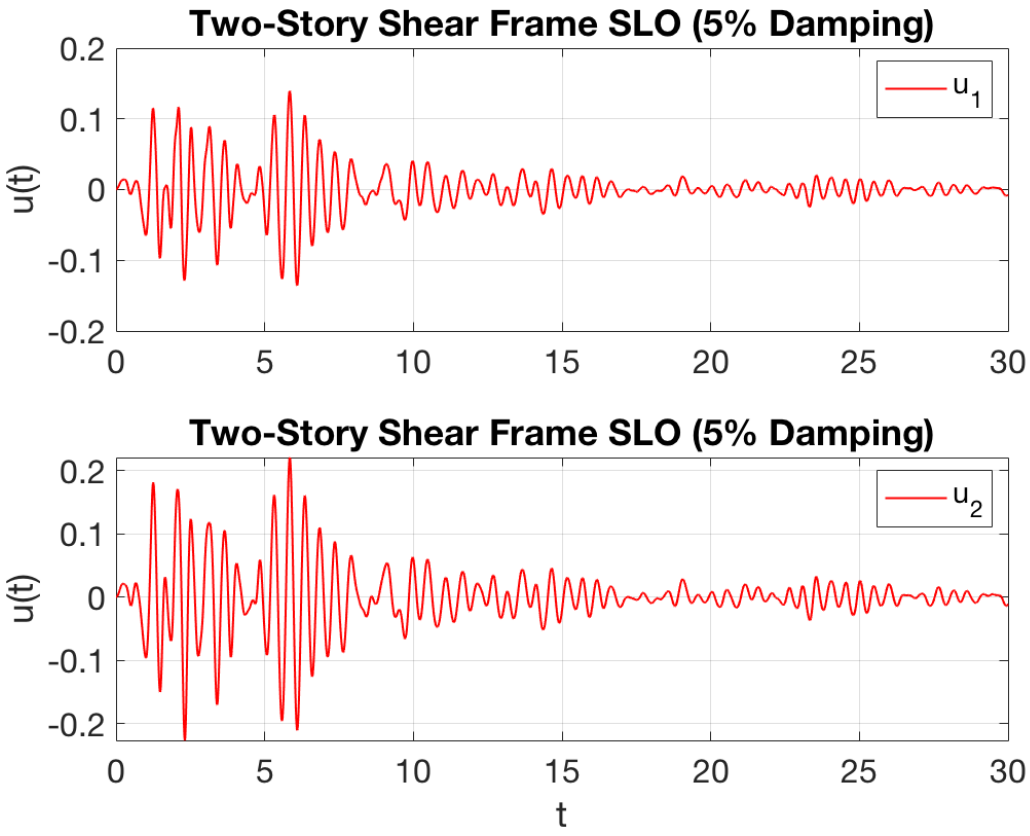

Figure 39: Two-Story SLO 324 Displacement History (ξ = 0.05)

The analytical maximum displacement response at each DOF for the San Luis Obispo 324 ground motion is now compared with the SRSS, CQC, and ABS methods shown below in Table 33, Table 34, and Table 35, respectively.

Table 33: Two-Story SLO 324 SRSS Method

San Luis Obispo 324 SRSS Method Maximum Displacement Response						
(ξ)	**U_{1MAX} Analytical**	**U_{2MAX} Analytical**	**U_{1MAX} SRSS**	**U_1 Error SRSS**	**U_{2MAX} SRSS**	**U_2 Error SRSS**
0.025	0.1557”	0.2408”	0.1548”	0.0053	0.2393”	0.0064
0.050	0.1395”	0.2267”	0.1420”	0.0179	0.2199”	0.0304
0.075	0.1238”	0.2114”	0.1309”	0.0572	0.2029”	0.0404
0.100	0.1161”	0.1952”	0.1220”	0.0511	0.1892”	0.0308

Table 34: Two-Story SLO 324 CQC Method

San Luis Obispo 324 CQC Method Maximum Displacement Response						
(ξ)	**U_{1MAX} Analytical**	**U_{2MAX} Analytical**	**U_{1MAX} CQC**	**U_1 Error CQC**	**U_{2MAX} CQC**	**U_2 Error CQC**
0.025	0.1557”	0.2408”	0.1549”	0.0049	0.2392”	0.0066
0.050	0.1395”	0.2267”	0.1421”	0.0190	0.2197”	0.0309
0.075	0.1238”	0.2114”	0.1312”	0.0594	0.2027”	0.0415
0.100	0.1161”	0.1952”	0.1224”	0.0546	0.1888”	0.0325

Table 35: Two-Story SLO 324 ABS Method

San Luis Obispo 324 ABS Method Maximum Displacement Response						
(ξ)	**U_{1MAX} Analytical**	**U_{2MAX} Analytical**	**U_{1MAX} ABS**	**U_1 Error ABS**	**U_{2MAX} ABS**	**U_2 Error ABS**
0.025	0.1557”	0.2408”	0.1730”	0.1115	0.2543”	0.0562
0.050	0.1395”	0.2267”	0.1555”	0.1148	0.2310”	0.0188
0.075	0.1238”	0.2114”	0.1418”	0.1452	0.2119”	0.0019
0.100	0.1161”	0.1952”	0.1313”	0.1311	0.1968”	0.0082

The fourth earthquake ground motion applied to the two-story shear frame is the Loma Prieta Earthquake which took place on 10/17/1989. The ground motion was recorded by CSMIP Station 57007 in the 00 (N-S) direction. The record shows a PGA of 0.630 g, a PGV of 21.731 inches per second, and a PGD of 3.756 inches. Figure 40 below shows the analytical displacement history for each DOF and a damping of 5%. In addition to Figure 40, the analytical displacement histories for the Loma Prieta Earthquake at 2.5%, 7.5%, and 10% damping are shown in Appendix R.

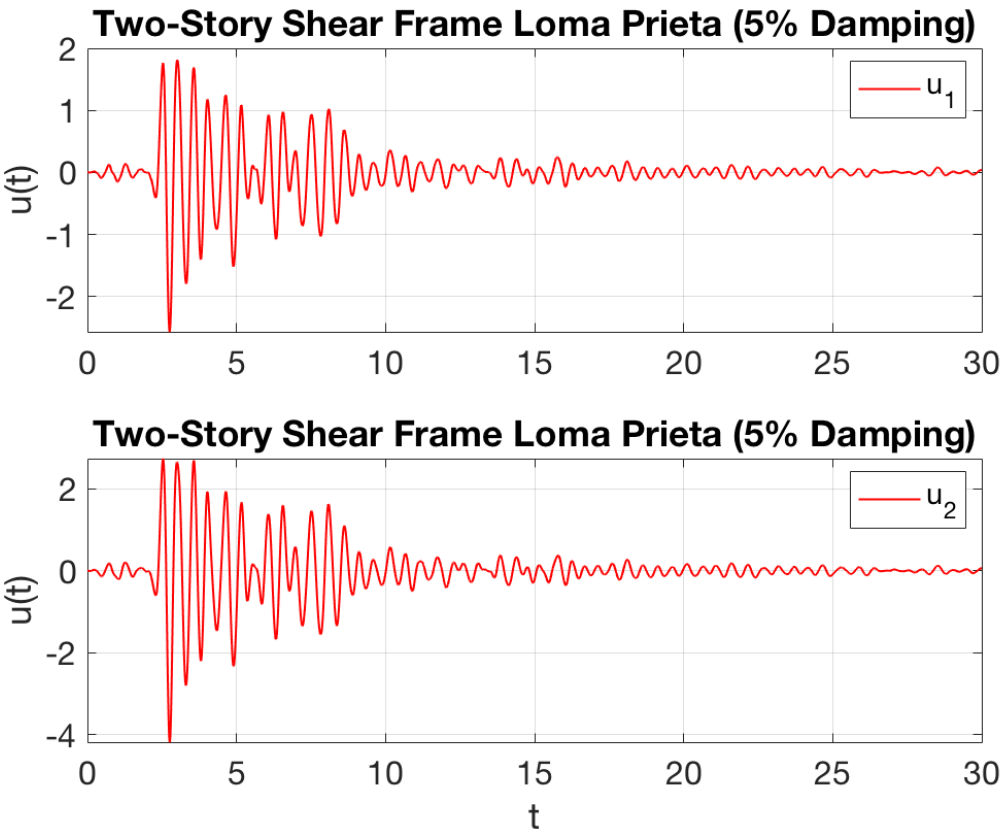

Figure 40: Two-Story Loma Prieta 00 Displacement History (ξ = 0.05)

The analytical maximum displacement response at each DOF for the Loma Prieta 00 ground motion is now compared with the SRSS, CQC, and ABS methods shown below in Table 36, Table 37, and Table 38, respectively.

Table 36: Two-Story Loma Prieta 00 SRSS Method

Loma Prieta 00 SRSS Method Maximum Displacement Response						
(ξ)	**U_{1MAX} Analytical**	**U_{2MAX} Analytical**	**U_{1MAX} SRSS**	**U_1 Error SRSS**	**U_{2MAX} SRSS**	**U_2 Error SRSS**
0.025	2.7789”	4.5491”	2.8759”	0.0349	4.4680”	0.0178
0.050	2.5699”	4.1830”	2.6546”	0.0330	4.1241”	0.0141
0.075	2.3685”	3.8430”	2.4437”	0.0318	3.7963”	0.0122
0.100	2.1820”	3.5403”	2.2492”	0.0308	3.4939”	0.0131

Table 37: Two-Story Loma Prieta 00 CQC Method

Loma Prieta 00 CQC Method Maximum Displacement Response						
(ξ)	**U_{1MAX} Analytical**	**U_{2MAX} Analytical**	**U_{1MAX} CQC**	**U_1 Error CQC**	**U_{2MAX} CQC**	**U_2 Error CQC**
0.025	2.7789”	4.5491”	2.8756”	0.0348	4.4682”	0.0178
0.050	2.5699”	4.1830”	2.6556”	0.0333	4.1233”	0.0143
0.075	2.3685”	3.8430”	2.4459”	0.0327	3.7946”	0.0126
0.100	2.1820”	3.5403”	2.2528”	0.0325	3.4909”	0.0140

Table 38: Two-Story Loma Prieta 00 ABS Method

Loma Prieta 00 ABS Method Maximum Displacement Response						
(ξ)	**U_{1MAX} Analytical**	**U_{2MAX} Analytical**	**U_{1MAX} ABS**	**U_1 Error ABS**	**U_{2MAX} ABS**	**U_2 Error ABS**
0.025	2.7789”	4.5491”	2.9713”	0.0692	4.5453”	0.0008
0.050	2.5699”	4.1830”	2.7447”	0.0680	4.1972”	0.0034
0.075	2.3685”	3.8430”	2.5311”	0.0686	3.8672”	0.0063
0.100	2.1820”	3.5403”	2.3342”	0.0698	3.5629”	0.0064

The final earthquake ground motion applied to the two-story shear frame is the Northridge Earthquake which took place on 1/17/1994. The ground motion was recorded by USC Station 5303 in the 00 (N-S) direction. The record shows a PGA of 0.453 g, a PGV of 24.081 inches per second, and a PGD of 7.011 inches. Figure 40 below shows the analytical displacement history for each DOF and a damping of 5%. In addition to Figure 41, the analytical displacement histories for the Northridge Earthquake at 2.5%, 7.5%, and 10% damping are shown in Appendix S.

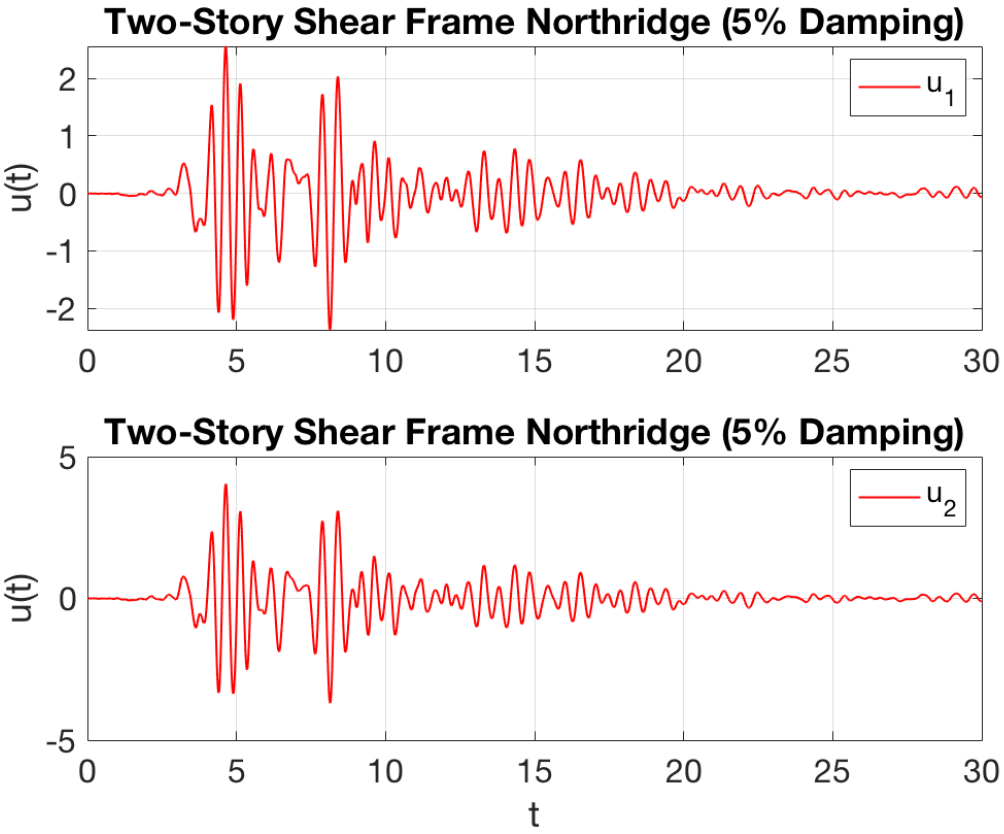

Figure 41: Two-Story Northridge 00 Displacement History (ξ = 0.05)

The analytical maximum displacement response at each DOF for the Loma Prieta 00 ground motion is now compared with the SRSS, CQC, and ABS methods shown below in Table 39, Table 40, and Table 41, respectively.

Table 39: Two-Story Northridge 00 SRSS Method

Northridge 00 SRSS Method Maximum Displacement Response						
(ξ)	**U_{1MAX} Analytical**	**U_{2MAX} Analytical**	**U_{1MAX} SRSS**	**U_1 Error SRSS**	**U_{2MAX} SRSS**	**U_2 Error SRSS**
0.025	2.8977”	4.5733”	2.9267”	0.0100	4.5464”	0.0059
0.050	2.5590”	4.0387”	2.5771”	0.0071	4.0033”	0.0088
0.075	2.2585”	3.5621”	2.2740”	0.0091	3.5402”	0.0061
0.100	2.0157”	3.1621”	2.0273”	0.0058	3.1491”	0.0041

Table 40: Two-Story Northridge 00 CQC Method

Northridge 00 CQC Method Maximum Displacement Response						
(ξ)	**U_{1MAX} Analytical**	**U_{2MAX} Analytical**	**U_{1MAX} CQC**	**U_1 Error CQC**	**U_{2MAX} CQC**	**U_2 Error CQC**
0.025	2.8977”	4.5733”	2.9270”	0.0101	4.5462”	0.0059
0.050	2.5590”	4.0387”	2.5781”	0.0075	4.0024”	0.0090
0.075	2.2585”	3.5621”	2.2812”	0.0100	3.5384”	0.0066
0.100	2.0157”	3.1621”	2.0308”	0.0075	3.1462”	0.0050

Table 41: Two-Story Northridge 00 ABS Method

Northridge 00 ABS Method Maximum Displacement Response						
(ξ)	**U_{1MAX} Analytical**	**U_{2MAX} Analytical**	**U_{1MAX} ABS**	**U_1 Error ABS**	**U_{2MAX} ABS**	**U_2 Error ABS**
0.025	2.8977”	4.5733”	3.0362”	0.0478	4.6353”	0.0136
0.050	2.5590”	4.0387”	2.6725”	0.0444	4.0808”	0.0104
0.075	2.2585”	3.5621”	2.3676”	0.0483	3.6121”	0.0140
0.100	2.0157”	3.1621”	2.1086”	0.0461	3.2151”	0.0167

As shown in the tables above, the SRSS and CQC results were considerably accurate and similar to one another. With the exception of the San Luis Obispo 324 ground motion, all of the errors for the SRSS and CQC methods were below 5%. As mentioned previously, the SRSS and CQC results should closely resemble one another for the two-story shear frame since the frequencies and modes are well spaced for the two-story shear frame. Surprisingly, the SRSS and CQC methods did not always produce conservative maximum displacement results. For instance, in the case of the Loma Prieta 00 and Northridge 00 ground motions, the maximum response at the first DOF was higher than the analytical response, but the maximum response at the second DOF was lower than the analytical response. Similarly, for the El Centro 00 ground motion, for smaller damping ratios (0.025 and 0.050) the maximum response at both DOFs was lower than the analytical, but for higher damping ratios the responses were larger. From the SRSS and CQC results for the five earthquakes, there is no distinct relationship between the damping ratio and accuracy of the two methods. In some cases, the methods are more accurate for higher damping ratios, but in other cases lower damping ratios produce more accurate results. With the exception of the Kern County 111 ground motion, the average accuracy of each method was the highest for the SRSS method and lowest for the ABS method. Although the SRSS method yields more accurate results for four of the five earthquakes when compared with the CQC method, the difference between the two is essentially negligible. As a whole, the ABS method produces the most inaccurate and inconsistent results, but the inaccuracy is mainly due to the first

DOF response. For all five earthquakes, the ABS method produced maximum responses at the second DOF that are comparable with the SRSS and CQC results. In the case of the Loma Prieta 00 and Northridge 00 ground motions, the ABS method actually yields the most accurate maximum displacement responses for the second DOF. On the other hand, the maximum responses produced by the ABS method for the first DOF were considerably more inaccurate. When analyzing the accuracy of the ABS method for the five earthquakes, it is evidenced that a higher peak ground displacement (PGD) results in a more accurate maximum response for the second DOF. For each modal combination, the San Luis Obispo 324 ground motion resulted in the most inaccurate results.

In addition to the two-story shear frame, the three-story shear frame is subjected to the five earthquake ground motions and analyzed. Once again, the maximum displacement response at each natural period of the three-story shear frame is determined using the displacement response spectrums developed in Section 5.4. The values of the maximum displacement response for each natural period are shown in Table 42 on the next page.

Table 42: Max Displacement Response for Three-Story Shear Frame

U_{1MAX} (in) for T_{n1} = 0.7123s					
(ξ)	**El Centro**	**Kern**	**SLO**	**Loma Prieta**	**Northridge**
0	5.2402	2.0184	0.5398	19.023	12.0120
0.025	3.4714	1.4042	0.4772	8.4947	6.6122
0.050	3.0091	1.2254	0.4247	5.6722	4.9610
0.075	2.7346	1.0670	0.3807	4.2121	4.4655
0.100	2.5457	0.9363	0.3434	3.3294	4.0458
U_{2MAX} (in) for T_{n2} = 0.2584s					
(ξ)	**El Centro**	**Kern**	**SLO**	**Loma Prieta**	**Northridge**
0	1.8851	0.9702	0.2383	4.0358	1.3942
0.025	0.7253	0.3040	0.1035	1.4318	0.7192
0.050	0.5834	0.2362	0.0741	1.2525	0.6081
0.075	0.4874	0.2112	0.0663	1.1167	0.5592
0.100	0.4147	0.1974	0.0596	0.9985	0.5252
U_{3MAX} (in) for T_{n3} = 0.1835s					
(ξ)	**El Centro**	**Kern**	**SLO**	**Loma Prieta**	**Northridge**
0	0.3769	0.6739	0.0977	0.7632	0.6333
0.025	0.2644	0.1577	0.0729	0.3898	0.4277
0.050	0.2321	0.1256	0.0569	0.3583	0.3698
0.075	0.2088	0.1063	0.0464	0.3394	0.3245
0.100	0.1913	0.0919	0.0391	0.3253	0.2917

Following the same process for the three-story shear frame as the two-story shear frame, MATLAB code is generated, and the displacement histories for each DOF are developed for the five earthquakes. The displacement time history for each earthquake and 5% damping is shown below. Additionally, the analytical displacement histories at 2.5%, 7.5%, and 10% damping for the El Centro, Kern County, San Luis Obispo, Loma Prieta, and Northridge Earthquake are shown in Appendix T, Appendix U, Appendix V, Appendix W, and Appendix X, respectively. Also, tables are generated to compare the analytical response with the results of the three modal combination methods and shown below.

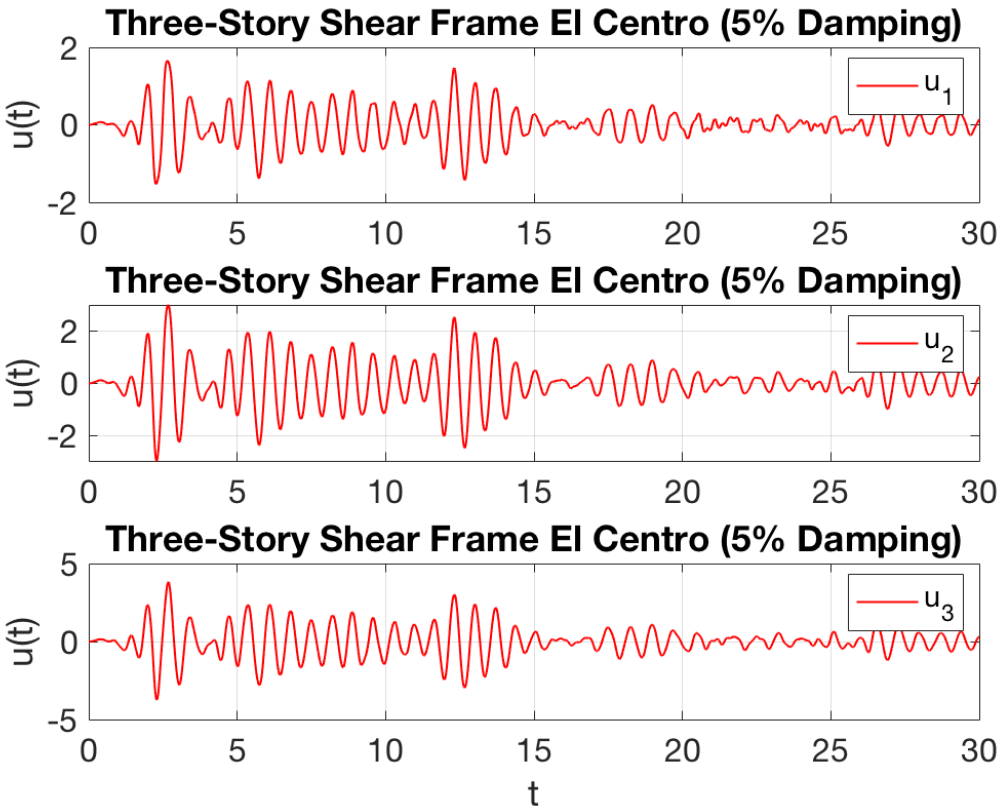

Figure 42: Three-Story El Centro 00 Displacement History (ξ = 0.05)

Table 43: Three-Story El Centro 00 Analytical Maximum Response

El Centro 00 Analytical Maximum Response			
(ξ)	**U_{1MAX}**	**U_{2MAX}**	**U_{3MAX}**
0.025	1.8967”	3.4508”	4.4514”
0.050	1.6564”	2.9930”	3.8199”
0.075	1.4454”	2.7563”	3.4648”
0.100	1.3523”	2.5682”	3.2172”

Table 44: Three-Story El Centro 00 SRSS Method

El Centro 00 SRSS Method Maximum Displacement Response						
(ξ)	U_{1MAX} SRSS	U_1 Error SRSS	U_{2MAX} SRSS	U_2 Error SRSS	U_{3MAX} SRSS	U_3 Error SRSS
0.025	1.9959”	0.0523	3.5227”	0.0209	4.2874”	0.0368
0.050	1.7284”	0.0434	3.0535”	0.0181	3.7158”	0.0273
0.075	1.5690”	0.0855	2.7749”	0.0067	3.3762”	0.0256
0.100	1.4593”	0.0791	2.5831”	0.0058	3.1425”	0.0232

Table 45: Three-Story El Centro 00 CQC Method

El Centro 00 CQC Method Maximum Displacement Response						
(ξ)	U_{1MAX} CQC	U_1 Error CQC	U_{2MAX} CQC	U_2 Error CQC	U_{3MAX} CQC	U_3 Error CQC
0.025	1.9965”	0.0526	3.5229”	0.0209	4.2870”	0.0369
0.050	1.7302”	0.0436	3.0539”	0.0179	3.7144”	0.0277
0.075	1.5663”	0.0836	2.7741”	0.0065	3.3786”	0.0249
0.100	1.4552”	0.0761	2.5820”	0.0054	3.1460”	0.0221

Table 46: Three-Story El Centro 00 ABS Method

El Centro 00 ABS Method Maximum Displacement Response						
(ξ)	U_{1MAX} ABS	U_1 Error ABS	U_{2MAX} ABS	U_2 Error ABS	U_{3MAX} ABS	U_3 Error ABS
0.025	2.2505”	0.1865	3.6311”	0.0523	4.5225”	0.0160
0.050	1.9363”	0.1690	3.1433”	0.0480	3.9072”	0.0228
0.075	1.7444”	0.2068	2.8515”	0.0345	3.5370”	0.0208
0.100	1.6103”	0.1908	2.6500”	0.0318	3.2805”	0.0197

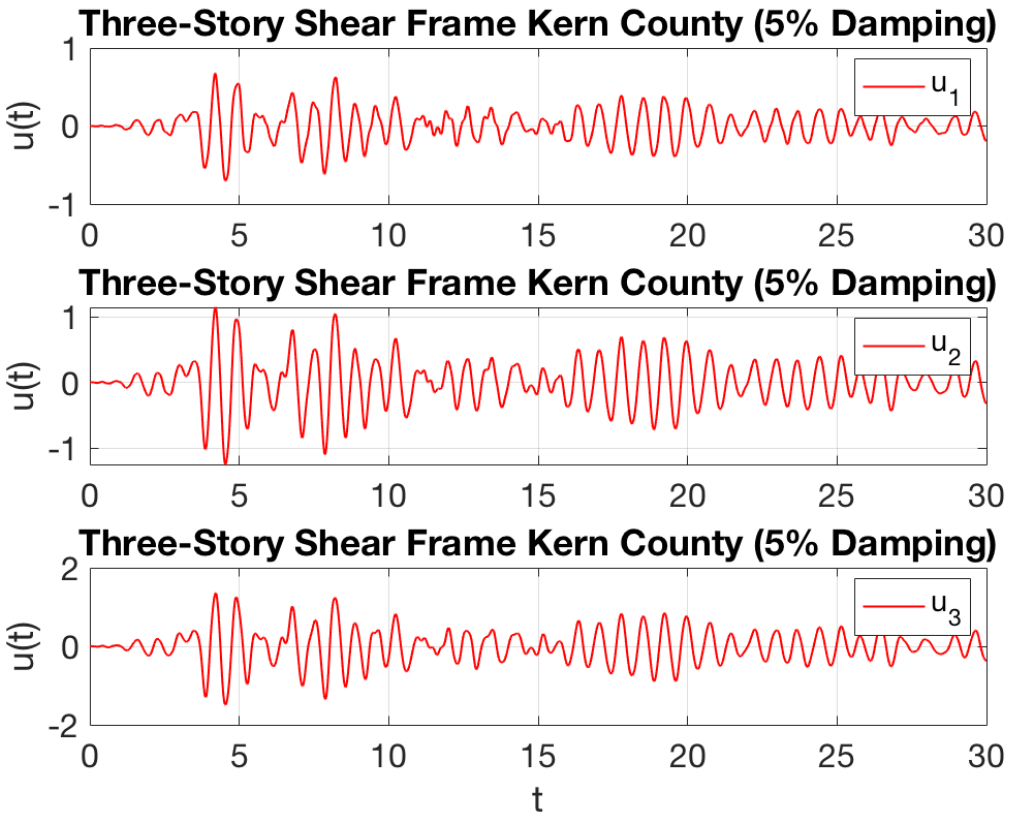

Figure 43: Three-Story Kern County 111 Displacement History (ξ = 0.05)

Table 47: Three-Story Kern County 111 Analytical Maximum Response

Kern County 111 Analytical Maximum Response			
(ξ)	**U_{1MAX}**	**U_{2MAX}**	**U_{3MAX}**
0.025	0.8224”	1.4413”	1.6956”
0.050	0.6998”	1.2501”	1.4918”
0.075	0.6115”	1.0855”	1.3069”
0.100	0.5524”	0.9471”	1.1613”

Table 48: Three-Story Kern County 111 SRSS Method

Kern County 111 SRSS Method Maximum Displacement Response						
(ξ)	U_{1MAX} SRSS	U_1 Error SRSS	U_{2MAX} SRSS	U_2 Error SRSS	U_{3MAX} SRSS	U_3 Error SRSS
0.025	0.8079”	0.0177	1.4251”	0.0112	1.7345”	0.0230
0.050	0.7038”	0.0057	1.2435”	0.0052	1.5132”	0.0143
0.075	0.6130”	0.0024	1.0828”	0.0025	1.3177”	0.0082
0.100	0.5384”	0.0252	0.9502”	0.0033	1.1564”	0.0042

Table 49: Three-Story Kern County 111 CQC Method

Kern County 111 CQC Method Maximum Displacement Response						
(ξ)	U_{1MAX} CQC	U_1 Error CQC	U_{2MAX} CQC	U_2 Error CQC	U_{3MAX} CQC	U_3 Error CQC
0.025	0.8081”	0.0174	1.4251”	0.0112	1.7343”	0.0228
0.050	0.7043”	0.0064	1.2438”	0.0050	1.5126”	0.0139
0.075	0.6140”	0.0041	1.0833”	0.0020	1.3165”	0.0074
0.100	0.5408”	0.0208	0.9506”	0.0037	1.1546”	0.0057

Table 50: Three-Story Kern County 111 ABS Method

Kern County 111 ABS Method Maximum Displacement Response						
(ξ)	U_{1MAX} ABS	U_1 Error ABS	U_{2MAX} ABS	U_2 Error ABS	U_{3MAX} ABS	U_3 Error ABS
0.025	0.9185”	0.1168	1.4761”	0.0241	1.8363”	0.0830
0.050	0.7906”	0.1297	1.2836”	0.0268	1.5927”	0.0677
0.075	0.6900”	0.1283	1.1179”	0.0298	1.3883”	0.0623
0.100	0.6095”	0.1034	0.9821”	0.0369	1.2219”	0.0522

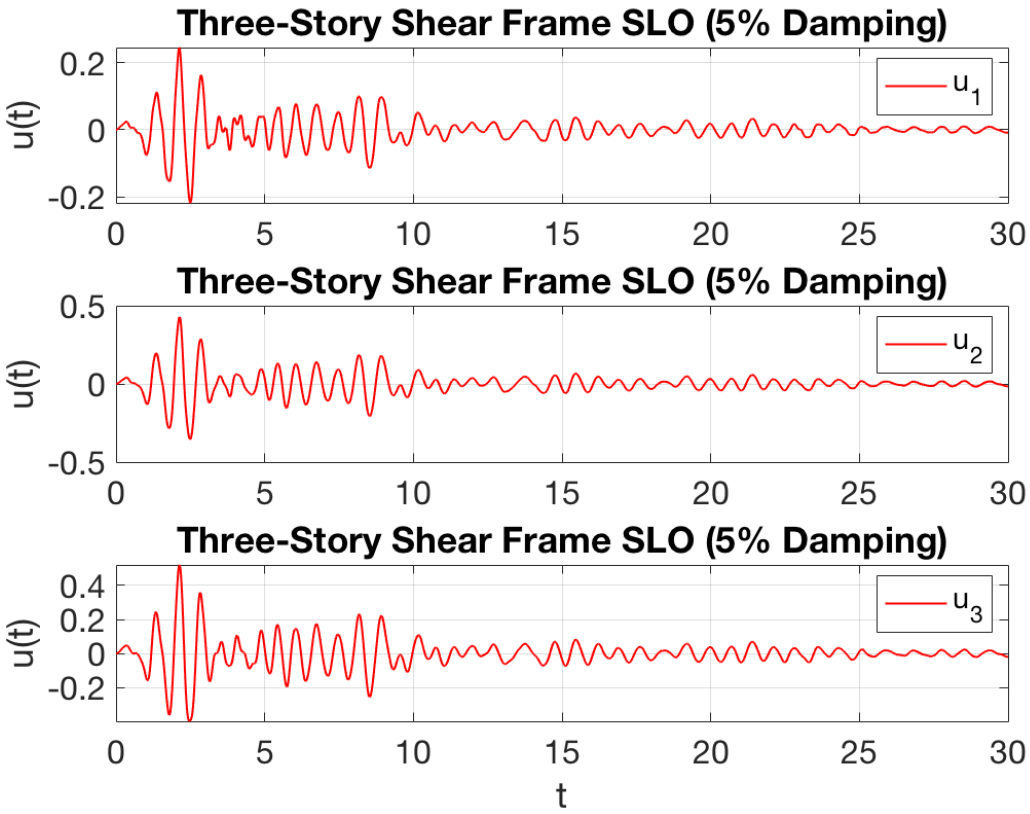

Figure 44: Three-Story SLO 324 Displacement History (ξ = 0.05)

Table 51: Three-Story SLO 324 Analytical Maximum Response

SLO 324 Analytical Maximum Response			
(ξ)	**U_{1MAX}**	**U_{2MAX}**	**U_{3MAX}**
0.025	0.2776”	0.4833”	0.5899”
0.050	0.2455”	0.4276”	0.5206”
0.075	0.2199”	0.3822”	0.4647”
0.100	0.1993”	0.3454”	0.4182”

Table 52: Three-Story SLO 324 SRSS Method

San Luis Obispo 324 SRSS Method Maximum Displacement Response						
(ξ)	U_{1MAX} SRSS	U_1 Error SRSS	U_{2MAX} SRSS	U_2 Error SRSS	U_{3MAX} SRSS	U_3 Error SRSS
0.025	0.2746”	0.0109	0.4843”	0.0021	0.5894”	0.0009
0.050	0.2437”	0.0076	0.4310”	0.0079	0.5244”	0.0073
0.075	0.2184”	0.0067	0.3863”	0.0106	0.4700”	0.0113
0.100	0.1970”	0.0117	0.3485”	0.0089	0.4240”	0.0137

Table 53: Three-Story SLO 324 CQC Method

San Luis Obispo 324 CQC Method Maximum Displacement Response						
(ξ)	U_{1MAX} CQC	U_1 Error CQC	U_{2MAX} CQC	U_2 Error CQC	U_{3MAX} CQC	U_3 Error CQC
0.025	0.2746”	0.0108	0.4843”	0.0022	0.5893”	0.0010
0.050	0.2435”	0.0083	0.4310”	0.0078	0.5245”	0.0076
0.075	0.2180”	0.0083	0.3862”	0.0104	0.4703”	0.0119
0.100	0.1964”	0.0146	0.3483”	0.0085	0.4244”	0.0149

Table 54: Three-Story SLO 324 ABS Method

San Luis Obispo 324 ABS Method Maximum Displacement Response						
(ξ)	U_{1MAX} ABS	U_1 Error ABS	U_{2MAX} ABS	U_2 Error ABS	U_{3MAX} ABS	U_3 Error ABS
0.025	0.3139”	0.1308	0.5039”	0.0428	0.6254”	0.0602
0.050	0.2726”	0.1102	0.4457”	0.0422	0.5506”	0.0577
0.075	0.2439”	0.1092	0.3989”	0.0435	0.4931”	0.0611
0.100	0.2197”	0.1021	0.3595”	0.0407	0.4446”	0.0631

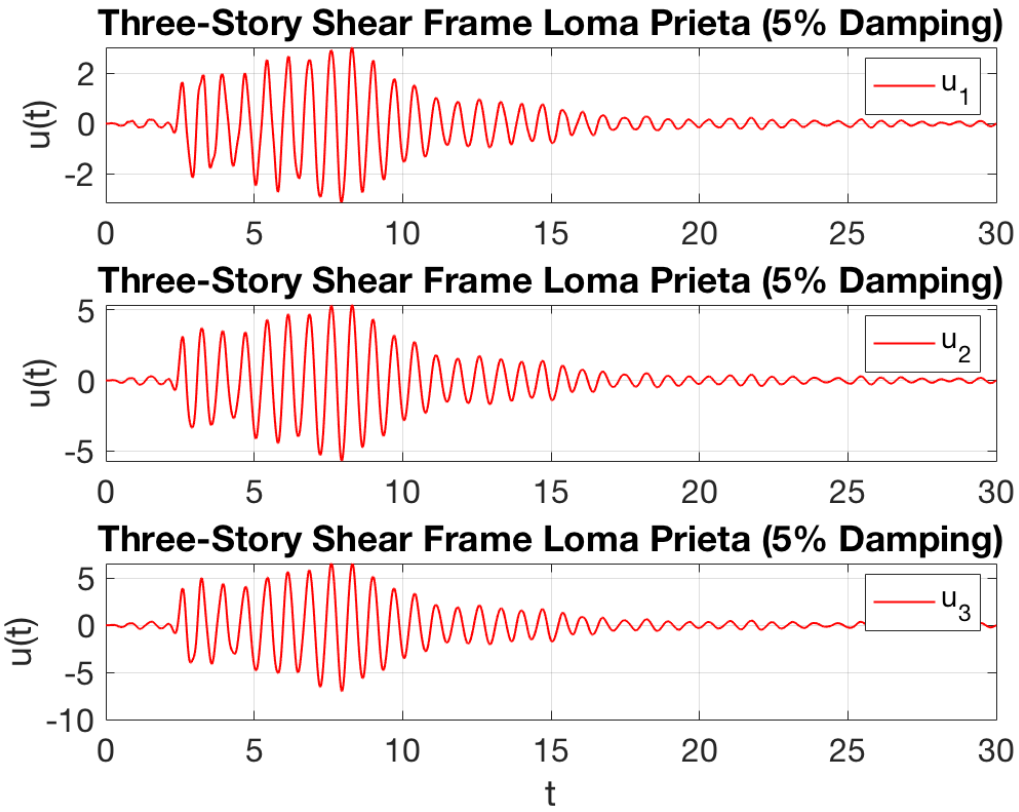

Figure 45: Three-Story Loma Prieta 00 Displacement History (ξ = 0.05)

Table 55: Three-Story Loma Prieta 00 Analytical Maximum Response

Loma Prieta 00 Analytical Maximum Response			
(ξ)	**U_{1MAX}**	**U_{2MAX}**	**U_{3MAX}**
0.025	4.8740”	8.5326”	10.4702”
0.050	3.1231”	5.6895”	7.0080”
0.075	2.2875”	4.2036”	5.1920”
0.100	1.8109”	3.3218”	4.1082”

Table 56: Three-Story Loma Prieta 00 SRSS Method

Loma Prieta 00 SRSS Method Maximum Displacement Response						
(ξ)	U_{1MAX} SRSS	U_1 Error SRSS	U_{2MAX} SRSS	U_2 Error SRSS	U_{3MAX} SRSS	U_3 Error SRSS
0.025	4.8710”	0.0006	8.6194”	0.0102	10.4866”	0.0016
0.050	3.2641”	0.0452	5.7562”	0.0117	7.0067”	0.0002
0.075	2.4330”	0.0636	4.2751”	0.0170	5.2065”	0.0028
0.100	1.9297”	0.0656	3.3796”	0.0174	4.1179”	0.0024

Table 57: Three-Story Loma Prieta 00 CQC Method

Loma Prieta 00 CQC Method Maximum Displacement Response						
(ξ)	U_{1MAX} CQC	U_1 Error CQC	U_{2MAX} CQC	U_2 Error CQC	U_{3MAX} CQC	U_3 Error CQC
0.025	4.8720”	0.0004	8.6196”	0.0102	10.4857”	0.0015
0.050	3.2606”	0.0440	5.7551”	0.0115	7.0099”	0.0003
0.075	2.4260”	0.0605	4.2728”	0.0165	5.2129”	0.0040
0.100	1.9187”	0.0595	3.3761”	0.0163	4.1280”	0.0048

Table 58: Three-Story Loma Prieta 00 ABS Method

Loma Prieta 00 ABS Method Maximum Displacement Response						
(ξ)	U_{1MAX} ABS	U_1 Error ABS	U_{2MAX} ABS	U_2 Error ABS	U_{3MAX} ABS	U_3 Error ABS
0.025	5.3675”	0.1012	8.8177”	0.0334	10.9434”	0.0452
0.050	3.6934”	0.1826	5.9314”	0.0425	7.4050”	0.0566
0.075	2.8126”	0.2296	4.4333”	0.0546	5.5612”	0.0711
0.100	2.2676”	0.2522	3.5235”	0.0607	4.4353”	0.0796

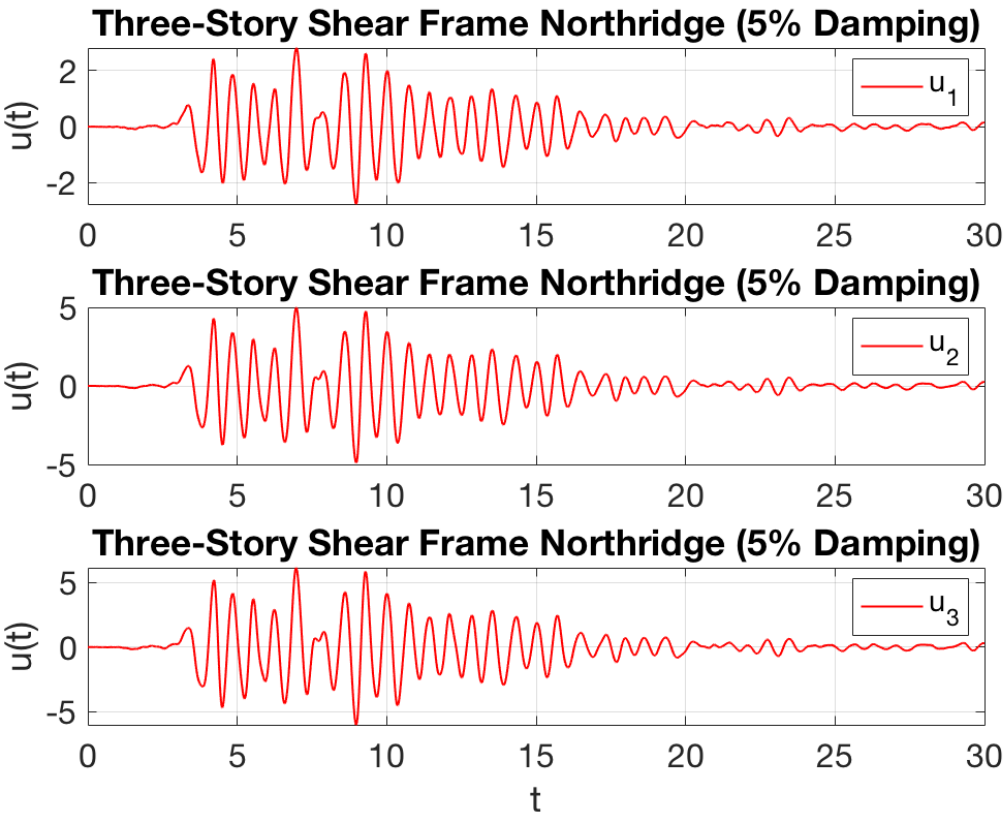

Figure 46: Three-Story Northridge 00 Displacement History (ξ = 0.05)

Table 59: Three-Story Northridge 00 Analytical Maximum Response

Northridge 00 Analytical Maximum Response			
(ξ)	**U_{1MAX}**	**U_{2MAX}**	**U_{3MAX}**
0.025	3.7329”	6.6570”	8.1737”
0.050	2.8026”	4.9819”	6.1317”
0.075	2.5363”	4.5046”	5.5146”
0.100	2.3060”	4.0825”	4.9833”

Table 60: Three-Story Northridge 00 SRSS Method

Northridge 00 SRSS Method Maximum Displacement Response						
(ξ)	U_{1MAX} SRSS	U_1 Error SRSS	U_{2MAX} SRSS	U_2 Error SRSS	U_{3MAX} SRSS	U_3 Error SRSS
0.025	3.7806”	0.0128	6.7087”	0.0078	8.1586”	0.0019
0.050	2.8381”	0.0127	5.0336”	0.0104	6.1218”	0.0016
0.075	2.5550”	0.0074	4.5308”	0.0058	5.5105”	0.0007
0.100	2.3153”	0.0040	4.1050”	0.0055	4.9927”	0.0019

Table 61: Three-Story Northridge 00 CQC Method

Northridge 00 CQC Method Maximum Displacement Response						
(ξ)	U_{1MAX} CQC	U_1 Error CQC	U_{2MAX} CQC	U_2 Error CQC	U_{3MAX} CQC	U_3 Error CQC
0.025	3.7812”	0.0129	6.7088”	0.0078	8.1581”	0.0019
0.050	2.8365”	0.0121	5.0329”	0.0102	6.1234”	0.0014
0.075	2.5577”	0.0084	4.5323”	0.0061	5.5074”	0.0013
0.100	2.3198”	0.0060	4.1074”	0.0061	4.9877”	0.0009

Table 62: Three-Story Northridge 00 ABS Method

Northridge 00 ABS Method Maximum Displacement Response						
(ξ)	U_{1MAX} ABS	U_1 Error ABS	U_{2MAX} ABS	U_2 Error ABS	U_{3MAX} ABS	U_3 Error ABS
0.025	4.0551”	0.0863	6.8366”	0.0270	8.4064”	0.0285
0.050	3.0701”	0.0954	5.1426”	0.0323	6.3316”	0.0326
0.075	2.7667”	0.0909	4.6292”	0.0276	5.7022”	0.0340
0.100	2.5128”	0.0897	4.1958”	0.0277	5.1718”	0.0378

As shown by the results above, a majority of the trends established for the two-story shear frame also hold true in the case of the three-story shear frame. The SRSS and CQC results were not only very similar, but also the methods produced even more accurate results with the increase in DOFs. On the contrary, the ABS method results decreased in accuracy for the three-story shear frame. Once again, the ABS method yields very inaccurate responses for the first DOF. The accuracy of the ABS method did increase for the second and third DOFs relative to the first, but in this case, the results of the maximum response at the second and third DOFs are less accurate than the respective SRSS and CQC responses. Similar to the two-story shear frame case, the SRSS and CQC results for the El Centro 00 ground motion produced responses that were both larger and smaller than the analytical response. In the two-story case, the damping ratio was the main factor that influenced the variation in results, but in the three-story shear frame case, the SRSS and CQC methods produced higher maximum displacement responses for the first and second DOF, whereas the maximum responses were lower than the analytical responses for the third DOF. Finally, a few of the earthquake analyses for the three-story shear frame show a trend between the damping ratio and accuracy of the SRSS and CQC methods. For the El Centro 00 ground motion, the accuracy of the responses at the second and third DOFs increase with an increase in damping ratio. Also, for the Kern County 111 ground motion the accuracy of the responses at the third DOF increase in accuracy with an increase in damping ratio. On the other hand, the

San Luis Obispo 324 ground motion resulted an opposite relationship between the accuracy of the response at the third DOF and the damping ratio.

In conclusion, for both the two-story and three-story shear frame, the SRSS and CQC yield extremely accurate results. When compared with one another, the SRSS method was more accurate than the CQC method, but the difference is miniscule. On the contrary, the ABS method proves to be inaccurate and inconsistent. Although some of the ABS method results were accurate, the method never produces consistently accurate solutions for the responses at each DOF.

5.6 Numerical Response Analysis of MDOF Shear Frames

In this section, the maximum displacement responses of the shear frames are calculated through the use of the numerical displacement response spectrums. In Section 5.3, the displacement response spectrums were developed using two numerical methods, the Average Acceleration Method (AAM) and the Linear Acceleration Method (LAM). With the displacement response spectrums developed using the AAM and LAM, and the various modal combination methods, the maximum displacement response for the MDOF shear frames is determined.

First, the two-story shear frame is subjected to the Loma Prieta 00 and Northridge 00 ground motions and analyzed using the AAM and LAM response spectrums. The results are compared with the analytical response obtained through THA, in order to analyze the accuracy of each method. Table 63 and

Table 64 shown below tabulate the error of each method for the Loma Prieta and Northridge Earthquake.

Table 63: Two-Story Loma Prieta 00 Numerical Spectrum Error

Loma Preita 00 Two-Story						
ξ	**U_{1MAX} SRSS Err.**	**U_{2MAX} SRSS Err.**	**U_{1MAX} CQC Err.**	**U_{2MAX} CQC Err.**	**U_{1MAX} ABS Err.**	**U_{2MAX} ABS Err.**
AAM – 0.025	0.0341	0.0186	0.0342	0.0186	0.0691	0.0013
LAM – 0.025	0.0347	0.0180	0.0348	0.0180	0.0697	0.0007
AAM – 0.050	0.0321	0.0149	0.0325	0.0151	0.0671	0.0027
LAM – 0.050	0.0327	0.0143	0.0331	0.0145	0.0681	0.0033
AAM – 0.075	0.0309	0.0130	0.0318	0.0135	0.0681	0.0056
LAM – 0.075	0.0314	0.0125	0.0323	0.0129	0.0687	0.0062
AAM – 0.100	0.0314	0.0126	0.0331	0.0134	0.0710	0.0072
LAM – 0.100	0.0319	0.0120	0.0337	0.0129	0.0716	0.0078

Table 64: Two-Story Northridge 00 Numerical Spectrum Error

Northridge 00 Two-Story						
ξ	**U_{1MAX} SRSS Err.**	**U_{2MAX} SRSS Err.**	**U_{1MAX} CQC Err.**	**U_{2MAX} CQC Err.**	**U_{1MAX} ABS Err.**	**U_{2MAX} ABS Err.**
AAM – 0.025	0.0098	0.0062	0.0099	0.0662	0.0481	0.0135
LAM – 0.025	0.0104	0.0055	0.0105	0.0056	0.0486	0.0141
AAM – 0.050	0.0062	0.0097	0.0066	0.0099	0.0434	0.0095
LAM – 0.050	0.0067	0.0091	0.0071	0.0093	0.0440	0.0101
AAM – 0.075	0.0088	0.0064	0.0098	0.0069	0.0479	0.0137
LAM – 0.075	0.0094	0.0058	0.0103	0.0063	0.0485	0.0143
AAM – 0.100	0.0056	0.0043	0.0073	0.0052	0.0458	0.0165
LAM – 0.100	0.0061	0.0038	0.0079	0.0047	0.0464	0.0171

As shown by the tables above, all three of the modal combination methods with either the AAM or LAM produce reasonably accurate maximum responses. For the Loma Prieta and Northridge Earthquakes, the AAM ABS results are more accurate than the LAM results. Although there are slight differences in the AAM

and LAM responses for the two-story shear frame, the difference is small. Furthermore, as evidenced by the tables, the displacement response at the first DOF may be more accurate for the LAM, but this is balanced by the AAM's more accurate displacement response at the second DOF.

In addition to the two-story shear frame, the three-story shear frame is also analyzed. As shown by the tables on the following pages, the accuracy of the AAM and LAM increase for the three-story shear frame in comparison to the two-story shear frame. Once again, the difference between the AAM and LAM results are negligible. For example, the AAM and LAM yield identical responses when the three-story shear frame is subjected to the Loma Prieta 00 ground motion with a damping coefficient of 0.050 and the Northridge 00 ground motion with a damping coefficient of 0.075.

Interestingly, in some cases using the numerical displacement response spectrums resulted in more accurate results than the analytical displacement response spectrum. For example, when solving for U_{1MAX} using the SRSS method and a damping coefficient of 0.025, both the AAM and LAM produce more accurate results than the analytical spectrum. All in all, both of the numerical methods are adequate for performing accurate analysis. Although this may be the case for the systems studied in this thesis, it is important to note that the specific properties of a shear frame likely play a role in the results.

Table 65: Three-Story Loma Prieta 00 SRSS Numerical Error

Loma Prieta 00 Three-Story SRSS			
ξ	U_{1MAX} SRSS Err.	U_{2MAX} SRSS Err.	U_{3MAX} SRSS Err.
AAM – 0.025	0.0001	0.0107	0.0021
LAM – 0.025	0.0001	0.0105	0.0020
AAM – 0.050	0.0494	0.0158	0.0039
LAM – 0.050	0.0494	0.0158	0.0039
AAM – 0.075	0.0647	0.0180	0.0038
LAM – 0.075	0.0648	0.0181	0.0039
AAM – 0.100	0.0661	0.0176	0.0026
LAM – 0.100	0.0663	0.0178	0.0028

Table 66: Three-Story Northridge 00 SRSS Numerical Error

Northridge 00 Three-Story SRSS			
ξ	U_{1MAX} SRSS Err.	U_{2MAX} SRSS Err.	U_{3MAX} SRSS Err.
AAM – 0.025	0.0128	0.0078	0.0018
LAM – 0.025	0.0131	0.0081	0.0015
AAM – 0.050	0.0142	0.0118	0.0002
LAM – 0.050	0.0144	0.0120	0.0000
AAM – 0.075	0.0103	0.0087	0.0021
LAM – 0.075	0.0103	0.0087	0.0021
AAM – 0.100	0.0075	0.0090	0.0054
LAM – 0.100	0.0077	0.0092	0.0055

Table 67: Three-Story Loma Prieta 00 CQC Numerical Error

Loma Prieta 00 Three-Story CQC			
ξ	U_{1MAX} CQC Err.	U_{2MAX} CQC Err.	U_{3MAX} CQC Err.
AAM – 0.025	0.0004	0.0107	0.0020
LAM – 0.025	0.0003	0.0106	0.0018
AAM – 0.050	0.0513	0.0161	0.0032
LAM – 0.050	0.0513	0.0161	0.0031
AAM – 0.075	0.0701	0.0188	0.0019
LAM – 0.075	0.0701	0.0189	0.0020
AAM – 0.100	0.0768	0.0192	0.0011
LAM – 0.100	0.0769	0.0194	0.0010

Table 68: Three-Story Northridge 00 CQC Numerical Error

Northridge 00 Three-Story CQC			
ξ	U_{1MAX} CQC Err.	U_{2MAX} CQC Err.	U_{3MAX} CQC Err.
AAM – 0.025	0.0131	0.0078	0.0019
LAM – 0.025	0.0134	0.0081	0.0016
AAM – 0.050	0.0153	0.0119	0.0006
LAM – 0.050	0.0155	0.0121	0.0004
AAM – 0.075	0.0127	0.0090	0.0013
LAM – 0.075	0.0128	0.0090	0.0013
AAM – 0.100	0.0120	0.0095	0.0038
LAM – 0.100	0.0121	0.0097	0.0040

Table 69: Three-Story Loma Prieta 00 ABS Numerical Error

Loma Prieta 00 Three-Story ABS			
ξ	U_{1MAX} ABS Err.	U_{2MAX} ABS Err.	U_{3MAX} ABS Err.
AAM – 0.025	0.1038	0.0343	0.0466
LAM – 0.025	0.1037	0.0342	0.0464
AAM – 0.050	0.1870	0.0467	0.0608
LAM – 0.050	0.1870	0.0466	0.0608
AAM – 0.075	0.2310	0.0557	0.0723
LAM – 0.075	0.2311	0.0558	0.0724
AAM – 0.100	0.2539	0.0612	0.0804
LAM – 0.100	0.2540	0.0614	0.0808

Table 70: Three-Story Northridge 00 ABS Numerical Error

Northridge 00 Three-Story CQC			
ξ	U_{1MAX} ABS Err.	U_{2MAX} ABS Err.	U_{3MAX} ABS Err.
AAM – 0.025	0.0870	0.0271	0.0288
LAM – 0.025	0.0874	0.0274	0.0291
AAM – 0.050	0.0982	0.0339	0.0345
LAM – 0.050	0.0984	0.0341	0.0348
AAM – 0.075	0.0938	0.0306	0.0369
LAM – 0.075	0.0939	0.0306	0.0370
AAM – 0.100	0.0932	0.0313	0.0413
LAM – 0.100	0.0934	0.0315	0.0415

6. Analysis of Midrise Buildings

To further compare seismic analysis methods, the Equivalent Lateral Force Procedure (ELFP), modal response spectrum analysis (RSA), and time history analysis (THA) methods are applied to midrise shear frames up to ten stories in height. The material properties and frame dimensions remain consistent with the former analyses, where each story has a lateral stiffness of 90.78 kips per inch, and floor and roof weights equal to 100 kips and 80 kips, respectively. Also, each analysis case assumes constant 5% damping. The analysis in this chapter allows for a deeper understanding of the accuracy and consistency of seismic analysis methods.

6.1 ELFP and RSA Comparison

First, the ELFP and RSA methods are applied to shear frames up to ten stories using the formerly developed Design Basis Earthquake (DBE) for San Luis Obispo, CA 93407. Once again, when applying RSA to the shear frames, the maximum responses of each mode are combined through the Absolute Sum (ABS), Square-Root-of-the-Sum-of-Squares (SRSS), and Complete Quadratic Combination (CQC) methods. In this study, the goal is not to design the individual members of each shear frame, so the scaling of response values is of little importance as long as consistency is maintained between the methods. Accordingly, the RSA results herein are divided by 4.5 to account for the response modification factor (R), detailed in Chapter 3, which reduces the ELFP results by a factor of 4.5.

In previous chapters, the response parameter of interest is the lateral displacement response at each DOF. Along with the displacement response, the maximum base shear response is analyzed in this chapter. In RSA, the maximum base shear is calculated by using modal combination methods to combine the total base shear resulting from each mode of vibration. The maximum base shear results of the ELFP and RSA are shown below in Table 71.

Table 71: Maximum Base Shear Response ELFP versus RSA

Number of Stories	V_{ELFP} (kips)	V_{ABS} (kips)	V_{SRSS} (kips)	V_{CQC} (kips)
2	31.50	31.45	30.02	30.04
3	49.00	39.93	36.10	36.14
4	65.59	43.49	37.06	37.11
5	69.31	46.79	37.69	37.77
6	72.38	50.10	38.31	38.42
7	75.00	53.37	38.93	39.07
8	78.30	56.10	39.40	39.58
9	79.38	57.89	39.60	39.80
10	81.24	59.65	39.78	40.01

As shown by Table 71, the SRSS and CQC methods yield very similar results, and as the number of stories increases the difference in results between the two methods and the ELFP increases. Figure 47 exhibits the relationship between the ELFP and RSA methods by plotting the maximum base shear against the number of stories.

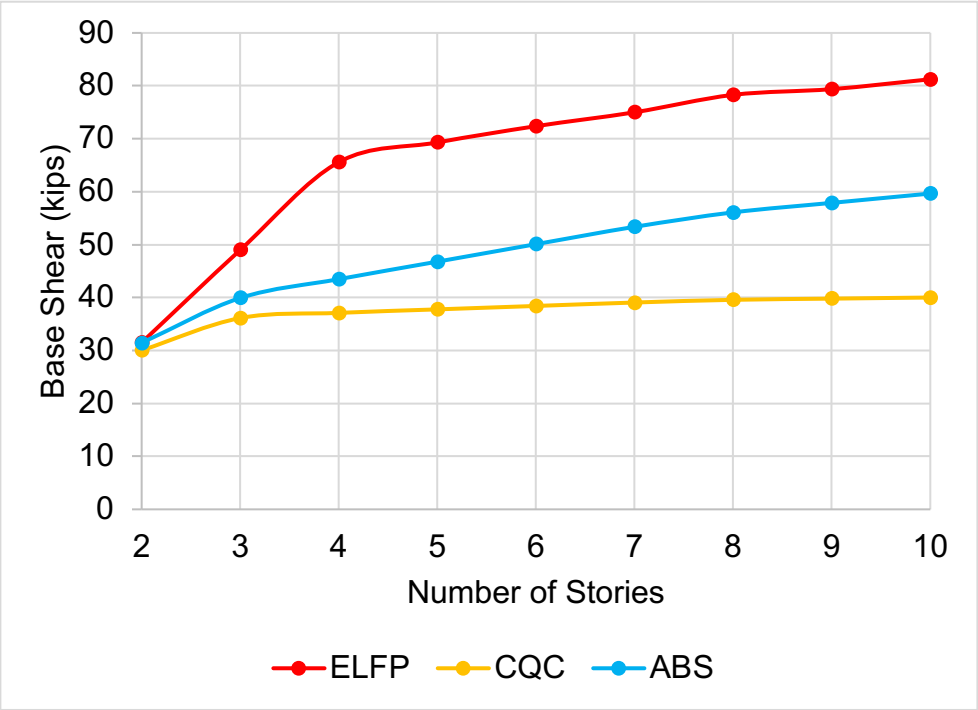

Figure 47: Base Shear Results ELFP versus RSA

Since the SRSS and CQC methods yield similar results, Figure 47 only shows the CQC trend. As displayed by Figure 47, the ELFP base shear results are considerably higher than the RSA results. For the two-story shear frame, the results are similar regardless of method used. For shear frames with two to four stories, the ELFP base shear response significantly increases with each additional story. Between four to ten stories, the base shear results of the ELFP and ABS method increase with story height at a similar rate, whereas the CQC base shear results barely increase with each additional story. Although the rate at which the base shear increases with number of stories is more pronounced for the ELFP in all cases, for shear frames above four stories, the rate decreases and is more comparable with the rate of the RSA results. The pronounced rate is due to the formerly detailed seismic response coefficient (C_s). For shear frames

up to three stories, the C_s value for the ELFP remains constant and is governed by Equation 3.3. For shear frames that are four stories or higher, the C_s value for the ELFP is instead governed by the ASCE 7-10 upper bound equation shown by Equation 3.3a. For example, the C_s values for the three-story and four-story shear frame are 0.175 and 0.173, respectively. Although the difference between the two equations is small for the four-story shear frame, as the stories increase, the fundamental period of the shear frame increases, and Equation 3.3a yields smaller C_s values. Furthermore, the maximum lateral displacements are also analyzed. The displacement results of the ELFP and RSA methods and the response reduction (RR) of each modal combination method as a percentage of the ELFP response are shown in the tables below.

Table 72: Two-Story Frame ELFP versus RSA

	ELFP	ABS	SRSS	CQC	$\%RR_{ABS}$	$\%RR_{SRSS}$	$\%RR_{CQC}$
U_1	0.3470”	0.3465”	0.3309”	0.3307”	0.14%	4.64%	4.68%
U_2	0.5607”	0.5264”	0.5135”	0.5136”	6.11%	8.42%	8.40%

Table 73: Three-Story Frame ELFP versus RSA

	ELFP	ABS	SRSS	CQC	$\%RR_{ABS}$	$\%RR_{SRSS}$	$\%RR_{CQC}$
U_1	0.5398”	0.4398”	0.3981”	0.3977”	18.52%	26.25%	26.32%
U_2	0.9796”	0.7237”	0.7044”	0.7044”	26.12%	28.09%	28.10%
U_3	1.2195”	0.8962”	0.8578”	0.8580”	26.51%	29.67%	29.64%

Table 74: Four-Story Frame ELFP versus RSA

	ELFP	ABS	SRSS	CQC	$\%RR_{ABS}$	$\%RR_{SRSS}$	$\%RR_{CQC}$
U_1	0.7225”	0.4790”	0.4088”	0.4082”	33.70%	43.41%	43.50%
U_2	1.3662”	0.8190”	0.7565”	0.7562”	40.05%	44.63%	44.65%
U_3	1.8524”	1.0282”	1.0053”	1.0054”	44.49%	45.73%	45.72%
U_4	2.1023”	1.2000”	1.1255”	1.1259”	42.92%	46.46%	46.44%

Table 75: Five-Story Frame ELFP versus RSA

	ELFP	ABS	SRSS	CQC	$\%RR_{ABS}$	$\%RR_{SRSS}$	$\%RR_{CQC}$
U_1	0.7635”	0.5154”	0.4161”	0.4152”	32.49%	45.50%	45.62%
U_2	1.4722”	0.8913”	0.7858”	0.7851”	39.46%	46.62%	46.67%
U_3	2.0711”	1.1546”	1.0841”	1.0839”	44.25%	47.65%	47.67%
U_4	2.5054”	1.3500”	1.2930”	1.2933”	46.12%	48.39%	48.38%
U_5	2.7202”	1.5135”	1.3933”	1.3940”	44.36%	48.78%	48.76%

Table 76: Six-Story Frame ELFP versus RSA

	ELFP	ABS	SRSS	CQC	$\%RR_{ABS}$	$\%RR_{SRSS}$	$\%RR_{CQC}$
U_1	0.7973”	0.5518”	0.4233”	0.4220”	30.79%	46.92%	47.07%
U_2	1.5541”	0.9656”	0.8077”	0.8065”	37.87%	48.03%	48.10%
U_3	2.2297”	1.2719”	1.1349”	1.1343”	42.95%	49.10%	49.13%
U_4	2.7835”	1.4574”	1.3946”	1.3945”	47.64%	49.90%	49.90%
U_5	3.1749”	1.6699”	1.5752”	1.5757”	47.40%	50.39%	50.37%
U_6	3.3633”	1.8375”	1.6615”	1.6625”	45.37%	50.60%	50.57%

Table 77: Seven-Story Frame ELFP versus RSA

	ELFP	ABS	SRSS	CQC	$\%RR_{ABS}$	$\%RR_{SRSS}$	$\%RR_{CQC}$
U_1	0.8262”	0.5879”	0.4304”	0.4288”	28.85%	47.91%	48.10%
U_2	1.6211”	1.0347”	0.8262”	0.8246”	36.18%	49.03%	49.13%
U_3	2.3533”	1.3633”	1.1727”	1.1716”	42.07%	50.17%	50.21%
U_4	2.9914”	1.6135”	1.4637”	1.4632”	46.06%	51.07%	51.09%
U_5	3.5041”	1.7607”	1.6937”	1.6939”	49.75%	51.66%	51.66%
U_6	3.8600”	2.0010”	1.8537”	1.8546”	48.16%	51.98%	51.95%
U_7	4.0278”	2.1712”	1.9301”	1.9315”	46.09%	52.08%	52.05%

Table 78: Eight-Story Frame ELFP versus RSA

	ELFP	ABS	SRSS	CQC	$\%RR_{ABS}$	$\%RR_{SRSS}$	$\%RR_{CQC}$
U_1	0.8625”	0.6180”	0.4360”	0.4341”	28.35%	49.45%	49.67%
U_2	1.7000”	1.0958”	0.8410”	0.8389”	35.54%	50.53%	50.65%
U_3	2.4764”	1.4572”	1.2024”	1.2007”	41.16%	51.45%	51.51%
U_4	3.1779”	1.7456”	1.5155”	1.5145”	45.07%	52.31%	52.34%
U_5	3.7793”	1.9211”	1.7781”	1.7778”	49.17%	52.95%	52.96%
U_6	4.2556”	2.1072”	1.9857”	1.9862”	50.48%	53.34%	53.33%
U_7	4.5819”	2.3342”	2.1298”	2.1310”	49.06%	53.52%	53.49%
U_8	4.7332”	2.5042”	2.1984”	2.2001”	47.09%	53.55%	53.52%

Table 79: Nine-Story Frame ELFP versus RSA

	ELFP	ABS	SRSS	CQC	$\%RR_{ABS}$	$\%RR_{SRSS}$	$\%RR_{CQC}$
U_1	0.8744”	0.6377”	0.4385”	0.4363”	27.07%	49.85%	50.11%
U_2	1.7283”	1.1364”	0.8498”	0.8473”	34.25%	50.83%	50.98%
U_3	2.5414”	1.5268”	1.2231”	1.2211”	39.92%	51.87%	51.95%
U_4	3.2930”	1.8285”	1.5546”	1.5532”	44.47%	52.79%	52.83%
U_5	3.9628”	2.0744”	1.8421”	1.8415”	47.65%	53.51%	53.53%
U_6	4.5302”	2.2051”	2.0831”	2.0832”	51.32%	54.02%	54.02%
U_7	4.9749”	2.4406”	2.2727”	2.2735”	50.94%	54.32%	54.30%
U_8	5.2763”	2.6531”	2.4033”	2.4047”	49.72%	54.45%	54.42%
U_9	5.4140”	2.8240”	2.4650”	2.4669”	47.84%	54.47%	54.43%

Table 80: Ten-Story Frame ELFP versus RSA

	ELFP	ABS	SRSS	CQC	$\%RR_{ABS}$	$\%RR_{SRSS}$	$\%RR_{CQC}$
U_1	0.8949”	0.6571”	0.4408”	0.4382”	26.57%	50.75%	51.03%
U_2	1.7811”	1.1764”	0.8570”	0.8541”	33.95%	51.88%	52.05%
U_3	2.6451”	1.5819”	1.2396”	1.2371”	40.19%	53.13%	53.23%
U_4	3.4704”	1.9015”	1.5853”	1.5835”	45.21%	54.32%	54.37%
U_5	4.2390”	2.1986”	1.8924”	1.8913”	48.13%	55.36%	55.38%
U_6	4.9306”	2.3797”	2.1588”	2.1584”	51.74%	56.22%	56.22%
U_7	5.5239”	2.5077”	2.3815”	2.3818”	54.60%	56.89%	56.88%
U_8	5.9961”	2.7628”	2.5559”	2.5569”	53.92%	57.37%	57.36%
U_9	6.3231”	2.9785”	2.6753”	2.6769”	52.89%	57.69%	57.66%
U_{10}	6.4800”	3.1463”	2.7314”	2.7336”	51.45%	57.85%	57.82%

As shown by the above tables, the ELFP yields conservative lateral displacement results in each case. Similarly, the displacements are plotted against the number of stories. The ten-story result is shown in Figure 48 below.

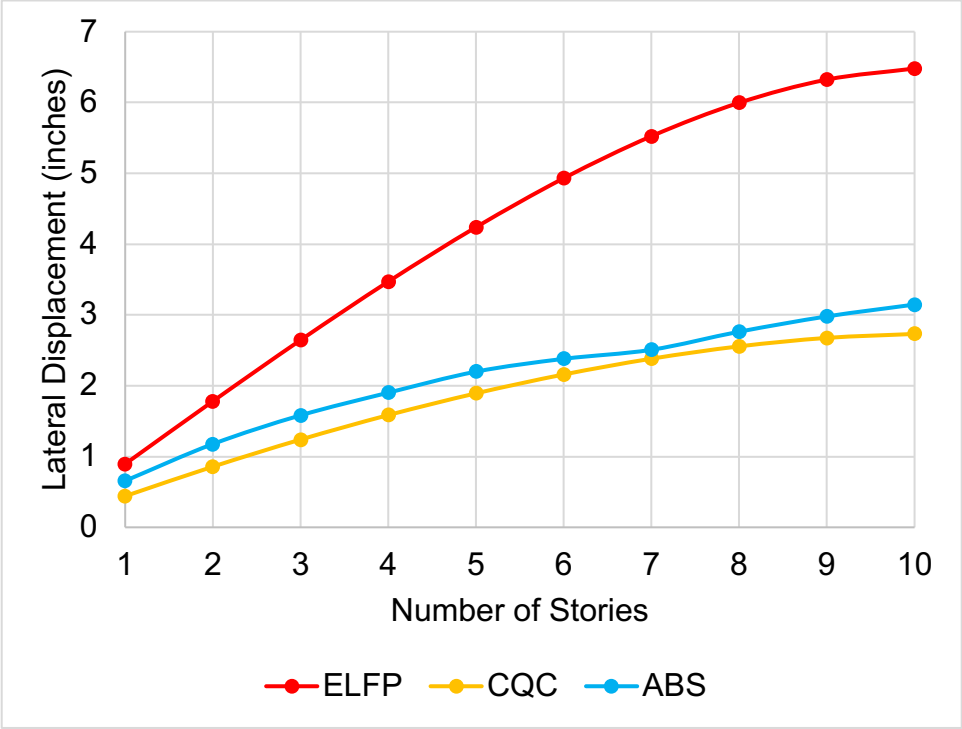

Figure 48: Ten-Story Displacement Results ELFP versus RSA

The ELFP results for shear frames with more than three stories show a parabolic trend between lateral displacements and number of stories. The parabolic trend can be attributed to the ELFP's method for distributing forces outlined in ASCE 7-10. As shown by Equation 3.4, the vertical force distribution depends on the height of each story which is raised to a constant value k. For the two-story and three-story shear frame, k is equal to 1, resulting in a linear relationship. On the contrary, for story heights above three stories, the k value increases with each additional story. Consequently, the parabolic trend is more noticeable as the number of stories increases.

6.2 RSA and THA Comparison

In this section, RSA and THA are applied to shear frames up to ten stories, and the results are compared. First, the shear frames are subject to the 1994 Northridge Earthquake ground motions in the 00 direction (N-S). The maximum base shear results of the RSA and THA are shown below in Table 81.

Table 81: Total Base Shear Response Northridge 00

Number of Stories	V_{THA} (kips)	V_{ABS} (kips)	V_{SRSS} (kips)	V_{CQC} (kips)
2	232.31	242.61	233.95	234.03
3	252.34	278.13	257.02	256.87
4	305.26	342.97	291.68	292.11
5	271.17	341.22	269.40	270.03
6	396.22	472.15	376.44	377.24
7	248.12	359.83	251.41	252.59
8	255.51	359.82	243.63	244.96
9	396.83	514.26	374.52	375.88
10	341.20	539.88	374.49	376.24

Unlike the relationship between the ELFP and RSA, the base shear results when the shear frames are subject to the Northridge Earthquake ground motion record do not necessarily increase with number of stories. To visualize the results in Table 81, the total base shear is plotted against the number of stories in Figure 49.

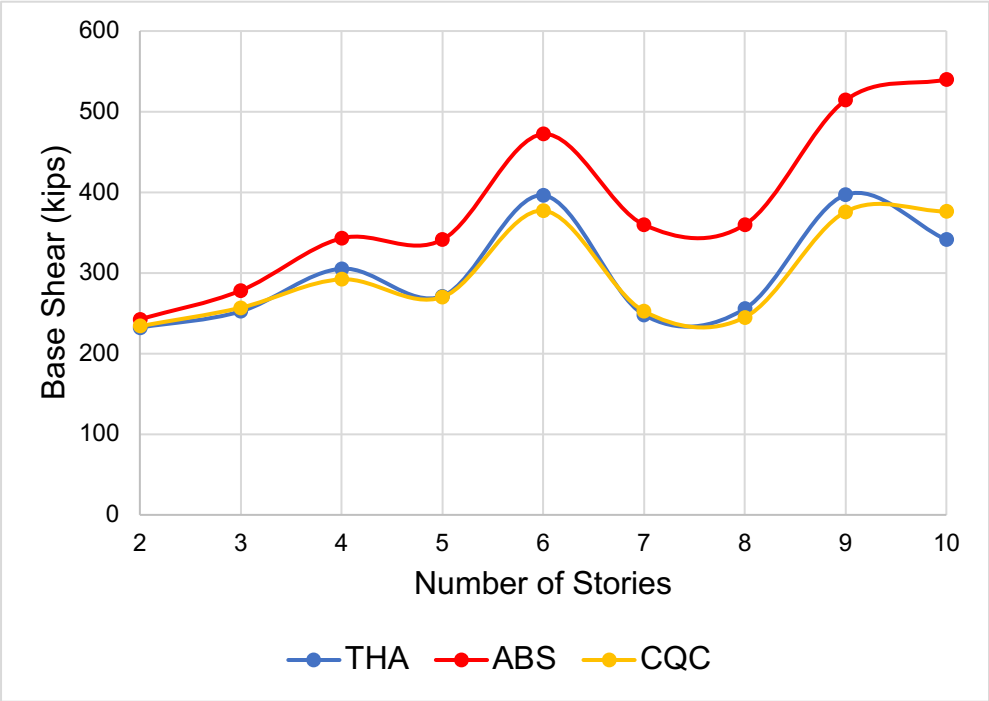

Figure 49: Northridge Base Shear Results RSA versus THA

As shown by Figure 49, the relationship between base shear and number of stories is not linear. For instance, the six-story shear frame yields a larger base shear than the seven-story and eight-story shear frame, despite the fact it has less seismic reactive weight. The heightened base shear response of the six-story shear frame is due to the nature of the ground motion. Even though the fundamental period of the frames increases with each additional story, a higher fundamental period doesn't necessarily correlate to a higher displacement response. In this case, the fundamental period of the six-story shear frame correlates to a larger displacement response than the fundamental period of the seven-story or eight-story shear frame. Furthermore, this is exemplified by the Northridge Earthquake maximum displacement spectrum developed in Section 5.3. As a whole, the displacement spectrum trends upwards with small

fundamental periods, but the upward trend is characterized by a jagged displacement response for small variations in period. Moreover, the dependence of the base shear response on the nature of the ground motion is shown by applying the 1989 Loma Prieta ground motion in the 00 direction (N-S) to the shear frames. The base shear results are shown in Table 82 below.

Table 82: Total Base Shear Response Loma Prieta 00

Number of Stories	V_{THA} (kips)	V_{ABS} (kips)	V_{SRSS} (kips)	V_{CQC} (kips)
2	233.30	249.16	240.98	241.07
3	280.06	334.65	295.61	295.95
4	214.71	237.18	176.47	177.11
5	146.34	237.41	163.19	164.11
6	143.03	260.85	163.68	165.17
7	166.09	236.11	134.81	136.84
8	174.15	267.87	153.11	155.26
9	164.66	278.53	151.89	154.59
10	251.41	336.40	180.80	184.05

Once again, the increase in story height doesn't necessarily correlate with an increase in base shear response. Although the SRSS and CQC methods produce very similar results, the SRSS produces slightly more accurate results when the two methods overestimate the base shear response. Similarly, the CQC method yields slightly more accurate results when the two methods underestimate the base shear response. Figure 50 exhibits the relationship between base shear response and number of stories under the Loma Prieta ground motion.

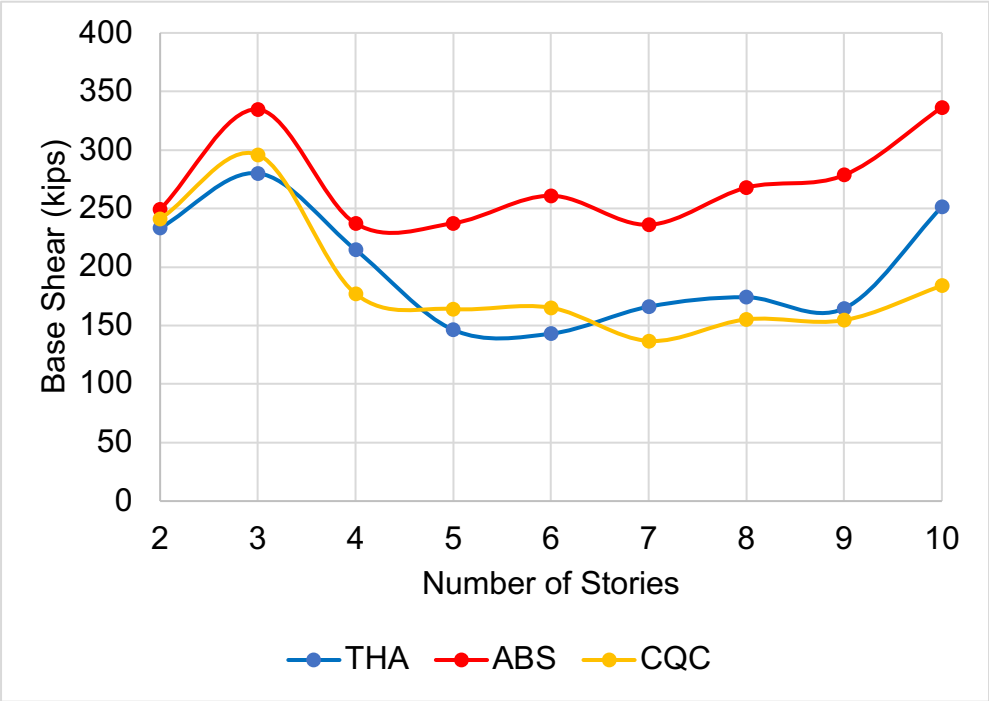

Figure 50: Loma Prieta Base Shear Results RSA versus THA

As shown by Figure 50, the relationship between base shear and number of stories significantly varies depending on the nature of the ground motion. When the frames are subject to the Loma Prieta ground motion, the three-story shear frame yields the peak base shear response, whereas the ten-story shear frame yields the peak base shear response when the Northridge Earthquake is applied. In both earthquake cases, the ABS method overestimates the base shear response regardless of system. When comparing the RSA results for both earthquakes, Figure 49 and 50 display that the SRSS and CQC methods yield more accurate results when the Northridge Earthquake is applied to the frames. Consider the previously developed maximum displacement spectrums for the Northridge and Loma Prieta Earthquakes (Section 5.3 and Appendix L). In comparison, the Loma Prieta displacement spectrum is more jagged. In

accordance with literature, the SRSS and CQC methods tend to yield errors in the range of 10% to 30% when a jagged response spectrum characterized by one ground motion is used (Chopra, 1995). Generally, the response spectrums used for seismic design are smooth curves developed from the analysis of numerous ground motions and system responses.

In addition to the total base shear, the maximum lateral displacement responses resulting from RSA and THA are analyzed. The responses of each shear frame due to the Northridge Earthquake are presented by the tables below.

Table 83: Two-Story Frame RSA versus THA - Northridge

	THA	ABS	SRSS	CQC	E_{ABS}	E_{SRSS}	E_{CQC}
U_1	2.5590”	2.6725”	2.5781”	2.5771”	4.44%	0.75%	0.71%
U_2	4.0387”	4.0808”	4.0024”	4.0033”	1.04%	0.90%	0.88%

Table 84: Three-Story Frame RSA versus THA - Northridge

	THA	ABS	SRSS	CQC	E_{ABS}	E_{SRSS}	E_{CQC}
U_1	2.8026”	3.0701”	2.8355”	2.8381”	9.54%	1.17%	1.27%
U_2	4.9819”	5.1426”	5.0325”	5.0336”	3.23%	1.02%	1.04%
U_3	6.1317”	6.3316”	6.1245”	6.1218”	3.26%	0.12%	0.16%

Table 85: Four-Story Frame RSA versus THA - Northridge

	THA	ABS	SRSS	CQC	E_{ABS}	E_{SRSS}	E_{CQC}
U_1	3.3264”	3.7734”	3.2131”	3.2084”	13.44%	3.40%	3.55%
U_2	5.9882”	6.4502”	5.9391”	5.9360”	7.72%	0.82%	0.87%
U_3	7.7357”	8.0477”	7.8906”	7.8913”	4.03%	2.00%	2.01%
U_4	8.4943”	9.4468”	8.8416”	8.8456”	11.21%	4.09%	4.14%

Table 86: Five-Story Frame RSA versus THA - Northridge

	THA	ABS	SRSS	CQC	E_{ABS}	E_{SRSS}	E_{CQC}
U_1	2.9871”	3.7588”	2.9617”	2.9676”	25.83%	0.85%	0.65%
U_2	5.4263”	6.4854”	5.5717”	5.5781”	19.52%	2.68%	2.80%
U_3	7.5011”	8.2171”	7.6617”	7.6648”	9.54%	2.14%	2.18%
U_4	9.3795”	9.5975”	9.1454”	9.1432”	2.32%	2.50%	2.52%
U_5	10.4151”	10.8573”	9.8745”	9.8675”	4.25%	5.19%	5.26%

Table 87: Six-Story Frame RSA versus THA - Northridge

	THA	ABS	SRSS	CQC	E_{ABS}	E_{SRSS}	E_{CQC}
U_1	4.3646”	5.2011”	4.1505”	4.1467”	19.17%	4.90%	4.99%
U_2	7.9531”	9.3075”	7.9606”	7.9533”	17.03%	0.09%	0.00%
U_3	10.9681”	12.3598”	11.2173”	11.2101”	12.69%	2.27%	2.21%
U_4	13.2327”	14.2489”	13.7961”	13.7939”	7.68%	4.26%	4.24%
U_5	14.8001”	16.3803”	15.5799”	15.5847”	10.68%	5.27%	5.30%
U_6	15.5643”	17.8917”	16.4262”	16.4345”	14.95%	5.54%	5.59%

Table 88: Seven-Story Frame RSA versus THA - Northridge

	THA	ABS	SRSS	CQC	E_{ABS}	E_{SRSS}	E_{CQC}
U_1	2.7332”	3.9638”	2.7696”	2.7694”	45.03%	1.34%	1.33%
U_2	5.0302”	6.9040”	5.2864”	5.2809”	37.25%	5.09%	4.98%
U_3	6.7433”	8.8844”	7.4484”	7.4390”	31.75%	10.46%	10.32%
U_4	8.8446”	10.4221”	9.2491”	9.2419”	17.84%	4.57%	4.49%
U_5	10.4216”	11.1865”	10.6827”	10.6825”	7.34%	2.51%	2.50%
U_6	11.9642”	12.8329”	11.7035”	11.7102”	7.26%	2.18%	2.12%
U_7	12.7832”	14.0757”	12.2063”	12.2152”	10.11%	4.51%	4.44%

Table 89: Eight-Story Frame RSA versus THA - Northridge

	THA	ABS	SRSS	CQC	E_{ABS}	E_{SRSS}	E_{CQC}
U_1	2.8146”	3.9637”	2.6851”	2.6837”	40.83%	4.60%	4.65%
U_2	5.4790”	6.9728”	5.1491”	5.1543”	27.26%	6.02%	5.93%
U_3	7.7750”	9.0906”	7.3203”	7.3305”	16.92%	5.85%	5.72%
U_4	9.4471”	10.8269”	9.2007”	9.2098”	14.61%	2.61%	2.51%
U_5	10.4323”	11.8492”	10.7867”	10.7900”	13.58%	3.40%	3.43%
U_6	12.0193”	12.9002”	12.0526”	12.0491”	7.33%	0.28%	0.25%
U_7	13.0710”	14.3617”	12.9465”	12.9393”	9.87%	0.95%	1.01%
U_8	13.8692”	15.5252”	13.3798”	13.3722”	11.94%	3.53%	3.58%

Table 90: Nine-Story Frame RSA versus THA - Northridge

	THA	ABS	SRSS	CQC	E_{ABS}	E_{SRSS}	E_{CQC}
U_1	4.3717”	5.6649”	4.1268”	4.1256”	29.59%	5.59%	5.62%
U_2	8.4442”	10.2801”	8.0593”	8.0550”	21.74%	4.56%	4.61%
U_3	11.9138”	13.9325”	11.6910”	11.6821”	16.94%	1.87%	1.94%
U_4	14.7868”	16.9275”	14.9629”	14.9504”	14.48%	1.19%	1.11%
U_5	17.1319”	19.5586”	17.8121”	17.8018”	14.17%	3.97%	3.91%
U_6	18.8388”	21.1723”	20.1750”	20.1725”	12.39%	7.09%	7.08%
U_7	20.1774”	23.2169”	22.0001”	22.0050”	15.06%	9.03%	9.06%
U_8	21.3533”	25.0397”	23.2339”	23.2436”	17.26%	8.81%	8.85%
U_9	21.9865”	26.4720”	23.8092”	23.8213”	20.40%	8.29%	8.34%

Table 91: Ten-Story Frame RSA versus THA - Northridge

	THA	ABS	SRSS	CQC	E_{ABS}	E_{SRSS}	E_{CQC}
U_1	3.7585”	5.9471”	4.1288”	4.1253”	58.23%	9.85%	9.76%
U_2	7.0239”	10.8212”	8.0662”	8.0613”	54.06%	14.84%	14.77%
U_3	9.7648”	14.6194”	11.7185”	11.7083”	49.71%	20.01%	19.90%
U_4	13.3028”	17.6834”	15.0417”	15.0256”	32.93%	13.07%	12.95%
U_5	16.4768”	20.5662”	17.9998”	17.9835”	24.82%	9.24%	9.14%
U_6	19.2038”	22.3994”	20.5579”	20.5486”	16.64%	7.05%	7.00%
U_7	21.5058”	23.7465”	22.6826”	22.6831”	10.42%	5.47%	5.47%
U_8	23.6864”	26.0274”	24.3342”	24.3426”	9.88%	2.74%	2.77%
U_9	25.5164”	28.0080”	25.4580”	25.4715”	9.76%	0.23%	0.18%
U_{10}	26.3674”	29.4761”	25.9837”	25.9998”	11.79%	1.46%	1.39%

As expected, the ABS method results are the most inaccurate and inconsistent. Also, the SRSS and CQC methods continue to yield comparable results with one another. For the shear frames with four or fewer stories, the SRSS and CQC methods produce errors less than 5%. The greatest errors occur for the modal combination methods at the nine-story and ten-story shear frames. In general, the errors tend to increase with increase in number of stories. To further analyze the trend, the displacements are plotted against the number of stories for the ten-story shear frame in Figure 51 below.

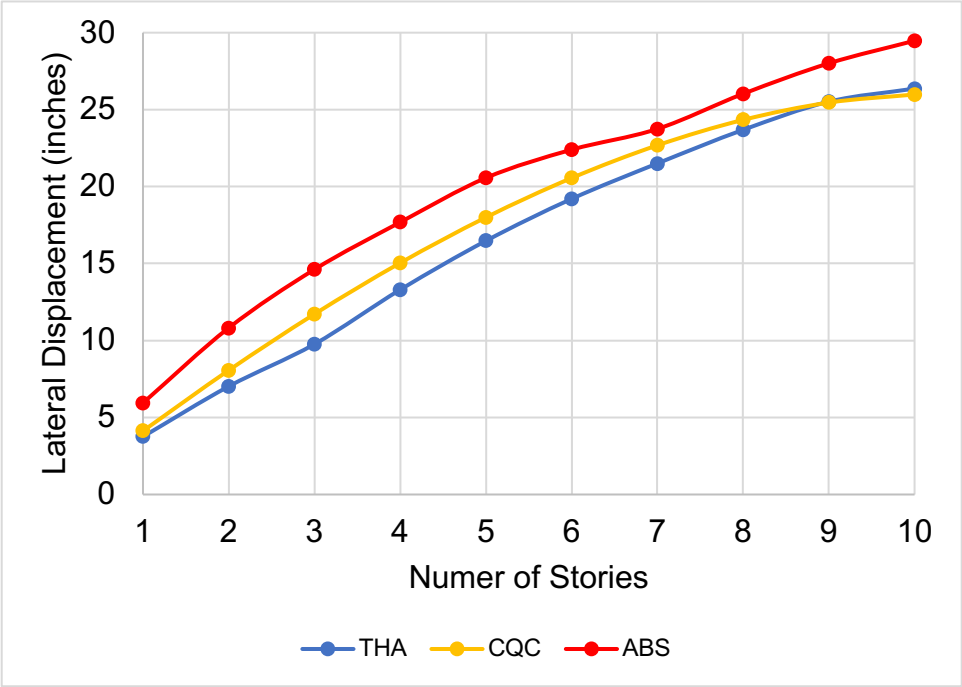

Figure 51: Northridge Displacement Results RSA versus THA

Although the displacement error of the CQC and SRSS results is small for the ninth and tenth story, the two methods overestimate the displacement responses for the intermediate stories, where the peak errors occur at the third story. Despite the errors, the SRSS and CQC still yield reasonably accurate results.

6.3 Special Building Cases

Thus far, the SRSS and CQC methods yield very similar results. The accuracy in the two methods is primarily due to the symmetry of the shear frames. For symmetric structures with gradually spaced modes, the correlation coefficients are relatively small, and the CQC method essentially reduces to the SRSS method. Generally, the two methods yield adequate results for two-dimensional structures; on the contrary, literature shows the application of the methods to three-dimensional structures can result in vastly different results due to mass irregularities (Wilson et al., 1981). Consider the five-story shear frame shown below in Figure 52.

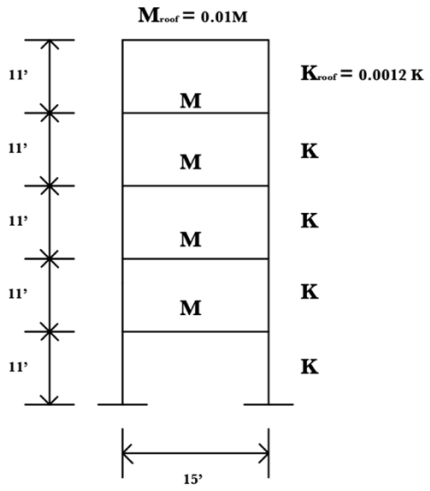

Figure 52: Five Story Shear Frame with Irregular Properties

The five-story shear frame shown above exhibits consistent mass and stiffness properties until the roof, where the mass and stiffness are considerably reduced. The reduction in stiffness and mass at the roof level represents a light appendage, which may occur in special cases (Chopra, 1995). Applying the same properties used throughout this study to the five-story shear frame with a

light appendage results in the natural periods (T_n), natural frequencies (w_n), and spectral displacements (S_d) shown in Table 92.

Table 92: Five-Story Frame with Irregular Properties

Mode	T_n (s)	w_n (rad/s)	S_d (in.)
1	0.9938	6.3224	8.0439
2	0.9307	6.7511	7.1912
3	0.3355	18.8427	1.5952
4	0.2177	28.8636	0.4949
5	0.1775	35.4050	0.3227

The spectral displacements in Table 92 are representative of the Northridge Earthquake. Evidently, the irregular distribution of mass and stiffness properties results in closely spaced first and second modes. Consequently, the correlation coefficient for the first and second modes is much higher. The correlation coefficients for modes i and j of the five-story shear frame are shown below in Table 93.

Table 93: Correlation Coefficients

Mode	j = 1	j = 2	j = 3	j = 4	j = 5
i = 1	1	0.6986	0.0065	0.0027	0.0019
i = 2	0.6986	1	0.0076	0.0031	0.0021
i = 3	0.0065	0.0076	1	0.0502	0.0226
i = 4	0.0027	0.0031	0.0502	1	0.1918
i = 5	0.0019	0.0012	0.0226	0.1918	1

Despite the essentially negligible correlation coefficients for higher modes, the closely spaced first and second mode results in a correlation coefficient of 0.6986. To analyze the impacts of the interacting modes on the response, the Northridge Earthquake is applied to the five-story shear frame and the

displacement and base shear results are presented in Table 94 and Table 95, respectively.

Table 94: Irregular Five-Story Frame Displacements - Northridge

	THA	ABS	SRSS	CQC	E_{ABS}	E_{SRSS}	E_{CQC}
U_1	3.307”	3.917”	2.380”	3.074”	18.46%	28.02%	7.03%
U_2	6.036”	6.750”	3.390”	5.707”	11.83%	27.27%	5.43%
U_3	7.992”	8.406”	5.874”	7.652”	5.17%	26.51%	4.25%
U_4	9.127”	10.045”	6.705”	8.718”	10.06%	26.53%	4.48%
U_5	42.552”	144.65”	102.80”	57.882”	239.9%	141.6%	36.03%

Table 95: Irregular Five-Story Frame Base Shear – Northridge

Method	V_b (kips)	Error
THA	300.17	0%
ABS	355.58	18.46%
SRSS	216.06	28.02%
CQC	279.05	7.03%

Both the SRSS and CQC methods underestimate the displacement response at the first four floors and overestimate the response at the fifth floor. Furthermore, the two methods also underestimate the total base shear result of the five-story shear frame. On average, the CQC method yields displacement responses and base shear responses that are approximately five and four times as accurate as the SRSS results, respectively. Although for the displacement at the fifth floor the CQC is still nearly four times as accurate as the SRSS method, the degree of error is considerably higher than the other four stories. The increased error is due to the spectral displacement value obtained from the Northridge Earthquake displacement spectrum. Even though the mass and stiffness properties are significantly reduced at the roof level, the fifth natural

frequency is still 35.41 radians per second. In comparison, when the mass and stiffness properties aren't reduced, the fifth natural frequency is 36.16 radians per second. The relatively unchanged natural frequency results in an overestimate of the displacement response at the roof level when applying modal combination methods.

All in all, the application of a light appendage to the five-story shear frame evidences the limitations of the SRSS method. The analysis proves that the presence of closely spaced modes significantly hinders the accuracy of the SRSS method. As a result, the CQC proves to be a more reliable method than the SRSS method. Even though the SRSS method yields good results throughout this thesis, its application is limited by structural irregularities. Therefore, regardless of the system, the CQC method should be used over the SRSS method.

6.4 Conclusion

From the analyses in this chapter, conclusions are drawn regarding the accuracy and application of various seismic analysis methods. First, although the ELFP is permitted by ASCE 7-10 for the shear frames, RSA should still always be performed. Despite the added level of complexity, RSA is still relatively simple and yields considerably more accurate results than the ELFP. The slight increase in complexity yields results that are typically multiple times more accurate. If solely the ELFP is applied, the structure will be inefficiently designed, resulting in an increase in time, materials, and costs.

Secondly, the ABS method is inconsistent and unreliable. As stated by ASCE 7-10, the ABS method isn't a permitted modal combination for seismic analysis. Even though the analyses herein exhibit the inadequacies of the ABS method, when comparing it to the ELFP, the ABS method yields more accurate results than the ELFP, which is a permitted method of seismic analysis. This further exemplifies the need to use RSA when performing seismic analysis.

Lastly, the results in Section 5.4 exhibit the limitations of the SRSS method. Although the mass and stiffness properties are specifically chosen to result in closely spaced modes, three-dimensional structures are more likely to have modal interactions. In turn, when applying RSA to a system, the CQC method should always be chosen for combining modal responses.

Obviously, when possible, THA analysis should be performed. In many cases, such as the analyses in Chapter 5, RSA yields good results and can replace THA. On the contrary, the results in this chapter show that the accuracy of the modal combination methods in RSA can be significantly hindered by the nature of the ground motion and system properties.

7. Friction Spring Dampers

In this chapter, the effects of friction spring dampers (FSDs) on the response of the two-story and three-story shear frame are analyzed. The dynamic response of each shear frame is determined through the application of nonlinear time history analysis (NTHA).

7.1 Classical and Nonclassical Damping

In the previous chapters, classical damping is assumed for the shear frames. In general, classical damping is appropriate to assume for systems with evenly distributed damping properties. Thus far, Rayleigh damping has been applied to the shear frames. Rayleigh damping allows for the application of modal analysis to damped systems and is defined by the following equation.

$$C = \alpha M + \beta K \qquad \text{(Equation 7.1)}$$

The Rayleigh damping model shown by Equation 7.1 uses the scalars α and β to express the damping matrix as a linear combination of the mass and stiffness matrices. Equation 7.1 maintains the orthogonality conditions of the modes, allowing for the application of modal analysis to MDOF damped systems. The damping ratio, ζ, is related to α and β through the equations shown below.

$$\frac{1}{2}\begin{bmatrix} \frac{1}{w_i} & w_i \\ \frac{1}{w_j} & w_j \end{bmatrix}\begin{Bmatrix}\alpha \\ \beta\end{Bmatrix} = \begin{Bmatrix}\xi_i \\ \xi_j\end{Bmatrix} \qquad \text{(Equation 7.2)}$$

$$\alpha = \xi\frac{2w_i w_j}{w_i + w_j} \qquad \text{(Equation 7.3)}$$

$$\beta = \xi\frac{2}{w_i + w_j} \qquad \text{(Equation 7.4)}$$

Where w_i and w_j are the natural frequencies of modes i and j, respectively, and Equations 7.3 and 7.4 assume a constant damping ratio for all modes. Note that the equations above can be expanded based on the number of DOFs in the system.

Although supplemental damping mechanisms are often used to dissipate energy, all dynamic systems illicit some level of damping for a number of reasons, such as the material properties, member connections, or even air resistance on the structure as it oscillates. In ASCE 7-10, damping ratios for steel buildings under wind loading are between 1% and 2%. For seismic applications, ASCE 7-10 suggests a damping ratio of 5% to be used for most structures. The reason for the higher assumed damping ratio in seismic analysis is because structures under earthquake loading are expected to respond inelastically, whereas an elastic response is expected due to wind loading. Furthermore, welded steel structures with a working stress below half of the yield point and above half of the yield point are recommended to have damping ratios between 2% and 3% and 5% to 7%, respectively (Chopra, 1995).

Generally, classical damping refers to structures with viscous damping effects. Although the exact effects resulting from viscous dampers are difficult to model, Rayleigh damping provides an accurate and relatively simple method for modelling the damping in structural systems with fairly consistent damping properties. On the contrary, the application of classical damping models is still limited, and a nonclassical damping model is often necessary. For example, for structures with special energy dissipating devices, nonclassical damping is

necessary (Chopra, 1995). In this study, friction spring dampers (FSDs) are added to the shear frames. The FSDs follow a nonclassical damping model, and nonlinear time history analysis (NTHA) must be applied to solve for the dynamic response of each system. The theory and application behind the FSDs and NTHA are detailed in the subsequent sections of this chapter.

7.2 Nonlinear Time History Analysis

The NTHA herein is performed in SAP2000, which provides a built-in function for modelling the FSDs. This section serves as a brief description of NTHA as it applies to systems with FSDs. A broader explanation of NTHA is readily available in a majority of structural dynamics and seismic engineering textbooks. Unlike velocity-dependent viscous dampers, the energy dissipation properties of the FSDs are displacement-dependent. The governing equation of motion is modified to include the effects of the FSDs and shown below.

$$M\ddot{u} + k(u - u_0)(t) = P(t) \qquad \text{(Equation 7.5)}$$

Where k is the stiffness of the FSDs at each instant of time, $u_0(t)$ is the initial displacement, u(t) is the displacement, and P(t) is the forcing function which is equal to the product of the mass and horizontal ground accelerations, $-m\ddot{u}_g(t)$.

Since the stiffness, displacements, and accelerations are all time-dependent quantities, numerical analysis methods must be used to solve for the dynamic response of the system. In SAP2000, several numerical methods are available for use, including the formerly detailed Newmark-beta Method. For each analysis case, the Newmark-beta method parameters reflect the Average

Acceleration Method (AAM). Recall that the Average Acceleration Method results in unconditionally stable solutions and yields good results for the classically damped two-story and three-story shear frames when THA is applied. Also, research proves that the AAM is still unconditionally stable for SDOF and MDOF systems with nonlinear damping models (Li et al., 2006).

7.3 Introduction to Friction Spring Dampers

The FSDs detailed herein consist of steel rings which dissipate energy through friction forces and elastic forces that develop as they move relative to one another. In this study, the dimensions and specifications of the FSDs are based on steel rings that are manufactured by the German company, RINGFEDER®. A generic model of the FSDs is available on the RINGFEDER® website and shown in Figure 53 below.

Figure 53: Friction Spring Damper Ring Assembly

Source: RINGFEDER® Damper Technology Catalog

As shown by Figure 53, the FSDs consist of inner and outer rings that are in series with one another. When the FSDs are subject to an axial compressive force, sliding occurs and friction forces develop along the mating surfaces of the inner and outer rings. Since the contact surfaces of the rings have wedged faces, the interface friction caused by the axial compressive force expands the outer rings radially and contracts the inner rings inwardly. The expansion and contraction of the outer and inner rings, respectively, results in an axial deflection along the length of the ring assembly. As the FSDs are loaded and unloaded, significant energy is dissipated each cycle in order to overcome the friction and deformation forces in the ring assembly.

In comparison to other damping mechanisms, the FSDs hold many advantages. First, the concentric distribution of the friction forces results in self-centering damping effects. Secondly, the implementation of FSDs into a structural system does not significantly hinder the scope of a project. The only materials required to construct the FSDs are the steel rings, and no major accommodations are needed to implement them into a structural system. When considering mechanisms that elicit similar levels of damping, the FSDs are much easier to involve into a structure's design. Also, the passive nature of the FSDs results in less maintenance and no external power source is necessary to center the effects of the damping or to achieve high levels of damping.

7.4 Mechanics of Friction Spring Dampers

The hysteric energy dissipation of the FSDs is defined by the force-travel diagram shown by Figure 54. The force-travel diagram represents a cycle of the

FSD response, which includes a loading and unloading phase of the ring assembly. The force-travel diagram represents each phase of the FSD response in a clockwise manner starting at the origin (Point A), where the force and displacement are equal to zero.

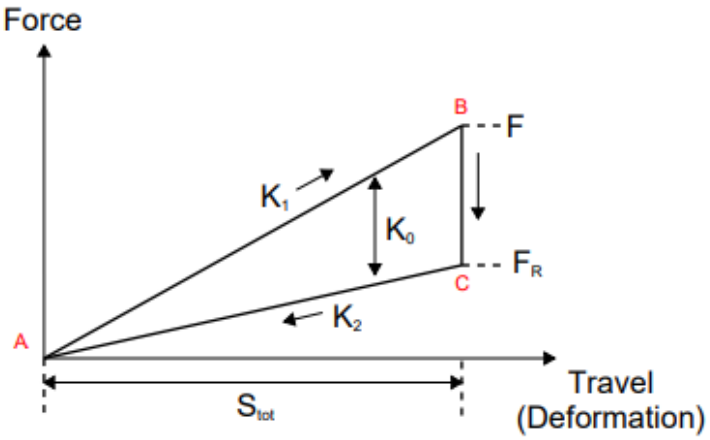

Figure 54: Force-Travel Diagram of FSDs without Preloading Force

The first part of the diagram, shown by Line AB, denotes the loading phase of the ring assembly. As mentioned previously, as the FSDs are axially loaded in compression, friction forces develop at the mating surfaces, and the outer and inner rings are forced to expand and contract. During the loading phase, the expansion and contraction of the rings along with the friction forces between the rings combine to dissipate energy. Since the friction forces are proportional to the forces required to expand and contract the rings, a linear relationship is maintained between the spring force and deformation in accordance with Hooke's Law. The peak force, F, and the maximum ring deformation, S_{tot}, occur at Point B, which is the instant in which the external force overcomes the dissipative forces in the ring assembly. The linear relationship

along Line AB is defined by the loading stiffness, K_1. The vertical portion of the diagram, shown by Line BC, is the transition phase between the loading (compression) and unloading (decompression) phases. At the transition point between the two phases, the friction forces at the interfaces of the rings also transition. In the loading phase, the friction force contributes to the dissipation of energy, but at the start of the unloading phase, the friction force counteracts the dissipation of energy. During the vertical phase, F is reduced by the counteractive friction force, and the decompression of the ring assembly starts once the friction force is overcome at Point C. The force at Point C is the recoil force, F_R, which is typically around a third of the peak force, F. Lastly, the unloading phase occurs along Line CA. Although the friction force counteracts the forces caused by the expansion and contraction of the rings, the relationship maintains linearity, and is characterized by the unloading stiffness, K_2. At the completion of the unloading phase, the ring assembly returns to its initial state.

Generally, the FSDs are subject to a preloading or precompression force, F_0, with typical values in the range of 5% to 10% of the ring's bearing capacity. In order to avoid damaging the lubricating film along the mating faces of the rings, the precompression force should not exceed half of the maximum force, F. It is recommended to apply a preloading force to the ring assembly because it helps to maintain the orientation of the rings and prevents the separation of the individual ring components. If preloaded, the rings will not start to slide relative to one another unless the axial compressive force applied to the ring assembly is

larger than the precompression force, F_0. The effects of applying a preloading force on the response of the FSDs is illustrated by Figure 55 below.

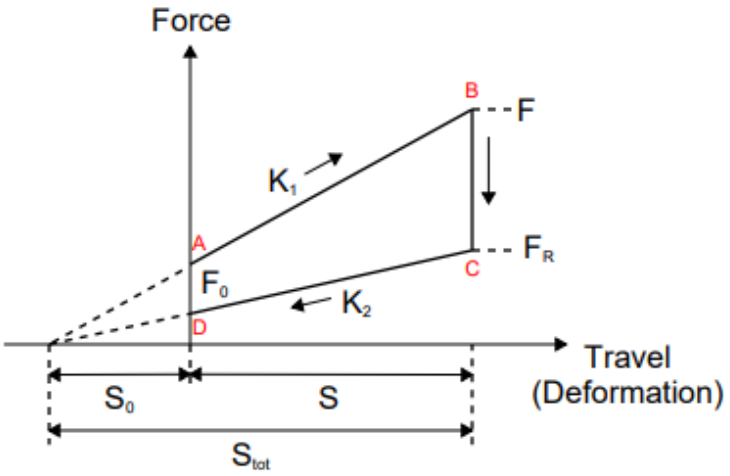

Figure 55: Force-Travel Diagram of FSDs with Preloading Force

As evidence by Figure 55, the preloading force shortens the loading and unloading phases of the FSD response. Instead of transitioning at force and displacement values of zero, the transition between the loading and unloading stages occurs when the difference between the two is equal to the preloading force. Additionally, the preloading force results in an initial displacement, S_0. As previously mentioned, the FSDs only activate if the external force is greater than the preloading force. Consequently, FSDs provide no energy dissipation under service loads. Although the primary effects of the FSDs occur under axially compression, the ring assemblies exhibit damping effects bidirectionally. As a result, the cyclic response relies on the dissipative properties of the FSDs under compression and tension. Whether an external compressive or external tensile force is applied to the ring assembly, the FSDs follow the same hysteric damping model detailed above. The bidirectional force-travel diagram of the FSD

response is shown in Figure 56. Figure 56 represents the entire cyclic response of the FSDs when a preloading force is applied to the ring assembly.

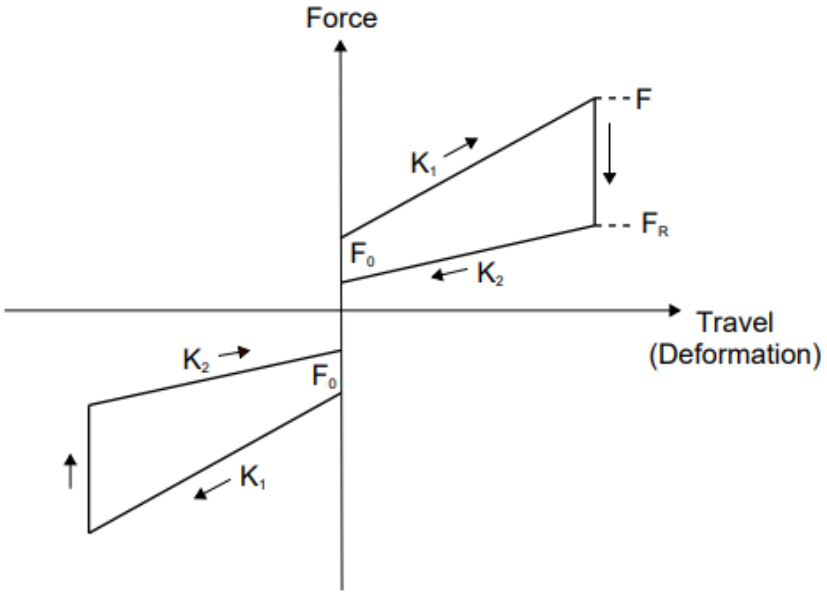

Figure 56: Cyclic Response of FSDs with a Preloading Force

7.5 Modeling and Analysis in SAP2000

This section covers the development and analysis of the two-story and three-story shear frame in SAP2000. A preliminary analysis is completed on the shear frames to determine where to implement the FSDs in each system. First, the FSDs were modelled horizontally at each story level, which slightly reduces the response of the system. Secondly, the FSDs were placed vertically at the two base columns and diagonally between each floor above the base. The second model decreases most of the system responses if modal damping is present, but also produces vastly inconsistent results. Thirdly, the FSDs are placed diagonally at each story level, including the base level, which yields the best results when compared with the other two cases. As a result, the third case is used to model

the two-story and three-story shear frame. The SAP2000 model of the three-story shear frame is shown in Figure 6.5 on the following page.

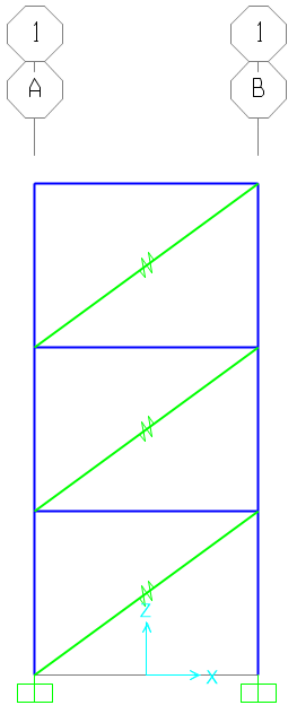

Figure 57: SAP2000 Model of Three-Story Shear Frame

The FSDs are represented by the green diagonal links between adjacent levels. Next, the stiffness values (K_1, K_2, K_0), the type and number of rings, and the preload are specified for the FSDs. In this study, the FSDs are designed based on a target stiffness of the ring assembly during the loading phase. Accordingly, K_1 is set equal to 10%, 25%, 50%, and 100% of the lateral stiffness of each individual floor, 90.78 kips per inch. The loading and unloading stiffnesses are defined by Equation 7.6 and Equation 7.7, respectively (Hill, 1995).

$$K_1 = \frac{2\pi E * tan(\beta + \rho)tan\beta}{n\left(\frac{D_{01}}{A_1} + \frac{D_{02}}{A_2}\right)} \qquad \text{(Equation 7.6)}$$

$$K_2 = \frac{2\pi E * tan(\beta - \rho)tan\beta}{n\left(\frac{D_{01}}{A_1} + \frac{D_{02}}{A_2}\right)} \qquad \text{(Equation 7.7)}$$

Where E is the Modulus of Elasticity, ρ is the friction angle where tan(ρ) is equal to the friction coefficient between rings, β is the angle of the wedge face between rings, n is the number of rings, and D, a, and b are all geometric properties of the rings where the inner and outer rings have subscript of 1 and 2, respectively. RINGFEDER® gives several options for steel rings, evidenced by Figure 58 which was taken from their product catalog.

RINGFEDER®
Friction Spring

Table of standard RINGFEDER® Friction Springs

Force-stroke-diagram

During the operation of the friction spring two thirds of the input energy is dissipated as frictional heat. The recoil force F_R at any point on the diagram is approximately equal to one third of the relative compressive force F. The capacity of the spring is represented by the total area shown below the load curve. The total energy absorption can be calculated by W_e multiplied by the number of elements.

Explanations to table

F	=	Spring end force
s_e	=	Spring stroke for one element
W_e	=	Energy absorption of one element
h_e	=	Length of one element
D_1, d_1	=	Outer and inner diameter
b/2	=	Half length of the ring
D_{2G}	=	Guiding diameter outside
d_{2G}	=	Inner guiding diameter
Gw_e	=	Weight of one element

Type	old type	Diagram				Dimensions			Guide		
		F	s_e	W_e	h_e	D_1	d_1	b/2	D_{2G}	d_{2G}	Gw_e
		lbs	inch	ft-lbs	inch	inch	inch	inch	inch	inch	lbs
01800	1201	1,124	0.016	0.74	0.087	0.713	0.567	0.071	0.74	0.55	0.004
02500	1202	2,023	0.024	1.99	0.122	0.984	0.819	0.098	1.02	0.79	0.009
03200	1203	3,146	0.031	4.13	0.157	1.260	1.063	0.126	1.30	1.03	0.015
03800	1204	4,495	0.035	6.64	0.185	1.496	1.248	0.150	1.55	1.20	0.026
04200	1205	5,843	0.039	9.59	0.205	1.661	1.362	0.165	1.72	1.31	0.040
04800	1206	7,641	0.043	13.79	0.232	1.898	1.551	0.189	1.96	1.50	0.057
05500	1207	8,989	0.051	19.18	0.268	2.165	1.811	0.217	2.23	1.75	0.077
06300	1208	12,136	0.055	27.88	0.303	2.480	2.043	0.248	2.56	1.98	0.123
07000	1209	14,608	0.063	38.35	0.339	2.756	2.291	0.276	2.84	2.22	0.163
08000	1310	18,653	0.071	55.32	0.386	3.150	2.638	0.315	3.27	2.52	0.231
09000	1311	22,474	0.079	73.76	0.433	3.543	2.972	0.354	3.66	2.87	0.320
10000	1312	28,092	0.087	101.78	0.480	3.937	3.307	0.394	4.06	3.19	0.448
12400	1314	44,947	0.102	191.77	0.591	4.882	4.016	0.488	5.04	3.86	0.899
13000	1313	35,958	0.102	153.41	0.591	5.118	4.390	0.488	5.28	4.25	0.829
14000	1315	56,184	0.118	276.59	0.669	5.512	4.567	0.551	5.67	4.41	1.252
16600	1316	78,658	0.146	477.95	0.787	6.535	5.276	0.630	6.69	5.12	1.916
19600	1318	134,842	0.173	973.59	0.921	7.638	6.102	0.748	7.83	5.91	3.695
20000	1317	114,616	0.154	733.88	0.882	7.795	6.378	0.728	7.99	6.18	3.461
22000	1319	161,811	0.173	1168.31	1.039	8.661	6.850	0.866	8.86	6.65	5.672
26200	1320	193,274	0.189	1522.34	1.016	10.315	8.189	0.827	10.55	7.95	7.529
30000	1221	224,737	0.228	2138.95	1.409	11.811	9.843	1.181	12.05	9.65	12.147
32000	1222	269,684	0.244	2743.76	1.504	12.598	10.354	1.260	12.83	10.16	15.565
35000	1223	314,632	0.260	3407.57	1.638	13.780	11.339	1.378	14.02	11.14	20.238
40000	1224	404,527	0.299	5044.98	1.874	15.748	12.992	1.575	16.02	12.76	29.895

Figure 58: RINGFEDER® Steel Ring Specification Table

Source: RINGFEDER® Damper Technology Catalog

Type 40000 rings with individual stroke displacements, s_e, of 0.299 inches, are chosen for this study. To determine the number of springs for each analysis case, K_1 is set equal to the target loading stiffness in Equation 7.6. The number of springs is rounded up to the nearest whole number, and K_1 is solved for. Next, with the whole number of rings necessary to obtain the target stiffness, Equation 7.7 is used to determine the unloading stiffness, K_2. The total ring deflection, S_{tot}, is calculated by multiplying the number of rings by the individual stroke displacement, s_e, of the Type 40000 rings. Lastly, the preloading displacement, S_0, is taken as 20% of S_{tot}, and the preloading stiffness, K_0, is taken as 10 times the loading stiffness. Table 96 shows the results for each target stiffness.

Table 96: Ring Design Parameters

Case	% K_{story}	n	K_0 (k/in)	K_1 (k/in)	K_2 (k/in)	S_{tot} (in)	S_0 (in)
1	10%	150	90.40	9.04	2.98	44.85	8.97
2	25%	60	226.00	22.60	7.45	17.94	3.59
3	50%	30	452.00	45.20	14.90	8.97	1.79
4	100%	15	904.00	90.39	29.80	4.49	0.90

As shown by Figure 57, the FSDs are input into SAP2000 as links, and in the drop dawn menu for link type, the “Damper – Friction Spring” option is selected. The values in Table 96 are input for the directional properties of the link. Note that K_0 and S_{tot} are the “initial (Nonslipping) Stiffness” and the “Stop displacement” inputs, respectively. The inputs to model the FSDs for Case 1, where the loading stiffness is approximately 10% of the story stiffness, are shown by Figure 59.

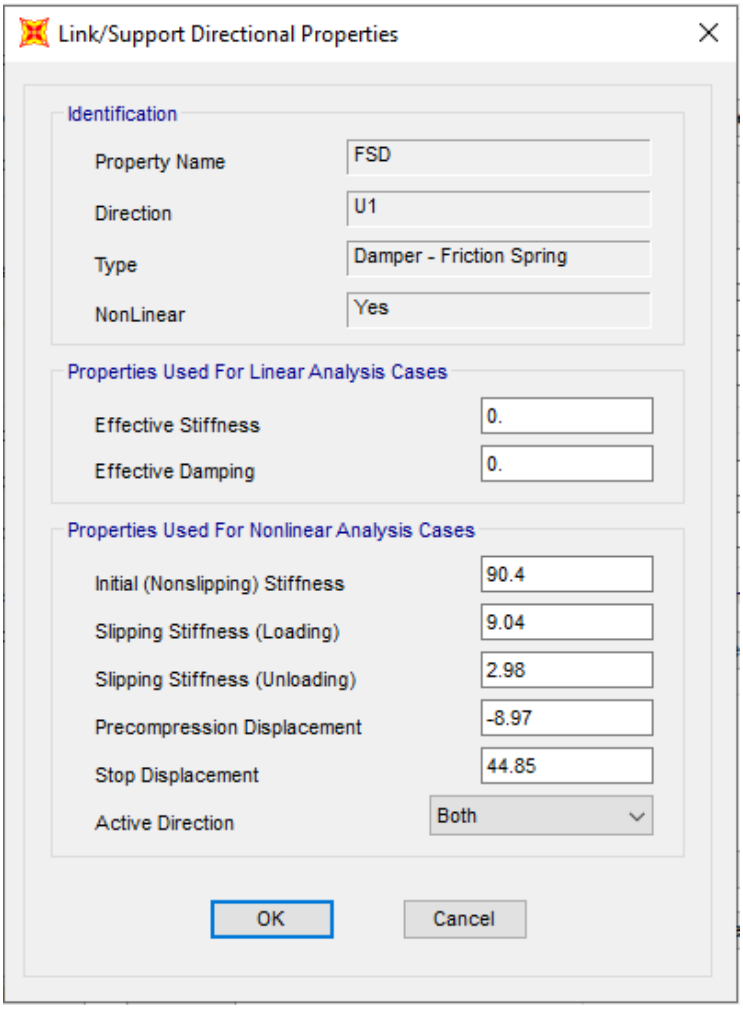

Figure 59: SAP 2000 FSD Property Input Box

Next, a user defined function is created by uploading the ground motion record for the earthquake(s) of interest. Additionally, the function definition tool allows for a time-step to be chosen. Finally, a load case is defined which applies NTHA to determine the dynamic response of the systems. In the upper right corner of the load case definition box, the load case type, analysis type, and solution type are defined as time integration, nonlinear, and direct integration, respectively. Also, the Newmark Method is selected for the time integration.

Figure 60 shows an example of the load case definition box for the 1994 Northridge Earthquake.

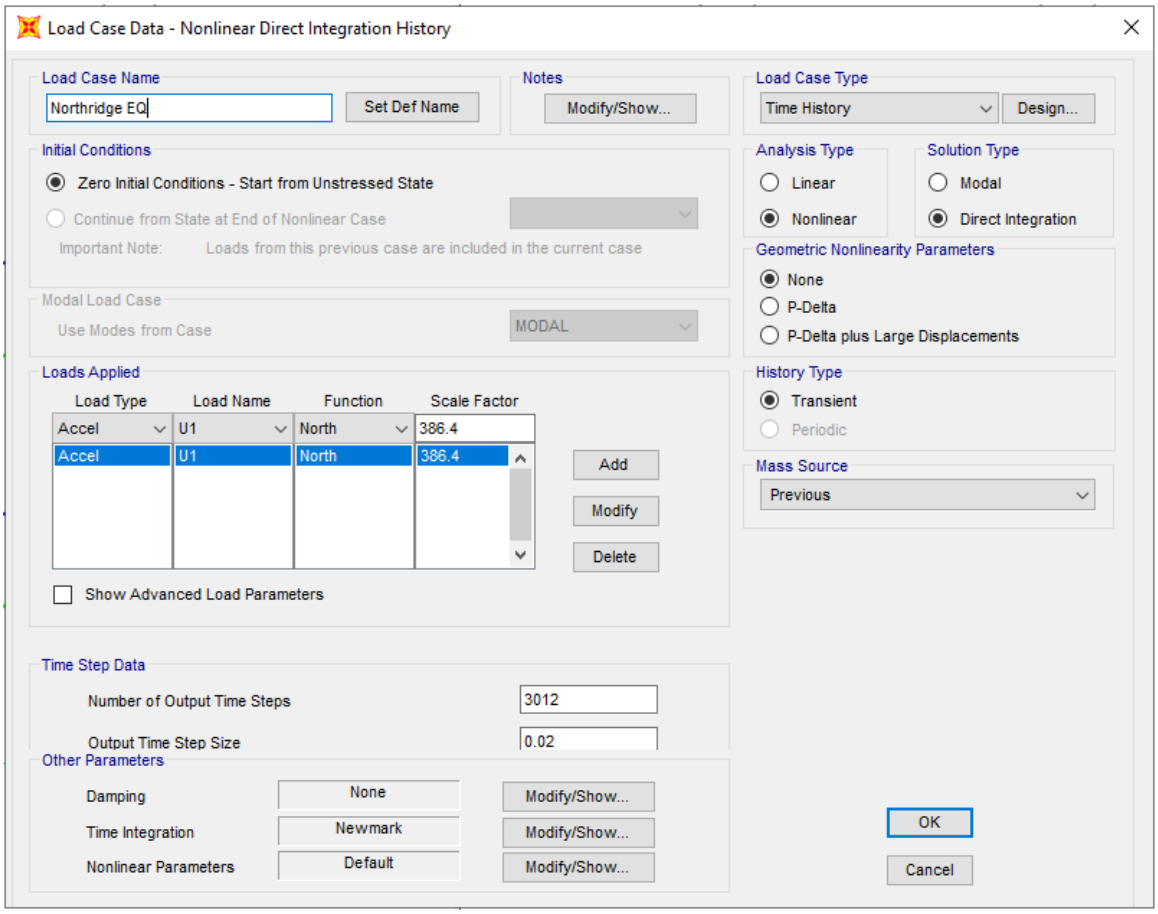

Figure 60: SAP2000 Load Case Definition Box for NTHA

The ground motion records of the same five earthquakes used earlier in this study are individually applied to the shear frames. The two-story and three-story shear frame with FSDs designed for each target loading stiffness, shown in Table 96, are subject to each of the five earthquakes, and the Average Acceleration Method (AAM) is applied to determine the dynamic response from NTHA. First, the dynamic response is determined considering solely the damping effects from the FSDs. Secondly, the dynamic response is determined when 1% modal damping is combined with the damping effects of the FSDs. The 1%

modal damping is a conservative estimate for the constant damping properties of steel frames. Lastly, the same NTHA is used to find the dynamic response of the systems without any damping effects and 5% modal damping without the presence of FSDs in SAP2000, where both cases serve as a reference point for determining the efficiency of the FSDs.

7.6 Two-Story Shear Frame Results

The maximum lateral displacement response at the height of the first story, U_1, and the roof, U_2, of the two-story shear frame with FSDs for each of the five earthquakes are shown in the following tables.

Table 97: Two-Story Response with FSDs - 1940 El Centro EQ

	1940 El Centro EQ Record (00 Direction)			
	FSDs with $\xi = 0$		**FSDs with $\xi = 0.01$**	
% K_{story}	**U_1**	**U_2**	**U_1**	**U_2**
10%	1.651”	2.599”	1.257”	1.862”
25%	0.869”	1.333”	0.821”	1.280”
50%	0.665”	0.869”	0.615”	0.814”
100%	0.318”	0.432”	0.306”	0.415”

Table 98: Two-Story Response with FSDs – 1952 Kern County EQ

	1952 Kern County EQ Record (111 Direction)			
	FSDs with $\xi = 0$		**FSDs with $\xi = 0.01$**	
% K_{story}	**U_1**	**U_2**	**U_1**	**U_2**
10%	1.173”	1.900”	0.623”	0.956”
25%	0.778”	1.142”	0.649”	0.993”
50%	0.360”	0.538”	0.272”	0.434”
100%	0.247”	0.377”	0.244”	0.374”

Table 99: Two-Story Response with FSDs – 1952 San Luis Obispo EQ

	1952 San Luis Obispo EQ Record (324 Direction)			
	FSDs with $\xi = 0$		FSDs with $\xi = 0.01$	
% K_{story}	U_1	U_2	U_1	U_2
10%	0.434”	0.692”	0.322”	0.513”
25%	0.135”	0.214”	0.124”	0.197”
50%	0.155”	0.250”	0.115”	0.187”
100%	0.098”	0.161”	0.080”	0.132”

Table 100: Two-Story Response with FSDs – 1989 Loma Prieta EQ

	1989 Loma Prieta EQ Record (00 Direction)			
	FSDs with $\xi = 0$		FSDs with $\xi = 0.01$	
% K_{story}	U_1	U_2	U_1	U_2
10%	2.347”	3.505”	2.279”	3.415”
25%	1.861”	2.586”	1.786”	2.450”
50%	1.484”	1.894”	1.339”	1.743”
100%	1.335”	1.720”	1.269”	1.651”

Table 101: Two-Story Response with FSDs - 1994 Northridge EQ

	1994 Northridge EQ Record (00 Direction)			
	FSDs with $\xi = 0$		FSDs with $\xi = 0.01$	
% K_{story}	U_1	U_2	U_1	U_2
10%	3.449”	5.124”	3.142”	4.627”
25%	1.420”	1.958”	1.333”	1.832”
50%	1.544”	1.974”	1.324”	1.756”
100%	0.481”	0.608”	0.466”	0.582”

For all of the cases except for the Kern County Earthquake 25% case with 1% modal damping and the Northridge Earthquake 50% case with 0% modal damping, an increase in the loading stiffness of the FSDs decreases the lateral displacement response. The energy dissipation of the FSDs is reliant on both the stiffness and total deflection properties of the ring assemblies. As the stiffness of

the FSDs increase, the total deflection decreases. Consequently, increasing the spring stiffness doesn't necessarily decrease the maximum displacement response, as shown by the two outlying cases. The reason for the increase in response under the Northridge Earthquake between the 25% and 50% cases is shown by the figures below.

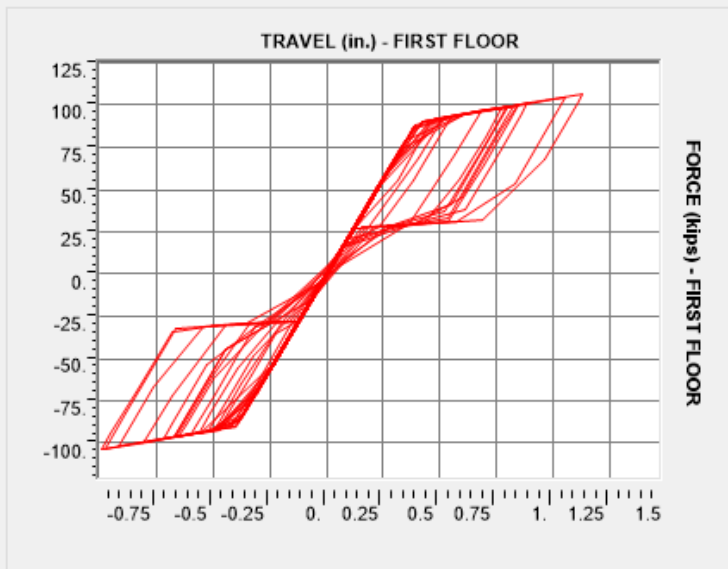

Figure 61: Force-Travel Two-Story Lower FSD Northridge - Case 2 (25%)

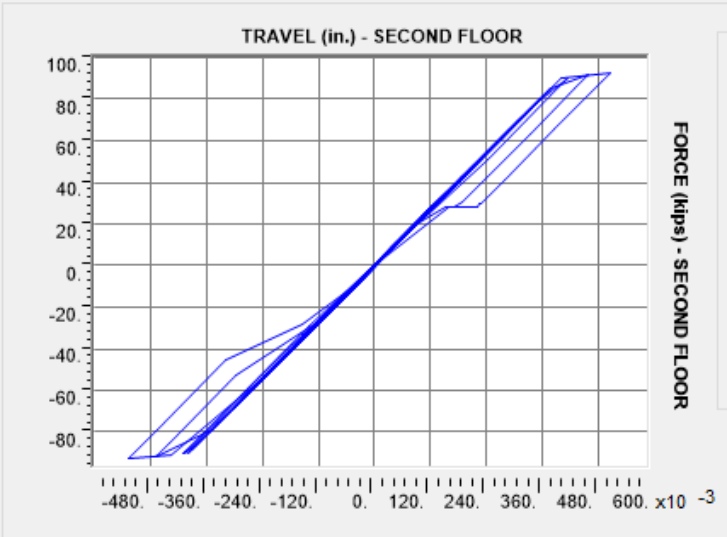

Figure 62: Force-Travel Two-Story Upper FSD Northridge - Case 2 (25%)

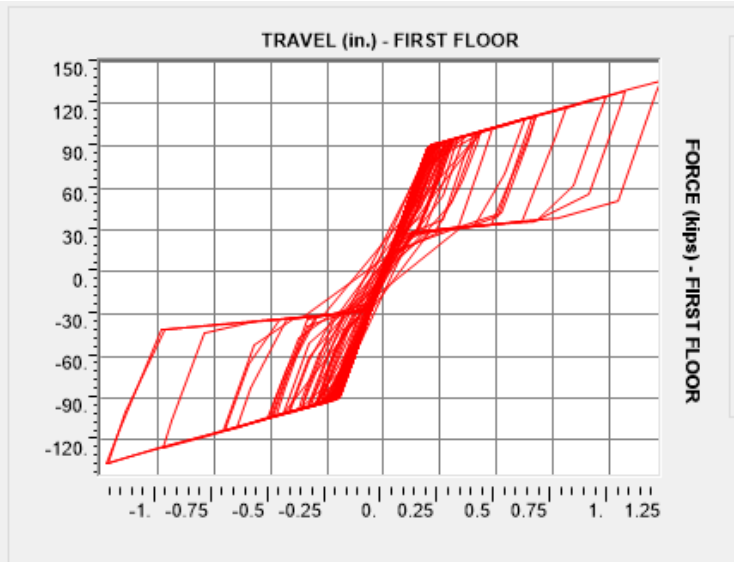

Figure 63: Force-Travel Two-Story Lower FSD Northridge - Case 3 (50%)

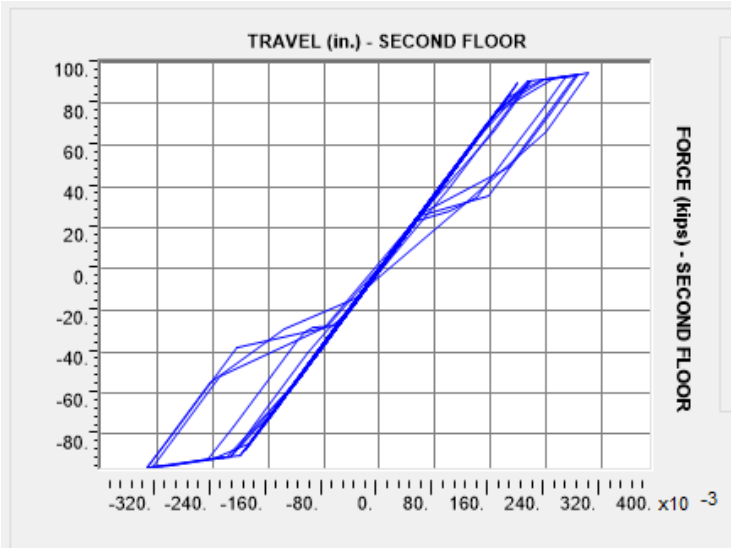

Figure 64: Force-Travel Two-Story Upper FSD Northridge - Case 3 (50%)

In both Case 2 and Case 3, the lower (first-story) FSDs, shown by Figure 63 and 64, yield the expected cyclic hysteric response, but the upper (second-story) FSDs yield less symmetric responses. In Case 2 where the FSDs are 25% of the story lateral stiffness, the upper FSD starts to respond hysterically and the cyclic response is only slightly asymmetric, which is shown by Figure 62. On the

contrary, in Case 3, even though the hysteric response of the upper FSD is more developed than in Case 2, the application of negative forces results in more pronounced deflections, which is evidenced by Figure 64. Although not shown in this chapter, the force-travel diagrams of each FSD in the two-story shear frame under the El Centro, Kern County, Loma Prieta, and Northridge earthquakes are presented in Appendix Y.

Furthermore, the application of 1% modal damping reduces the displacement response in each analysis when compared with the respective analysis where no modal damping is present. The addition of modal damping tends to cause a larger reduction in the maximum displacement response for FSDs with lower stiffness values. On the contrary, FSDs with higher stiffnesses generally yield similar maximum displacement responses with or without modal damping. Although the maximum responses are similar, the main difference between the 0% and 1% modal damping cases is evidenced by the displacement time histories. Consider the displacement time histories at each story resulting from the Northridge Earthquake with FSD stiffnesses equal to a 100% of the story stiffness having 0% and 1% modal damping. Figure 65 and Figure 66 on the following page present the displacement time histories with and without modal damping.

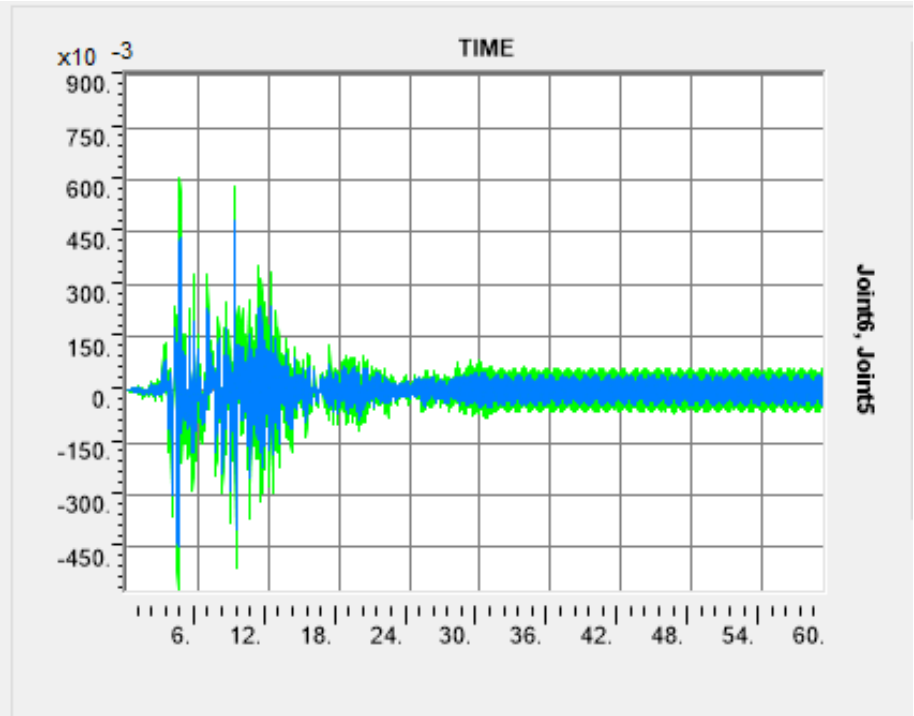

Figure 65: Northridge EQ DTH Case 4 - 0% Modal Damping

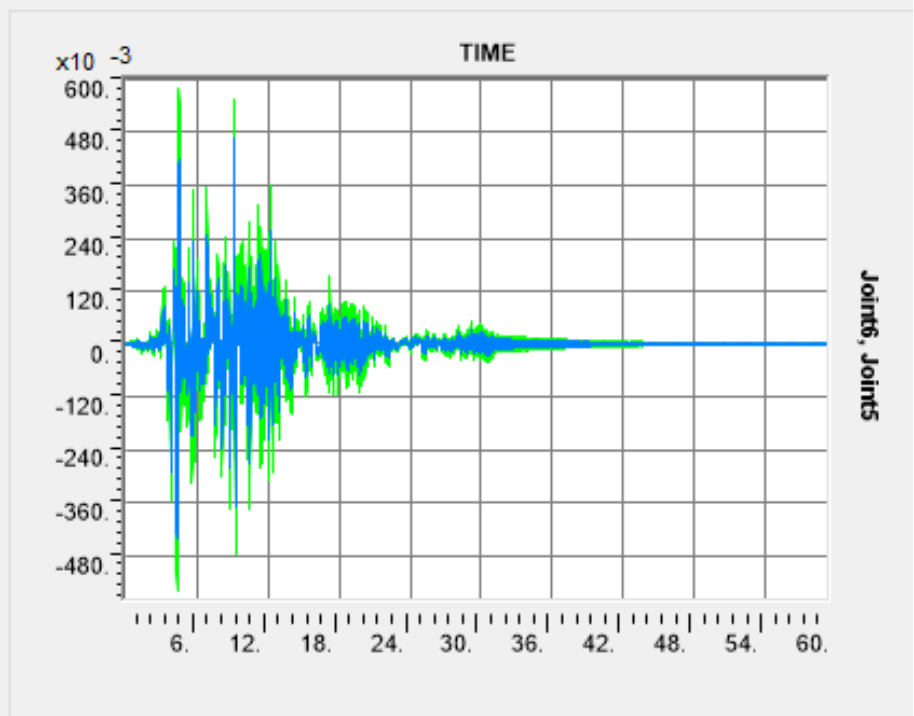

Figure 66: Northridge EQ DTH Case 4 – 1% Modal Damping

In both figures, the first floor and second floor DTHs are represented by the blue and green plots, respectively. Although the maximum displacement response is similar, Figure 66 shows that in the presence of modal damping, the frame displacements reach zero approximately 45 seconds into the ground motion, whereas without modal damping, the frames continue to displace for the entire 60 seconds. Even though the displacements at the tail end of Figure 65 are relatively small, as the stiffness of the FSDs decrease, the amplitude of the DTH increases. This trend remains consistent for each FSD stiffness case.

Next, the results of the analyses with FSDs are compared with the results in the absence of FSDs where 0% and 5% modal damping are assumed. The results are compared in the following tables. Note that a negative percentage means the FSDs yielded a larger maximum displacement comparatively.

Table 102: Two-Story Maximum Response Reduction - El Centro 00

		Undamped (ξ = 0)		**5% Damping (ξ = 0.05)**	
Case	**K_{story}**	**U_1**	**U_2**	**U_1**	**U_2**
FSDs & ξ = 0	**10%**	55.91%	55.26%	-2.17%	-3.59%
	25%	76.79%	77.05%	46.22%	46.87%
	50%	82.24%	85.04%	58.85%	65.36%
	100%	91.51%	92.56%	80.33%	82.77%
FSDs & ξ = 1%	**10%**	66.44%	67.95%	22.22%	25.79%
	25%	78.07%	77.97%	49.18%	48.98%
	50%	83.58%	85.98%	61.94%	67.54%
	100%	91.83%	92.86%	81.07%	83.48%

Table 103: Two-Story Maximum Response Decrease – Kern County 111

		Undamped (ξ = 0)		5% Damping (ξ = 0.05)	
Case	**K_{story}**	**U_1**	**U_2**	**U_1**	**U_2**
FSDs & ξ = 0	**10%**	8.72%	4.81%	-83.42%	-87.56%
	25%	39.49%	42.79%	-21.59%	-12.73%
	50%	71.95%	73.03%	43.64%	46.85%
	100%	80.75%	81.12%	61.33%	62.79%
FSDs & ξ = 1%	**10%**	51.53%	52.11%	2.61%	5.64%
	25%	49.49%	50.28%	-1.49%	2.02%
	50%	78.87%	78.26%	57.54%	57.17%
	100%	80.99%	81.24%	61.80%	63.04%

Table 104: Two-Story Maximum Response Decrease – SLO 324

		Undamped (ξ = 0)		5% Damping (ξ = 0.05)	
Case	**K_{story}**	**U_1**	**U_2**	**U_1**	**U_2**
FSDs & ξ = 0	**10%**	-129.25%	-121.53%	-204.49%	-206.74%
	25%	28.51%	31.50%	5.05%	5.15%
	50%	18.00%	19.77%	-8.91%	-11.09%
	100%	48.37%	48.48%	31.43%	28.66%
FSDs & ξ = 1%	**10%**	74.97%	74.32%	49.71%	49.41%
	25%	34.74%	36.91%	13.32%	12.64%
	50%	39.12%	40.24%	19.14%	17.26%
	100%	57.57%	57.74%	43.64%	41.48%

Table 105: Two-Story Maximum Response Decrease – Loma Prieta 00

		Undamped (ξ = 0)		5% Damping (ξ = 0.05)	
Case	**K_{story}**	**U_1**	**U_2**	**U_1**	**U_2**
FSDs & ξ = 0	**10%**	43.55%	46.96%	7.12%	15.77%
	25%	55.24%	60.87%	26.36%	37.85%
	50%	64.31%	71.34%	41.27%	54.48%
	100%	67.89%	73.97%	47.17%	58.66%
FSDs & ξ = 1%	**10%**	45.19%	48.32%	9.81%	17.93%
	25%	57.05%	62.92%	29.32%	41.12%
	50%	67.80%	73.62%	47.01%	58.11%
	100%	70.92%	75.02%	52.16%	60.32%

Table 106: Two-Story Maximum Response Decrease – Northridge 00

		Undamped ($\xi = 0$)		5% Damping ($\xi = 0.05$)	
Case	**K_{story}**	**U_1**	**U_2**	**U_1**	**U_2**
FSDs & $\xi = 0$	**10%**	6.23%	0.31%	-29.36%	-28.94%
	25%	58.83%	61.91%	43.20%	50.73%
	50%	55.23%	61.60%	38.24%	50.33%
	100%	86.06%	88.18%	80.76%	84.71%
FSDs & $\xi = 1\%$	**10%**	8.90%	9.98%	-25.68%	-16.43%
	25%	61.35%	64.36%	46.68%	53.90%
	50%	68.16%	73.43%	47.61%	57.80%
	100%	86.48%	88.68%	81.35%	85.35%

In each analysis case, except for the San Luis Obispo (SLO) Earthquake, the presence of the FSDs reduces the maximum displacement response when compared with the undamped case. For the SLO Earthquake, FSDs with 10% of the story stiffness significantly increase the maximum displacement. Clearly, in this case, the FSDs actually add energy to the system. The addition in energy is a result of the FSDs exhibiting a negative lateral stiffness on the shear frame due to the P-Δ effects. Negative stiffness occurs when the displacement increases while the force decreases. Recall that the SLO Earthquake in the 324 direction has a PGA of 0.05394g, which is considerably smaller when compared with the other four earthquakes in this study. The small PGA results in a small external force, which prevents the hysteric damping cycle from occurring. In compression, the external force transferred to the FSDs never overcomes the preloading force, and the rings remain stationary at their initial displacement (S_0 = 8.97”). Consequently, due to the large initial displacement, when the FSDs are loaded, the axial forces transferred to the ring assembly create second order moments. The P-Δ effects

occur throughout the entire dynamic loading of the system due to the external force not being large enough to elicit sliding in the ring assemblies. Although only Case 1 results in an increase in total response when compared with the undamped frame, P-Δ effects occur for each stiffness case under the SLO Earthquake, but the impacts are less pronounced due to smaller initial displacements that essentially work as moment arms. In practical applications, the stiffness and displacement relationship of the FSDs should be balanced to avoid undesirable responses. Despite its very specific application, the design procedure for Self-Centering-Energy-Absorbing-Rocking-Core-Systems (SCENARIO Systems), a new type of lateral force resisting system, provides specific design criteria for avoiding the development of negative stiffness in the FSDs due to P-Δ effects (Hu et al., 2019). As mentioned previously, the force-travel diagrams for the upper and lower links in the two-story shear frame for each analysis case are presented in Appendix Y.

Finally, the average response reduction, range (minimum to maximum value), and standard deviation (SD) of each FSD stiffness case is analyzed for the two-story shear frame. The tables below show the statistical results gathered from the El Centro, Kern County, Loma Prieta, and Northridge Earthquakes. Due to the relatively high inconsistency and inaccuracy of the responses, coupled with the inactivity of the FSDs, the responses from the SLO Earthquake analysis cases are omitted. First, Table 107 and Table 108 show the statistical results when comparing the two-story shear frame responses when FSDs (including either 0% or 1% damping) are present with the responses when the system is undamped.

Table 107: FSD Percentage Reduction of Undamped Two-Story

K_{story} %	$U_{1,MEAN}$ %	$RANGE_{U1}$ %	SD_{U1} %	$U_{2,MEAN}$ %	$RANGE_{U2}$ %	SD_{U2} %
10%	28.60	6.23 - 55.91	21.59	26.83	0.31 – 55.26	24.50
25%	57.59	39.49 – 76.79	13.26	60.65	31.50 – 77.05	12.14
50%	68.43	55.23 – 82.24	9.93	72.75	61.60 – 85.04	8.33
100%	81.55	67.89 – 91.51	8.76	83.96	73.97 – 92.56	7.06

Table 108: FSD Percentage Reduction of Undamped Two-Story

K_{story} %	$U_{1,MEAN}$ %	$RANGE_{U1}$ %	SD_{U1} %	$U_{2,MEAN}$ %	$RANGE_{U2}$ %	SD_{U2} %
10%	43.01	8.90 – 74.97	21.15	44.59	9.98 – 67.95	21.29
25%	61.49	49.49 – 78.07	10.47	63.88	50.28 – 77.97	9.81
50%	74.60	67.80 – 83.58	6.83	77.82	73.43 – 85.98	5.09
100%	82.56	70.92 – 91.83	7.73	84.45	75.02 – 92.86	6.85

As shown by the tables above, the higher the stiffness of the FSDs, the greater average response reduction. For FSD stiffnesses above 10%, the difference in results when 0% versus 1% damping is applied are small. The largest increase in reduction percentage is between the 10% and 25% stiffness cases. In general, the addition of 1% damping to the damping effects of the FSDs slightly reduces the range and standard deviation of the maximum displacement responses. Next, the same results are compared with the results obtained for the two-story shear frame with 5% modal damping.

Table 109: FSD Percentage Reduction of 5% Damped Two-Story

K_{story} %	$U_{1,MEAN}$ %	$RANGE_{U1}$ %	SD_{U1} %	$U_{2,MEAN}$ %	$RANGE_{U2}$ %	SD_{U2} %
10%	-26.95	- 83.4 – 7.12	35.25	-26.08	- 87.6 – 15.77	38.88
25%	23.54	- 21.6 – 46.22	27.14	30.68	- 12.7 – 50.73	25.50
50%	45.50	38.24 – 58.85	7.94	54.25	46.85 – 65.36	6.96
100%	67.40	47.17 – 80.33	14.07	72.23	58.66 – 84.71	11.62

Table 110: FSD Percentage Reduction of 5% Damped Two-Story

K_{story} %	$U_{1,MEAN}$ %	$RANGE_{U1}$ %	SD_{U1} %	$U_{2,MEAN}$ %	$RANGE_{U2}$ %	SD_{U2} %
10%	2.24	- 25.7 – 22.22	17.58	8.23	- 16.4 – 25.79	15.95
25%	30.93	- 1.49 – 49.18	20.22	36.51	2.02 – 53.90	20.42
50%	53.53	47.01 – 61.94	6.41	60.15	57.17 – 67.54	4.28
100%	69.09	52.16 – 81.35	12.59	73.05	60.32 – 85.35	11.43

As shown by Table 6.14, if the FSDs elicit the only damping effects in the system, the 10% FSD stiffness case is typically less effective than 5% constant modal damping. On the contrary, the other 10% and 25% FSD stiffness cases in Table 109 and Table 110 show positive average percent reductions. Although three out of four of the lower FSD stiffness cases perform better than the 5% damping on average, the range values show that the comparative efficiency is dependent on the earthquake. Finally, Table 109 and Table 110 display that the 50% and 100% stiffness cases yield the best results. First, the 50% stiffness case reduces the 5% damping response between 38.24% and 58.85% with solely the FSDs and between 47.01% and 61.94% with the FSDs combined with 1% modal damping. Secondly, the 100% stiffness case reduces the 5% damping response between 47.17% and 80.33% (FSDs only) and between 52.26% and 81.35%

(FSDs and 1% damping). Clearly, the FSDs are effective in reducing the maximum displacement response of the two-story shear frame, with the best results occurring at higher FSD stiffness.

7.7 Three-Story Shear Frame Results

The analysis performed in the previous section is now applied to the three-story shear frame. First, the maximum lateral displacement responses of the three-story shear frame with FSDs are compared with the maximum responses when 0% and 5% modal damping are assumed. The maximum reduction percent for each case is shown in the tables below.

Table 111: Three-Story Maximum Response Reduction - El Centro 00

		Undamped ($\xi = 0$)			**5% Damping ($\xi = 0.05$)**		
Case	**K_{story}**	**U_1**	**U_2**	**U_3**	**U_1**	**U_2**	**U_3**
FSDs & $\xi = 0$	**10%**	1.62%	7.71%	14.60%	-28.57%	-21.10%	-15.28%
	25%	35.85%	42.43%	49.31%	16.16%	24.46%	31.57%
	50%	68.20%	73.85%	76.78%	58.44%	65.69%	68.66%
	100%	76.55%	80.16%	82.51%	69.36%	73.97%	76.39%
FSDs & $\xi = 1\%$	**10%**	6.58%	11.67%	18.01%	-22.09%	-15.91%	-10.68%
	25%	36.82%	42.63%	49.18%	17.43%	24.73%	31.39%
	50%	64.15%	68.98%	73.26%	53.15%	59.30%	63.90%
	100%	76.82%	80.73%	82.89%	69.71%	74.71%	76.90%

Table 112: Three-Story Maximum Response Reduction – Kern County 111

		Undamped (ξ = 0)			5% Damping (ξ = 0.05)		
Case	**K_{story}**	**U_1**	**U_2**	**U_3**	**U_1**	**U_2**	**U_3**
FSDs & ξ = 0	**10%**	19.16%	8.80%	7.12%	-85.64%	-80.30%	-83.65%
	25%	30.29%	29.61%	31.59%	-60.09%	-39.16%	-35.25%
	50%	72.23%	71.23%	71.22%	36.23%	43.12%	43.09%
	100%	71.28%	71.55%	73.30%	34.04%	43.76%	47.21%
FSDs & ξ = 1%	**10%**	38.59%	30.07%	31.12%	-41.04%	-38.26%	-36.19%
	25%	36.39%	34.51%	35.59%	-46.09%	-29.47%	-27.35%
	50%	73.92%	72.65%	72.50%	40.11%	45.92%	45.62%
	100%	72.02%	71.69%	73.37%	35.74%	44.04%	47.35%

Table 113: Three-Story Maximum Response Reduction – SLO 324

		Undamped (ξ = 0)			5% Damping (ξ = 0.05)		
Case	**K_{story}**	**U_1**	**U_2**	**U_3**	**U_1**	**U_2**	**U_3**
FSDs & ξ = 0	**10%**	-14.95%	-13.0%	-14.7%	-50.63%	-45.2%	-47.1%
	25%	13.89%	12.67%	9.05%	-12.84%	-12.2%	-16.6%
	50%	43.81%	39.86%	38.31%	26.37%	22.73%	20.90%
	100%	66.70%	61.90%	58.45%	56.36%	51.05%	46.72%
FSDs & ξ = 1%	**10%**	84.99%	82.85%	82.56%	65.53%	66.10%	65.52%
	25%	46.02%	41.34%	38.66%	29.26%	24.64%	21.35%
	50%	52.12%	48.71%	46.67%	37.26%	34.10%	31.62%
	100%	96.92%	64.86%	61.74%	95.96%	54.85%	50.95%

Table 114: Three-Story Maximum Response Reduction – Loma Prieta 00

		Undamped (ξ = 0)			5% Damping (ξ = 0.05)		
Case	**K_{story}**	**U_1**	**U_2**	**U_3**	**U_1**	**U_2**	**U_3**
FSDs & ξ = 0	**10%**	70.09%	70.97%	71.64%	-0.22%	8.31%	12.47%
	25%	77.14%	77.57%	77.91%	23.41%	29.14%	31.83%
	50%	81.10%	80.83%	81.93%	36.68%	39.44%	44.23%
	100%	84.29%	83.70%	85.10%	47.35%	48.52%	54.00%
FSDs & ξ = 1%	**10%**	72.33%	73.12%	73.74%	7.28%	15.08%	18.94%
	25%	78.65%	78.19%	78.64%	28.46%	31.11%	34.09%
	50%	81.64%	81.32%	82.44%	38.47%	40.99%	45.82%
	100%	84.69%	84.19%	85.59%	48.70%	50.05%	55.53%

Table 115: Three-Story Maximum Response Reduction - Northridge 00

		Undamped ($\xi = 0$)			5% Damping ($\xi = 0.05$)		
Case	**K_{story}**	**U_1**	**U_2**	**U_3**	**U_1**	**U_2**	**U_3**
FSDs & $\xi = 0$	**10%**	71.43%	70.54%	69.55%	16.69%	16.97%	14.47%
	25%	65.71%	64.48%	66.81%	0.00%	-0.11%	6.77%
	50%	76.04%	75.35%	77.46%	30.13%	30.54%	36.67%
	100%	78.68%	78.35%	79.97%	37.82%	38.98%	43.73%
FSDs & $\xi = 1\%$	**10%**	70.74%	68.18%	67.73%	14.68%	10.33%	9.34%
	25%	70.34%	69.60%	71.84%	13.50%	14.32%	20.89%
	50%	81.21%	80.76%	82.22%	37.03%	39.22%	45.11%
	100%	79.56%	79.34%	81.01%	40.41%	41.77%	46.65%

Similar to the two-story shear frame, when the FSDs are the sole damping mechanisms in the three-story shear frame, the 10% FSD stiffness case energizes the system resulting in maximum displacement responses that are larger than the undamped case. The P-Δ effects cause the system to exhibit negative stiffness properties for the SLO Earthquake; consequently, the results are excluded from future analysis in this section. Each stiffness case for the Loma Prieta and Northridge Earthquake yields good results and reduces the undamped response between 70% to 90% and 65% to 85%, respectively. On the other hand, the 50% stiffness case for the El Centro and Kern County Earthquake reduce the undamped response twice as much as the 25% stiffness case. The first and second floor FSD force-travel diagrams for the 25% and 50% stiffness cases for the El Centro Earthquake are shown by the figures below.

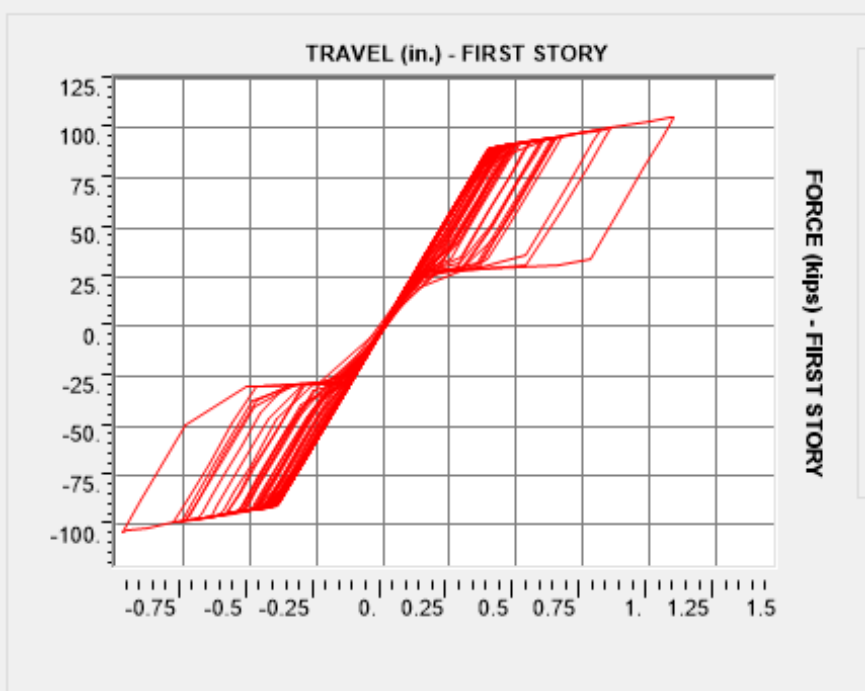

Figure 67: Force-Travel Three-Story Lower FSD El Centro - Case 2 (25%)

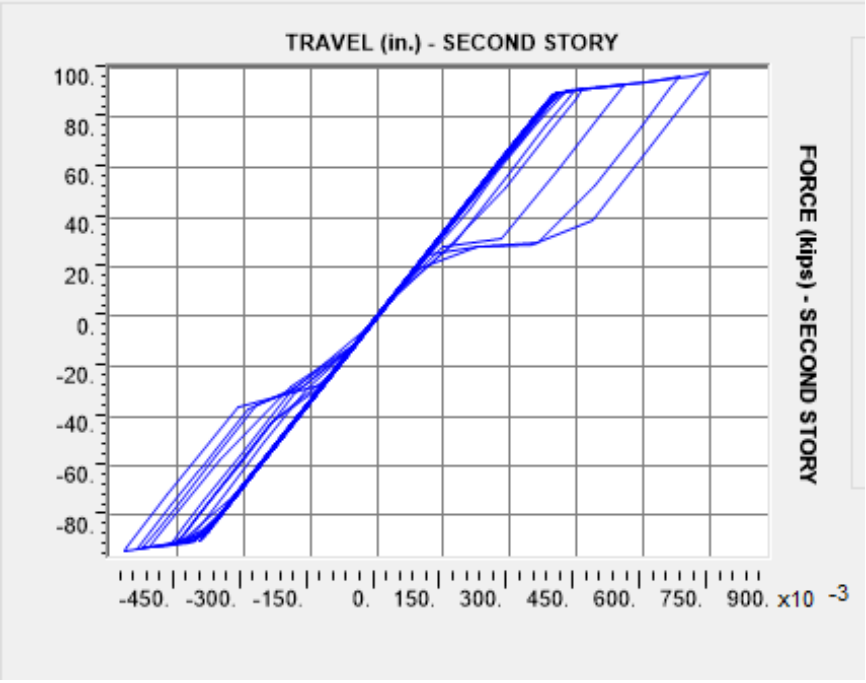

Figure 68: Force-Travel Three-Story Middle FSD El Centro - Case 2 (25%)

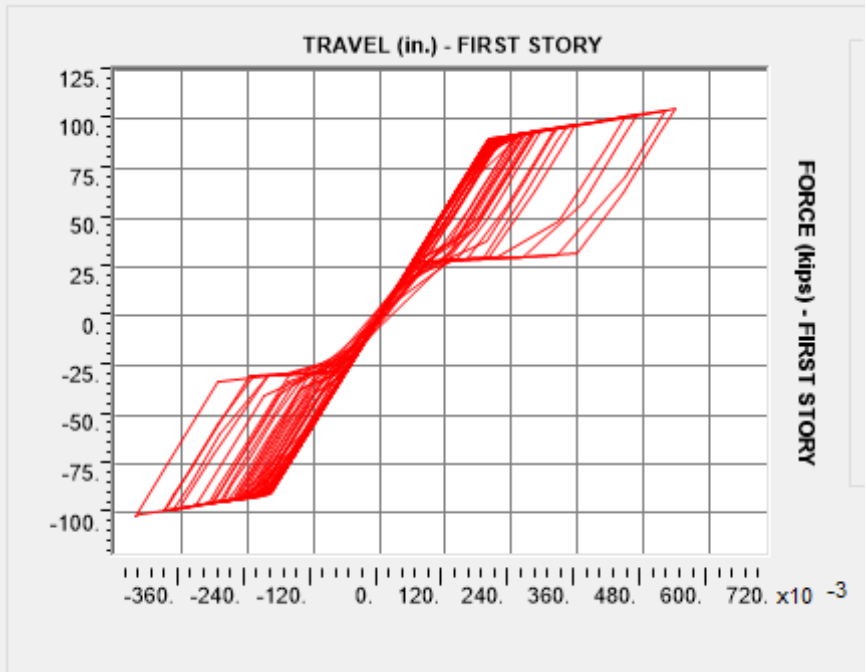

Figure 69: Force-Travel Three-Story Lower FSD El Centro - Case 3 (50%)

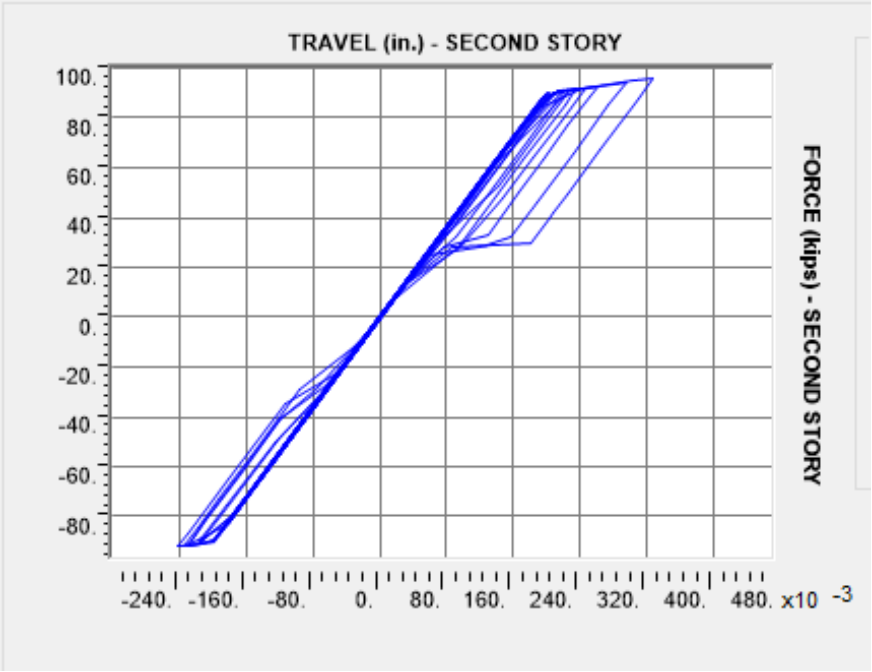

Figure 70: Force-Travel Three-Story Middle FSD El Centro – Case 3 (50%)

The force-travel diagrams evidence that both the FSDs in Case 2 and Case 3 are subject to the same force, but the FSDs in Case 3 displace approximately half as much, which reduces the responses to about 50% of each Case 2 response. Obviously, doubling the stiffness doesn't always result in half the displacement. For example, the 50% and 100% case reduce the undamped response by 68.20% and 76.55%, respectively. The force-travel diagrams for each FSD in the three-story shear frame subject to the El Centro, Kern County, Loma Prieta, and Northridge Earthquakes are displayed in Appendix Z. With regards to Appendix Z, a majority of the third story (upper) FSDs remain inactive. The upper FSDs remain primarily inactive simply due to the distribution of forces caused by the diagonal FSDs. For each stiffness case, the preloading force is approximately 81.1 kips, which is calculated by multiplying K_1 by S_0. In order for the third story FSD to activate, the external axial compressive force must exceed 81.1 kips. Considering the fact that the lateral forces are distributed to two additional FSDs, the third story FSD requires a relatively large earthquake to be activated. The maximum axial force imposed by each earthquake occurs when the stiffness of the FSDs are at a maximum (Case 4 – 100% story lateral stiffness). The maximum and minimum forces and displacements representative of the 100% FSD stiffness case are shown for the Kern County and Loma Prieta Earthquake below in Table 116.

Table 116: Max/Min Force-Travel Quantities Case 4 (Kern & Loma EQs)

		Loma Prieta 00		Kern County 111	
		U (in.)	**F (kips)**	**U (in.)**	**F (kips)**
First Story FSD	**Maximum**	0.8156	154.8	0.3457	112.3
	Minimum	-1.3160	-200.0	-0.2764	-106.1
Second Story FSD	**Maximum**	0.4623	122.9	0.1588	95.45
	Minimum	-1.0330	-174.5	-0.1630	-95.82
Third Story FSD	**Maximum**	0.1766	97.06	0.0668	60.28
	Minimum	-0.2820	-106.6	-0.0865	-78.15

As shown by Table 116, the maximum absolute value of the axial compressive force on the third story FSD is 78.15 kips for the Kern County Earthquake, which is too small to overcome the preloading force. Despite the fact that the Loma Prieta PGA is nearly 3.5 times the Kern County PGA, the maximum force in the third story FSD only increases by 36%, further showing that a large earthquake is necessary to activate the FSD at the third story. Next, the average displacement reduction and standard deviation are analyzed.

Table 117: FSD Average Percentage Reduction of Undamped Three-Story

		Undamped (ξ = 0)					
Case	**K_{story}**	**$U_{1,MEAN}$**	**$U_{2,MEAN}$**	**$U_{3,MEAN}$**	**SD_{U1}**	**SD_{U2}**	**SD_{U3}**
FSDs & ξ = 0	**10%**	40.58%	39.51%	40.73%	30.82%	31.25%	29.99%
	25%	52.25%	53.52%	56.41%	19.70%	18.66%	17.58%
	50%	74.39%	75.32%	76.85%	4.76%	3.51%	3.80%
	100%	77.70%	78.44%	80.22%	4.66%	4.42%	4.39%
FSDs & ξ = 1%	**10%**	47.06%	45.76%	47.65%	26.97%	25.79%	23.64%
	25%	55.55%	56.23%	58.81%	19.17%	18.15%	17.28%
	50%	75.23%	75.93%	77.60%	7.09%	5.28%	4.73%
	100%	78.27%	78.99%	80.71%	4.58%	4.57%	4.54%

Table 118: FSD Average Percentage Reduction of 5% Three-Story

		5% Damping (ξ = 0.05)					
Case	**K_{story}**	**$U_{1,MEAN}$**	**$U_{2,MEAN}$**	**$U_{3,MEAN}$**	**SD_{U1}**	**SD_{U2}**	**SD_{U3}**
FSDs & ξ = 0	**10%**	-24.44%	-19.03%	-18.00%	38.86%	38.08%	39.68%
	25%	-5.13%	3.58%	8.73%	32.84%	27.06%	27.36%
	50%	40.37%	44.70%	48.16%	10.75%	12.96%	12.18%
	100%	47.14%	51.31%	55.33%	13.71%	13.51%	12.71%
FSDs & ξ = 1%	**10%**	-10.29%	-7.19%	-4.65%	22.46%	21.47%	21.12%
	25%	3.33%	10.17%	14.76%	29.05%	23.66%	24.80%
	50%	42.19%	46.36%	50.11%	6.42%	7.87%	7.96%
	100%	48.64%	52.64%	56.61%	13.02%	13.09%	12.22%

The average reduction in the undamped maximum displacement response yields the best results at the 50% and 100% FSD stiffness values. The high stiffness cases reduce the results between 70% to 80% and maintain consistently small standard deviations. Lastly, at higher stiffnesses, the FSDs are more effective in decreasing the maximum displacement response than 5% modal damping.

7.8 Conclusion

Although the results are specific to shear frames with diagonally braced FSDs, conclusions and recommendations are drawn regarding the systems. First, models with FSDs should include some level of constant modal damping. As shown earlier, the FSDs converge much quicker if 1% modal damping is assumed. For practical applications, 1% modal damping is safe to assume for most structures simply based off of material properties. Secondly, the rings need to be designed to avoid the effects of negative lateral stiffness. Generally, one should avoid designing ring assemblies that are extremely stiff and have small

displacement properties or that are very flexible and have large displacement properties. The FSDs should be designed with target stiffness values that result in moderate displacements, in turn preventing unwanted effects such as negative stiffness. Lastly, at higher stiffness levels, the FSDs generally outperform 5% modal damping. As a whole, the FSDs with stiffnesses set to 50% of the story lateral stiffness yield the best results. In most cases, the largest jump in response reduction occurs at the 50% FSD stiffness case. Also, the 50% and 100% FSD stiffness cases produce comparable results with one another, despite the huge increase in stiffness. In the preliminary design phase of structures with FSDs, setting the loading stiffness equal to 50% of the lateral story stiffness is a great reference point. All in all, the FSDs prove to be efficient damping devices which can provide high levels of damping while maintaining a relatively simple and reliable design.

8. Conclusion

This thesis researched and compared seismic analysis methods and the response of systems with classical and nonclassical damping models. A wide range of systems were considered and the results and responses of each were evaluated. To generate the results, MATLAB code and SAP2000 models were developed. Throughout this thesis, the methods, theory, and results are thoroughly detailed and discussed. To conclude, the leading results, recommendations, and conclusions are reiterated and summarized herein.

First, it is recommended to always supplement the ELFP with dynamic seismic analysis methods. Generally, RSA yielded system responses 30% to 50% lower than the ELFP. The ELFP overestimated the system responses without exception, and the conservative nature of the results was more pronounced as the height of the frames increased.

Secondly, in most cases, RSA yielded very accurate results when using the SRSS and CQC methods to combine modal responses. For structures with irregular mass and stiffness distributions, both the SRSS and CQC methods underestimated the responses, but the CQC results were over four times as accurate as the SRSS results. Consequently, it is recommended to solely use the CQC method in RSA, because its application is not limited by irregular systems with closely spaced frequencies. Furthermore, the ABS method generated the most inaccurate and inconsistent results. Although inaccurate, the ABS method typically yielded better, less conservative results than the ELFP results.

Thirdly, both the AAM and LAM produced very accurate results that were generally within 1% of the analytical results. The difference in accuracy of the two methods was negligible, and in the analyses performed, neither method proved to be substantially more accurate.

Lastly, the FSDs were effective in decreasing the response of the shear frames. The best results occurred at stiffnesses equal to 50% of the story lateral stiffness, and typically reduced the peak response of the systems with 5% modal damping by 40% to 60%. Also, the inclusion of 1% damping with the FSDs benefited the responses of the systems by quickening the energy dissipation. When analyzing systems with FSDs, a low-level of modal damping should be included to better estimate the performance of the dampers. In some cases, the FSDs were not activated or negative lateral stiffness effects were exhibited in the ring assemblies, displaying the importance of proper design.

In conclusion, the analyses completed in this thesis focused on seismic analysis and its importance in structural engineering. Throughout this research, trends were developed, and suggestions for improvement were discussed. Each analysis in this study served a specific purpose. Numerous analyses were completed on diverse systems to display the tendencies of specific systems and to develop relationships between the dynamic response of the system, the accuracy of seismic analysis methods, and the system parameters and properties.

References

(ASCE 7-10) American Society of Civil Engineers. *Minimum Design Loads for Buildings and Other Structures*. ASCE, 2010.

(Chopra, 1995) Chopra, A. K. *Dynamics of Structures: Theory and Applications to Earthquake Engineering*. Englewood Cliffs, NJ: Prentice-Hall, 1995.

(Cobum et al., 1992) Cobum, A.W., Spence, R.J.S, & Pomonis, A. *Factors determining human casualty levels in earthquakes: Mortality prediction in building collapse.* Earthquake Engineering 10th World Conference, Balkema, Rotterdam, 1992.

(COSMOS) COSMOS. *COSMOS Strong-Motion Virtual Data Center*, www.strongmotion.org/.

(FEMA P-1050) *NEHRP (National Earthquake Hazards Reduction Program) Recommended Seismic Provisions for New Buildings and Other Structures*. FEMA, 2015.

(Goode & Annin, 2007) Goode, S.W., & Annin, S. *Differential Equations and Linear Alegbra*. Prentice Hall, 2007.

(Gurara, 2018) Gurara, G. *Nonlinear Dynamic Analysis of a Single-Story Frame with Friction Spring Damper in SAP2000*. Thesis. California Polytechnic State University, San Luis Obispo, 2018.

(Hill, 1995) Hill, K. E. *The Utility of Ring Springs in Seismic Isolation Systems*. Ph.D Thesis. Department of Mechanical Engineering, University of Canterbury; 1995.

(Hu et al., 2019) Hu, S., Wang, W., & Qu, B. Seismic Evaluation of Low-Rise Steel Building Frames with Self-Centering Energy-Absorbing Rigid Cores Designed Using a Force-Based Approach. *Engineering Structures*, vol. 204, 2019.

(Hughes, 2012) Hughes, T. J. R. *The Finite Element Method Linear Static and Dynamic Finite Element Analysis*. Dover Publications, 2012.

(Kasper & Hall, 2018) Kasper, E.P. & Hall, G.J. *An Introduction to Applied Structural Dynamics.* Second Edition, 2018.

(Kelly & Chambers, 2000) Kelly, T.E. & Chambers, J.D. *Analysis Procedures for Performance Based Design.* 12th World Conference on Earthquake Engineering, New Zealand Society for Earthquake Engineering, Upper Hutt, New Zealand, 2000.

(Li et al., 2006) Li. Y., Wu, B., & Ou, J. Stability of average acceleration method for structures with nonlinear damping. *Earthquake Engineering and Engineering Vibration,* 2006.

(Maghdid, 2002) Maghdid, D. *Stability and accuracy of Newmark's method.* Thesis. 2002. doi: 10.13140.

(MATLAB) The MathWorks, Inc., *MATLAB 2018b*. Natick, Massachusetts, United States, 2018.

(Nichols & Beavers, 2008) Nichols, J. M., & Beavers, J.E. World Earthquake Fatalities from the Past: Implications for the Present and Future. *Natural Hazards Review*, vol. 9, no. 4, 2008.

(PEER) Welcome to the PEER Ground Motion Database. *PEER Ground Motion Database - PEER Center*, ngawest2.berkeley.edu/.

(RINGFEDER®) Ringfeder® Power Transmission GMBH. (2019). *2019 Damping Technology Catalog*. Germany, 2019.

(SAP2000) CSI. *SAP2000: Integrated Structural Analysis & Design Software*. Computer and Structures, Inc., 2018.

(Shrestha, 2019) Shrestha, S. *A Comparative Study of Equivalent Lateral Force Method and Response Spectrum Analysis in Seismic Design of Structural Frames*. Thesis. Southern Illinois University, Carbondale, 2019.

(Statista Research Department, 2016) Statista Research Department. Deaths Due to Earthquakes Worldwide 2000-2015. *Statista*, 30 Sept. 2016, www.statista.com/statistics/263108/global-death-toll-due-to-earthquakes-since-2000/.

(USGS) U.S. Geological Survey. *USGS.gov | Science for a Changing World*, www.usgs.gov/.

(Wilson et al., 1981) Wilson, E. L., Kiureghian, A.D., & Bayo, E.P. A Replacement for the SRSS Method in Seismic Analysis. *Earthquake Engineering & Structural Dynamics*, vol. 9, no. 2, 1981.

Appendices

Appendix A: Site Parameters – San Luis Obispo, CA, 93407

OSHPD

1 Grand Ave, San Luis Obispo, CA 93410, USA

Latitude, Longitude: 35.3048767, -120.6572655

Date	5/9/2020, 4:02:04 AM
Design Code Reference Document	ASCE7-10
Risk Category	II
Site Class	D - Stiff Soil

Type	Value	Description
S_S	1.121	MCE_R ground motion. (for 0.2 second period)
S_1	0.427	MCE_R ground motion. (for 1.0s period)
S_{MS}	1.179	Site-modified spectral acceleration value
S_{M1}	0.672	Site-modified spectral acceleration value
S_{DS}	0.786	Numeric seismic design value at 0.2 second SA
S_{D1}	0.448	Numeric seismic design value at 1.0 second SA

Type	Value	Description
SDC	D	Seismic design category
F_a	1.052	Site amplification factor at 0.2 second
F_v	1.573	Site amplification factor at 1.0 second
PGA	0.442	MCE_G peak ground acceleration
F_{PGA}	1.058	Site amplification factor at PGA
PGA_M	0.468	Site modified peak ground acceleration
T_L	8	Long-period transition period in seconds
SsRT	1.121	Probabilistic risk-targeted ground motion. (0.2 second)
SsUH	1.167	Factored uniform-hazard (2% probability of exceedance in 50 years) spectral acceleration
SsD	1.579	Factored deterministic acceleration value. (0.2 second)
S1RT	0.427	Probabilistic risk-targeted ground motion. (1.0 second)
S1UH	0.436	Factored uniform-hazard (2% probability of exceedance in 50 years) spectral acceleration.
S1D	0.601	Factored deterministic acceleration value. (1.0 second)
PGAd	0.599	Factored deterministic acceleration value. (Peak Ground Acceleration)
C_{RS}	0.961	Mapped value of the risk coefficient at short periods
C_{R1}	0.981	Mapped value of the risk coefficient at a period of 1 s

Appendix B: Stiffness Coefficient Derivation – Beam Theory

1. Model a beam element and number the degrees of freedom at the nodes

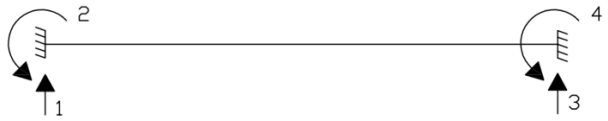

Step 2

2. Solve for element forces at each DOF caused by the unit displacement and make a cut in the beam element to derive the equation for the moment with respect to the distance along the length of the beam.

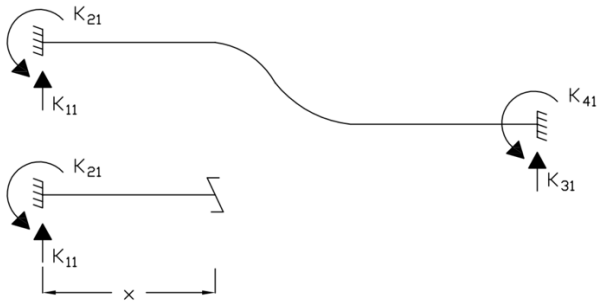

$$M = -K_{21} + K_{11}x$$

3. Plug the moment equation into the linear beam theory equation.

$$\frac{d^2u}{dx^2} = \frac{-K_{21} + K_{11}x}{EI}$$

4. Integrate the second order differential equation given by linear beam theory to obtain a function for the rotations of the beam element.

$$\int \frac{d^2u}{dx^2}dx = \frac{du}{dx} = \theta$$

$$\theta = \frac{x}{EI}\left(-K_{21} + \frac{1}{2}K_{11}x^2\right) + C_1$$

5. Integrate the function for the rotations of the beam element to obtain a function for the transverse displacement of the beam element.

$$u = \int \theta dx = \int \frac{du}{dx} = \int \frac{x}{EI}(-K_{21} + \frac{1}{2}K_{11}x^2 + C_1)dx$$

$$u = \frac{x^2}{EI}\left(-\frac{1}{2}K_{21} + \frac{1}{6}K_{11}x\right) + C_1x + C_2$$

6. Determine boundary conditions for the beam element.

$$u_1(x = 0) = 1$$

$$\phi_1(x = 0) = 0$$

7. Plug in boundary conditions to solve for C_1 and C_2.

$$\theta_1 = 0 = \frac{(0)}{EI}\left(-K_{21} + \frac{1}{2}K_{11}(0)\right) + C_1$$

$$C_1 = 0$$

$$u_1 = 1 = \frac{(0)^2}{EI}\left(-\frac{1}{2}K_{21} + \frac{1}{6}K_{11}(0)\right) + (0)x + C_2$$

$$C_2 = 1$$

8. Plug in the C_1 and C_2 values into the deflection and rotation equations for the beam element.

$$\phi_1 = \frac{x}{EI}(-K_{21} + \frac{1}{2}K_{11}x)$$

$$u_1 = \frac{x^2}{EI}\left(-\frac{1}{2}K_{21} + \frac{1}{6}K_{11}x\right) + 1$$

9. Use the rotation and deflection equations to substitute and solve for K_{11} and K_{21}.

$$K_{11} = \frac{12EI}{x^3} = \frac{12EI}{L^3}$$

$$K_{21} = \frac{6EI}{x^2} = \frac{6EI}{L^2}$$

10. Use equilibrium to solve for the remaining stiffness coefficients K_{31} and K_{41}.

$$K_{21} + K_{41} = 0$$

$$K_{41} = -K_{21}$$

$$K_{41} = -\frac{6EI}{L^2}$$

$$K_{11} + K_{31} = 0$$

$$K_{31} = -K_{11}$$

$$K_{31} = -\frac{12EI}{L^3}$$

11. Repeat the process of applying unit displacements at each degree of freedom and solve for the element forces to assemble the 4x4 stiffness matrix for the beam element.

Appendix C: Stiffness Coefficient Derivation – Shape Functions

1. Model a beam element and establish the DOFs at each node.

2. Establish a transverse displacement function and rotation function for a beam element. Since a beam element has 4 DOFs, a cubic function is used.

$$v(x) = C_0 + C_1x + C_2x^2 + C_3x^3$$

$$\phi(x) = v'(x) = C_1 + 2C_2x + 3C_3x^2$$

3. Establish boundary conditions to determine the unknown C values.

$$1.\, v(x = 0) = v_1$$

$$2.\, \phi(x = 0) = \phi_1$$

$$3.\, v(x = L) = v_2$$

$$4.\, \phi(x = L) = \phi_2$$

4. Plug the boundary conditions into the transverse displacement and rotation functions shown in Step 2.

$$1.\, v_1 = C_0 + C_1(0) + C_2(0)^2 + C_3(0)^3$$

$$v_1 = C_0$$

$$2.\, \phi_1 = C_1 + 2C_2(0) + 3C_3(0)^2$$

$$\phi_1 = C_1$$

$$3.\, v_2 = v_1 + \phi_1(L) + C_2(L)^2 + C_3(L)^3$$

$$C_2L^2 + C_3L^3 = v_2 - v_1 - \phi_1L$$

$$4.\ \phi_2 = \phi_1 + 2C_2(L) + 3C_3(L)^2$$

$$2C_2L + 3C_3L^2 = \phi_2 - \phi_1$$

5. Put the equations for v_1 and v_2 into matrix form.

$$\begin{bmatrix} L^2 & L^3 \\ 2L & 3L^2 \end{bmatrix}\begin{bmatrix} C_2 \\ C_3 \end{bmatrix} = \begin{bmatrix} v_2 - v_1 - \phi_1 L \\ \phi_2 - \phi_1 \end{bmatrix}$$

6. Rearrange the matrices to solve for the unknowns C_2 and C_3.

$$\begin{bmatrix} \frac{3}{L^2} & -\frac{1}{L} \\ -\frac{2}{L^3} & \frac{1}{L^2} \end{bmatrix}\begin{bmatrix} v_2 - v_1 - \phi_1 L \\ \phi_2 - \phi_1 \end{bmatrix} = \begin{bmatrix} C_2 \\ C_3 \end{bmatrix}$$

$$\begin{bmatrix} \frac{3v_2}{L^2} - \frac{3v_1}{L^2} - \frac{2\phi_1}{L} - \frac{\phi_2}{L} \\ -\frac{2v_2}{L^3} + \frac{2v_1}{L^3} + \frac{\phi_1}{L^2} + \frac{\phi_2}{L^2} \end{bmatrix} = \begin{bmatrix} C_2 \\ C_3 \end{bmatrix}$$

7. Plug the C values into the cubic displacement function and rearrange to obtain the shape functions which are Hermitian Polynomials for a beam element.

$$v(x) = v_1\left(1 - \frac{3x^2}{L^2} + \frac{2x^3}{L^3}\right) + \phi_1\left(x - \frac{2x^2}{L} + \frac{x^3}{L^2}\right) + v_2\left(\frac{3x^2}{L^2} - \frac{2x^3}{L^3}\right) + \phi_2\left(\frac{x^3}{L^2} + \frac{x^2}{L}\right)$$

$$N_1(x) = 1 - \frac{3x^2}{L^2} + \frac{2x^3}{L^3}$$

$$N_2(x) = x - \frac{2x^2}{L} + \frac{x^3}{L^2}$$

$$N_3(x) = \frac{3x^2}{L^2} - \frac{2x^3}{L^3}$$

$$N_4(x) = \frac{x^3}{L^2} + \frac{x^2}{L}$$

8. Take the second derivative of each shape function.

$$\frac{d^2N_1}{dx^2} = \frac{6}{L^2} + \frac{12x}{L^3}$$

$$\frac{d^2N_2}{dx^2} = \frac{6x}{L^2} - \frac{4}{L}$$

$$\frac{d^2N_3}{dx^2} = \frac{6}{L^2} - \frac{12x}{L^3}$$

$$\frac{d^2N_4}{dx^2} = \frac{6x}{L^2} + \frac{2}{L}$$

9. Determine each stiffness coefficient using the equation shown below.

$$K_{AB} = \int_0^L \frac{d^2N_a(x)}{dx^2} EI \frac{d^2N_b(x)}{dx^2} dx$$

10. Assemble the stiffness matrix for a beam element.

Appendix D: Matrix Structural Analysis – One Story Shear Frame

1. Establish node, element, and DOF numbers and map the DOFs in the local and global domain with respect to the element number. As previously mentioned, by definition, a shear frame would have a single lateral DOF at each story level, but to exemplify the process of matrix structural analysis, 3 DOFs at each node are maintained.

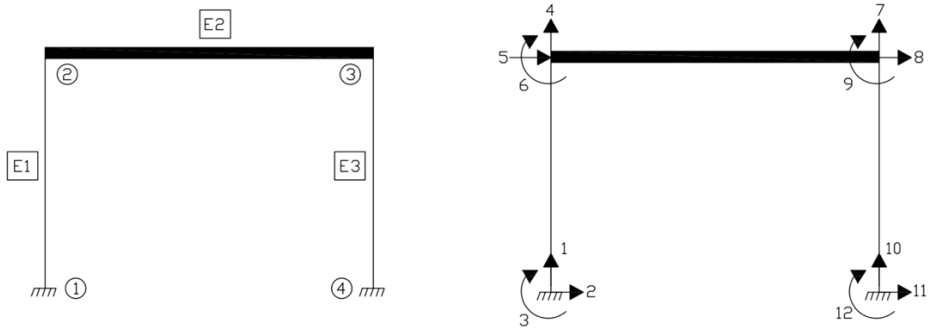

Element	Local DOF	Global DOF
1	1	1
	2	2
	3	3
	4	4
	5	5
	6	6
2	1	4
	2	5
	3	6
	4	7
	5	8
	6	9
3	1	7
	2	8
	3	9
	4	10
	5	11
	6	12

2. Determine the stiffness coefficients and assemble the local element stiffness matrix for each element using Equation 2.8.

$$k_e^1 = k_e^3 = \begin{bmatrix} 6590.9 & 0 & 0 & -6590.9 & 0 & 0 \\ 0 & 45.4 & 2995.9 & 0 & -45.4 & 2995.9 \\ 0 & 2995.9 & 263636.4 & 0 & -2995.9 & 131818.2 \\ -6590.9 & 0 & 0 & 6590.9 & 0 & 0 \\ 0 & -45.4 & -2995.9 & 0 & 45.4 & -2995.9 \\ 0 & 2995.9 & 131818.2 & 0 & -2995.9 & 263636.4 \end{bmatrix}$$

$$k_e^2 = \begin{bmatrix} 4833.3 & 0 & 0 & -4833.3 & 0 & 0 \\ 0 & 17.9 & 1611.1 & 0 & -17.9 & 1611.1 \\ 0 & 2995.9 & 193333.3 & 0 & -1611.1 & 96666.6 \\ -4833.3 & 0 & 0 & 4833.3 & 0 & 0 \\ 0 & -17.9 & -1611.11 & 0 & 17.9 & -1611.1 \\ 0 & 1611.1 & 96666.6 & 0 & -1611.1 & 193333.3 \end{bmatrix}$$

3. Form the transformation matrix for each element based off of the element's orientation with respect to the horizontal using Equation 2.10.

$$B_e^1 = B_e^3 = \begin{bmatrix} 0 & 1 & 0 & 0 & 0 & 0 \\ -1 & 0 & 0 & 0 & 0 & 0 \\ 0 & 0 & 1 & 0 & 0 & 0 \\ 0 & 0 & 0 & 0 & -1 & 0 \\ 0 & 0 & 0 & 1 & 0 & 0 \\ 0 & 0 & 0 & 0 & 0 & 1 \end{bmatrix}$$

$$B_e^2 = \begin{bmatrix} 1 & 0 & 0 & 0 & 0 & 0 \\ 0 & 1 & 0 & 0 & 0 & 0 \\ 0 & 0 & 1 & 0 & 0 & 0 \\ 0 & 0 & 0 & 1 & 0 & 0 \\ 0 & 0 & 0 & 0 & 1 & 0 \\ 0 & 0 & 0 & 0 & 0 & 1 \end{bmatrix}$$

4. Use Equation 2.9 to transform each element stiffness matrix from local to global coordinates.
5. Sum the global element stiffness matrixes to obtain the 12x12 global stiffness matrix of the one-story shear frame.

6. Assemble the global nodal force vector and unknown displacement vector.

$$F = \begin{Bmatrix} 0 \\ 0 \\ 0 \\ 0 \\ 0 \\ 0 \\ 0 \\ 14 \\ 0 \\ 0 \\ 0 \\ 0 \end{Bmatrix} \qquad u = \begin{Bmatrix} u_1 \\ u_2 \\ \theta_1 \\ u_4 \\ u_5 \\ \theta_2 \\ u_7 \\ u_8 \\ \theta_3 \\ u_{10} \\ u_{11} \\ \theta_4 \end{Bmatrix}$$

7. Use Equation 2.6 to find the unknown displacement values.

$$\{F\} = [K]\{u\}$$

$$[K]^{-1}\{F\} = \{u\}$$

$$u = \begin{Bmatrix} 0 \\ 0 \\ 0 \\ 0 \\ 0.1542" \\ 0 \\ 0 \\ 0.1542" \\ 0 \\ 0 \\ 0 \\ 0 \end{Bmatrix}$$

8. From the unknown displacement vector, pull out the lateral displacement value of the one-story shear frame at the roof level.

$$u_5 = u_8 = 0.1542"$$

Appendix E: Accelerograms

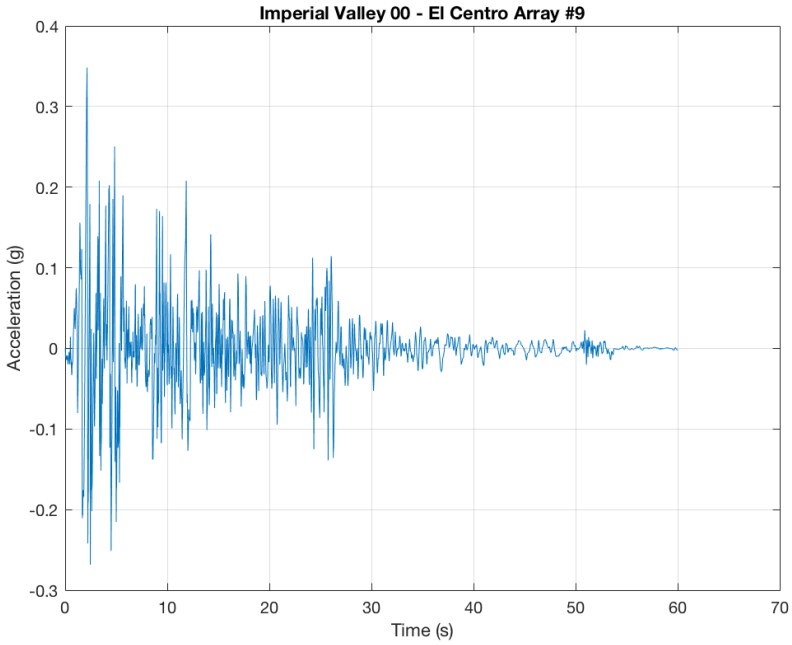

Figure 71: Imperial Valley EQ 00 (PGA = 0.3484g)

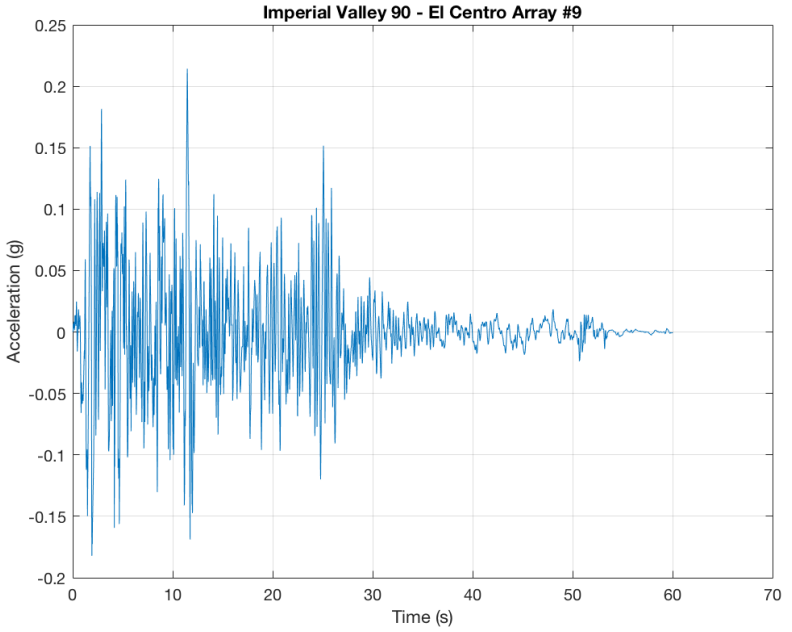

Figure 72: Imperial Valley EQ 90 (PGA = 0.2142g)

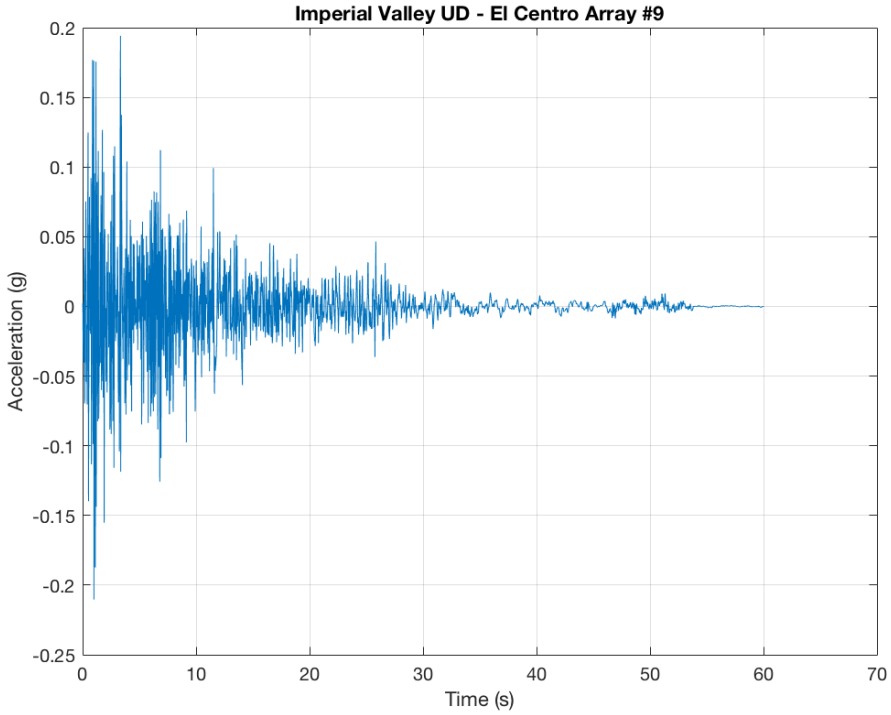

Figure 73: Imperial Valley EQ UD (PGA = -0.2104g)

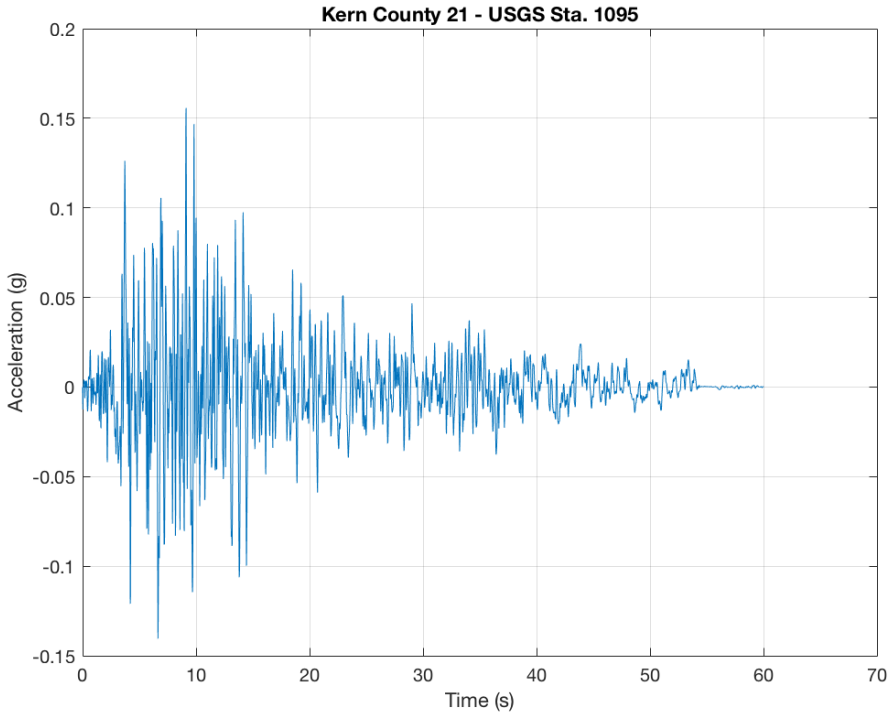

Figure 74: Kern County EQ 21 (PGA = 0.1557g)

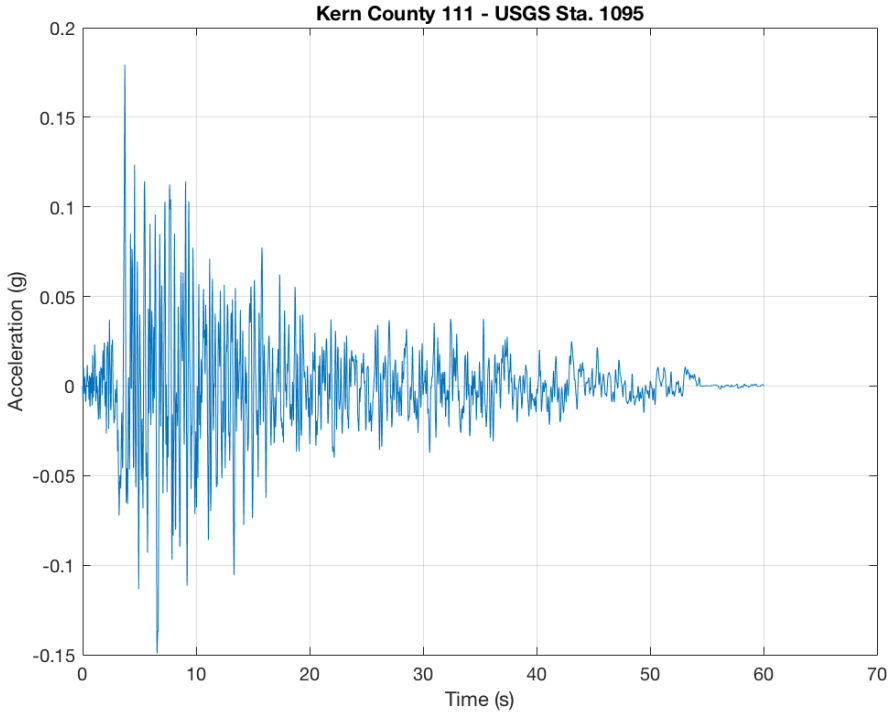

Figure 75: Kern County EQ 111 (PGA = 0.1794g)

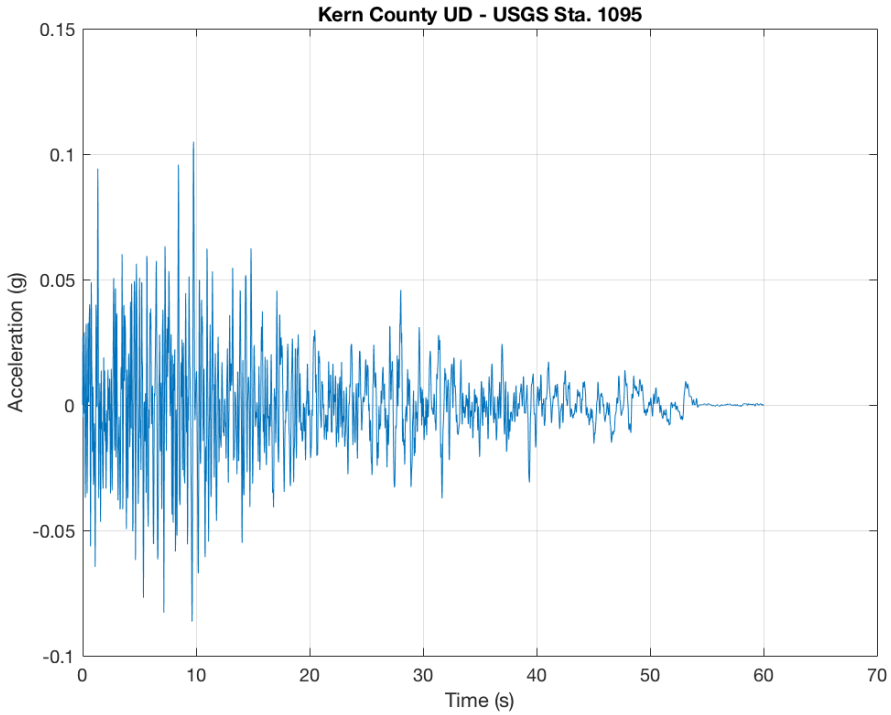

Figure 76: Kern County EQ UD (PGA = 0.1049g)

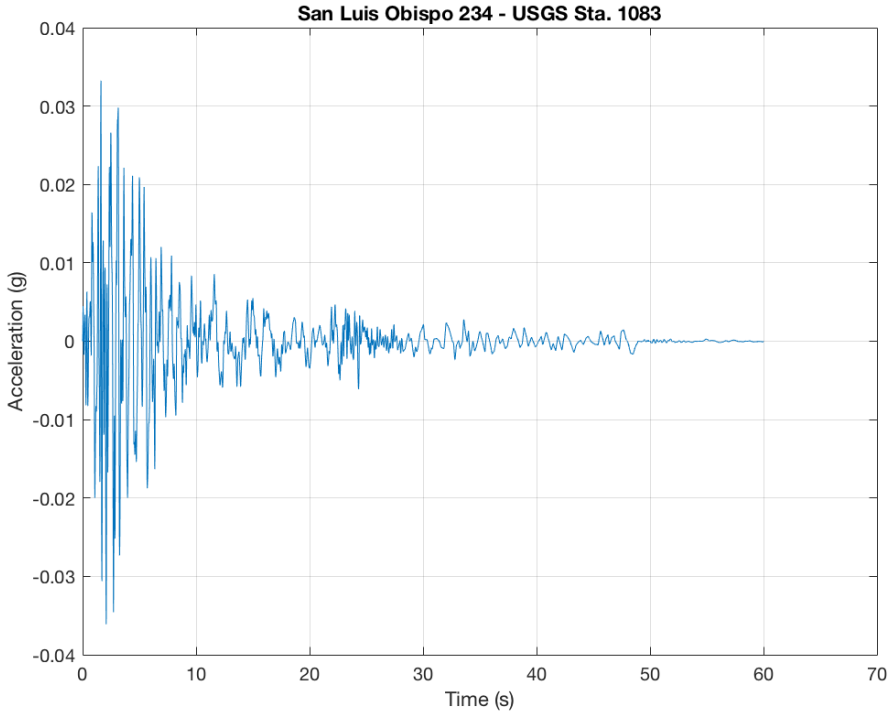

Figure 77: San Luis Obispo EQ 234 (PGA = -0.0361g)

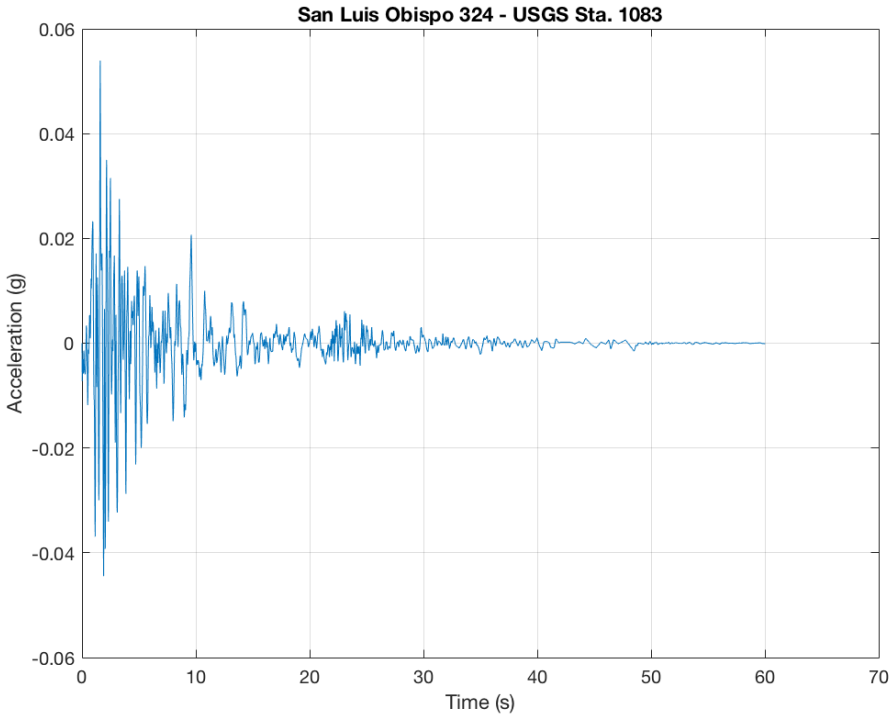

Figure 78: San Luis Obispo EQ 324 (PGA = 0.05394g)

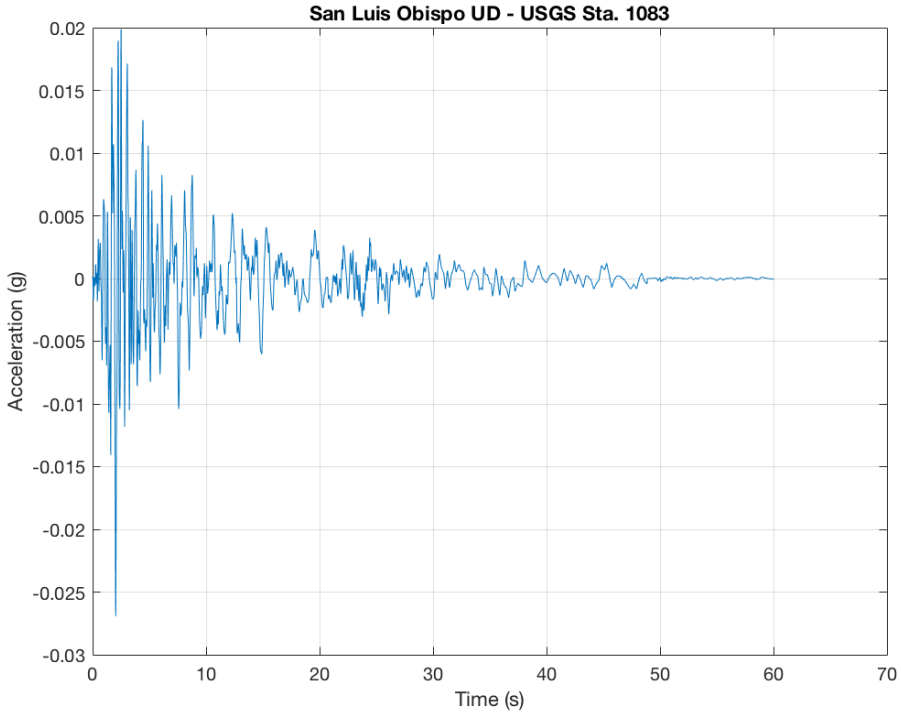

Figure 79: San Luis Obispo EQ UD (PGA = -0.02692g)

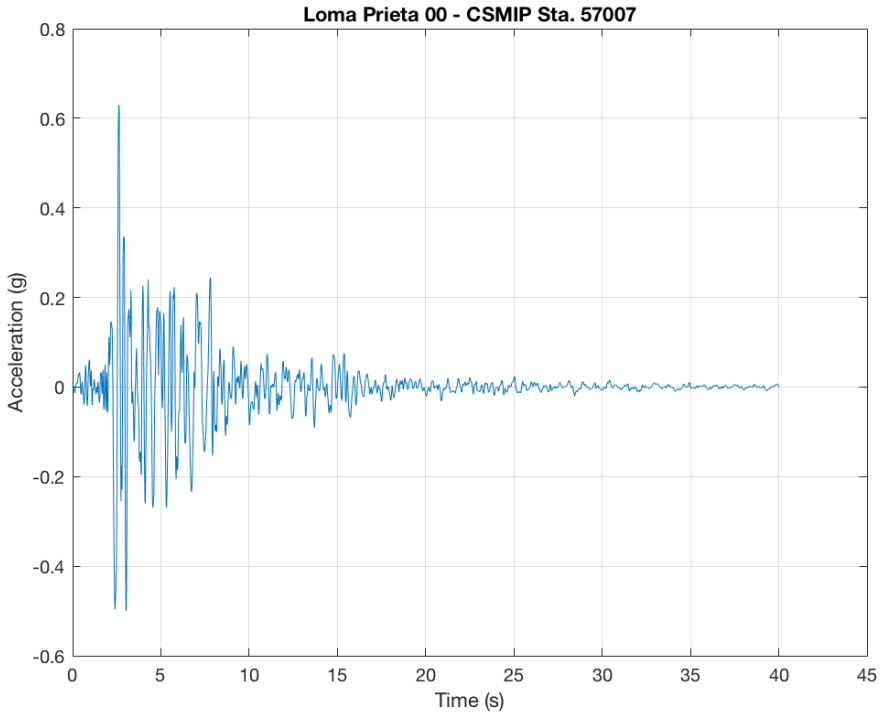

Figure 80: Loma Prieta EQ 00 (PGA = 0.6216g)

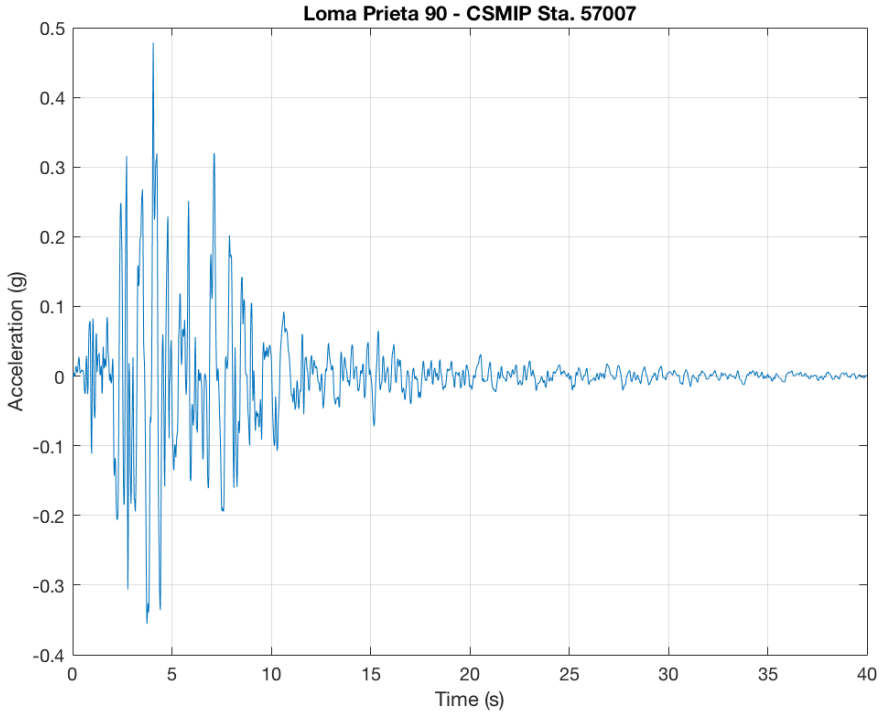

Figure 81: Loma Prieta EQ 90 (PGA = 0.4786g)

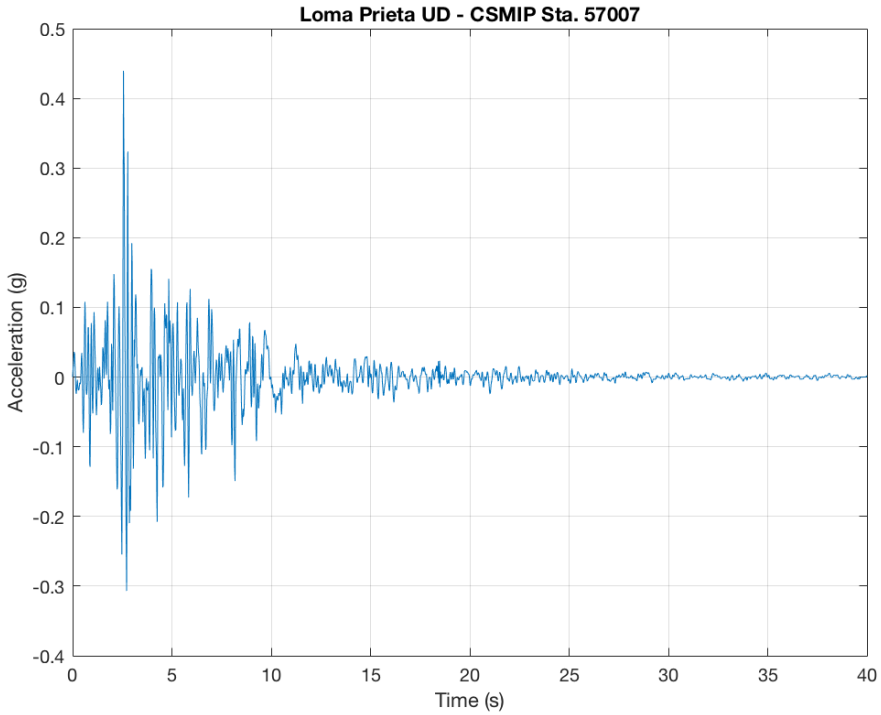

Figure 82: Loma Prieta EQ UD (PGA = 0.4396g)

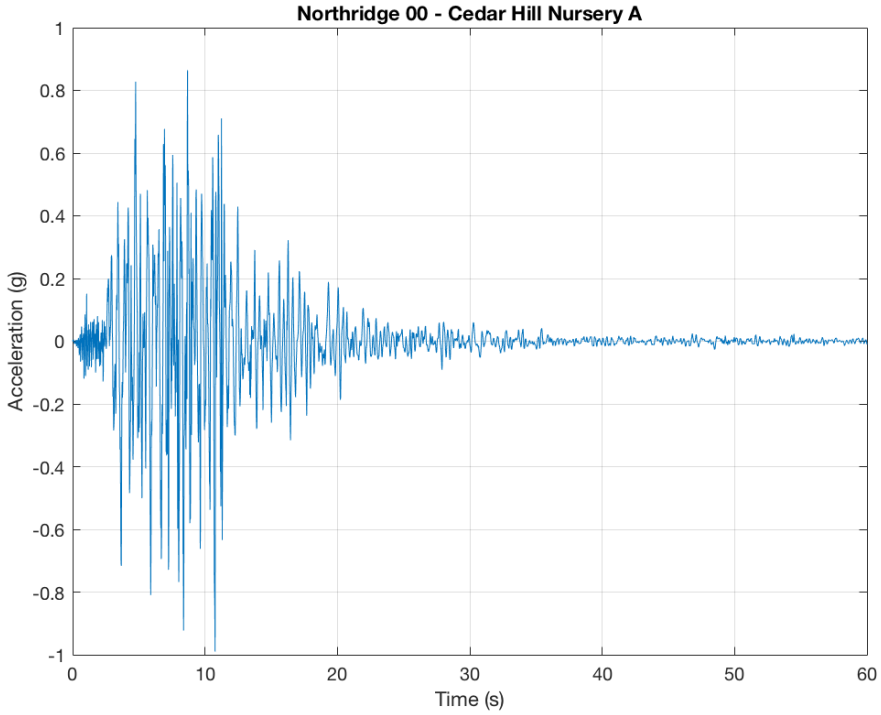

Figure 83: Northridge EQ 00 – Cedar Hill Nursery A (PGA = -0.9899g)

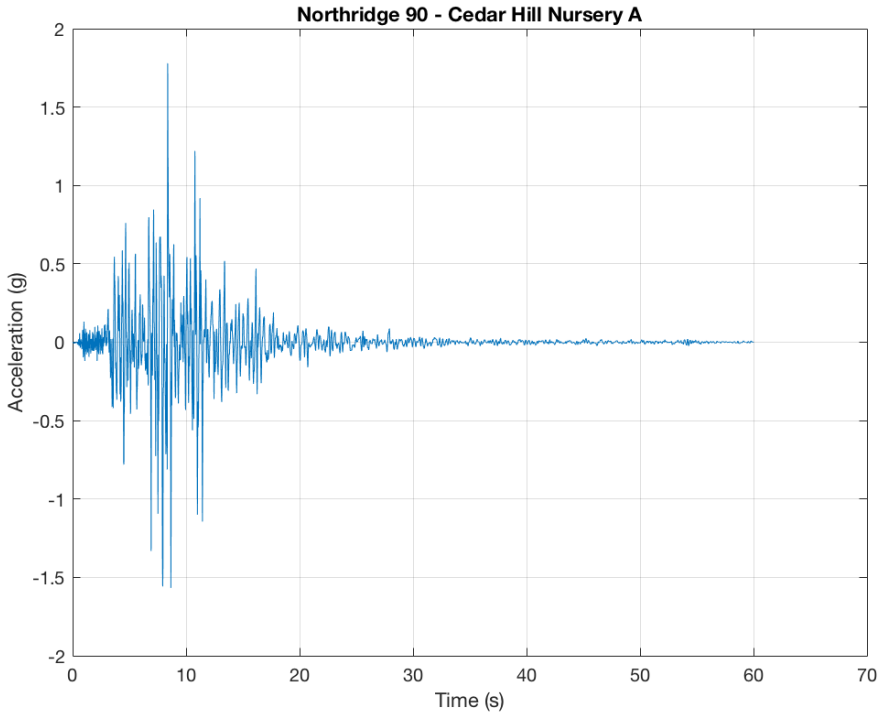

Figure 84: Northridge EQ 90 – Cedar Hill Nursery A (PGA = 1.779g)

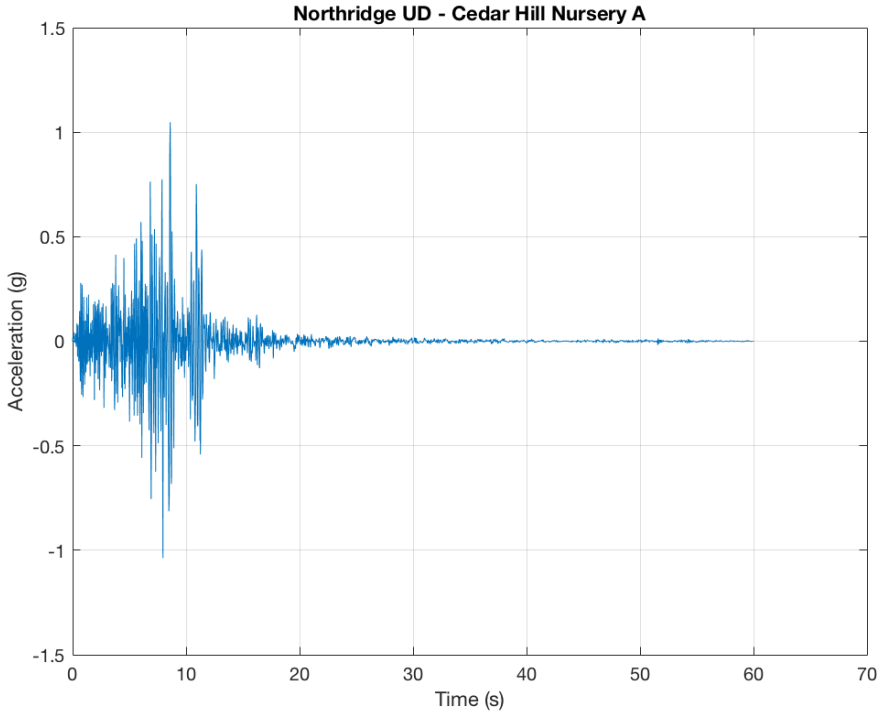

Figure 85: Northridge EQ UD – Cedar Hill Nursery A (PGA = 1.048g)

Appendix F: Displacement Time Histories – 5% Damping

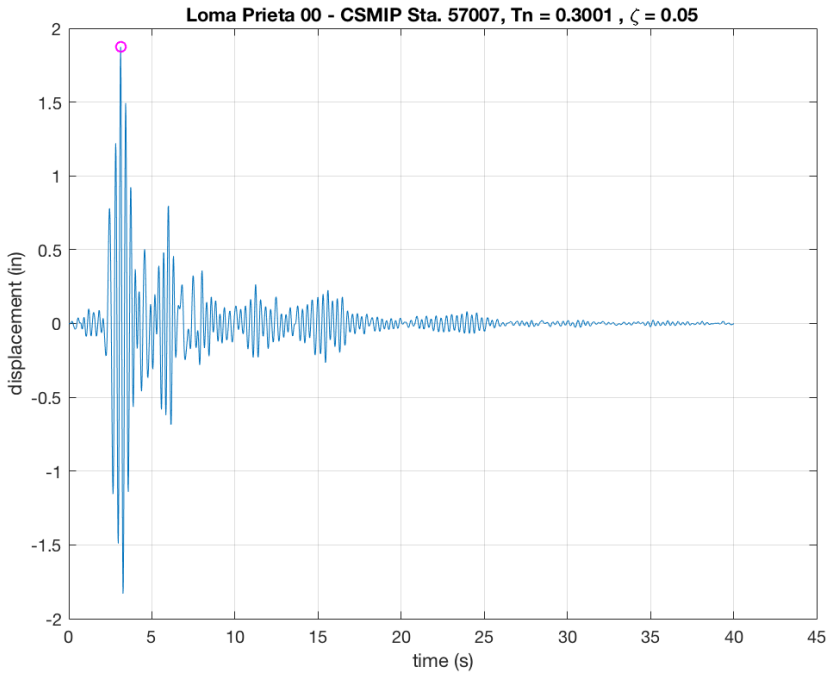

Figure 86: Loma 00 (T_n = 0.3001s) Displacement Time History

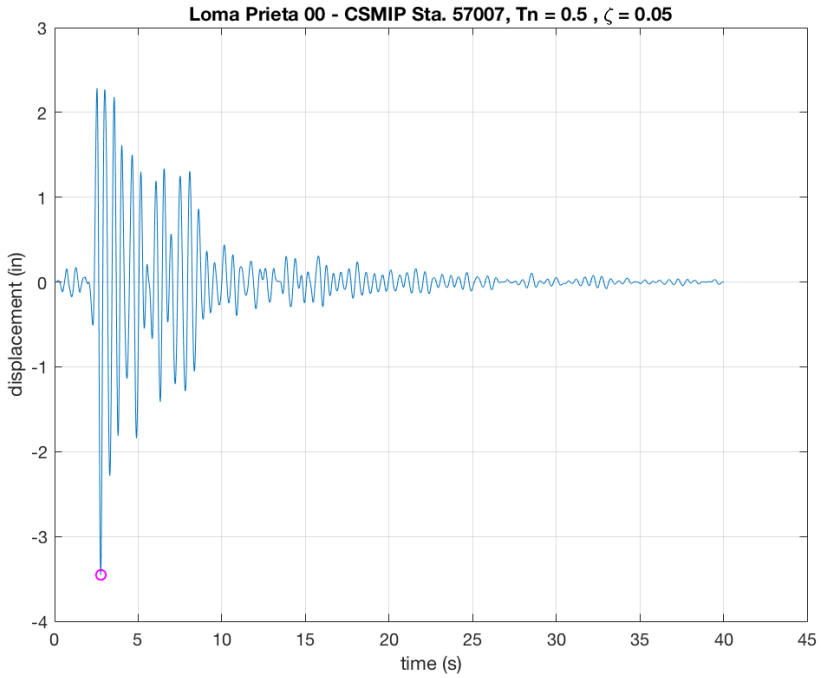

Figure 87: Loma 00 (T_n = 0.50s) Displacement Time History

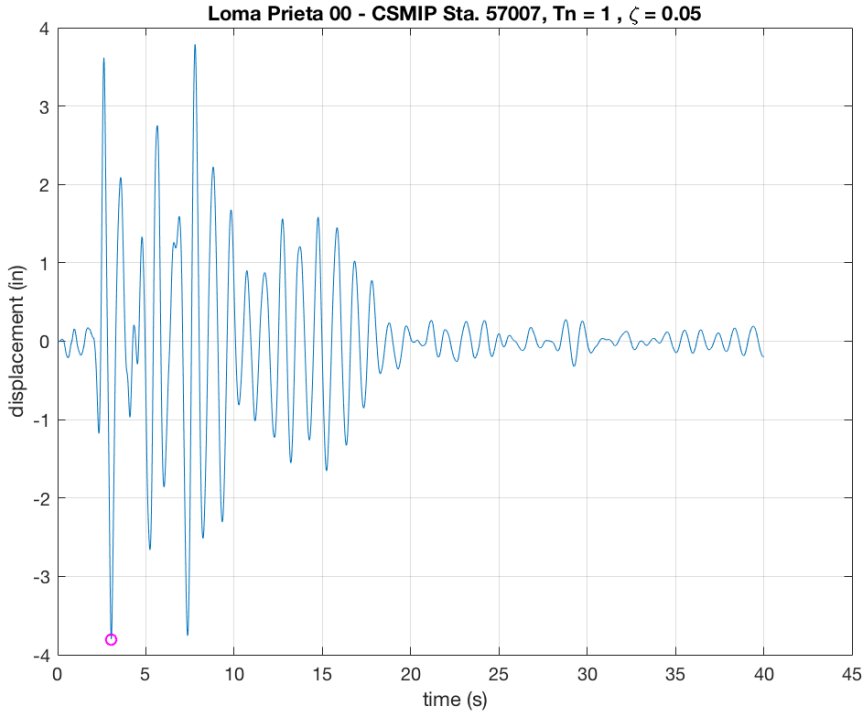

Figure 88: Loma 00 (T_n = 1.00s) Displacement Time History

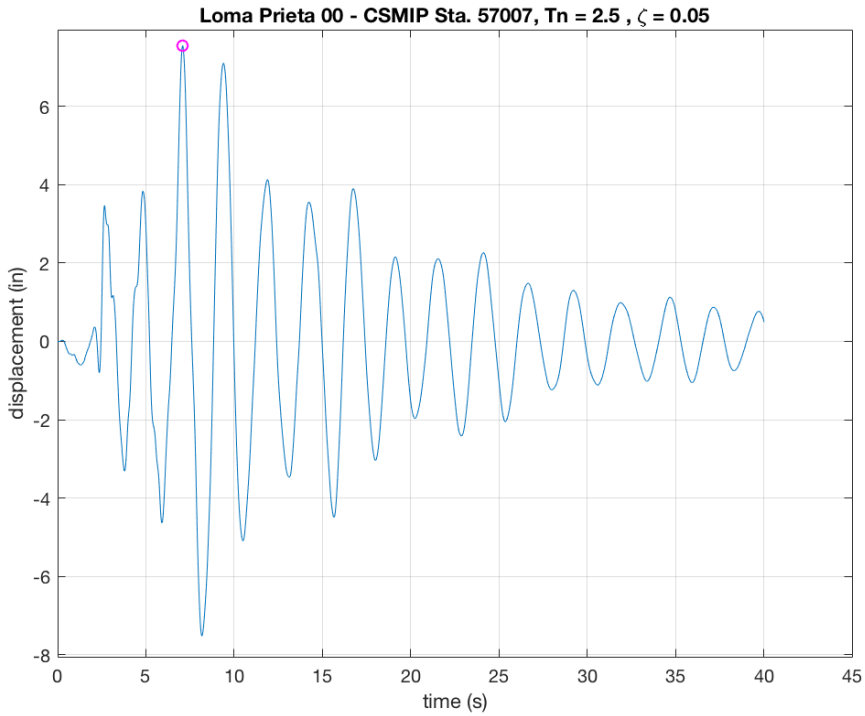

Figure 89: Loma 00 (T_n = 2.50s) Displacement Time History

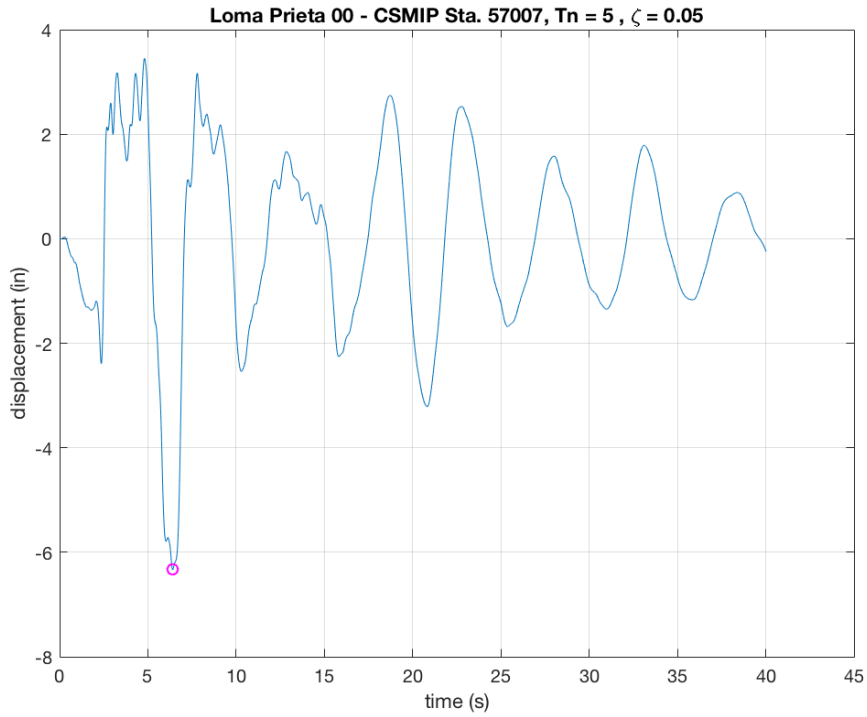

Figure 90: Loma 00 (T_n = 5.00s) Displacement Time History

Appendix G: Displacement Time Histories – T_n = 0.30s

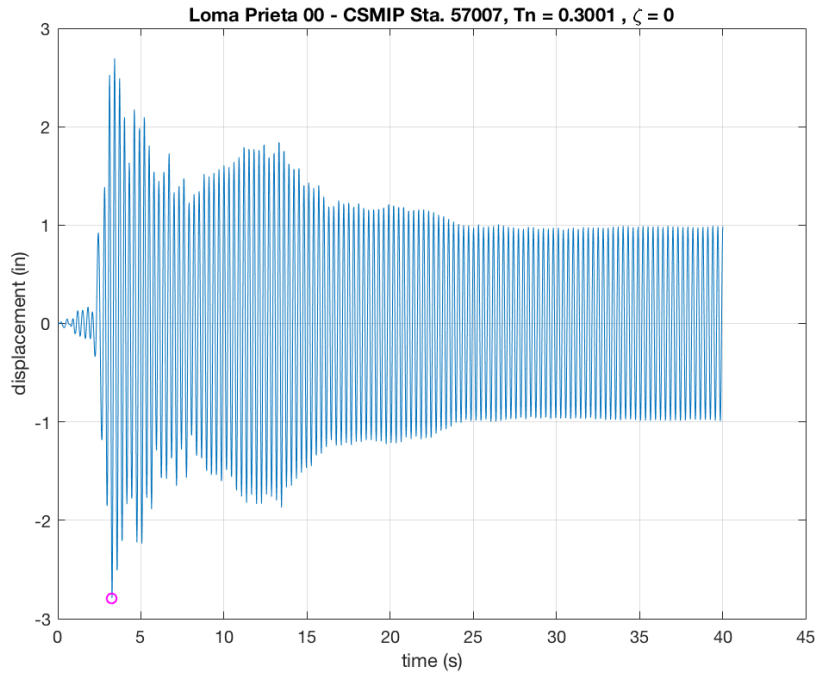

Figure 91: Loma 00 ($\xi = 0.00$) Displacement Time History

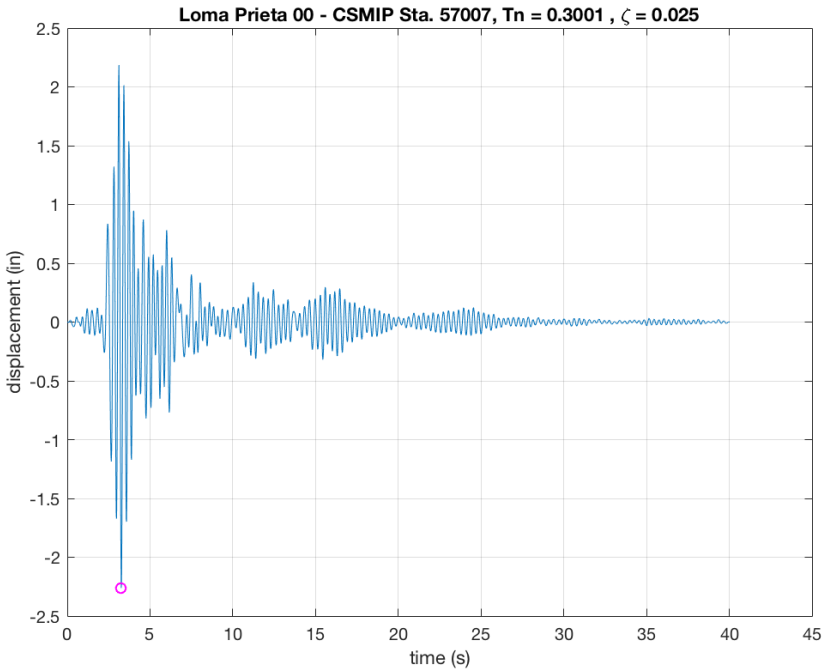

Figure 92: Loma 00 ($\xi = 0.025$) Displacement Time History

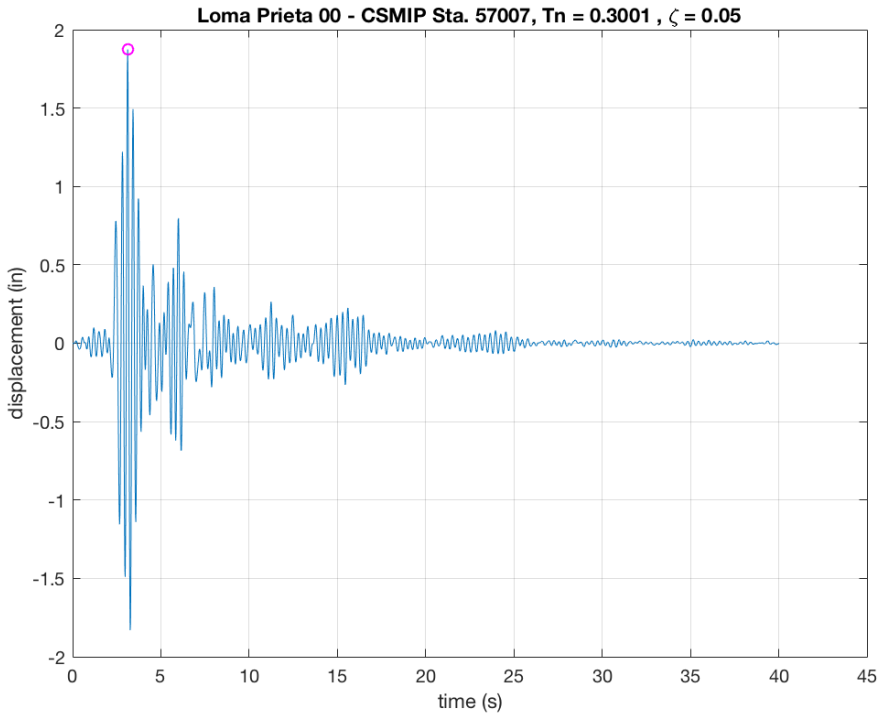

Figure 93: Loma 00 ($\xi = 0.050$) Displacement Time History

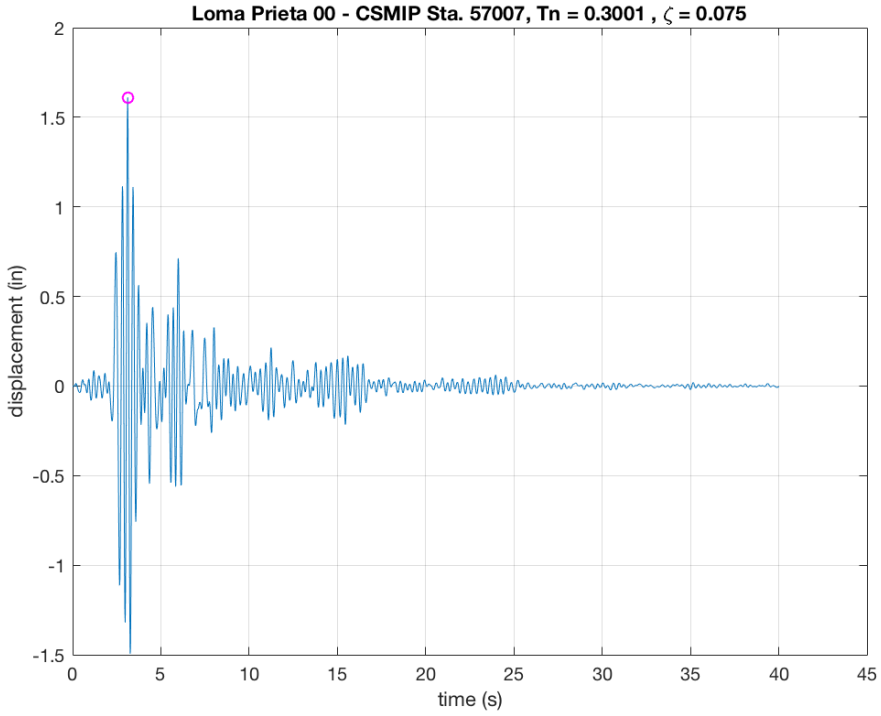

Figure 94: Loma 00 ($\xi = 0.075$) Displacement Time History

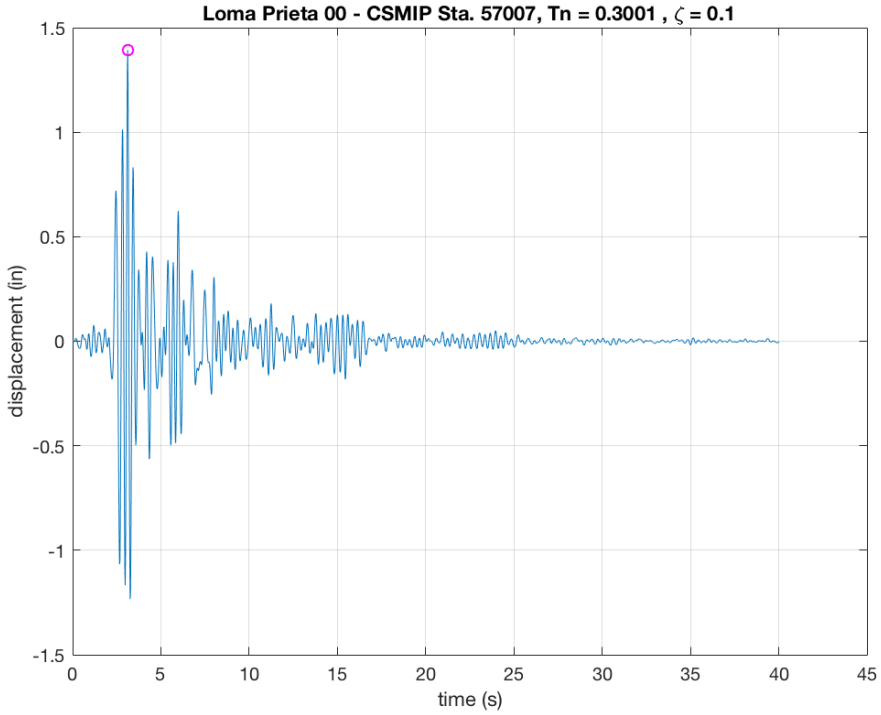

Figure 95: Loma 00 ($\xi = 0.100$) Displacement Time History

Appendix H: Average Acceleration Method Time Histories

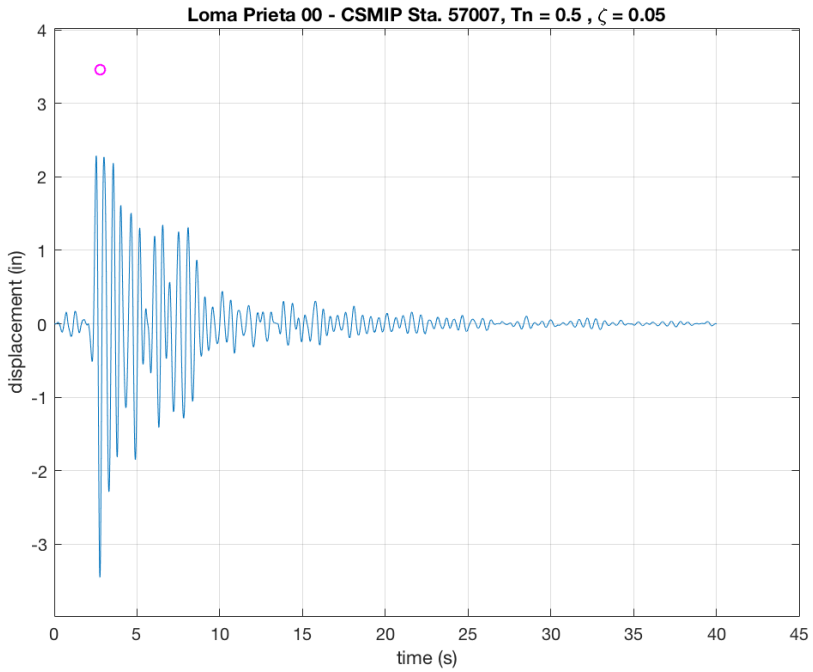

Figure 96: Loma 00 (T_n = 0.50s) Average Acceleration Method

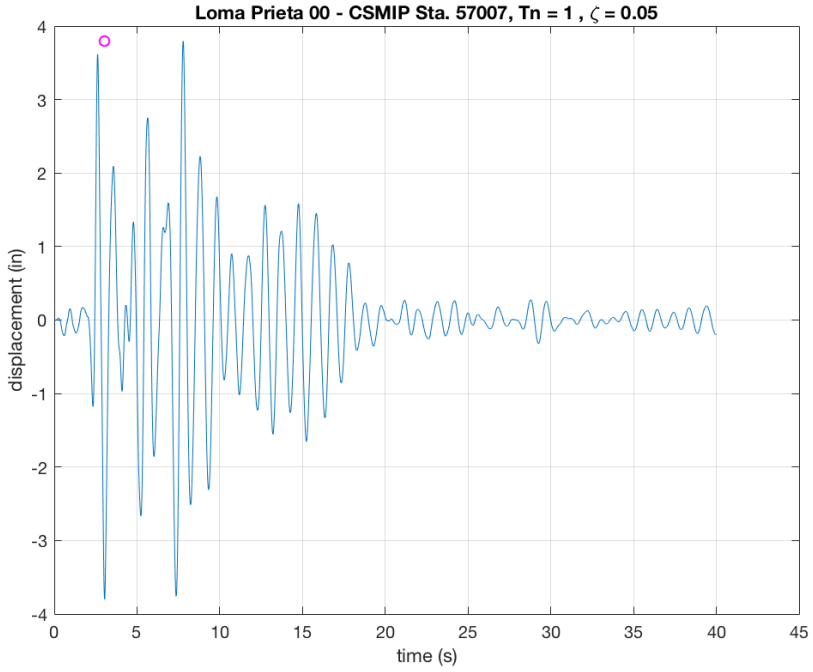

Figure 97: Loma 00 (T_n = 1.00s) Average Acceleration Method

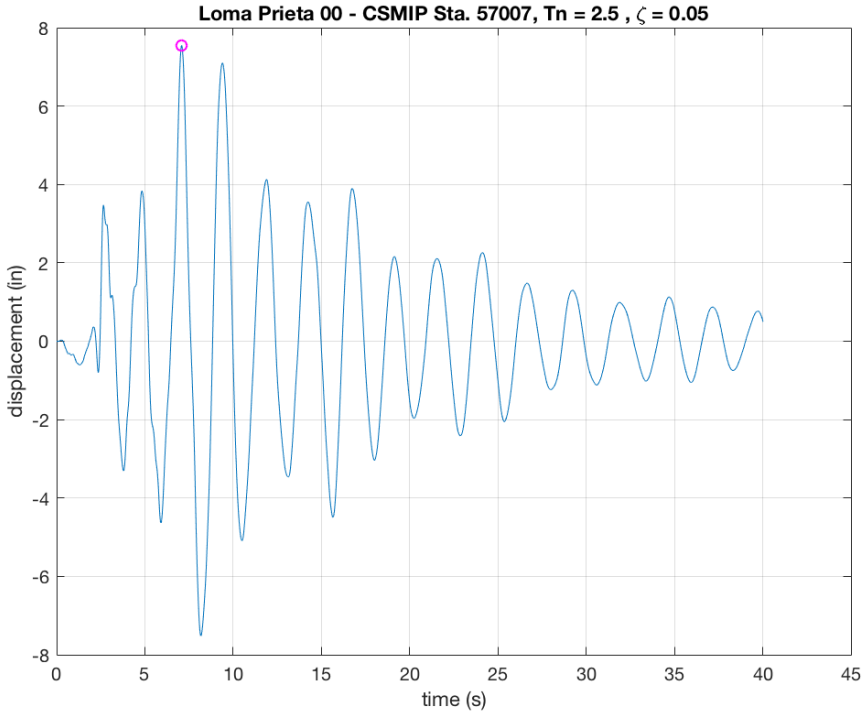

Figure 98: Loma 00 (T_n = 2.50s) Average Acceleration Method

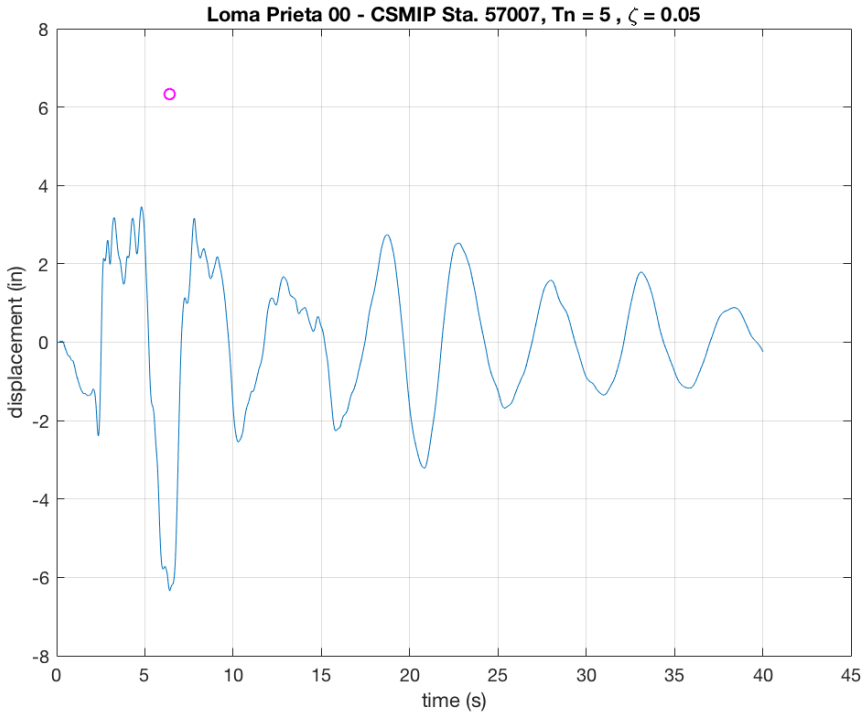

Figure 99: Loma 00 (T_n = 5.00s) Average Acceleration Method

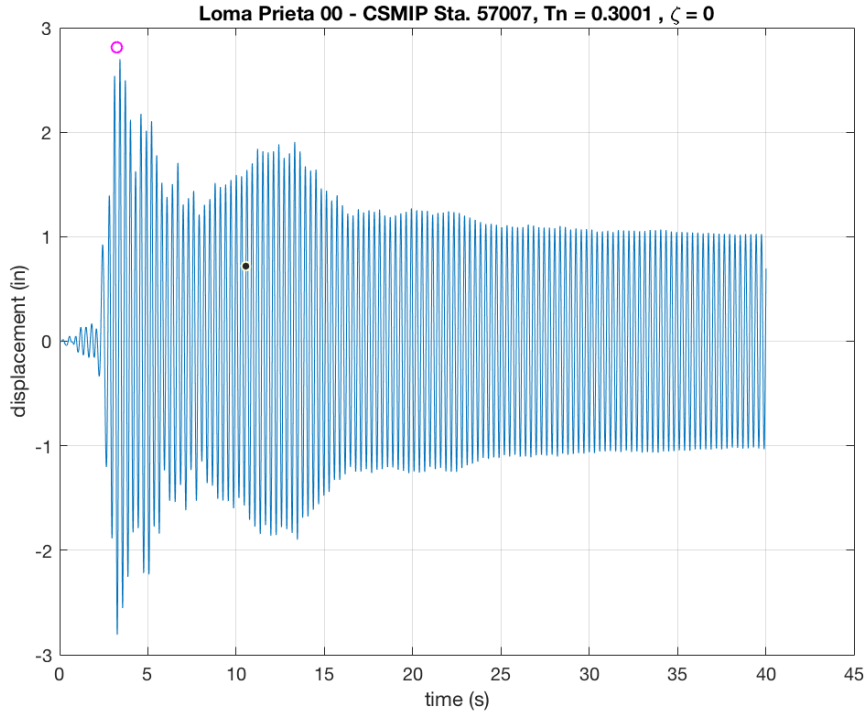

Figure 100: Loma 00 ($\xi = 0.00$) Average Acceleration Method

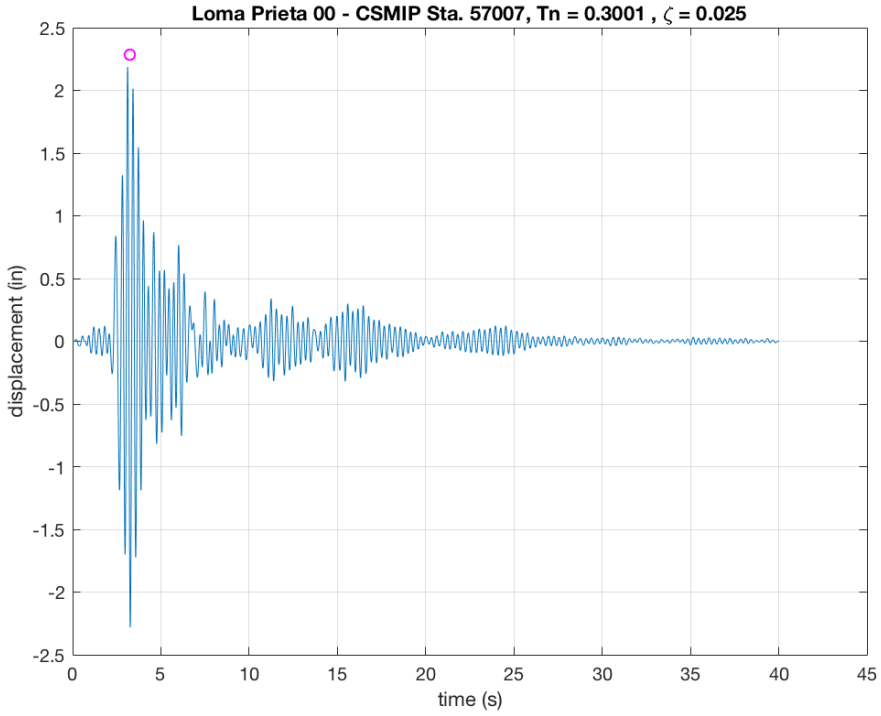

Figure 101: Loma 00 ($\xi = 0.025$) Average Acceleration Method

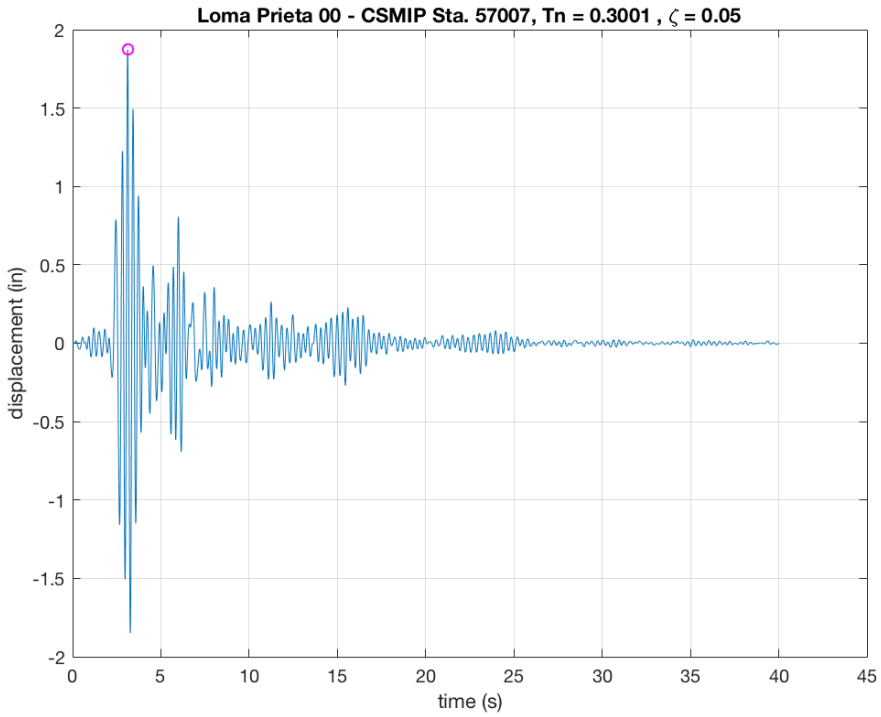

Figure 102: Loma 00 ($\xi = 0.050$) Average Acceleration Method

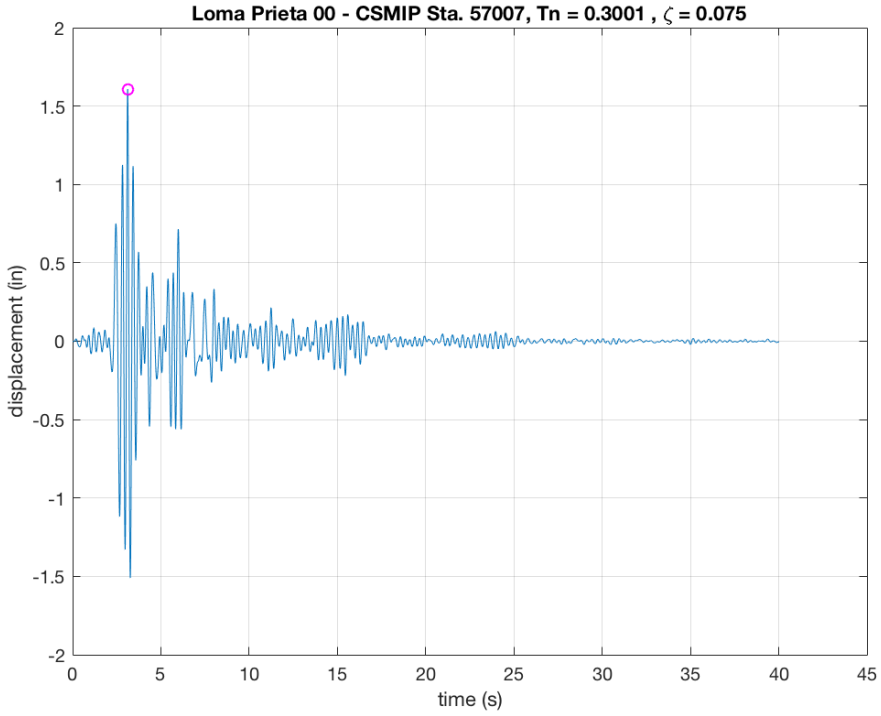

Figure 103: Loma 00 ($\xi = 0.075$) Average Acceleration Method

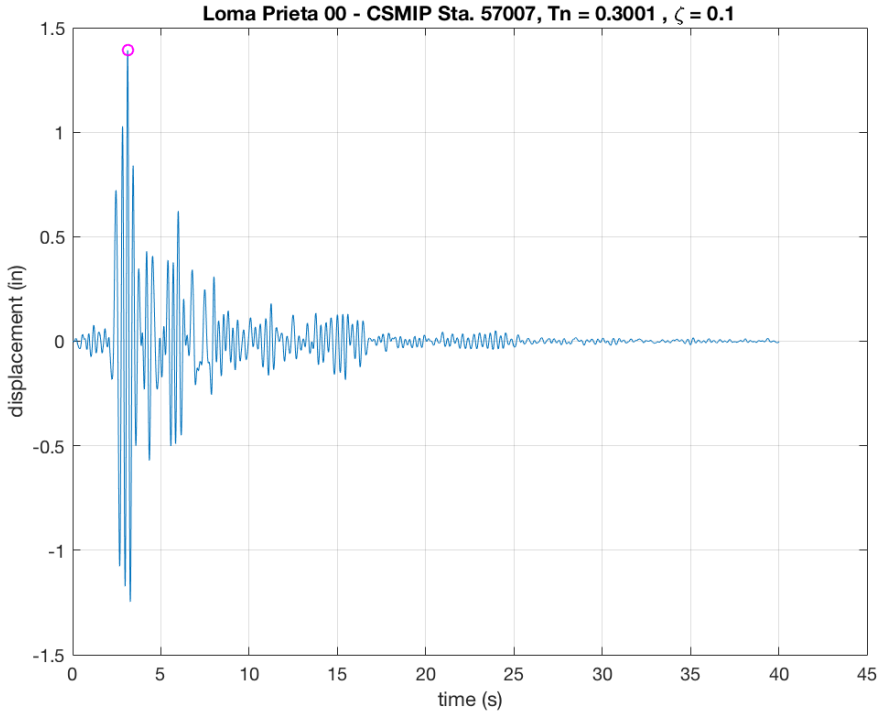

Figure 104: Loma 00 ($\xi = 0.100$) Average Acceleration Method

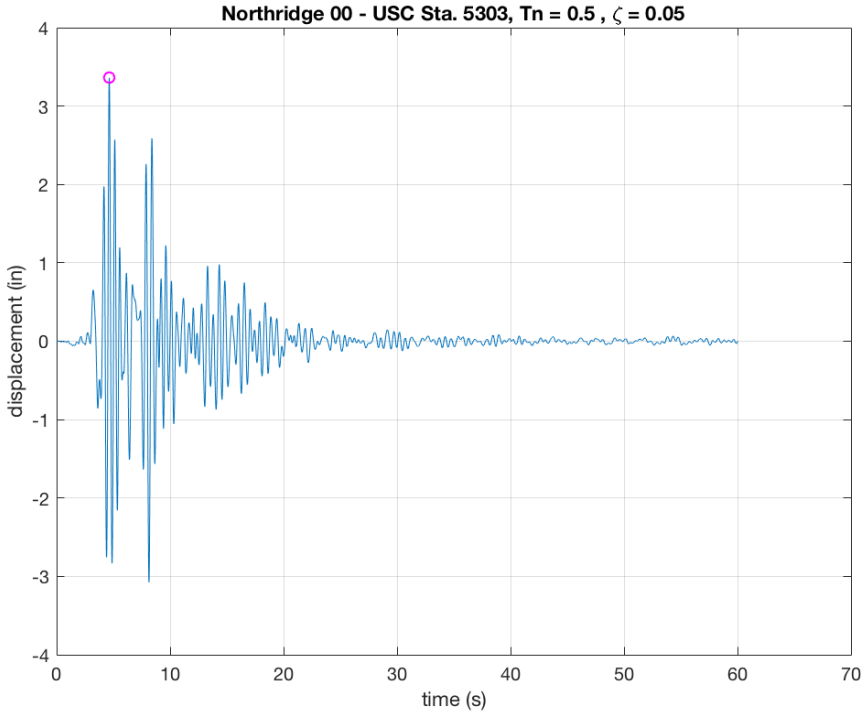

Figure 105: Northridge 00 (T_n = 0.50s) Average Acceleration Method

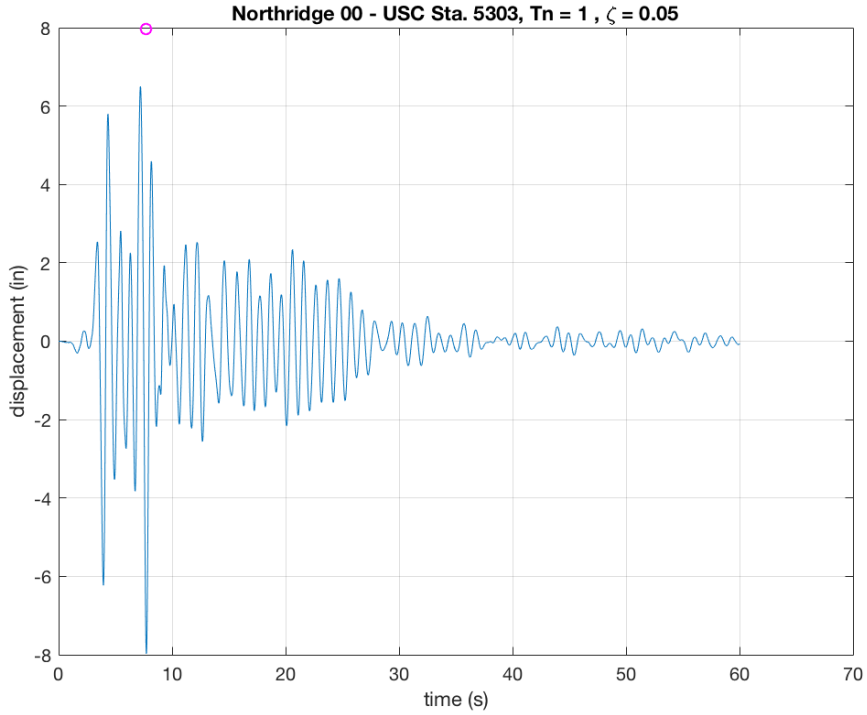

Figure 106: Northridge 00 (T_n = 1.00s) Average Acceleration Method

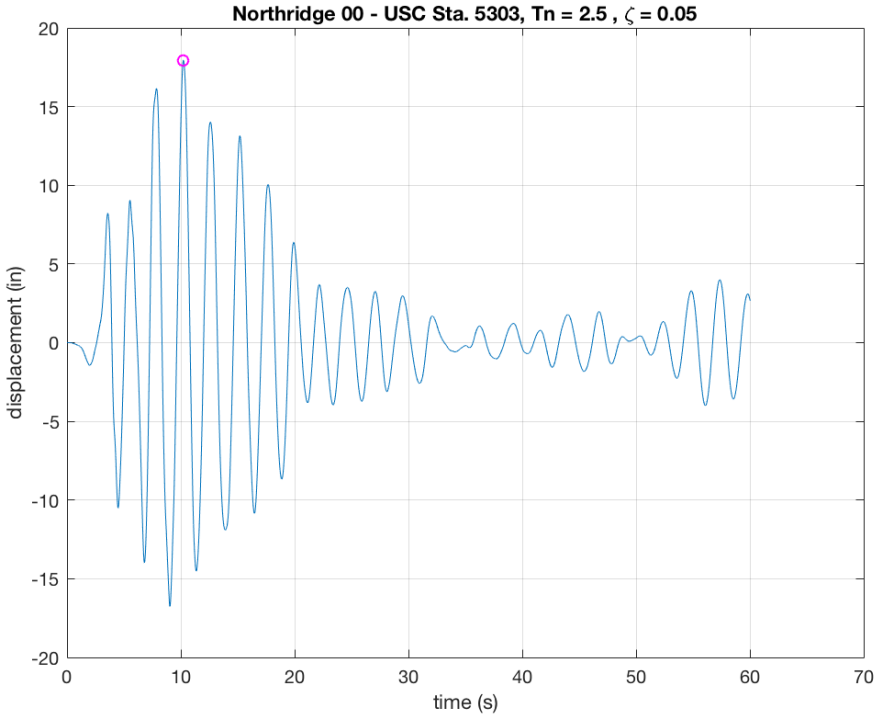

Figure 107: Northridge 00 (T_n = 2.50s) Average Acceleration Method

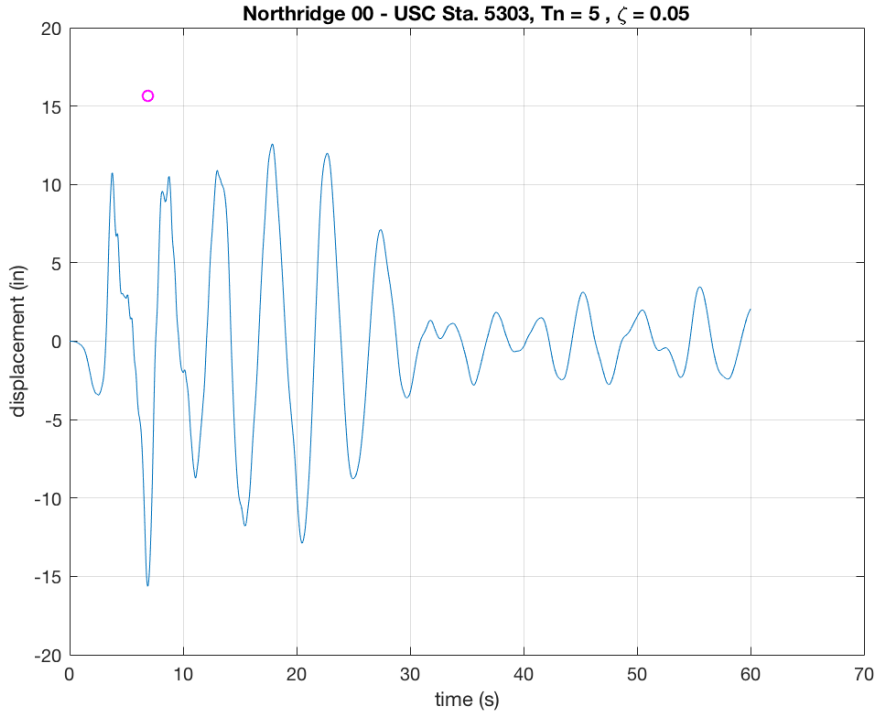

Figure 108: Northridge 00 (T_n = 5.00s) Average Acceleration Method

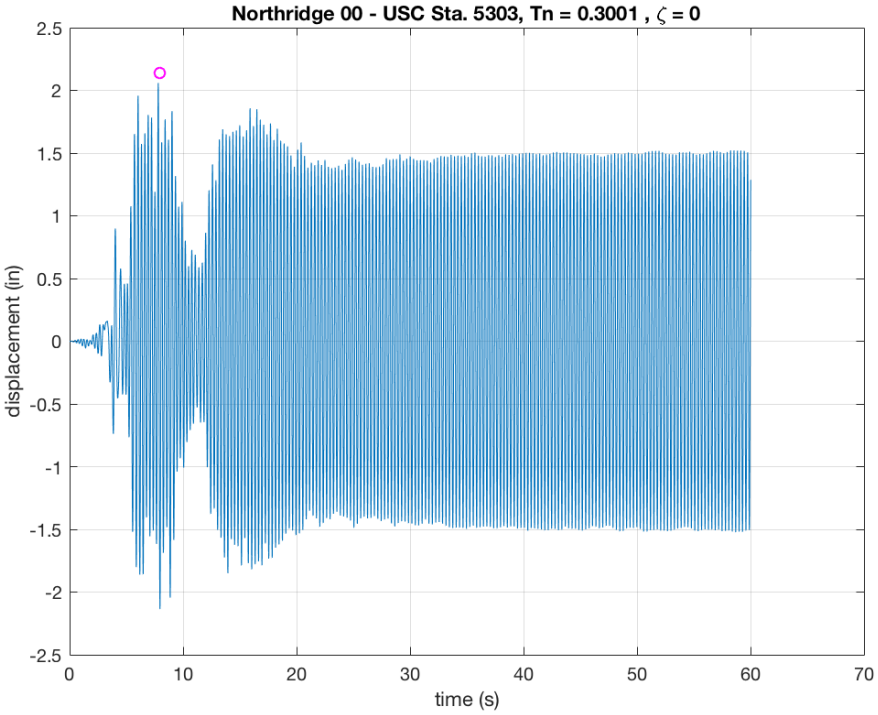

Figure 109: Northridge 00 ($\xi = 0.00$) Average Acceleration Method

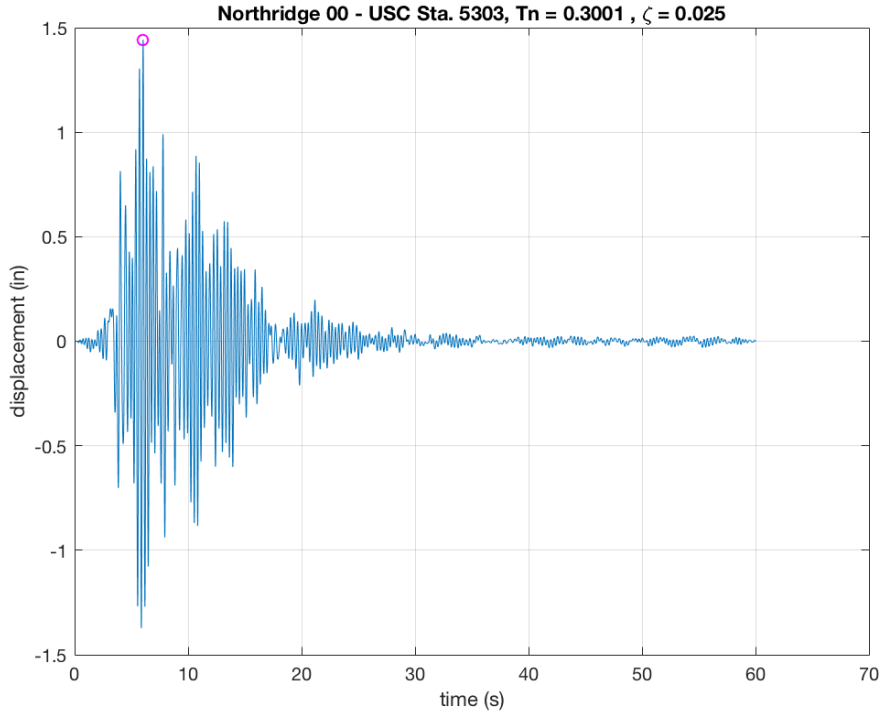

Figure 110: Northridge 00 ($\xi = 0.025$) Average Acceleration Method

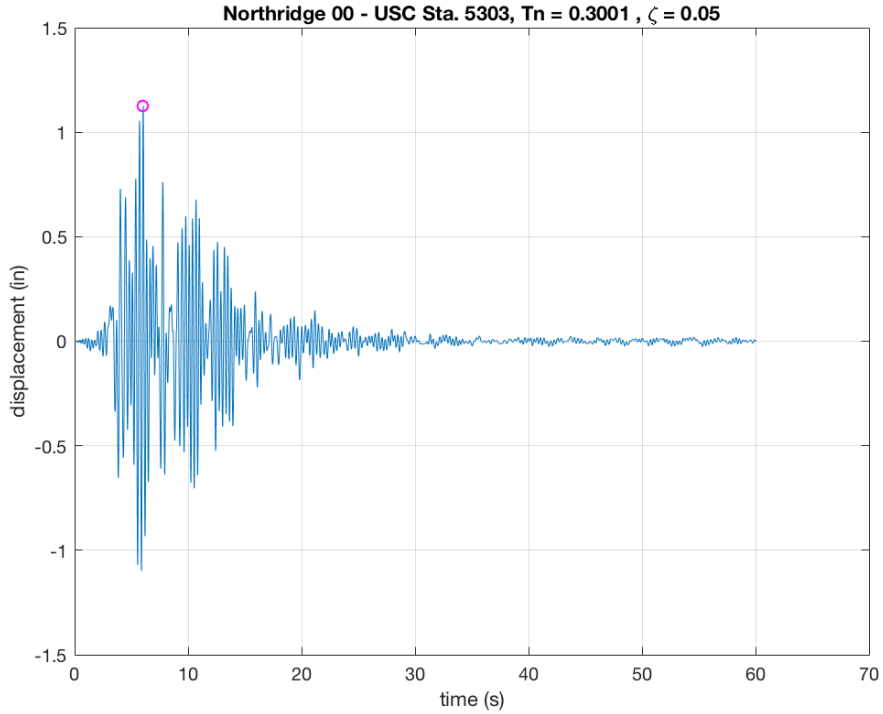

Figure 111: Northridge 00 ($\xi = 0.050$) Average Acceleration Method

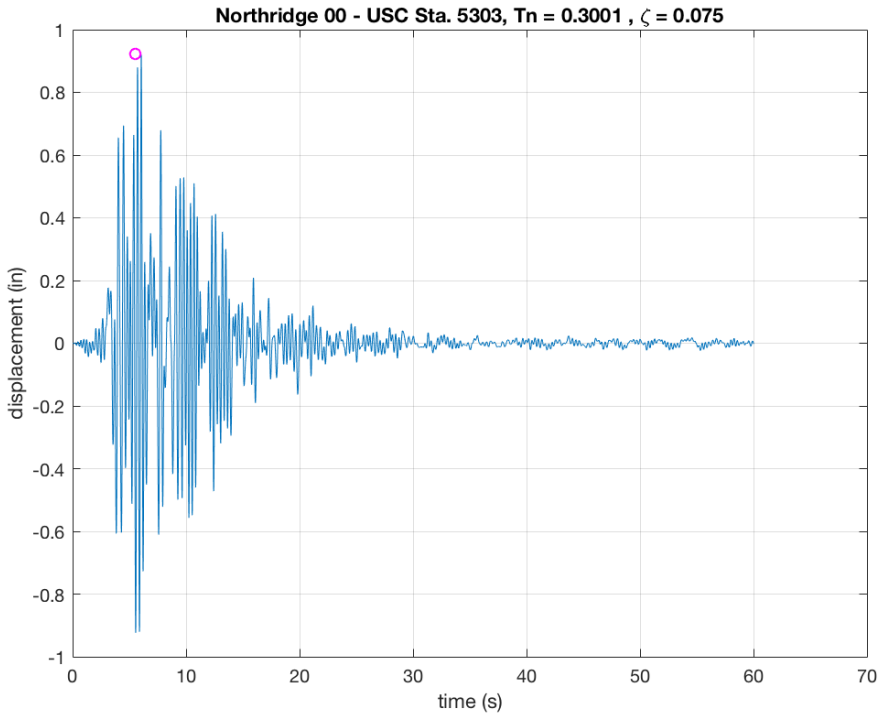

Figure 112: Northridge 00 ($\xi = 0.075$) Average Acceleration Method

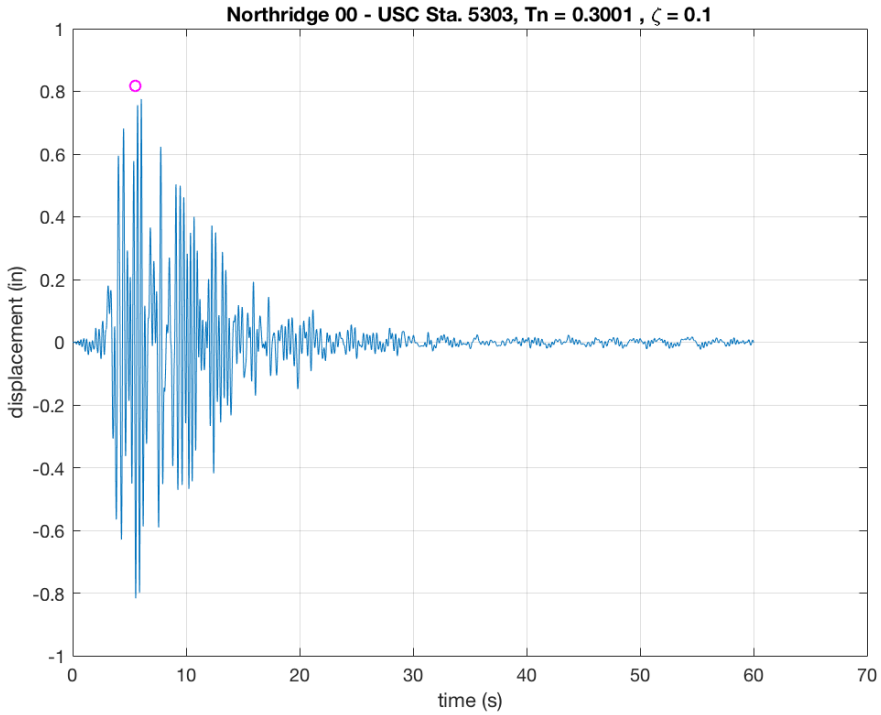

Figure 113: Northridge 00 ($\xi = 0.100$) Average Acceleration Method

Appendix I: Linear Acceleration Method Time Histories

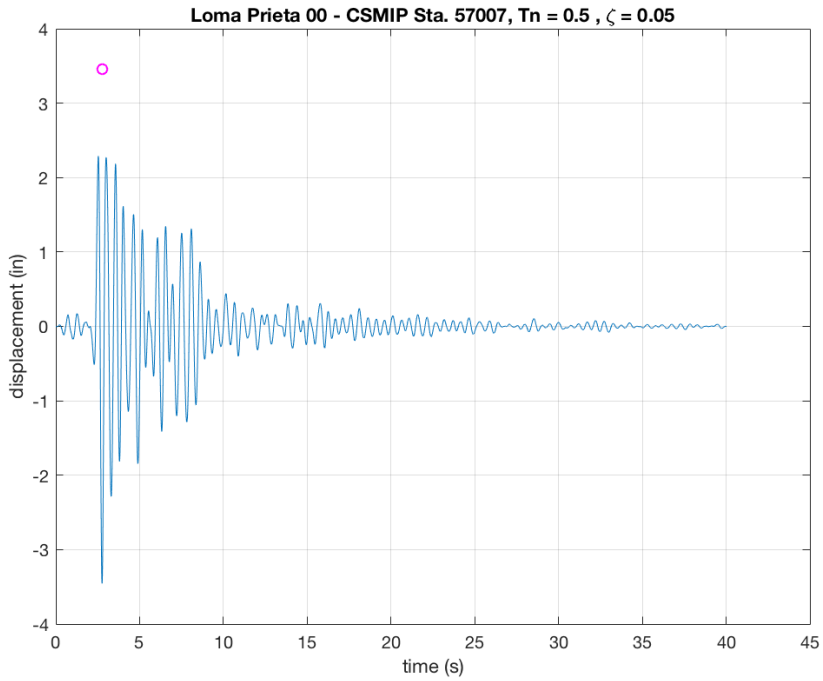

Figure 114: Loma 00 (T_n = 0.50s) Linear Acceleration Method

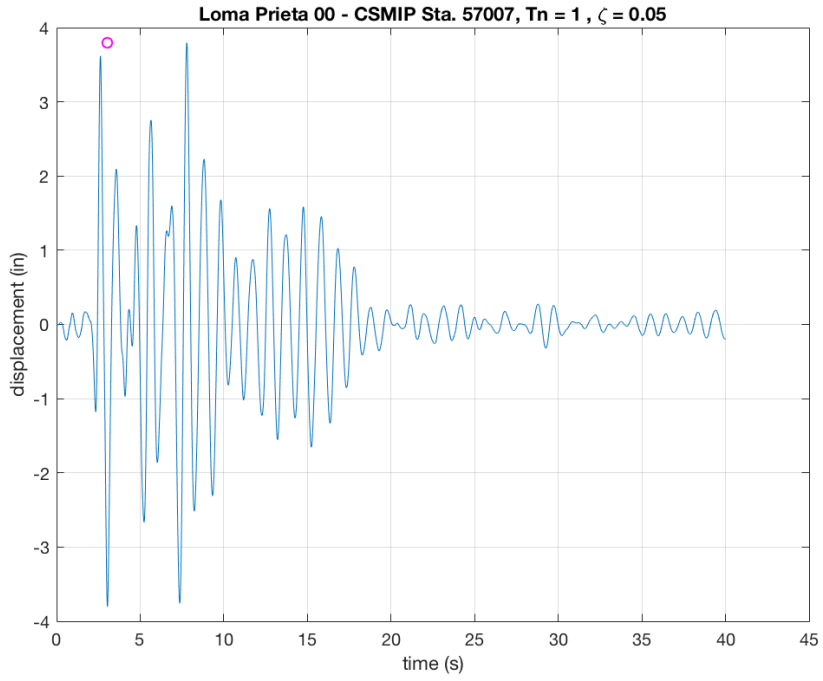

Figure 115: Loma 00 (T_n = 1.00s) Linear Acceleration Method

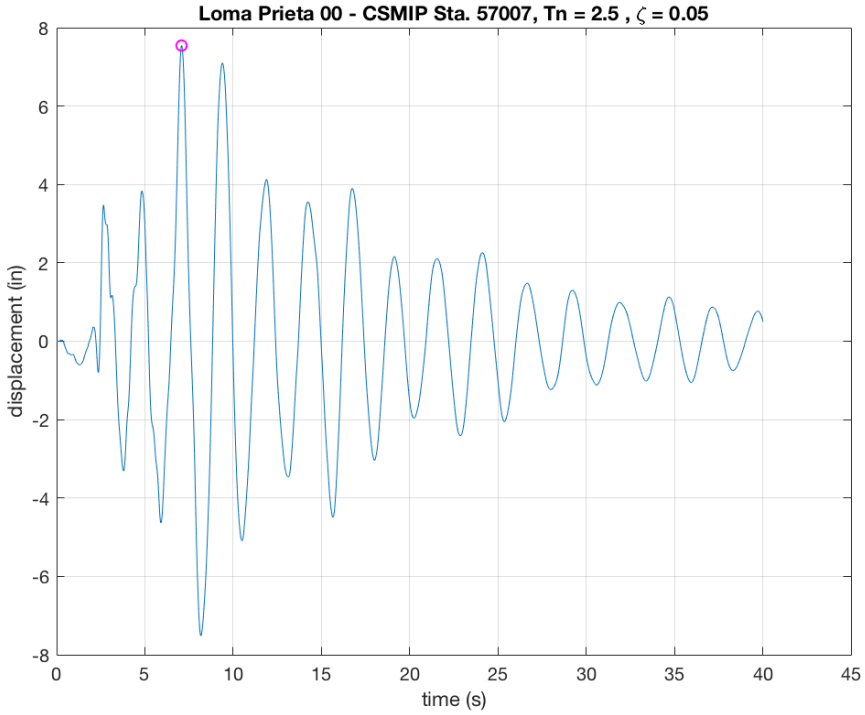

Figure 116: Loma 00 (T_n = 2.50s) Linear Acceleration Method

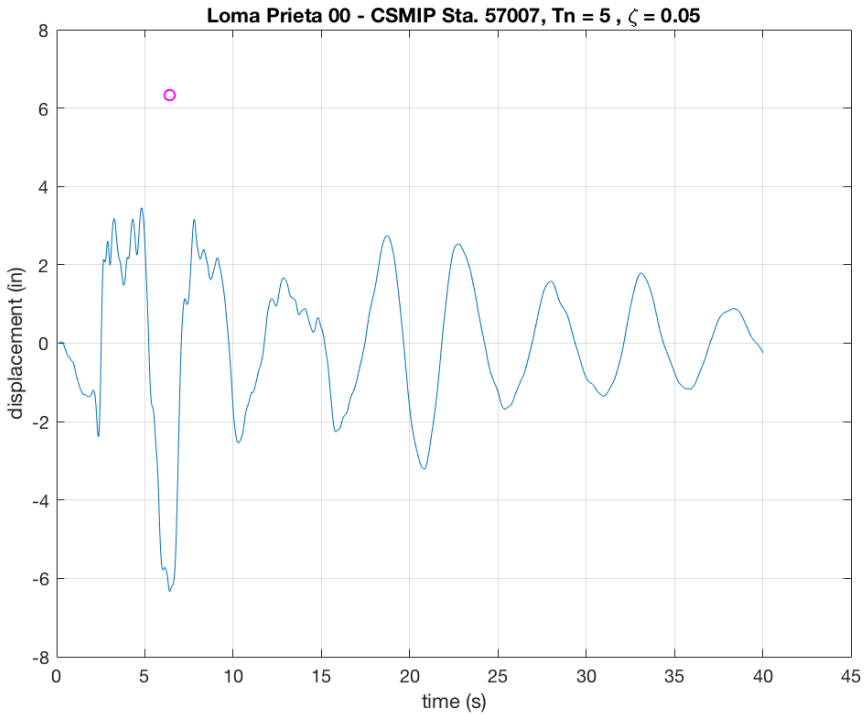

Figure 117: Loma 00 (T_n = 5.00s) Linear Acceleration Method

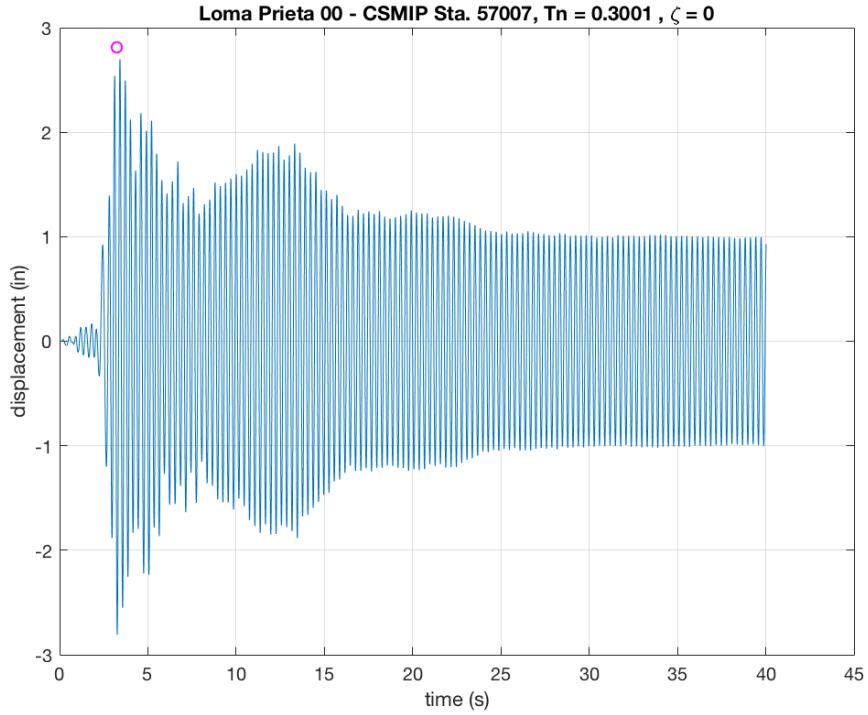

Figure 118: Loma 00 ($\xi = 0.00$) Linear Acceleration Method

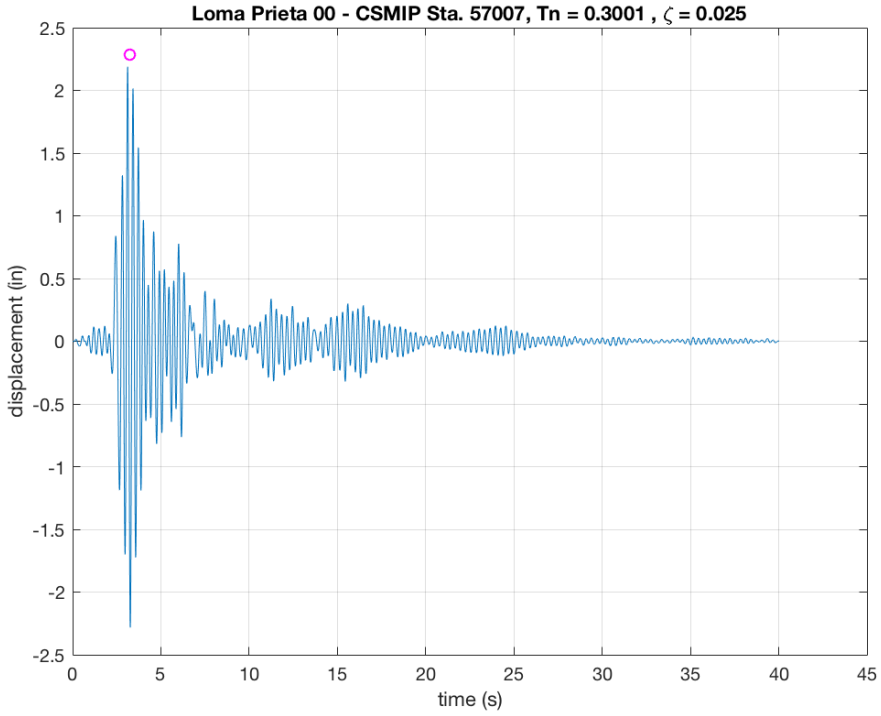

Figure 119: Loma 00 ($\xi = 0.025$) Linear Acceleration Method

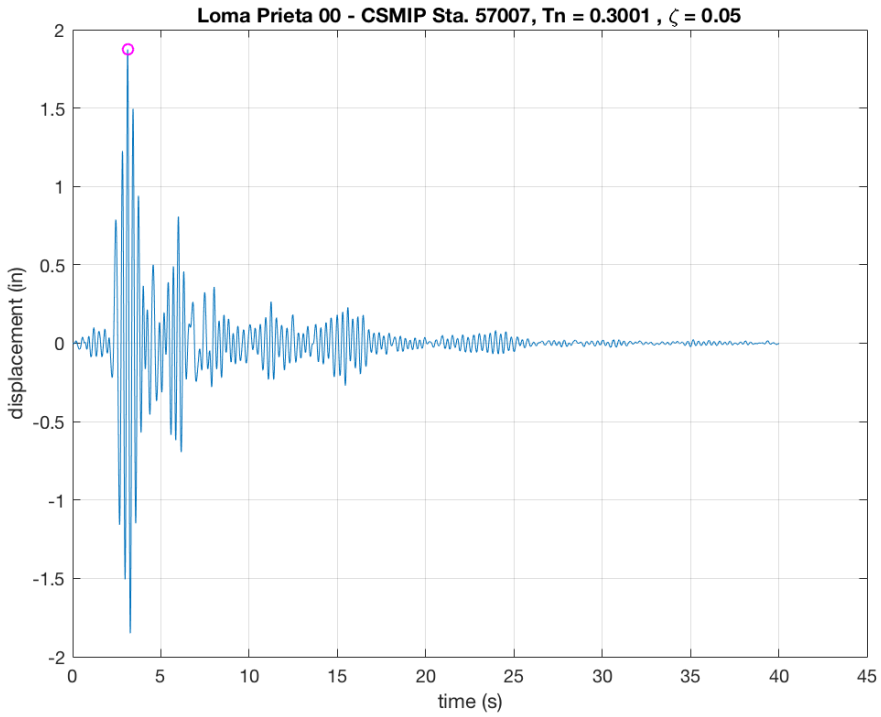

Figure 120: Loma 00 ($\xi = 0.050$) Linear Acceleration Method

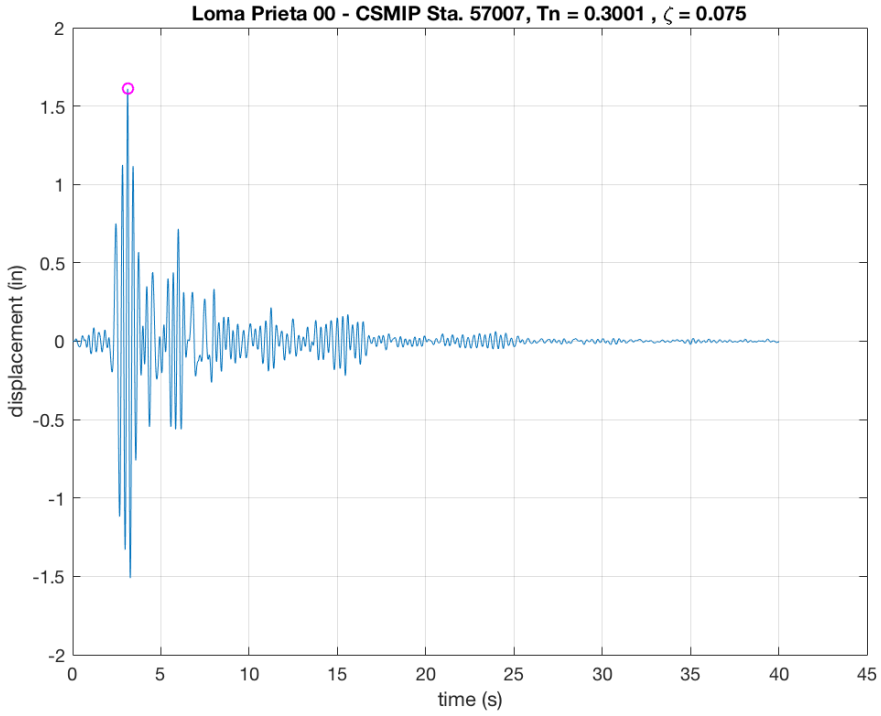

Figure 121: Loma 00 ($\xi = 0.075$) Linear Acceleration Method

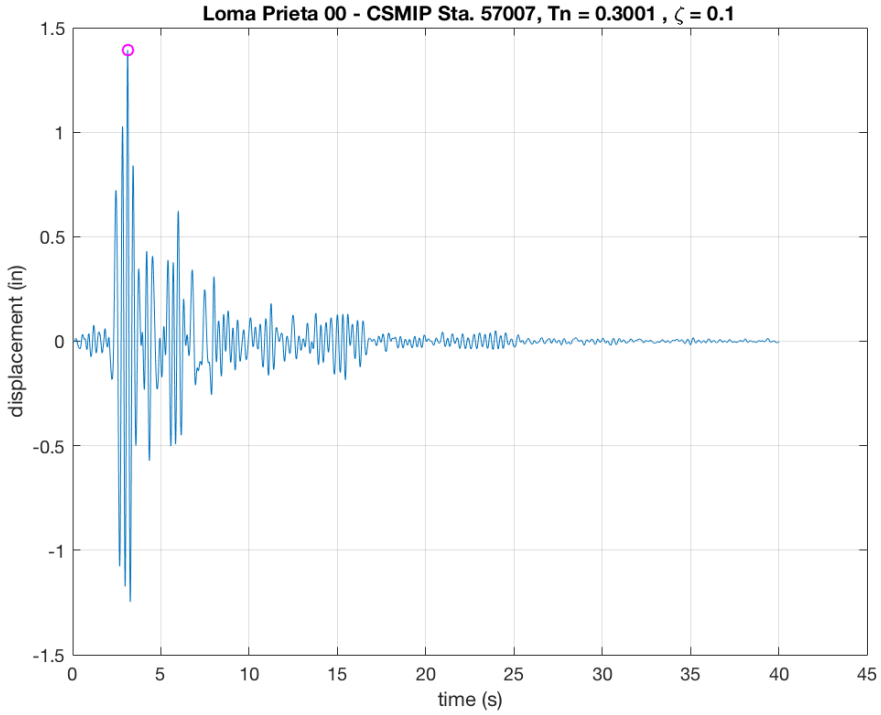

Figure 122: Loma 00 ($\xi = 0.100$) Linear Acceleration Method

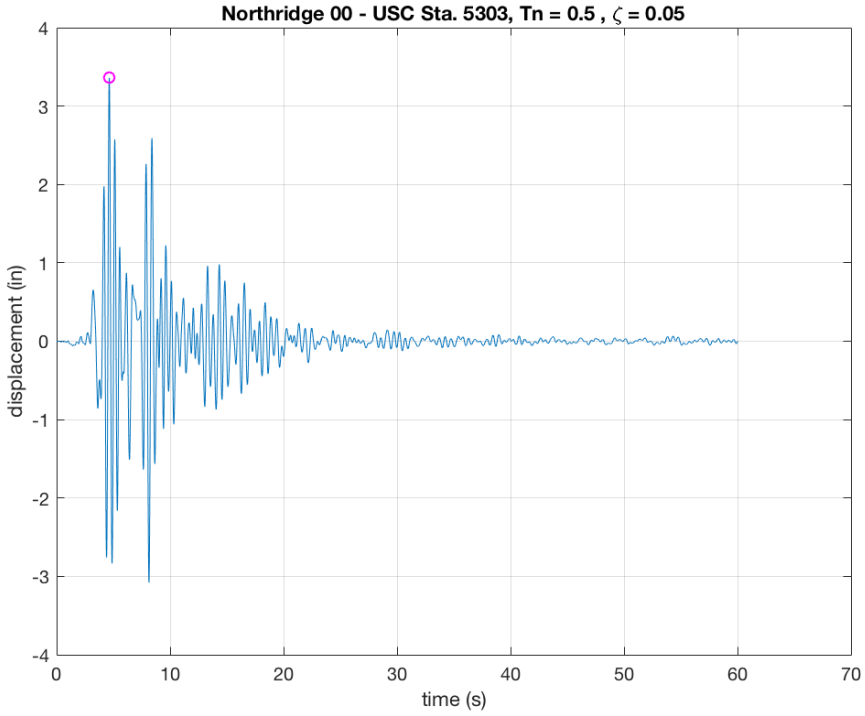

Figure 123: Northridge 00 (T_n = 0.50s) Linear Acceleration Method

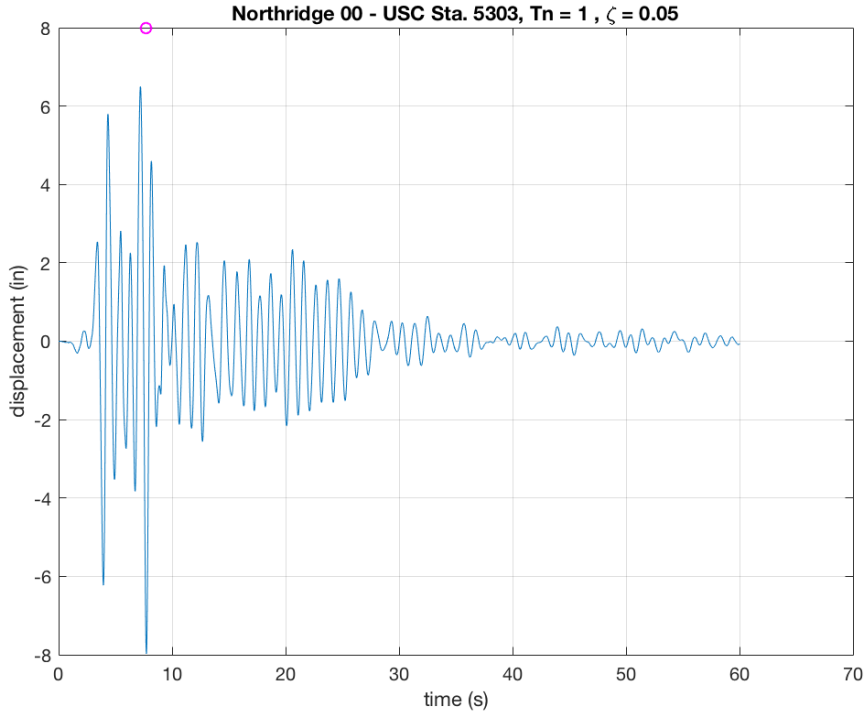

Figure 124: Northridge 00 (T_n = 1.00s) Linear Acceleration Method

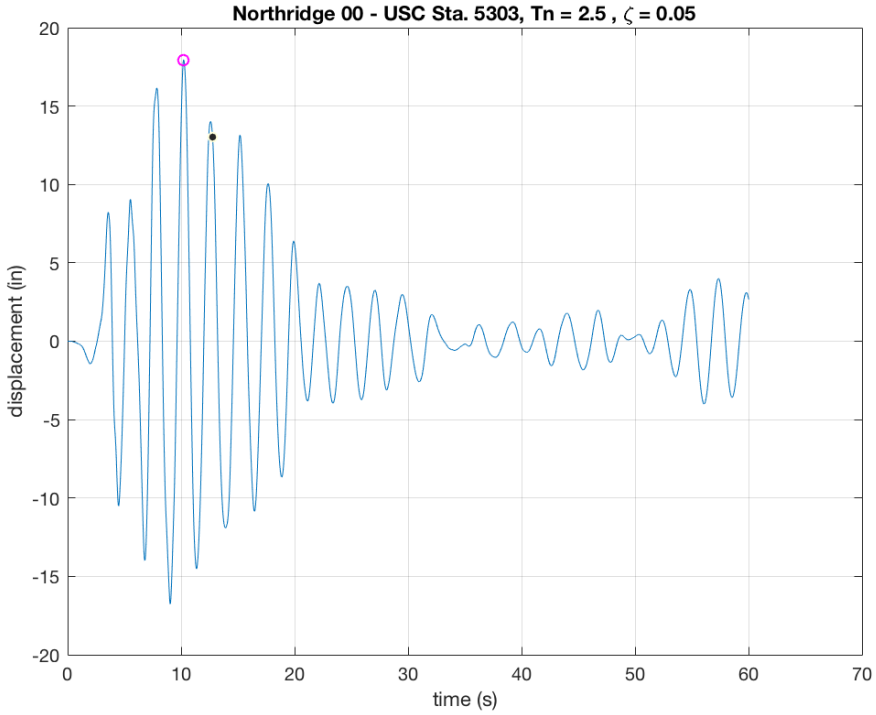

Figure 125: Northridge 00 (T_n = 2.50s) Linear Acceleration Method

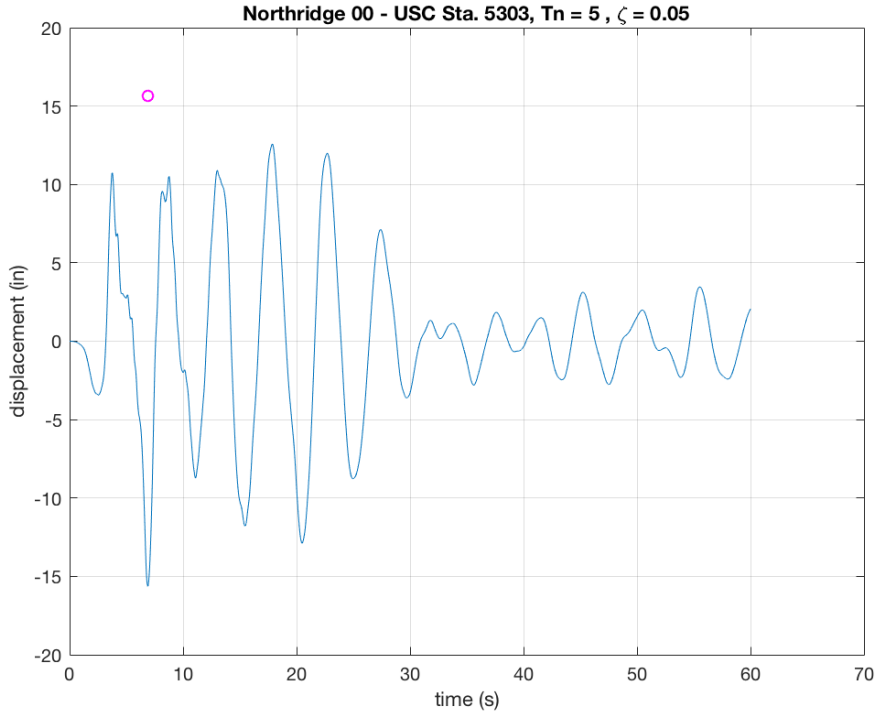

Figure 126: Northridge 00 (T_n = 5.00s) Linear Acceleration Method

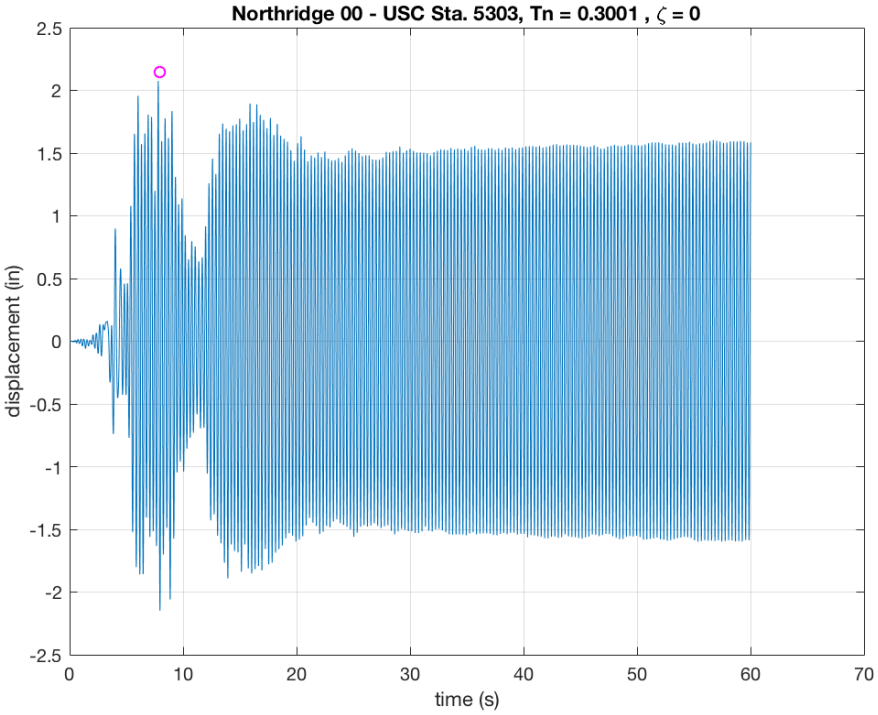

Figure 127: Northridge 00 ($\xi = 0.00$) Linear Acceleration Method

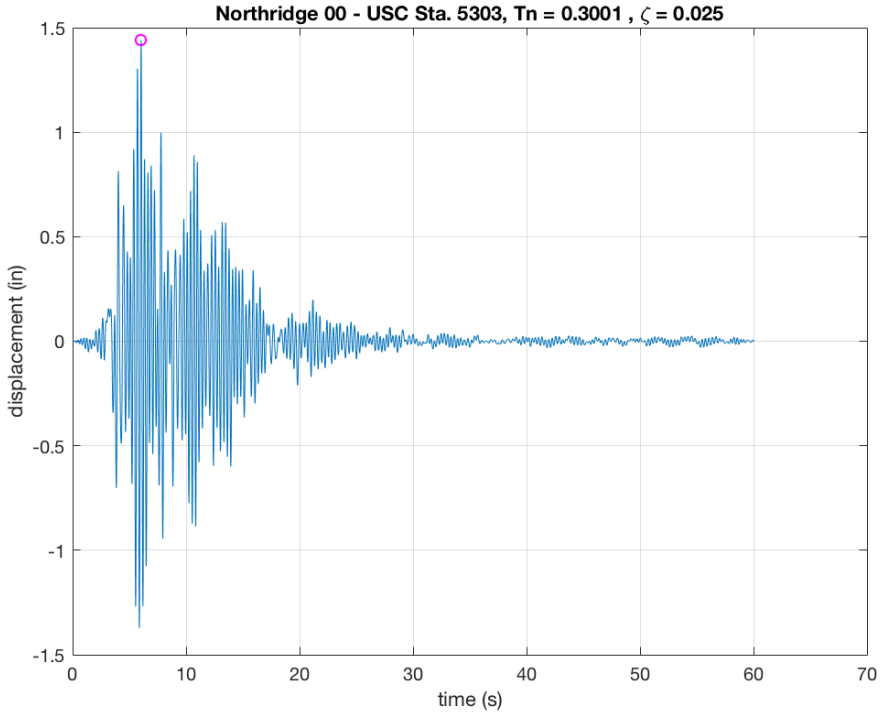

Figure 128: Northridge 00 ($\xi = 0.025$) Linear Acceleration Method

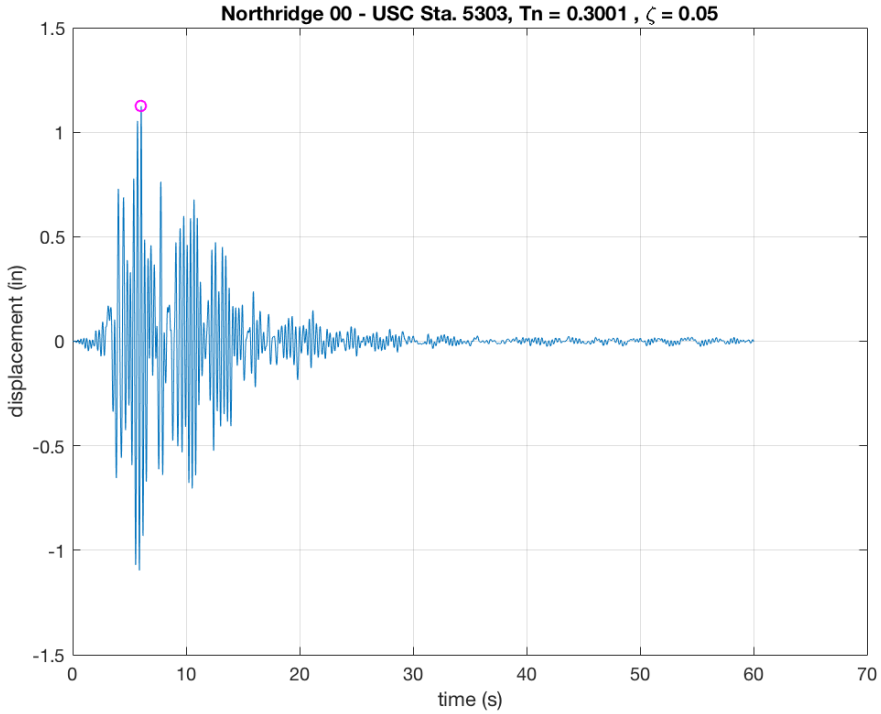

Figure 129: Northridge 00 ($\xi = 0.050$) Linear Acceleration Method

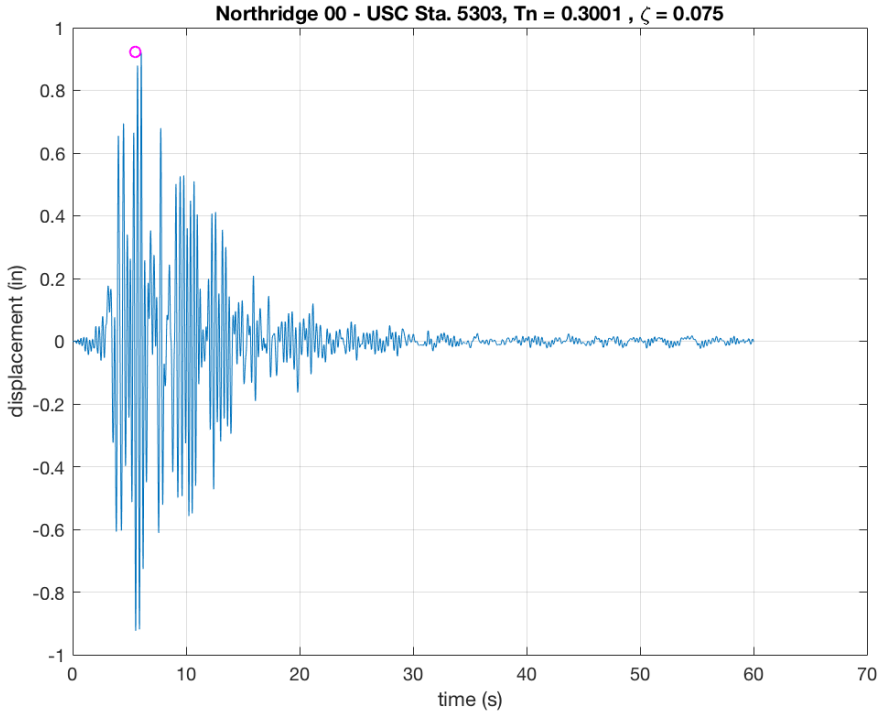

Figure 130: Northridge 00 ($\xi = 0.075$) Linear Acceleration Method

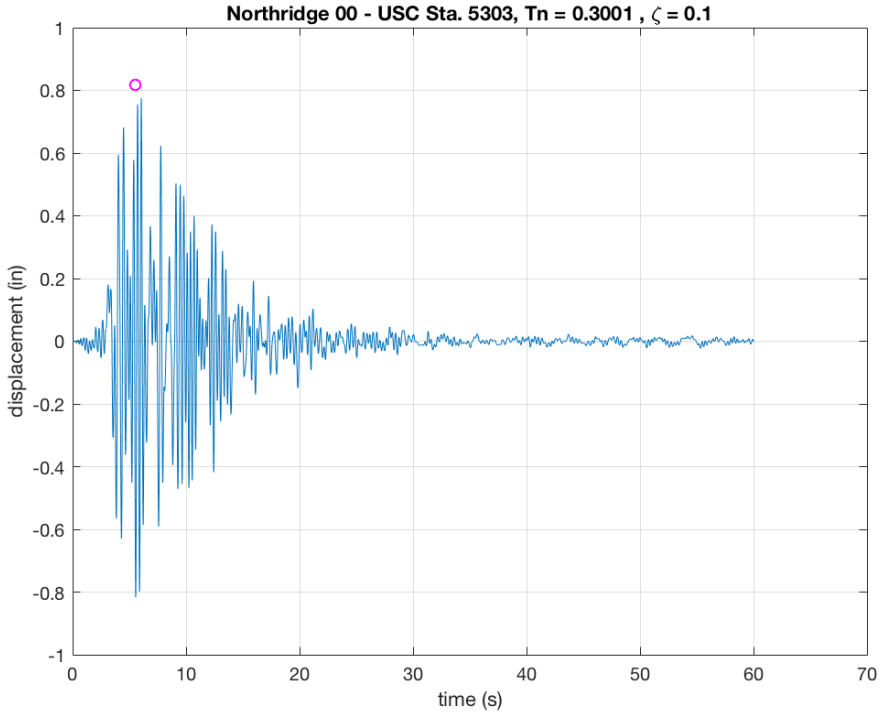

Figure 131: Northridge 00 ($\xi = 0.100$) Linear Acceleration Method

Appendix J: Pseudo-Acceleration Response Spectrums

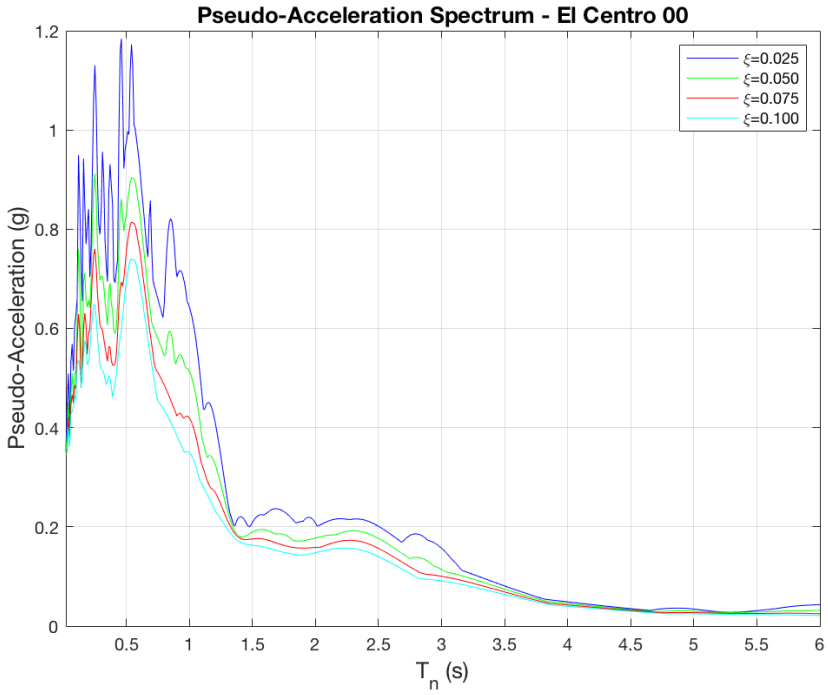

Figure 132: Pseudo-Acceleration Spectrum – El Centro 00

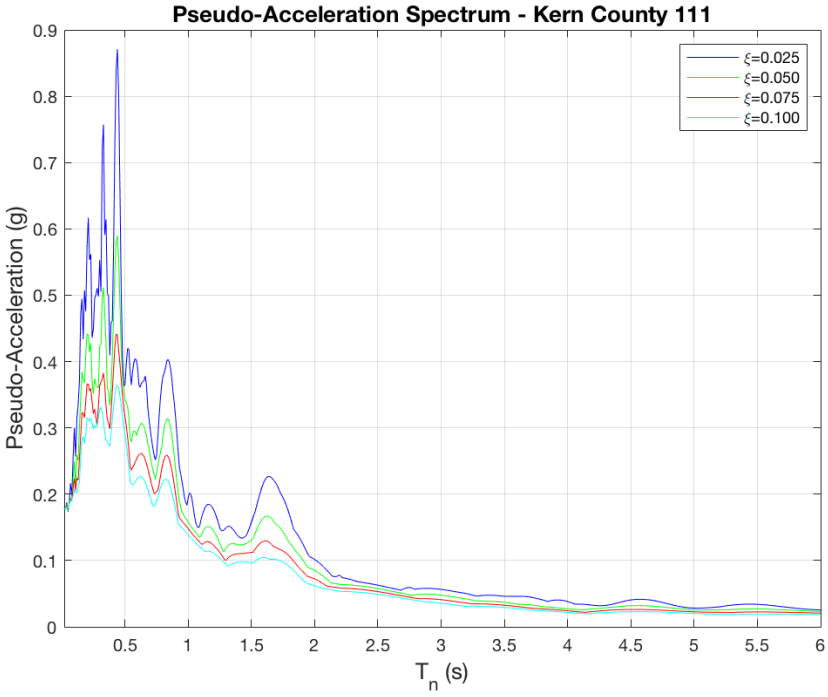

Figure 133: Pseudo-Acceleration Spectrum – Kern County 111

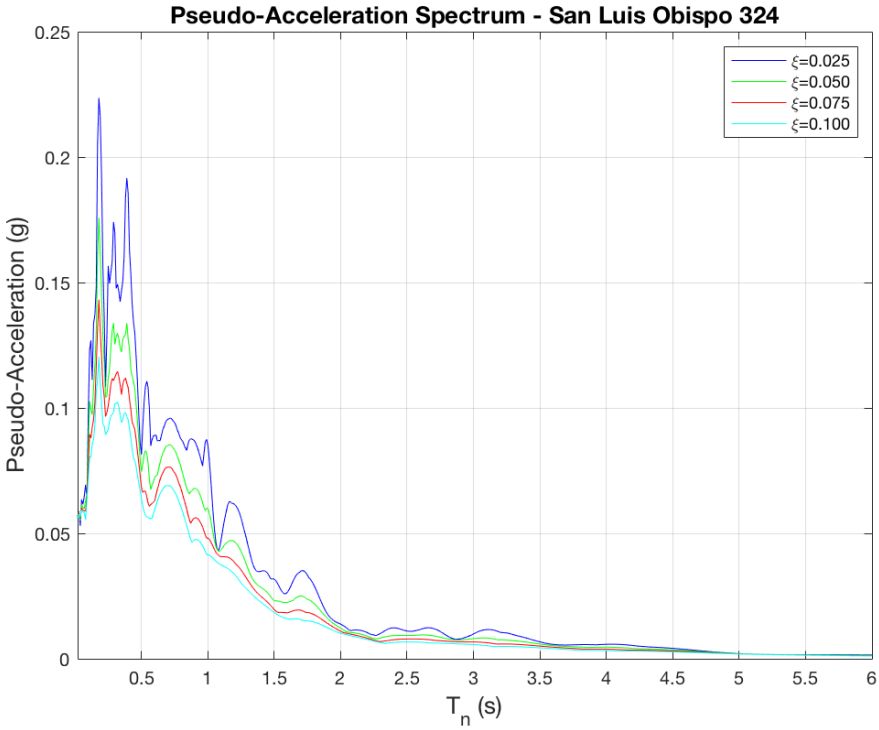

Figure 134: Pseudo-Acceleration Spectrum – San Luis Obispo 324

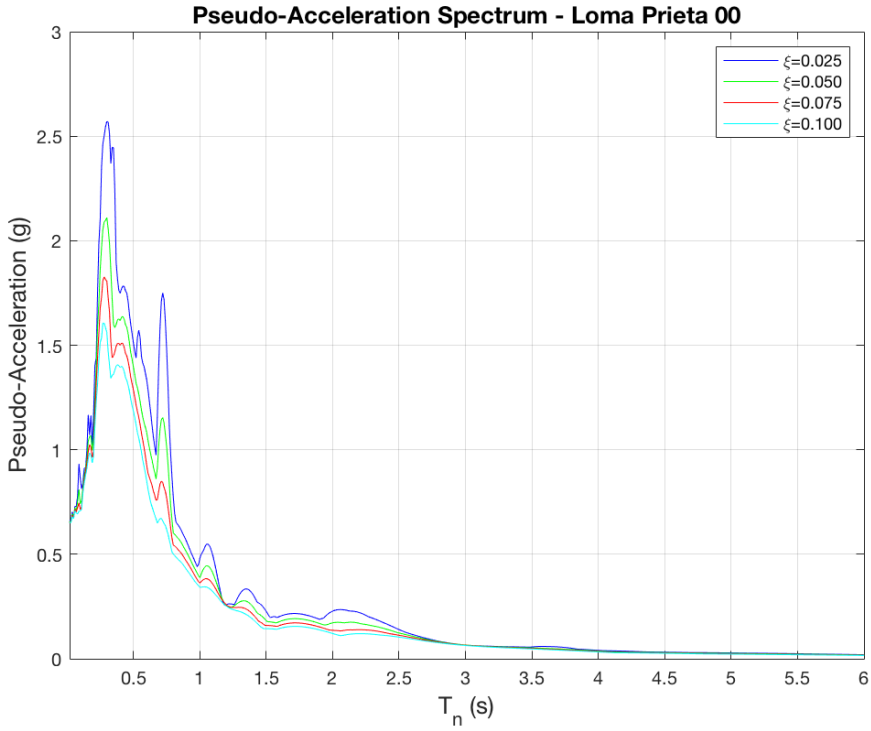

Figure 135: Pseudo-Acceleration Spectrum – Loma Prieta 00

Appendix K: Pseudo-Velocity Response Spectrums

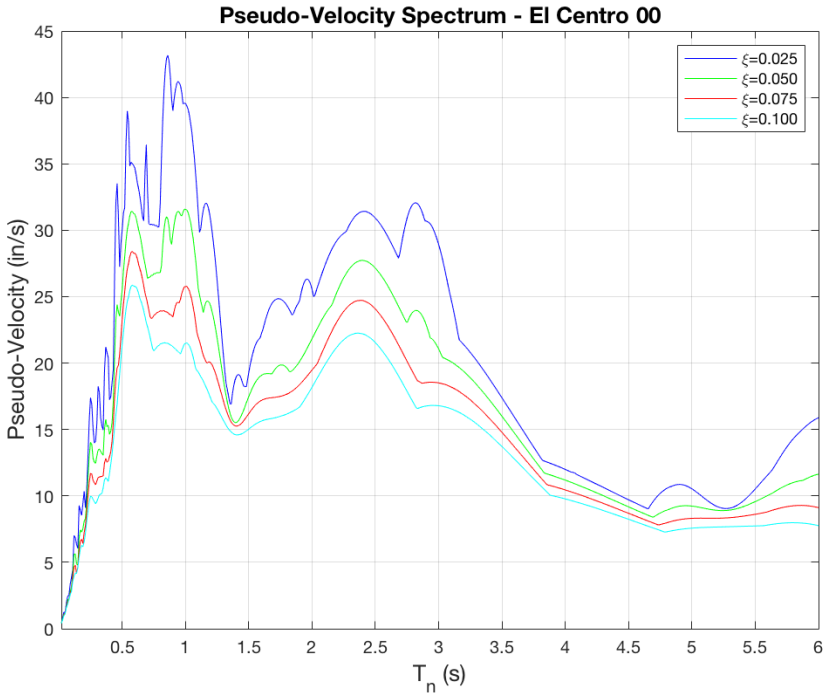

Figure 136: Pseudo-Velocity Spectrum – El Centro 00

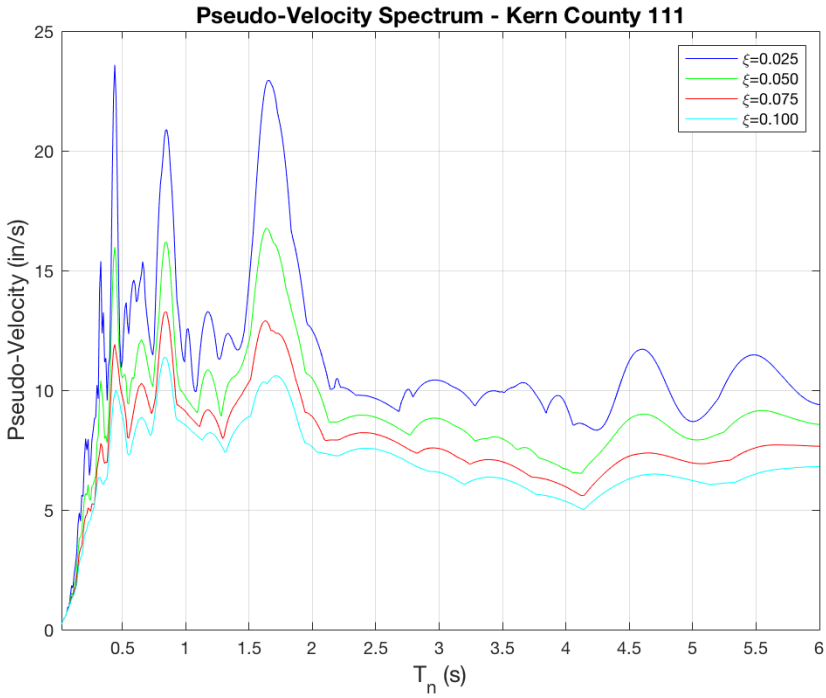

Figure 137: Pseudo-Velocity Spectrum – Kern County 111

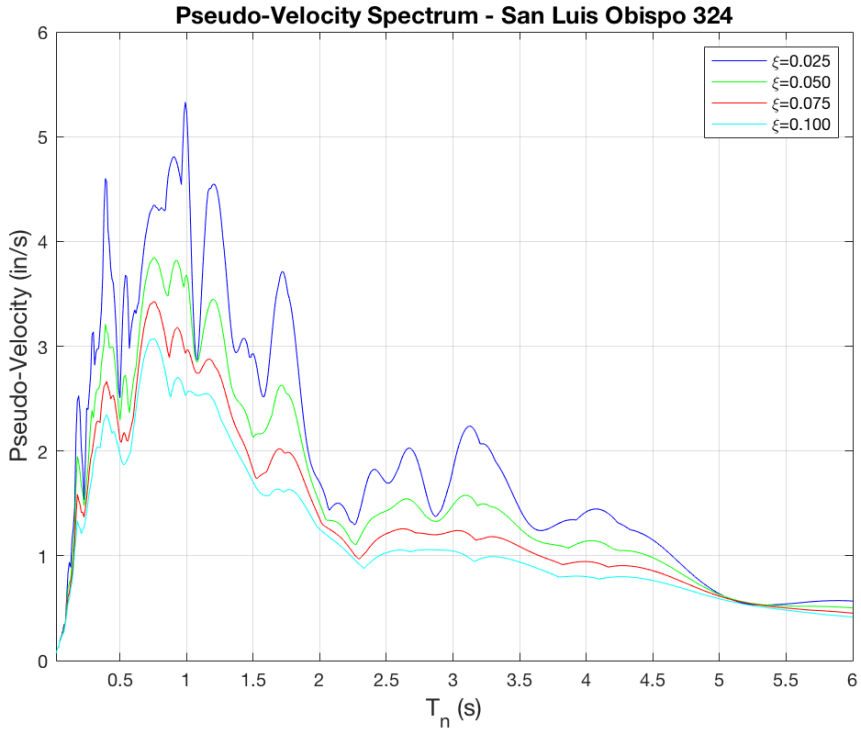

Figure 138: Pseudo-Velocity Spectrum – San Luis Obispo 324

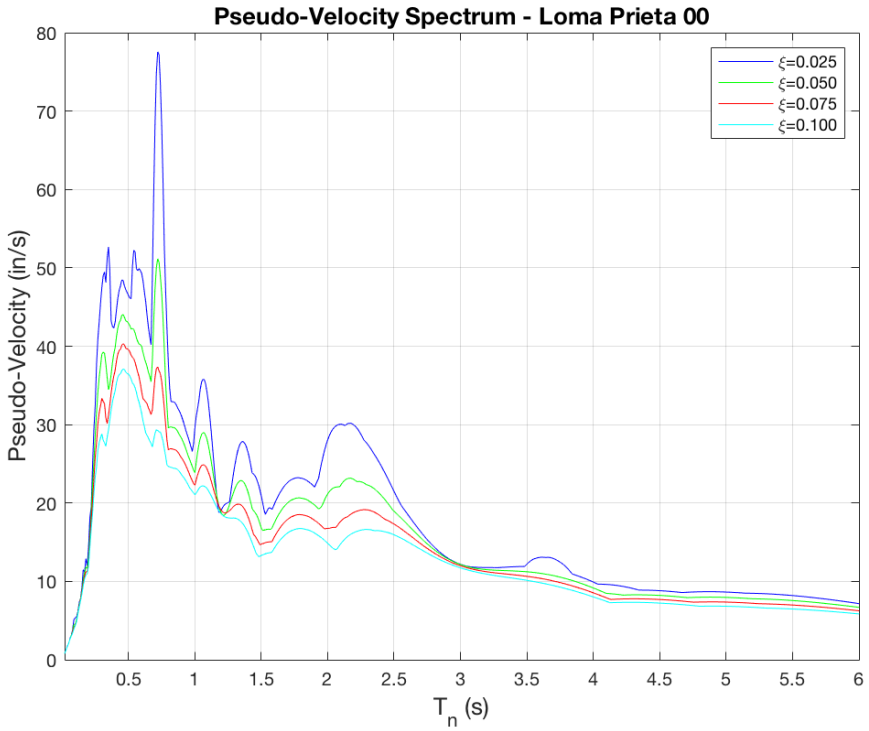

Figure 139: Pseudo-Velocity Spectrum – Loma Prieta 00

Appendix L: Spectral Displacement Response Spectrums

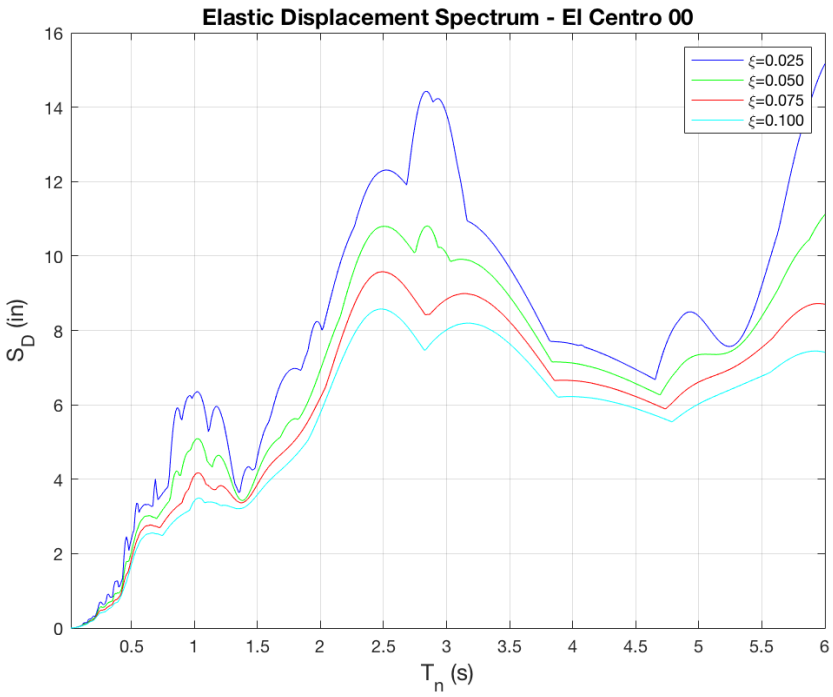

Figure 140: Maximum Displacement Spectrum – El Centro 00

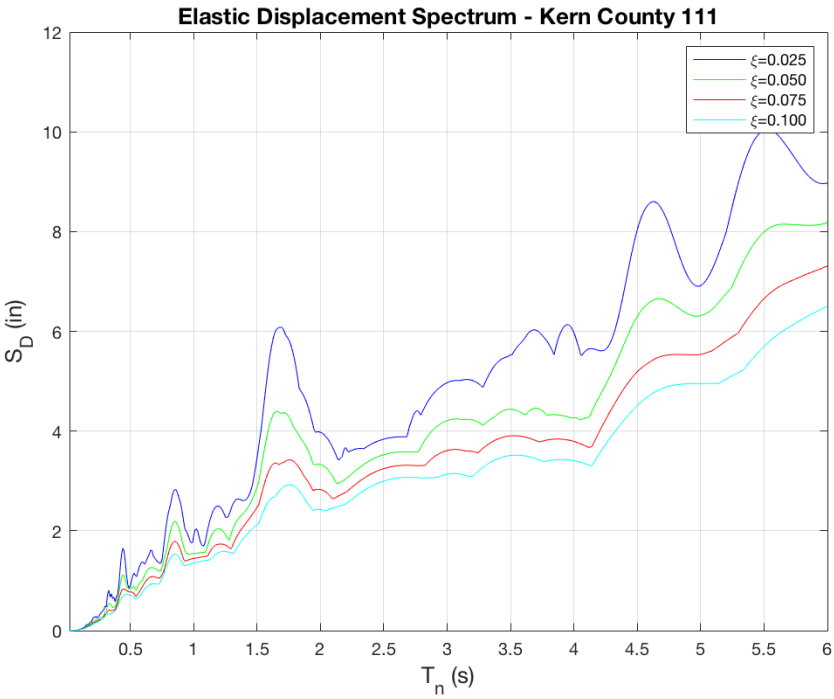

Figure 141: Maximum Displacement Spectrum – Kern County 111

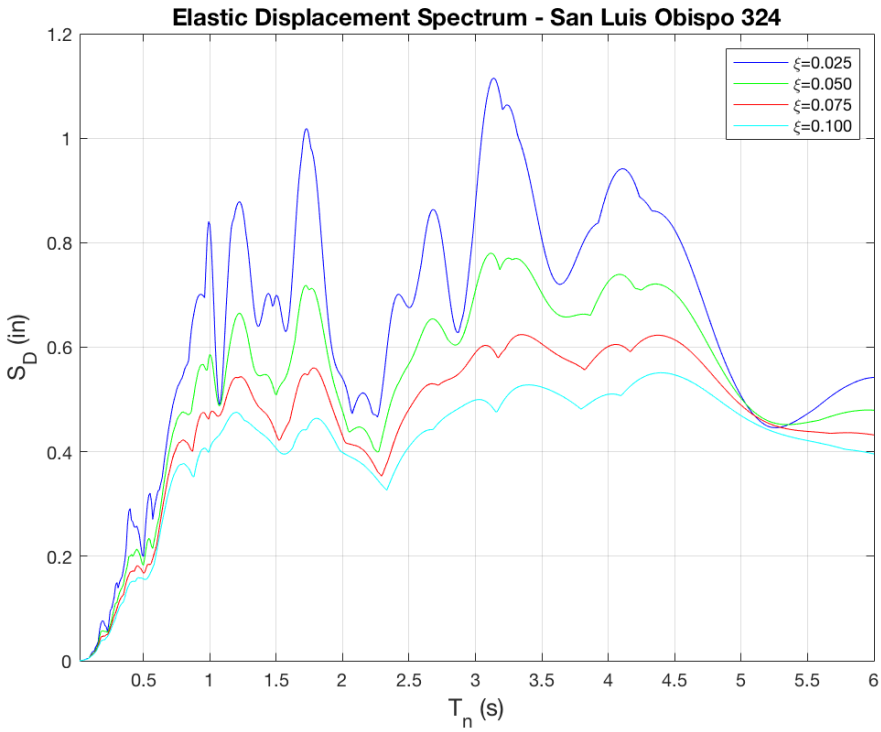

Figure 142: Maximum Displacement Spectrum – San Luis Obispo 324

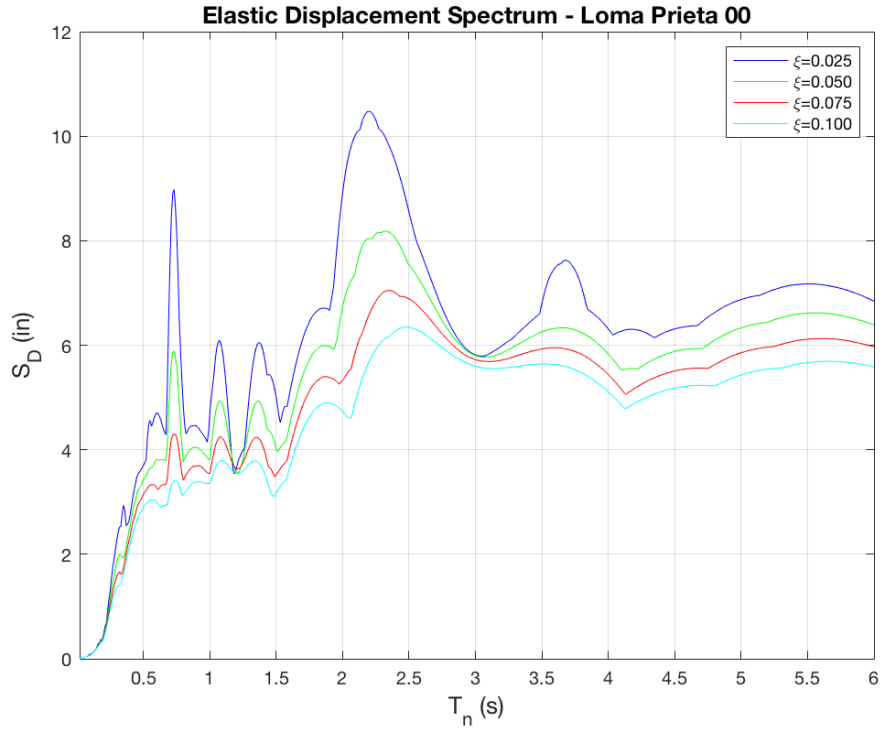

Figure 143: Maximum Displacement Spectrum – Loma Prieta 00

Appendix M: PSa versus Sa Response Spectrums

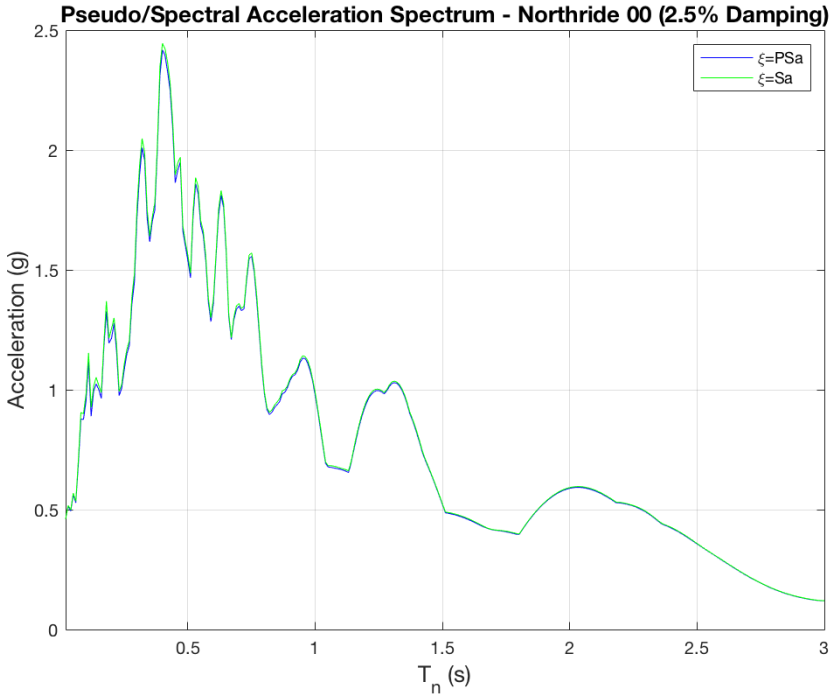

Figure 144: PSa and Sa (2.5% Damping) – Northridge 00 (USC Sta. 5303)

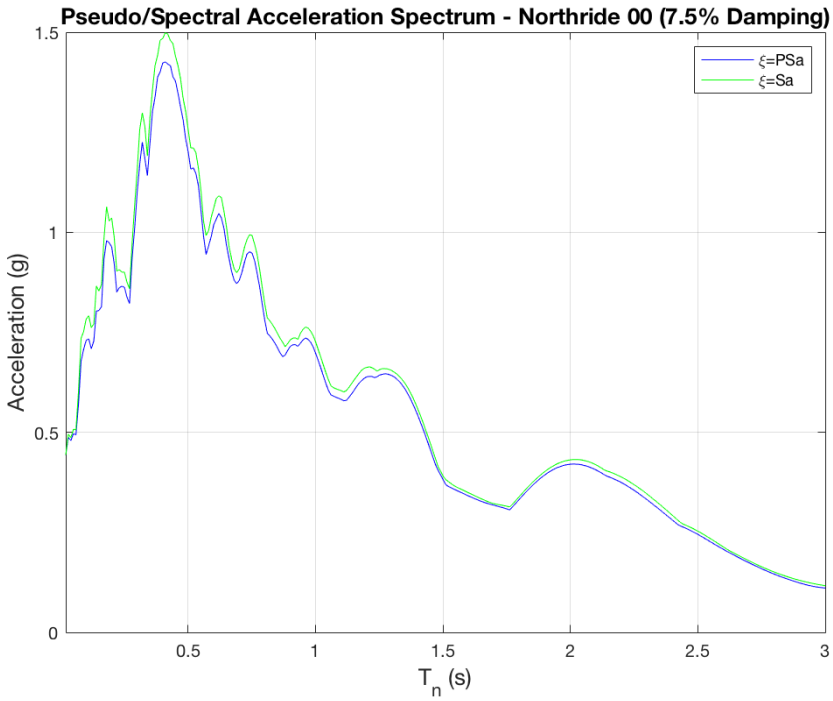

Figure 145: PSa and Sa (7.5% Damping) – Northridge 00 (USC Sta. 5303)

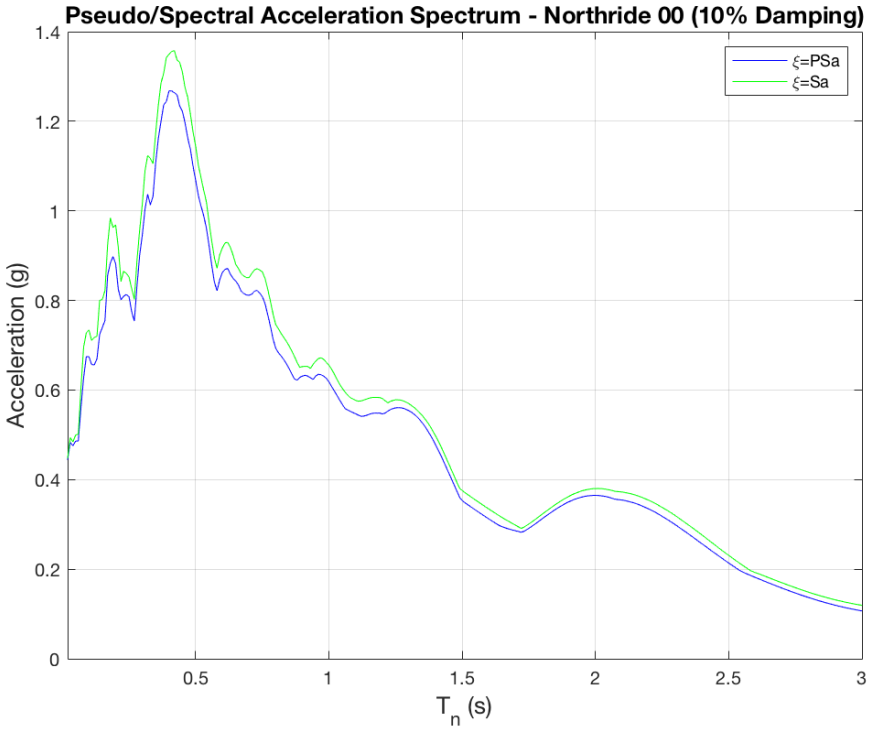

Figure 146: PSa and Sa (10% Damping) – Northridge 00 (USC Sta. 5303)

Appendix N: Normalized PSv Response Spectrums

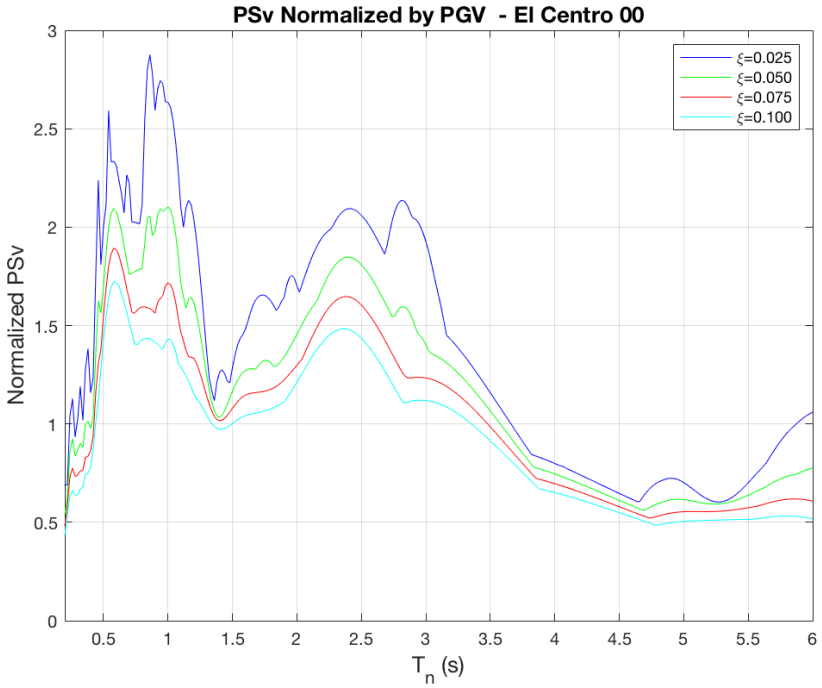

Figure 147: PSv Spectrum Normalized to PGV – El Centro 00

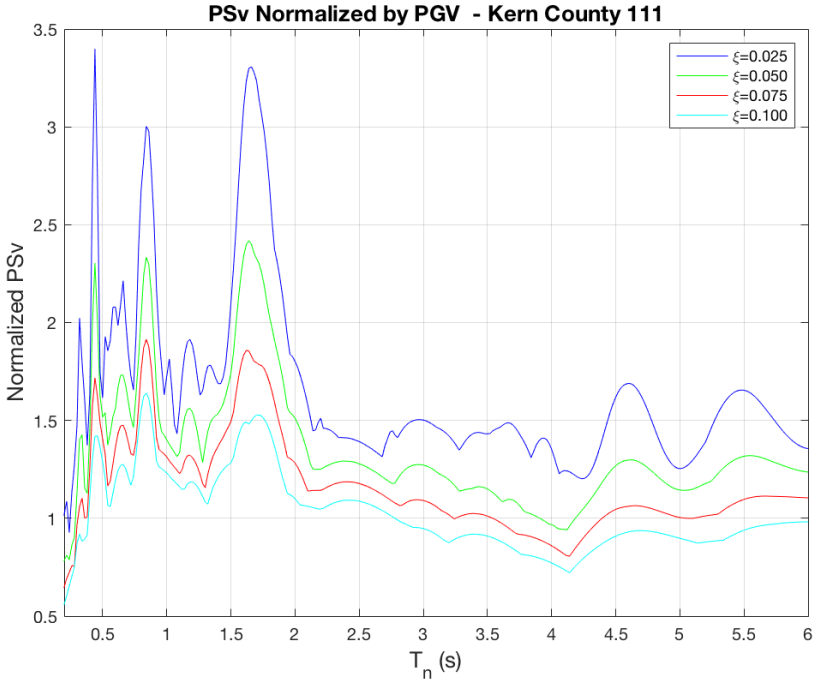

Figure 148: PSv Spectrum Normalized to PGV – Kern County 111

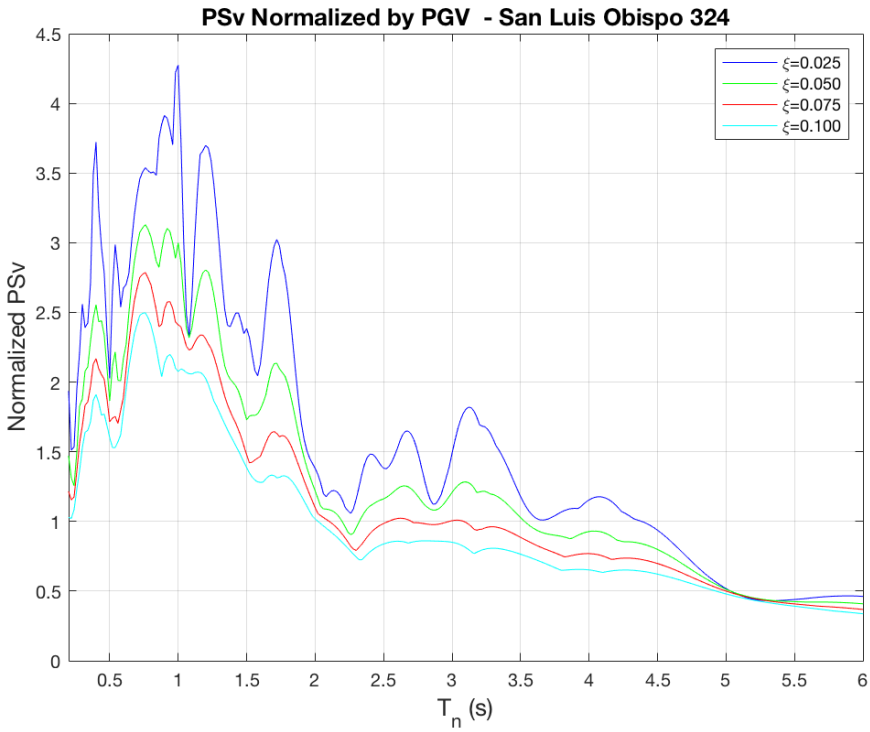

Figure 149: PSv Spectrum Normalized to PGV – San Luis Obispo 324

Appendix O: Two-Story Displacement History – El Centro

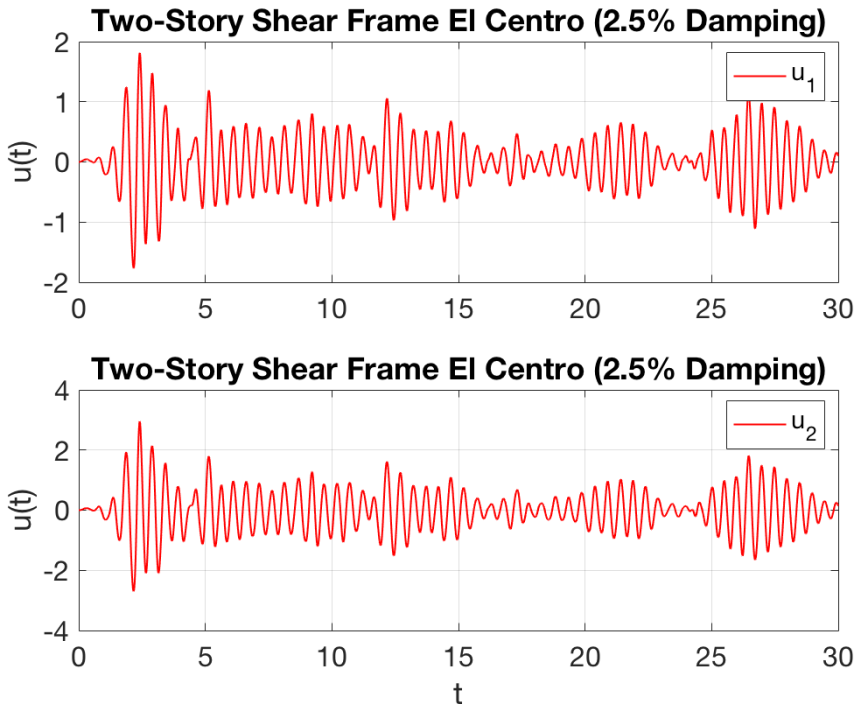

Figure 150: Two-Story El Centro Displacement History (ξ = 0.025)

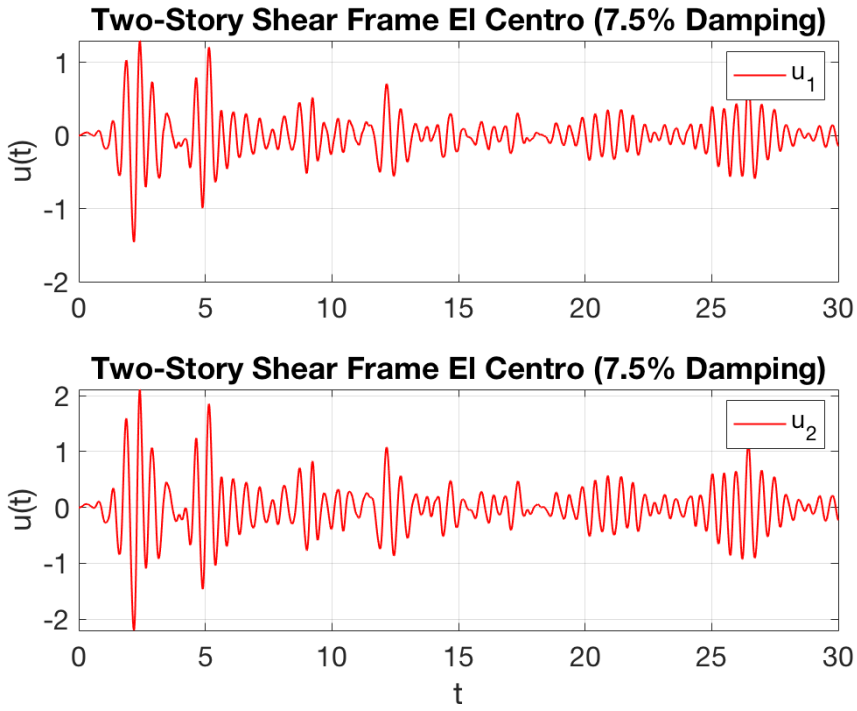

Figure 151: Two-Story El Centro Displacement History (ξ = 0.075)

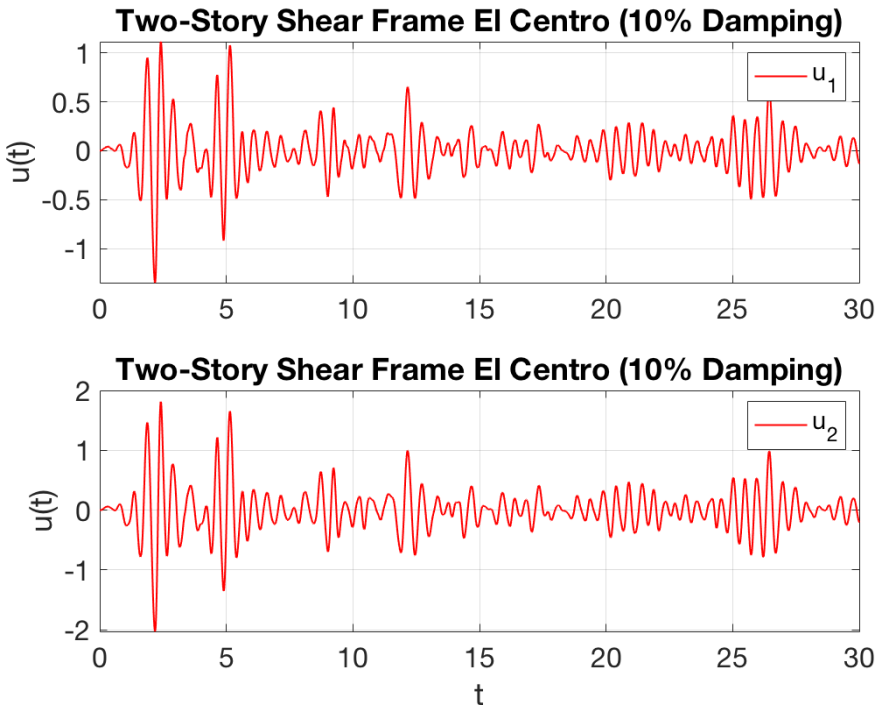

Figure 152: Two-Story El Centro Displacement History (ξ = 0.10)

Appendix P: Two-Story Displacement History – Kern County

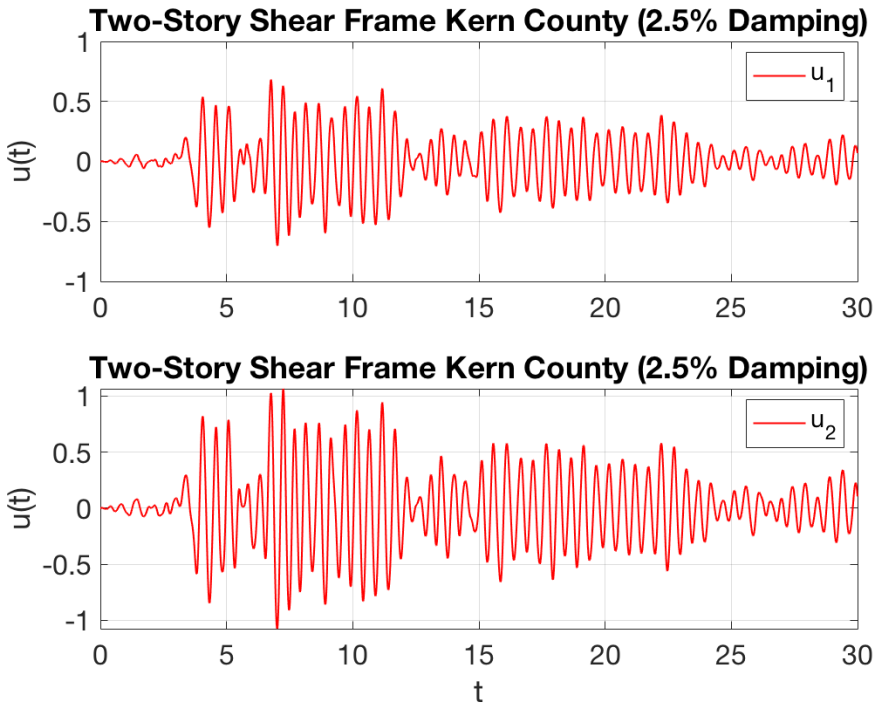

Figure 153: Two-Story Kern Displacement History (ξ = 0.025)

Figure 154: Two-Story Kern Displacement History (ξ = 0.075)

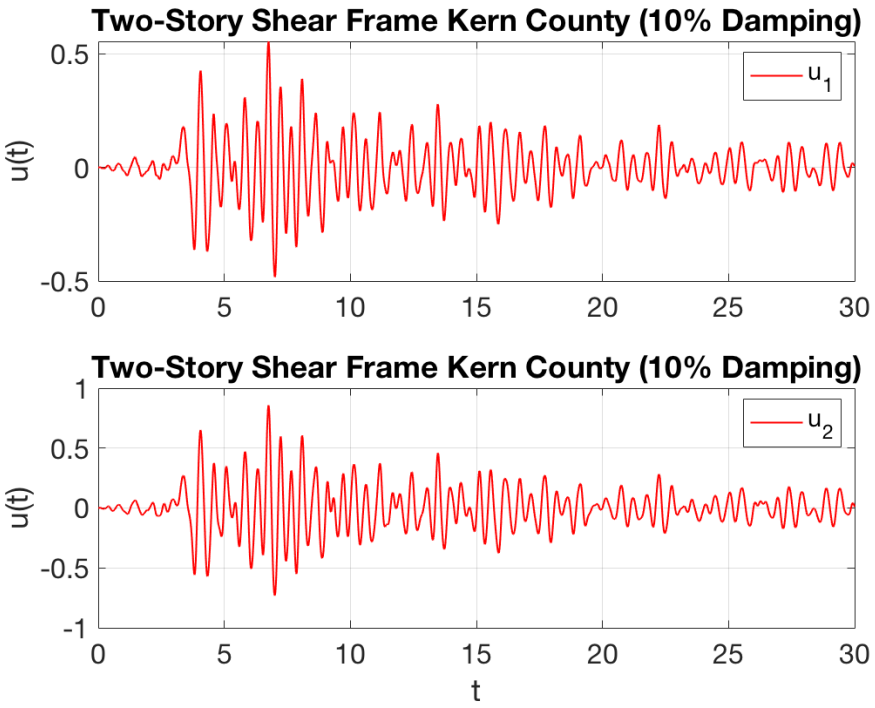

Figure 155: Two-Story Kern Displacement History (ξ = 0.10)

Appendix Q: Two-Story Displacement History – SLO

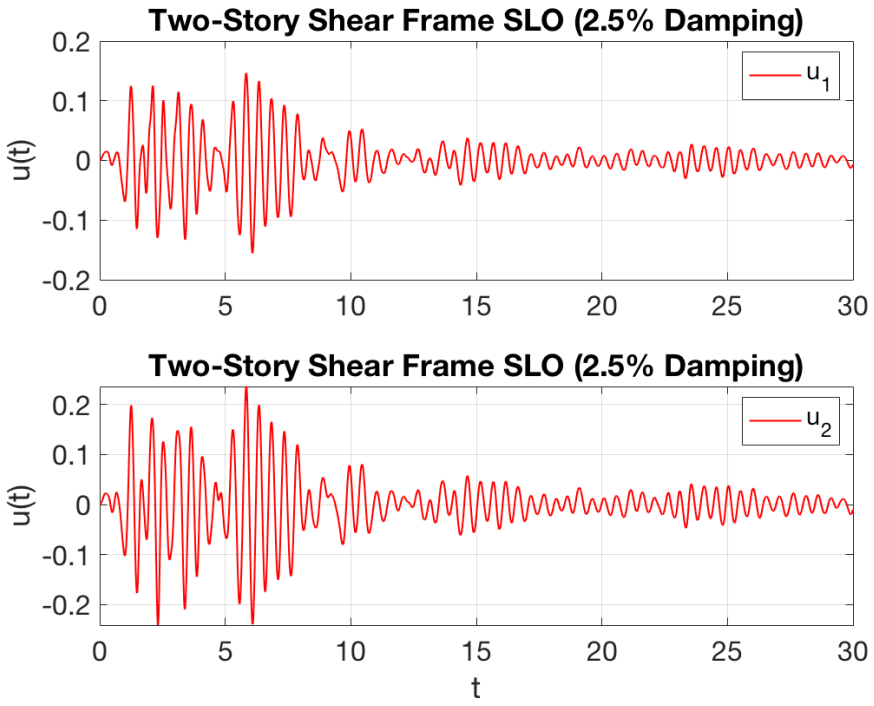

Figure 156: Two-Story SLO Displacement History (ξ = 0.025)

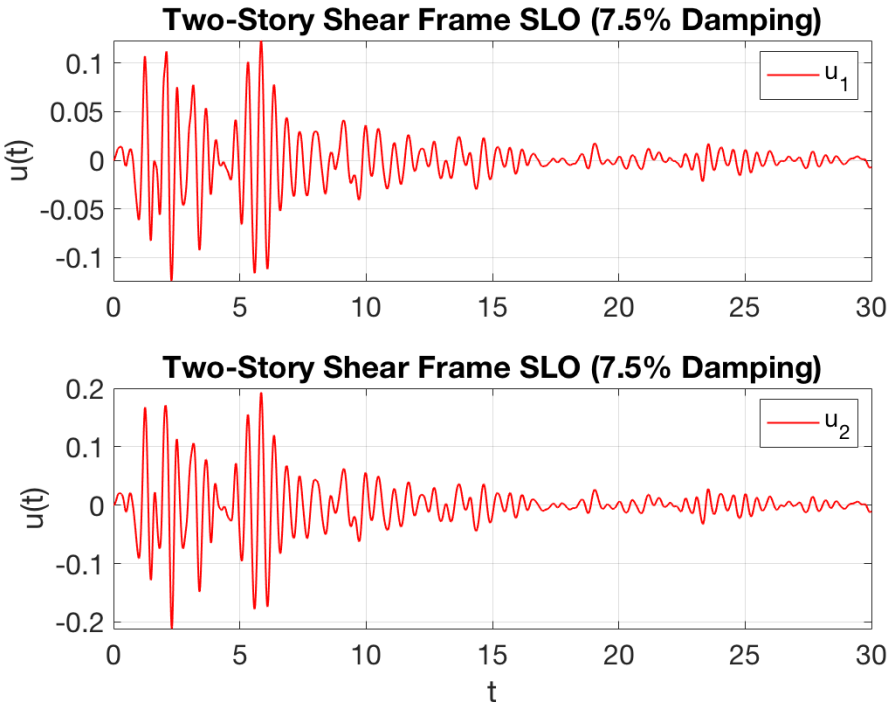

Figure 157: Two-Story SLO Displacement History (ξ = 0.075)

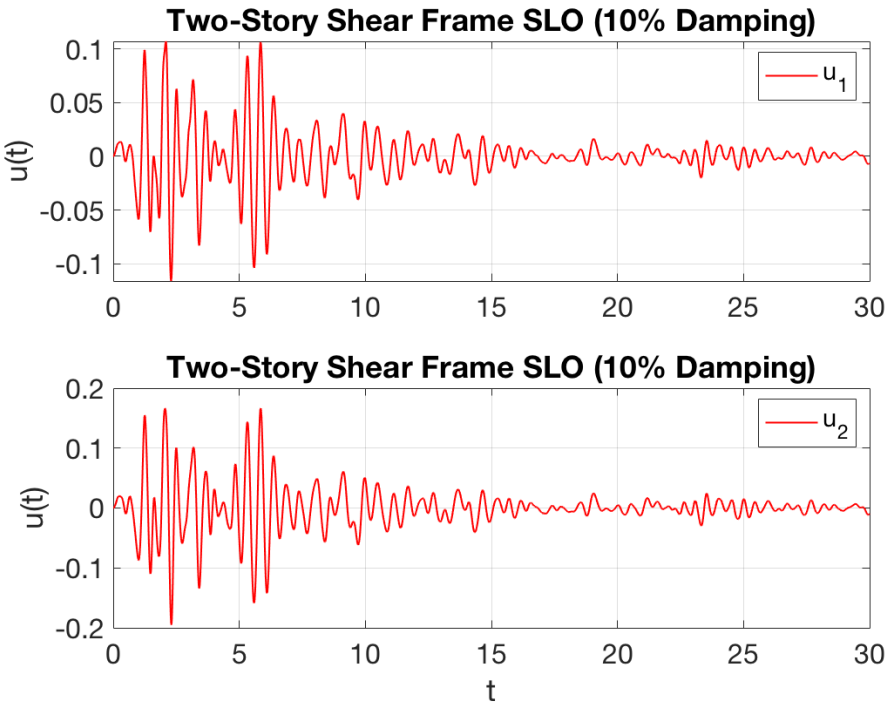

Figure 158: Two-Story SLO Displacement History (ξ = 0.10)

Appendix R: Two-Story Displacement History – Loma Prieta

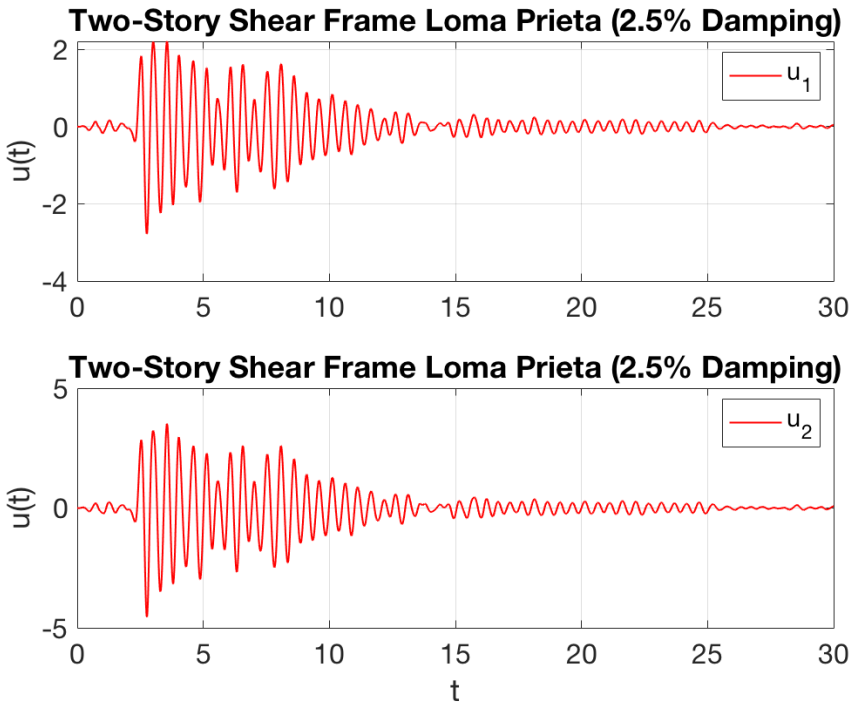

Figure 159: Two-Story Loma Displacement History (ξ = 0.025)

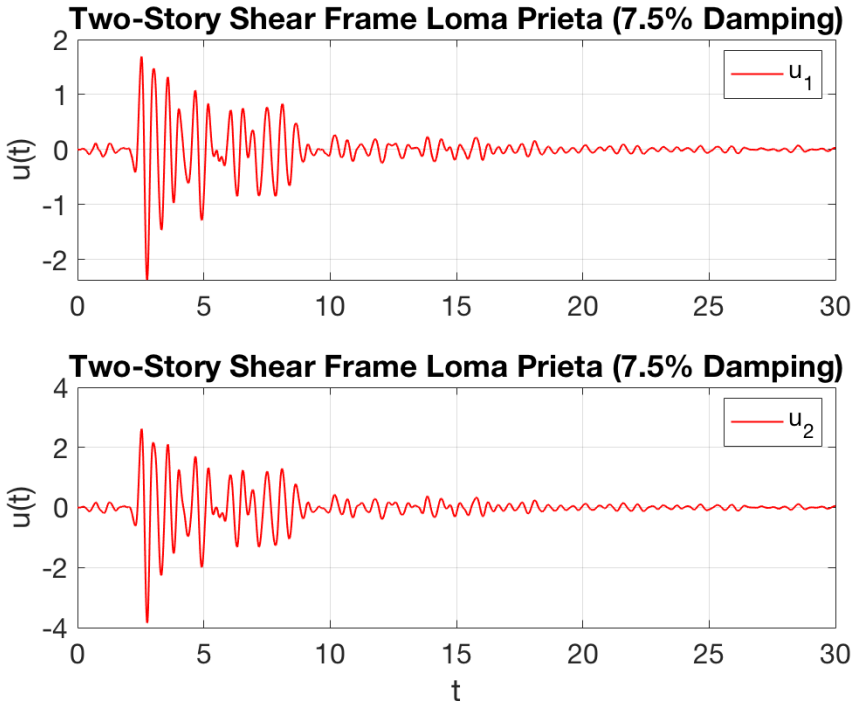

Figure 160: Two-Story Loma Displacement History (ξ = 0.075)

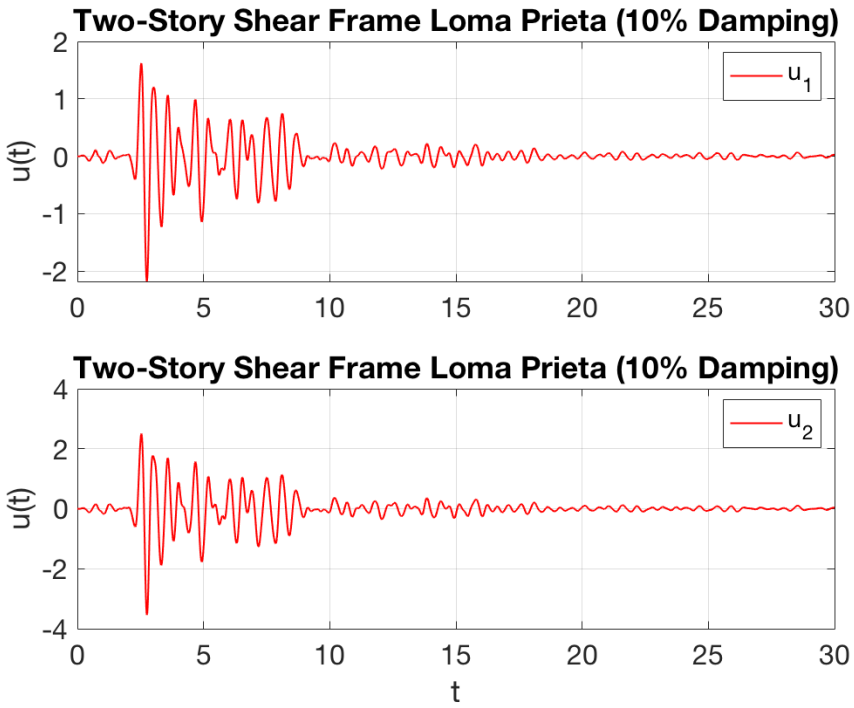

Figure 161: Two-Story Loma Displacement History (ξ = 0.10)

Appendix S: Two-Story Displacement History - Northridge

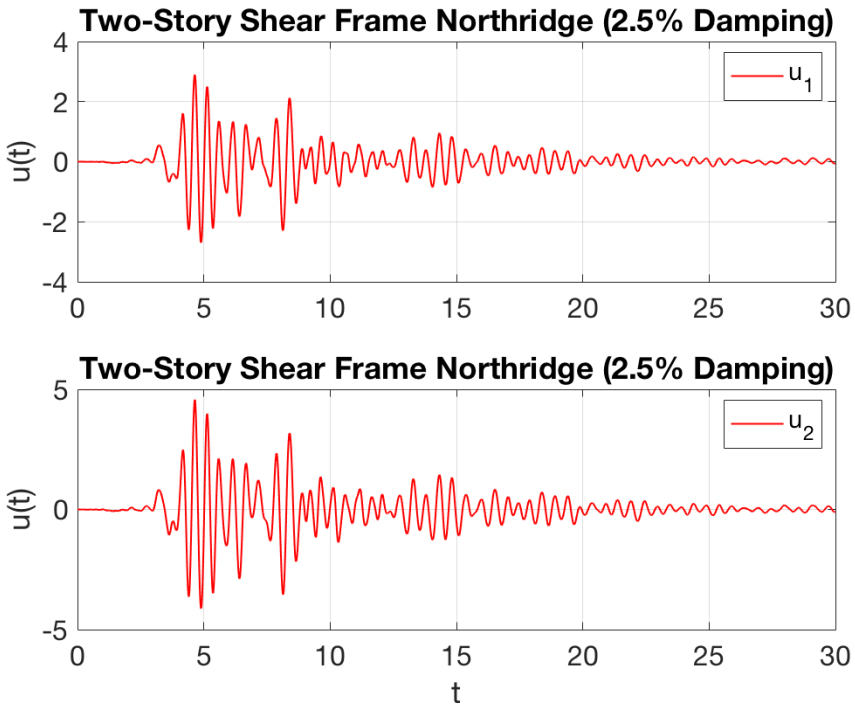

Figure 162: Two-Story Northridge Displacement History (ξ = 0.025)

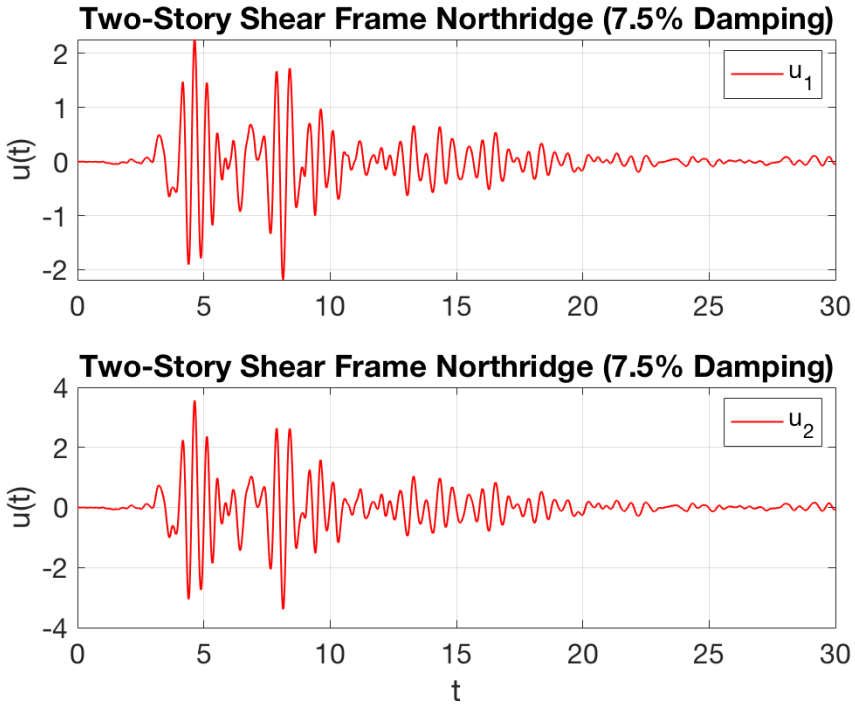

Figure 163: Two-Story Northridge Displacement History (ξ = 0.075)

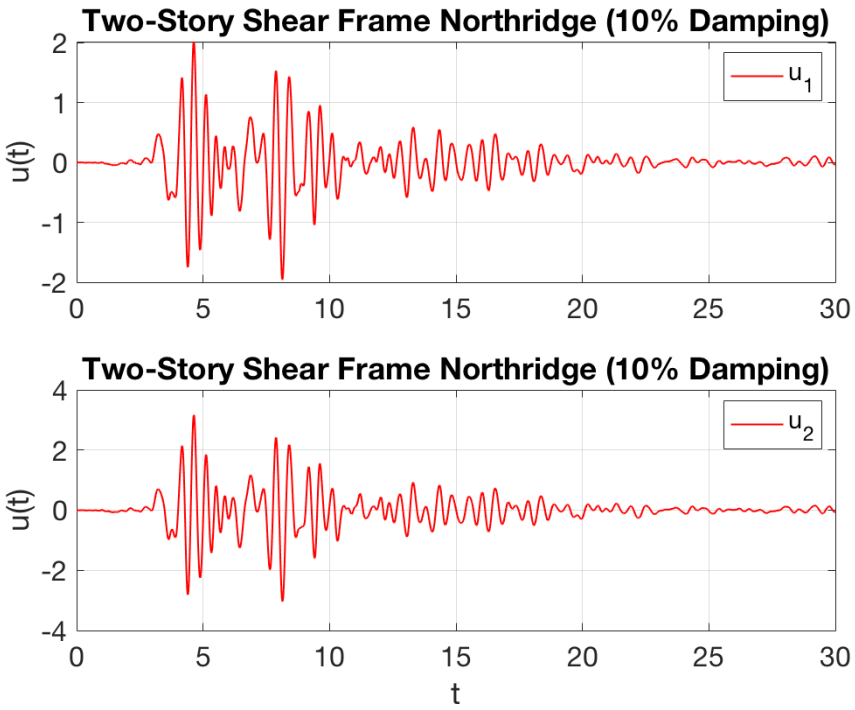

Figure 164: Two-Story Northridge Displacement History (ξ = 0.10)

Appendix T: Three-Story Displacement History – El Centro

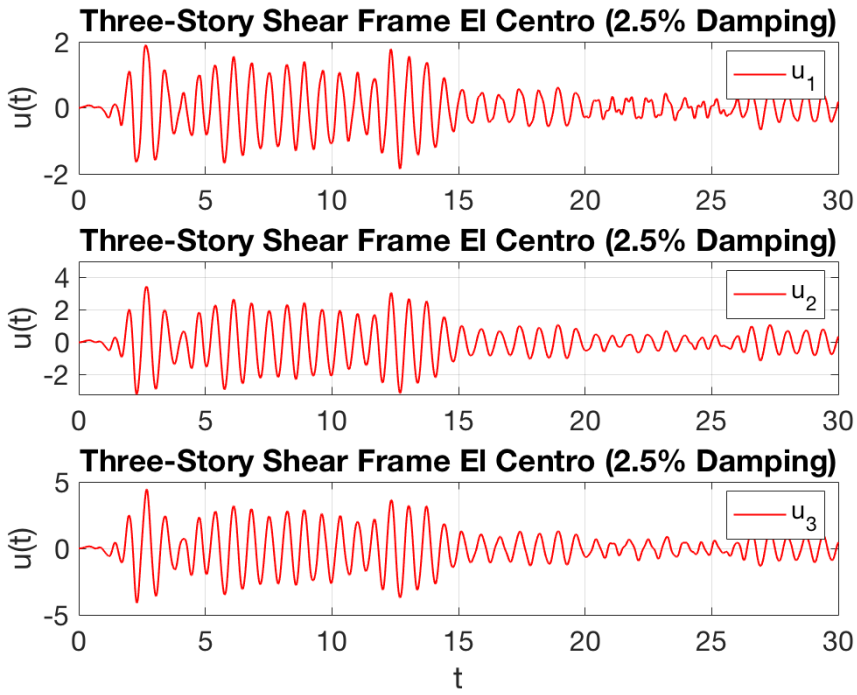

Figure 165: Three-Story El Centro Displacement History (ξ = 0.025)

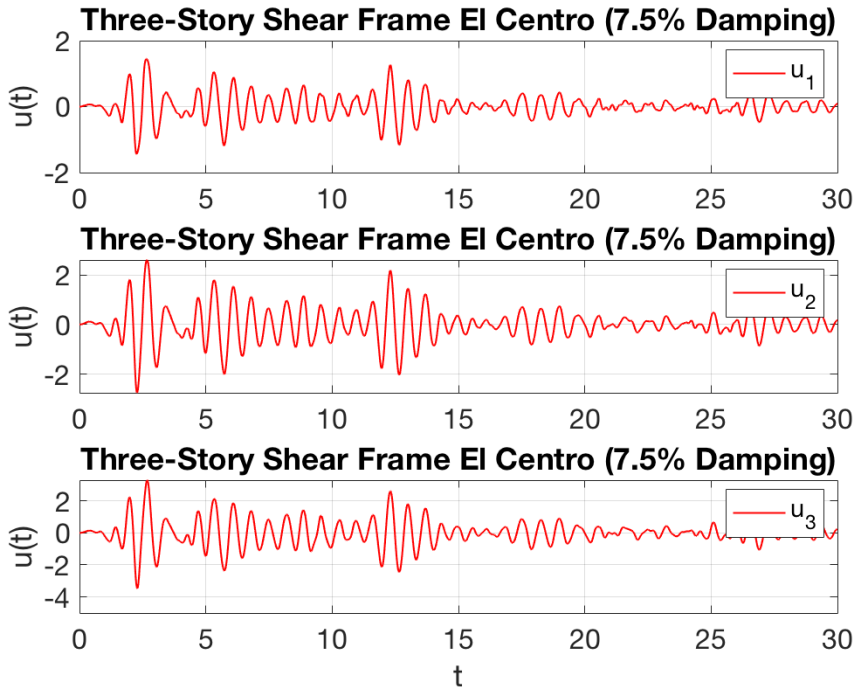

Figure 166: Three-Story El Centro Displacement History (ξ = 0.075)

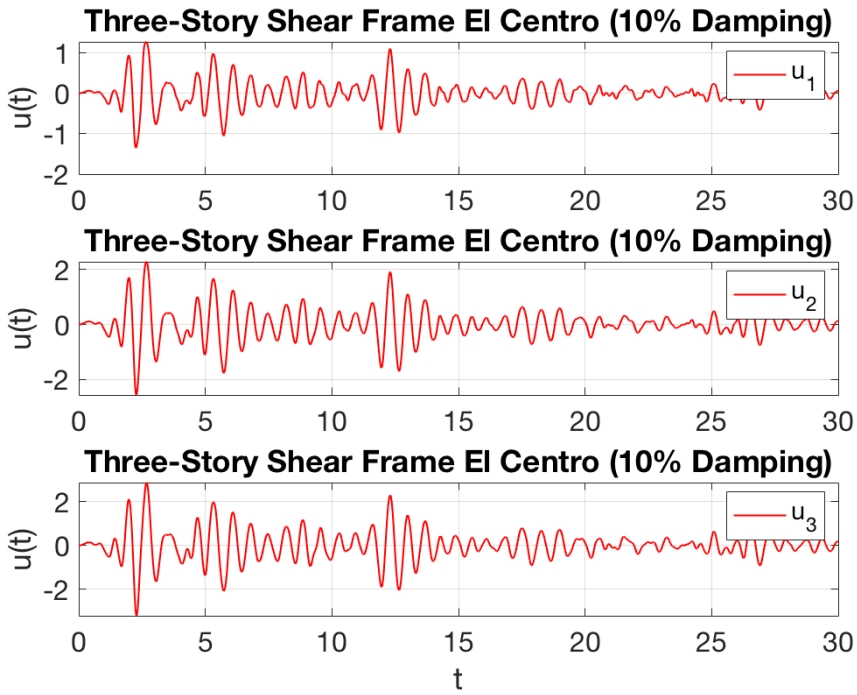

Figure 167: Three-Story El Centro Displacement History (ξ = 0.10)

Appendix U: Three-Story Displacement History – Kern County

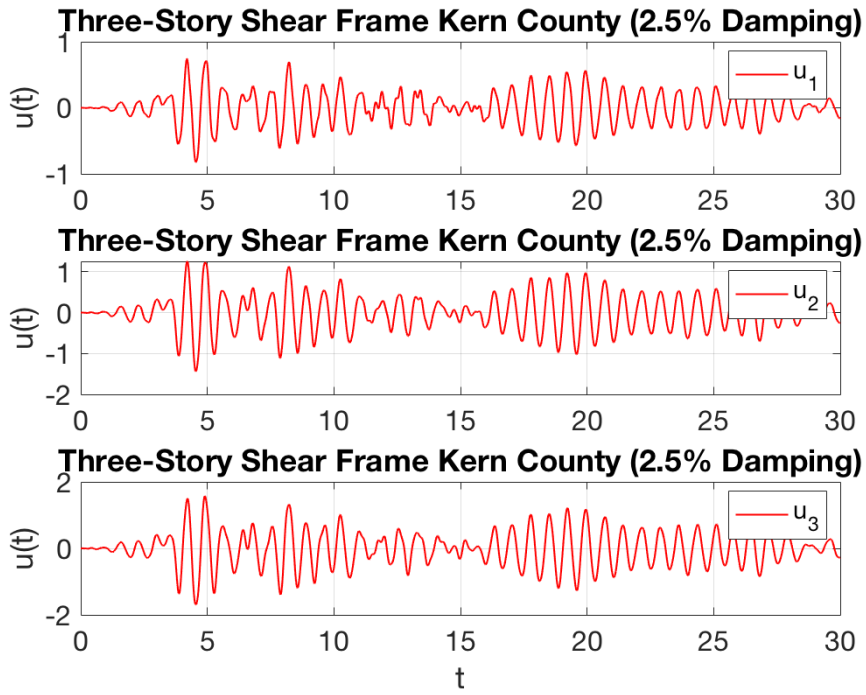

Figure 168: Three-Story Kern Displacement History (ξ = 0.025)

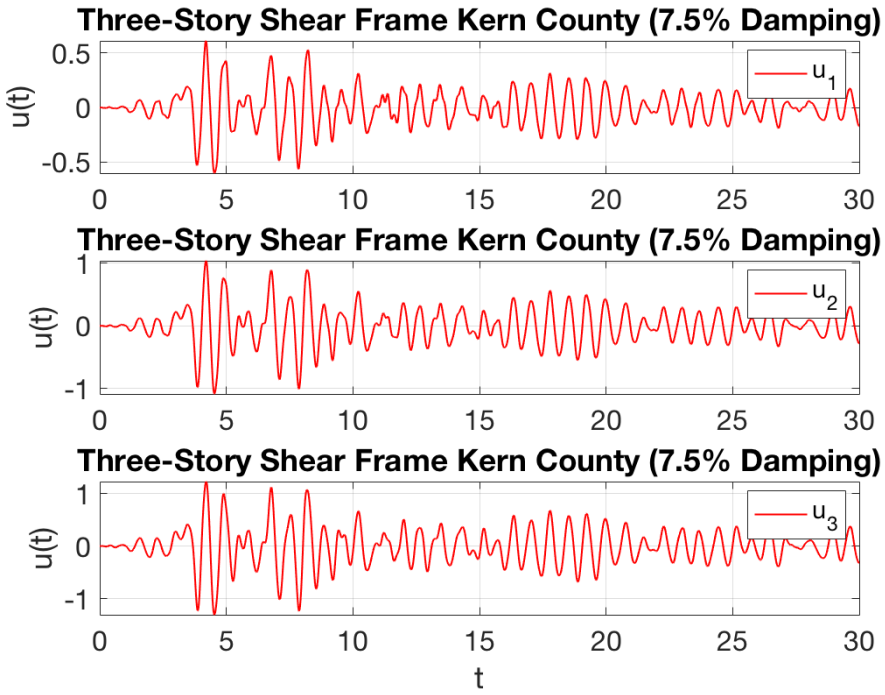

Figure 169: Three-Story Kern Displacement History (ξ = 0.075)

Figure 170: Three-Story Kern Displacement History (ξ = 0.10)

Appendix V: Three-Story Displacement History - SLO

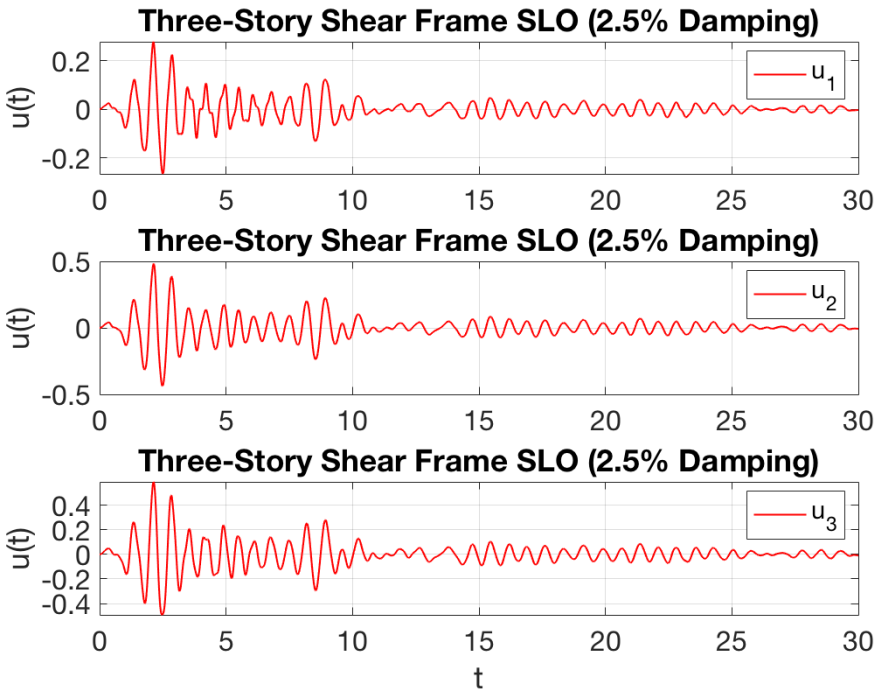

Figure 171: Three-Story SLO Displacement History (ξ = 0.025)

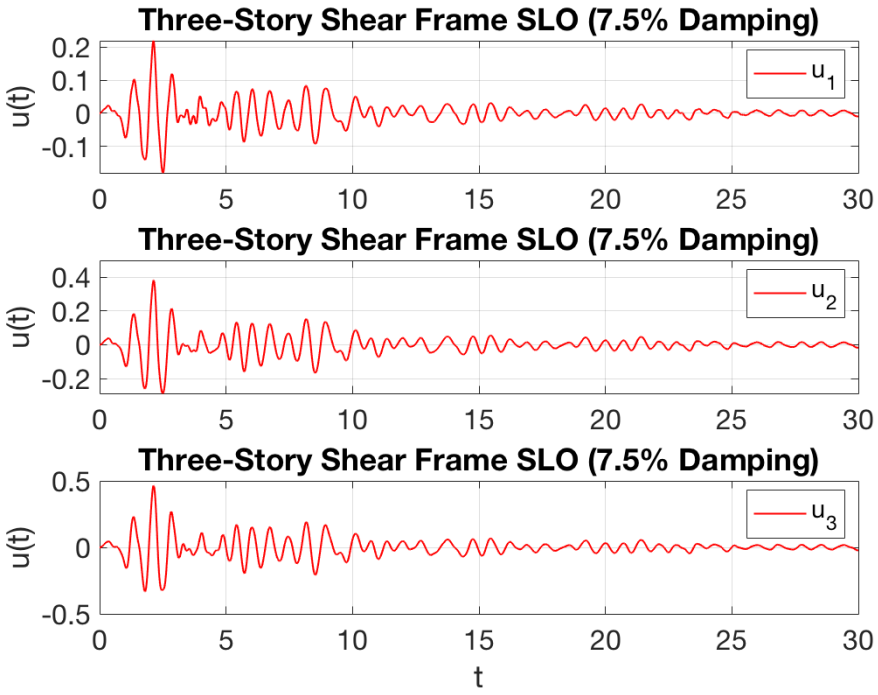

Figure 172: Three-Story SLO Displacement History (ξ = 0.075)

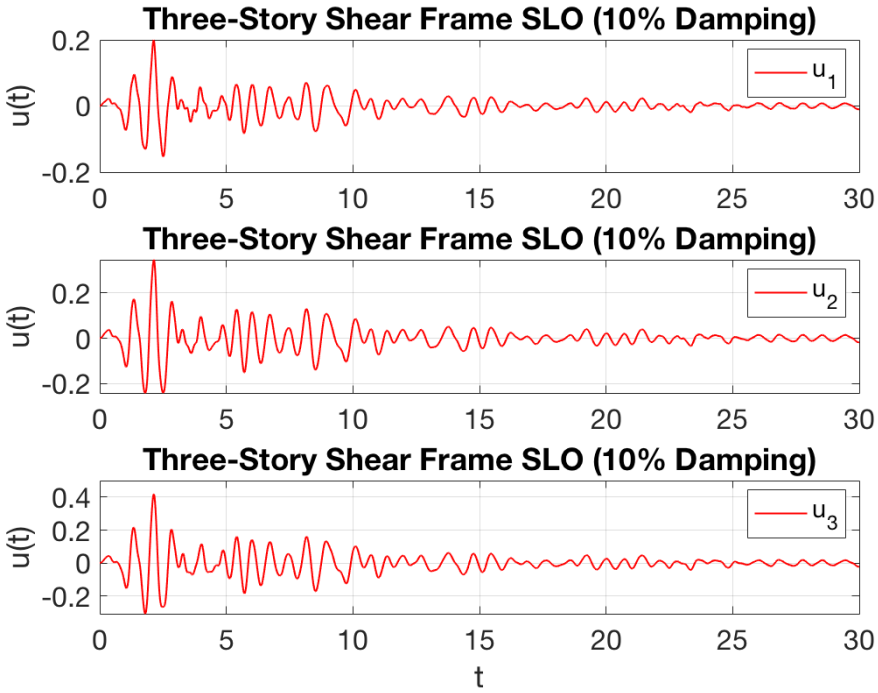

Figure 173: Three-Story SLO Displacement History (ξ = 0.10)

Appendix W: Three-Story Displacement History – Loma Prieta

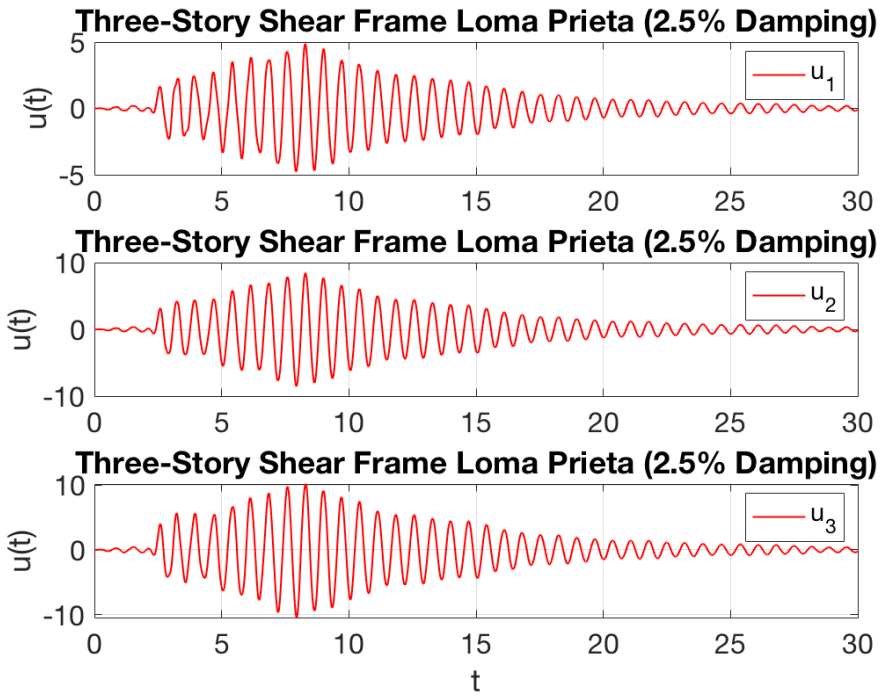

Figure 174: Three-Story Loma Displacement History (ξ = 0.025)

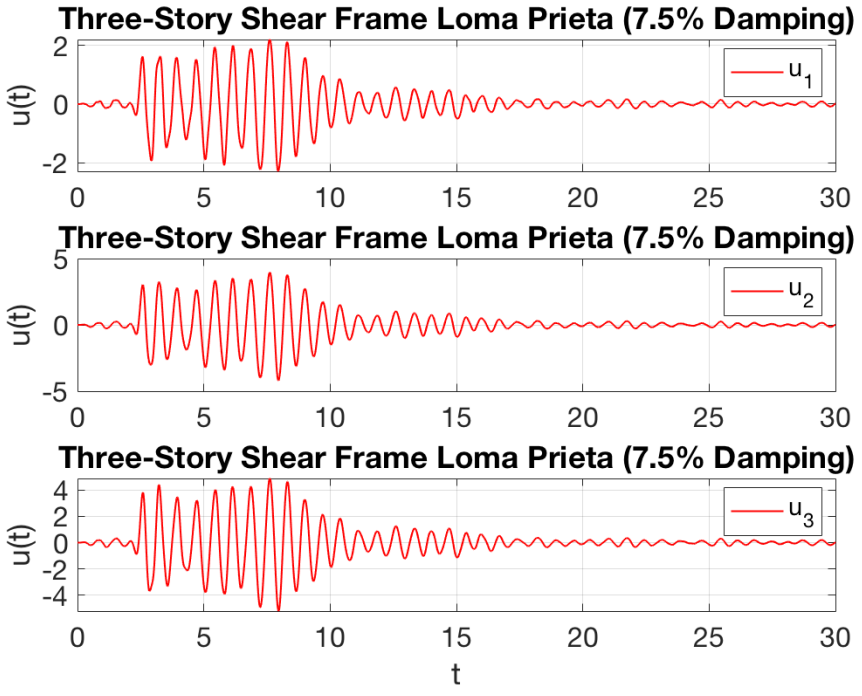

Figure 175: Three-Story Loma Displacement History (ξ = 0.075)

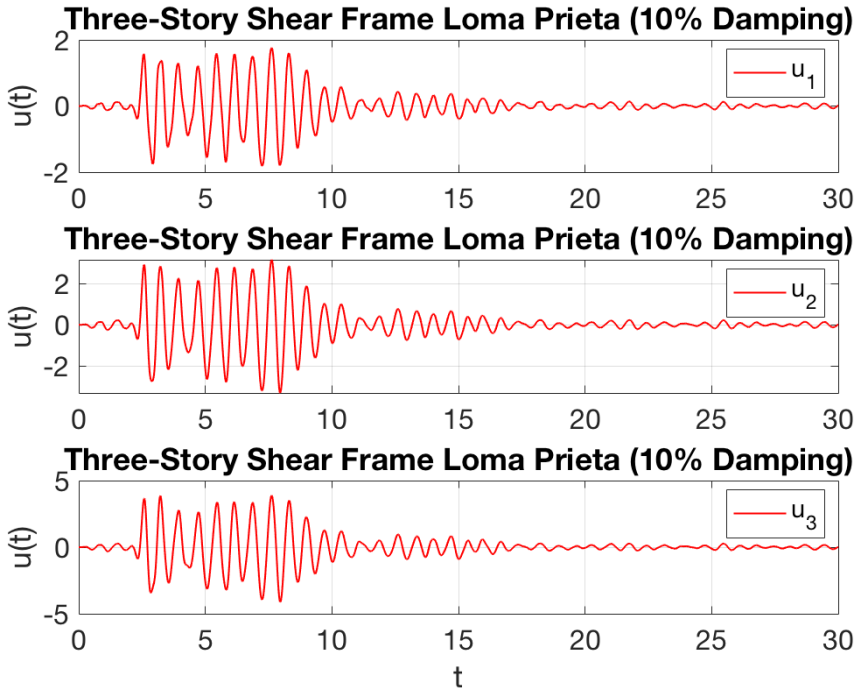

Figure 176: Three-Story Loma Displacement History (ξ = 0.10)

Appendix X: Three-Story Displacement History - Northridge

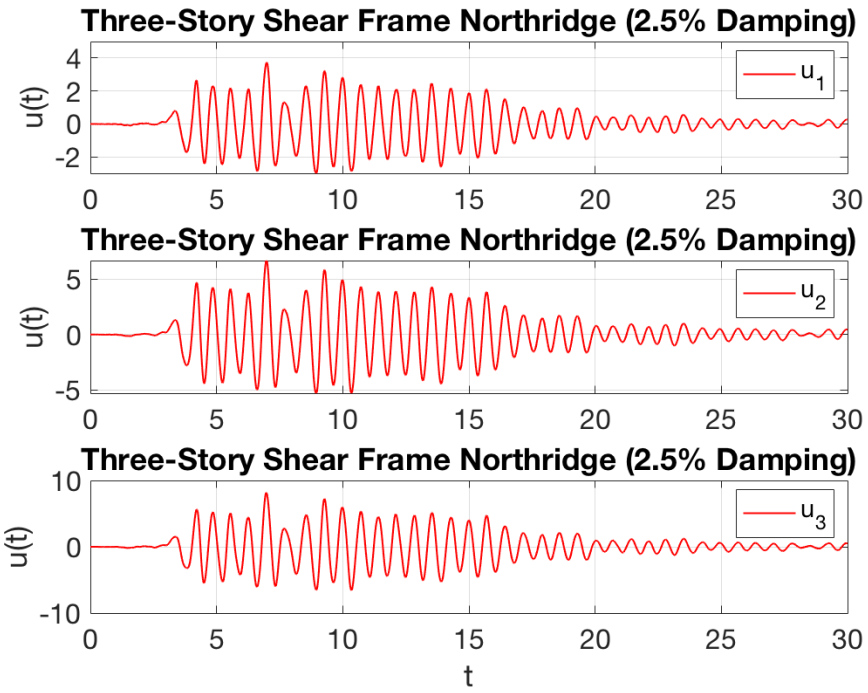

Figure 177: Three-Story Northridge Displacement History (ξ = 0.025)

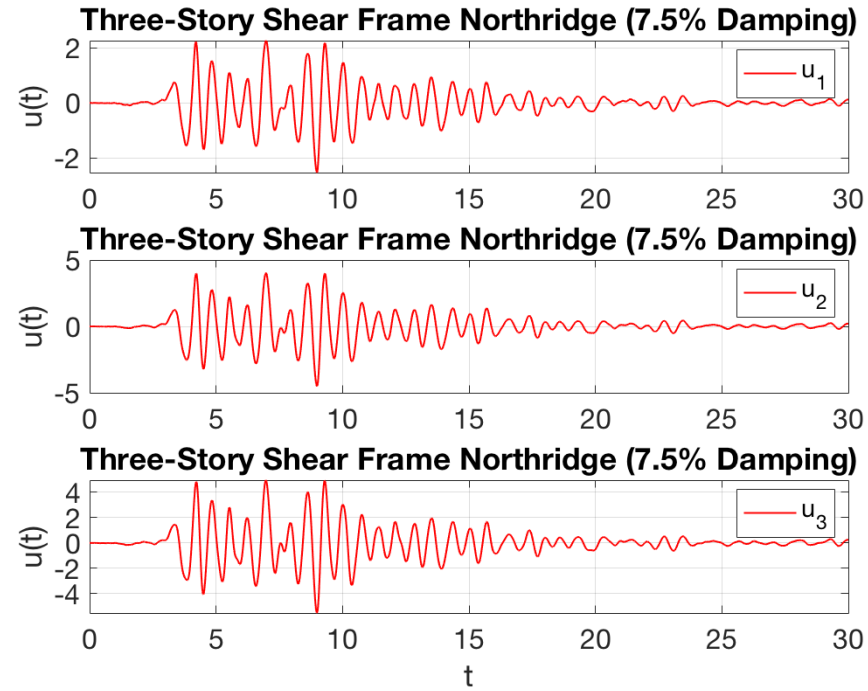

Figure 178: Three-Story Northridge Displacement History (ξ = 0.075)

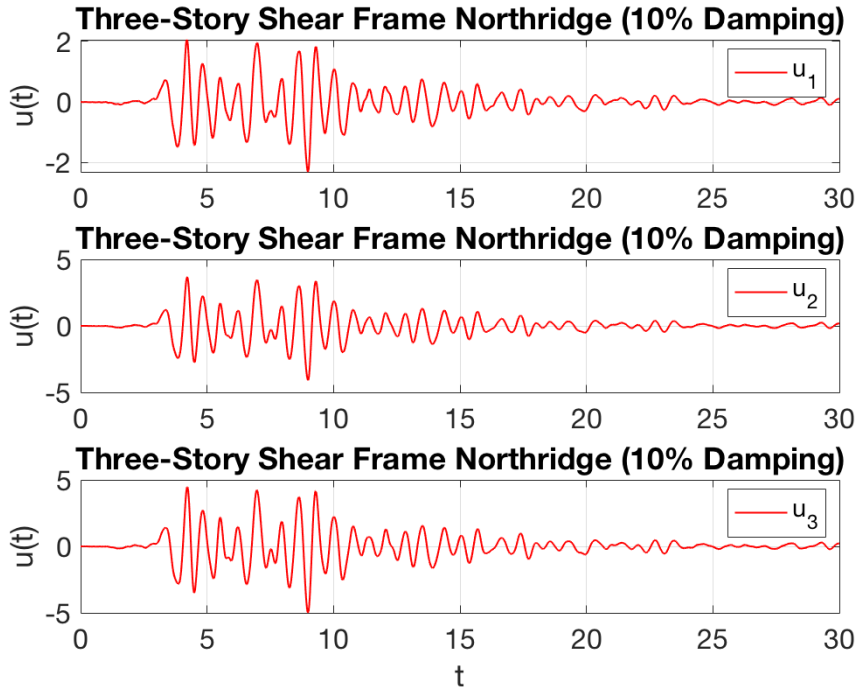

Figure 179: Three-Story Northridge Displacement History (ξ = 0.10)

Appendix Y: Two-Story FSD Force-Travel Diagrams

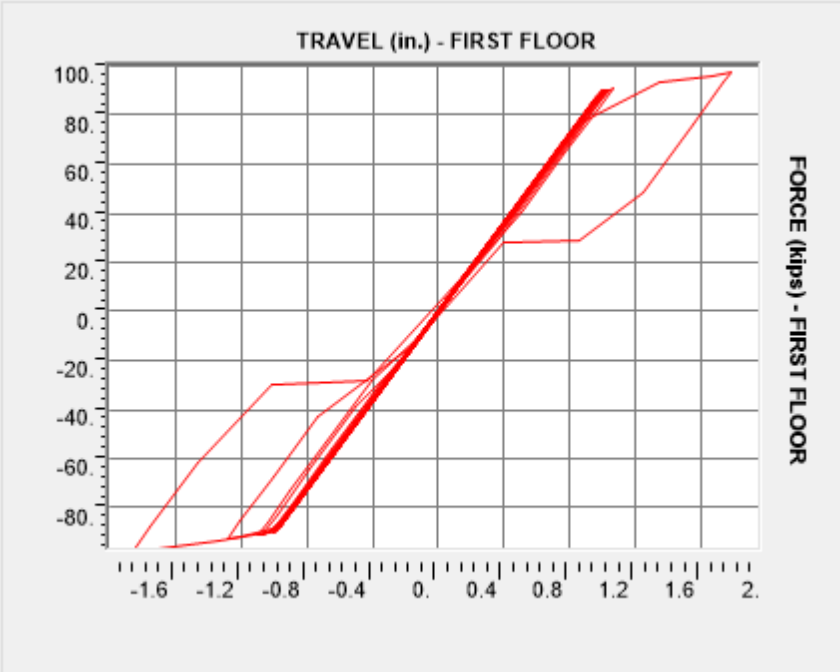

Figure 180: Force-Travel Two-Story Lower FSD Loma 10%

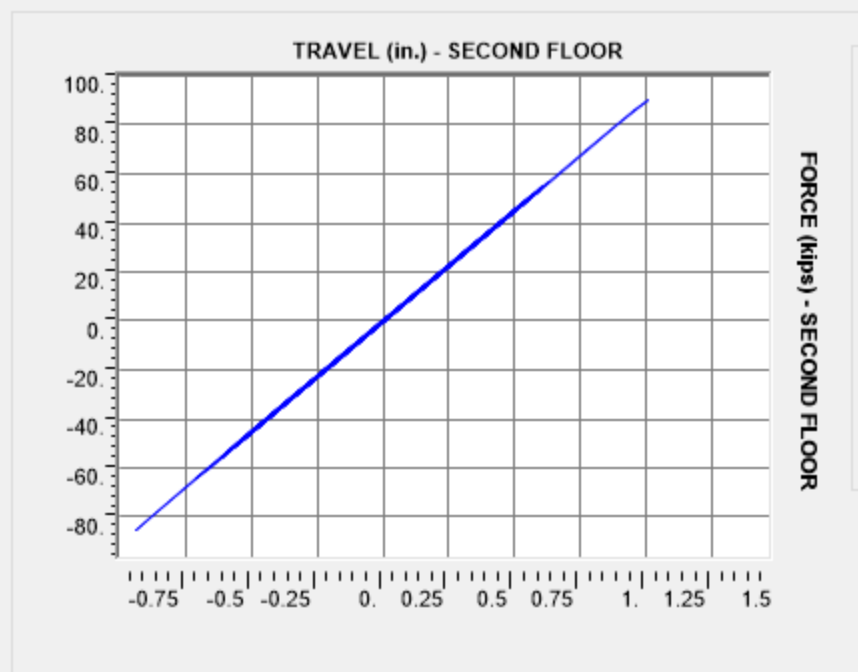

Figure 181: Force-Travel Two-Story Upper FSD Loma 10%

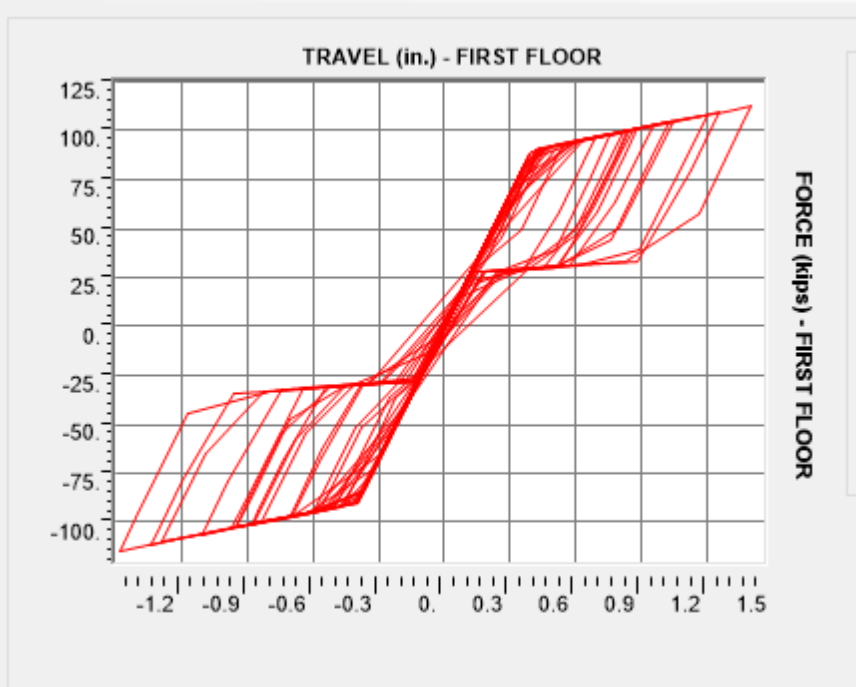

Figure 182: Force-Travel Two-Story Lower FSD Loma 25%

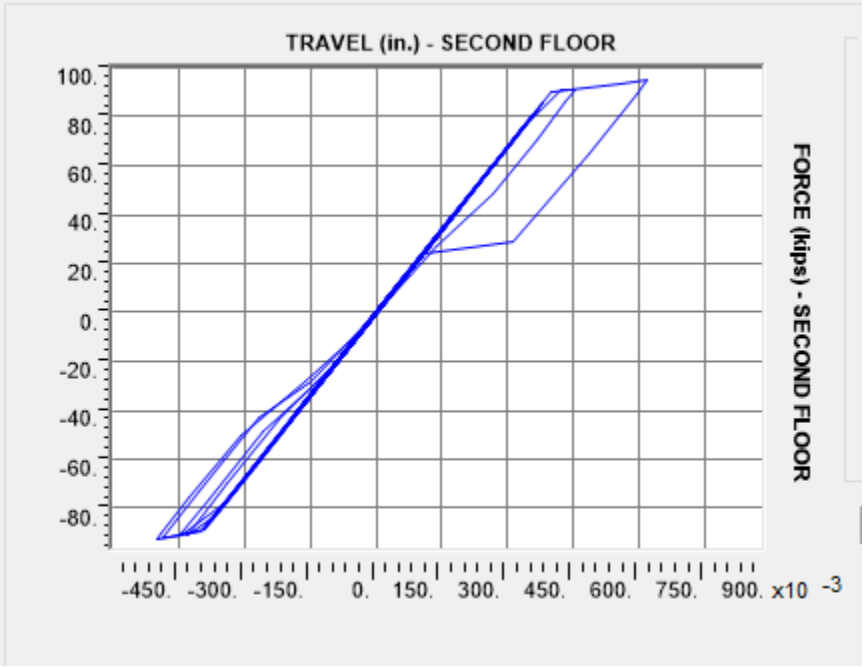

Figure 183: Force-Travel Two-Story Upper FSD Loma 25%

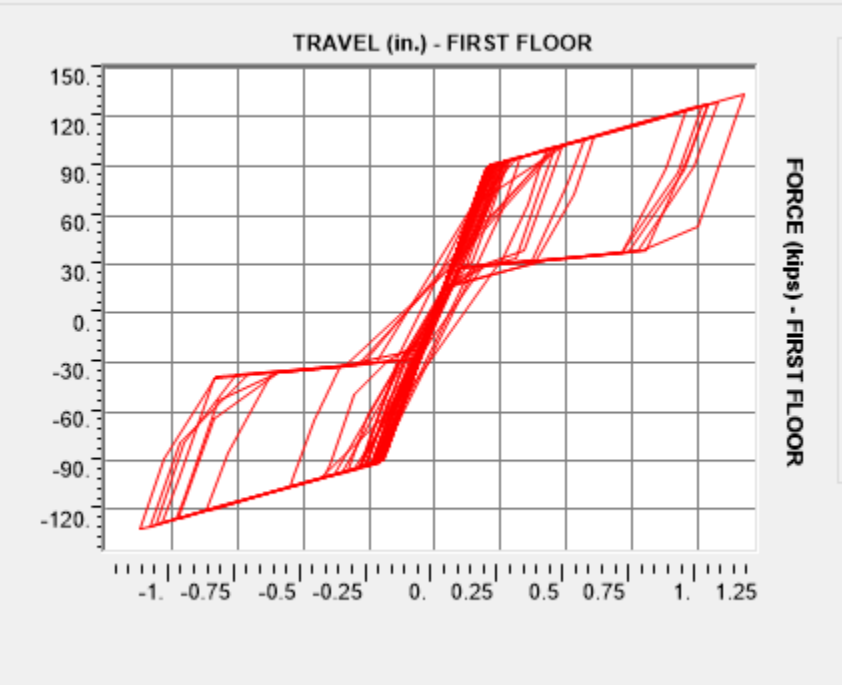

Figure 184: Force-Travel Two-Story Lower FSD Loma 50%

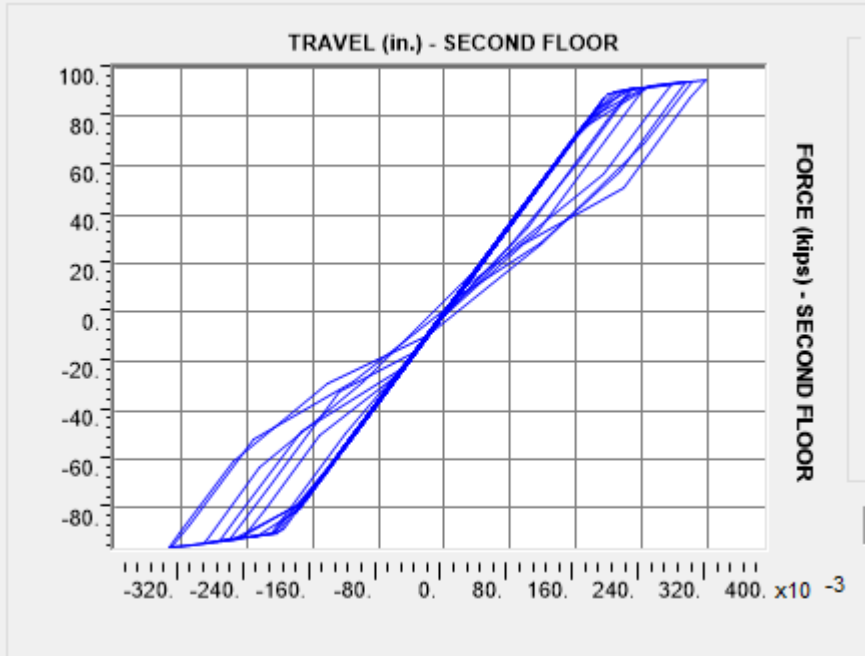

Figure 185: Force-Travel Two-Story Upper FSD Loma 50%

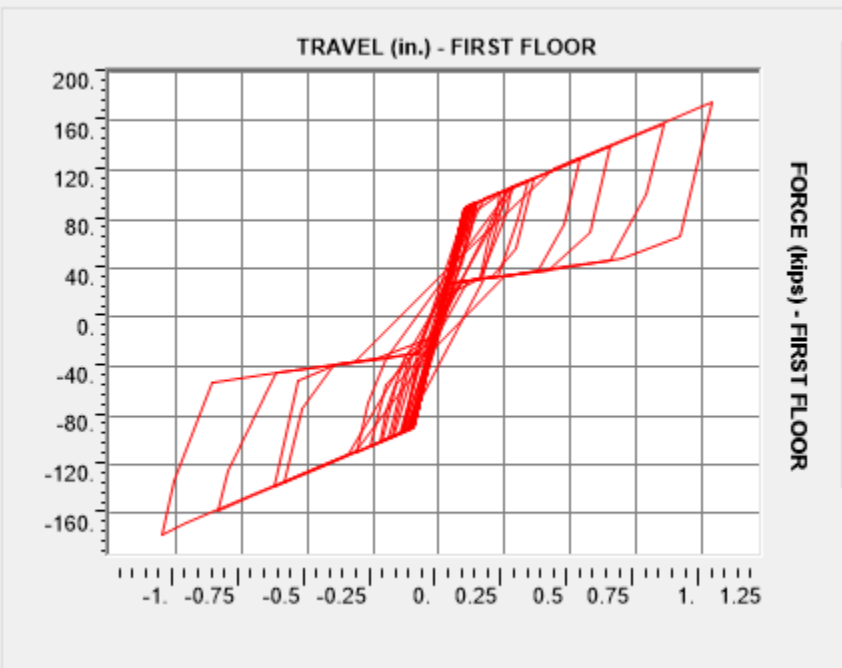

Figure 186: Force-Travel Two-Story Lower FSD Loma 100%

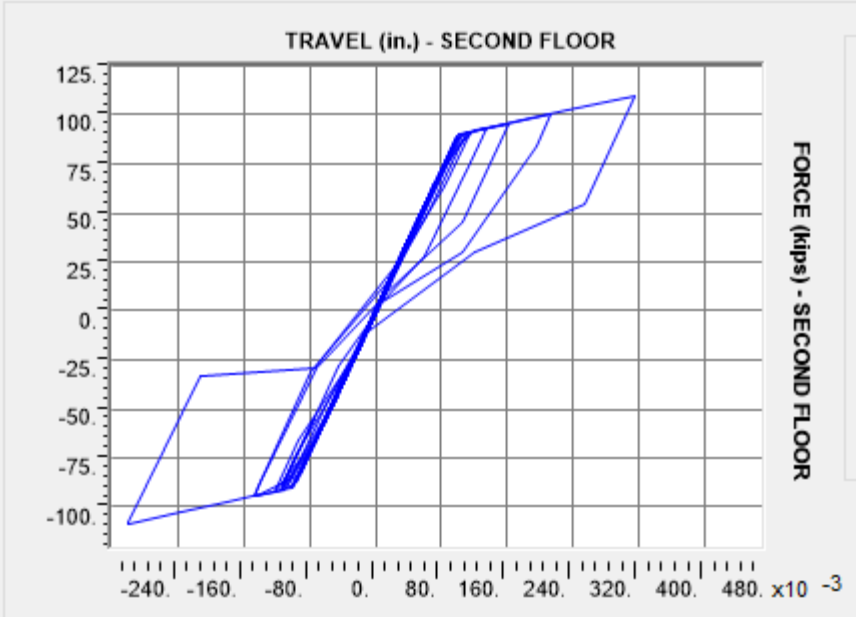

Figure 187: Force-Travel Two-Story Upper FSD Loma 100%

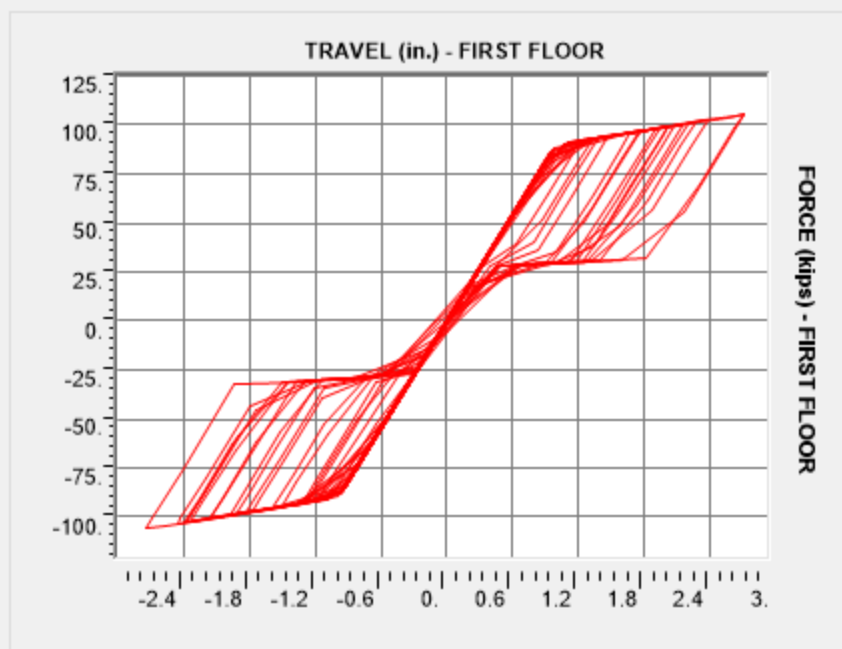

Figure 188: Force-Travel Two-Story Lower FSD Northridge 10%

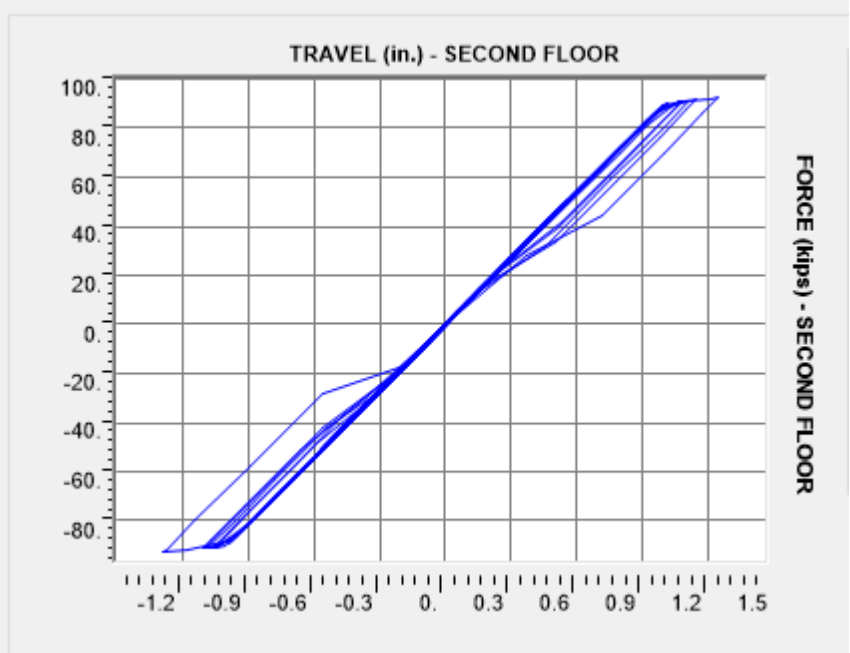

Figure 189: Force-Travel Two-Story Upper FSD Northridge 10%

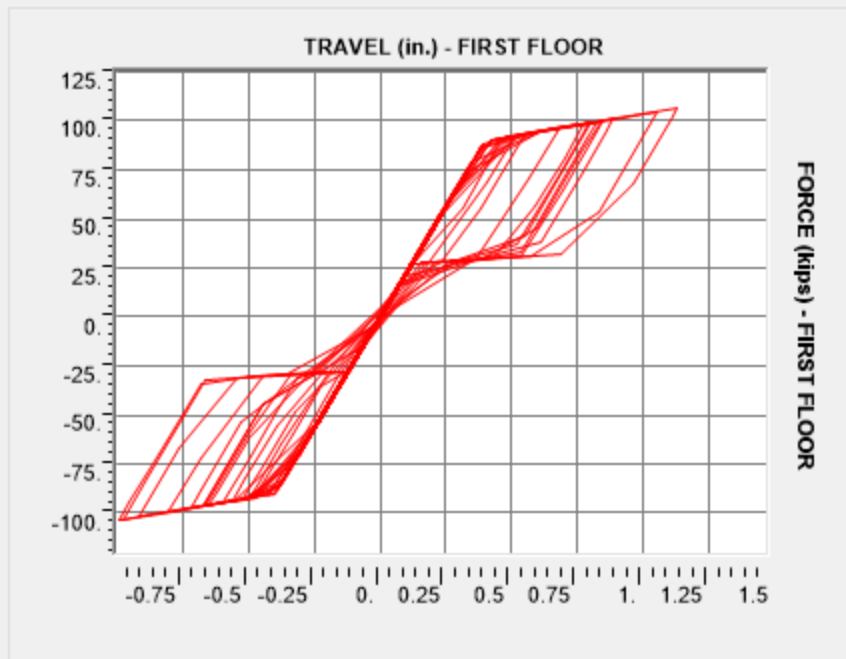

Figure 190: Force-Travel Two-Story Lower FSD Northridge 25%

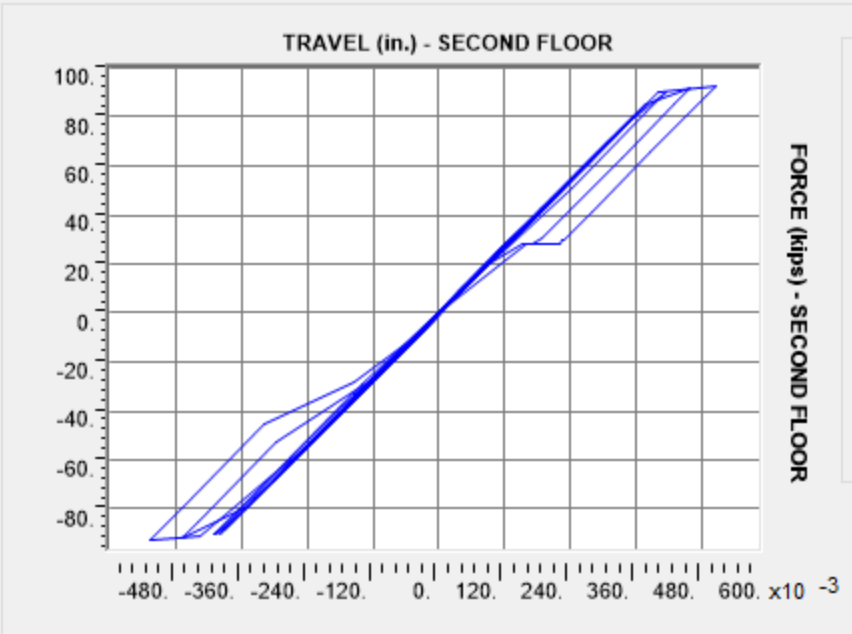

Figure 191: Force-Travel Two-Story Lower FSD Northridge 25%

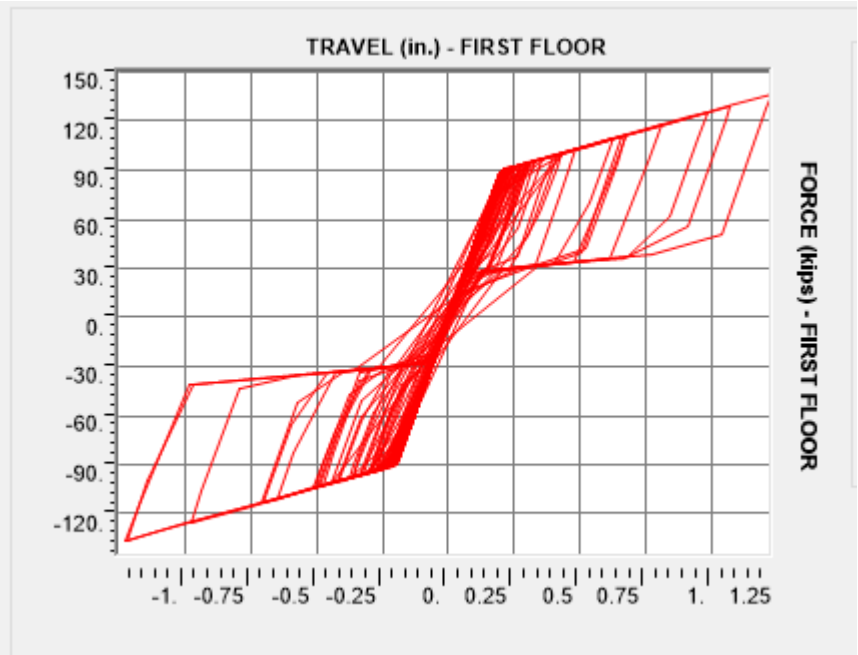

Figure 192: Force-Travel Two-Story Lower FSD Northridge 50%

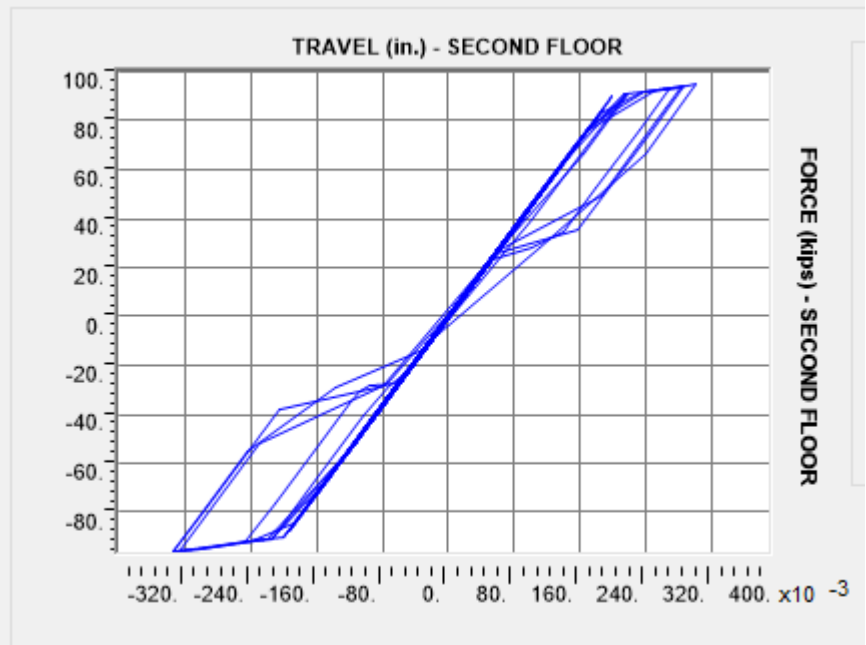

Figure 193: Force-Travel Two-Story Upper FSD Northridge 50%

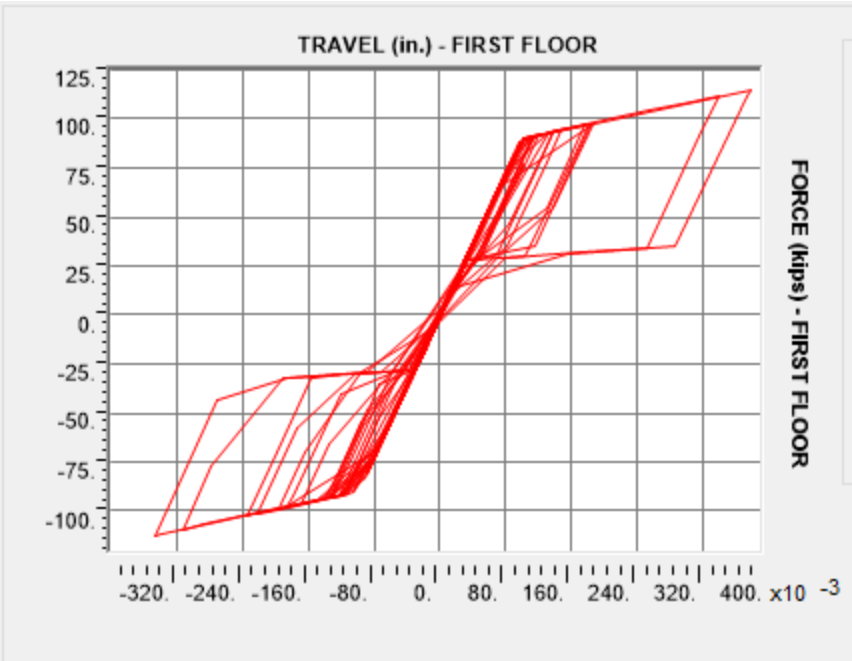

Figure 194: Force-Travel Two-Story Lower FSD Northridge 100%

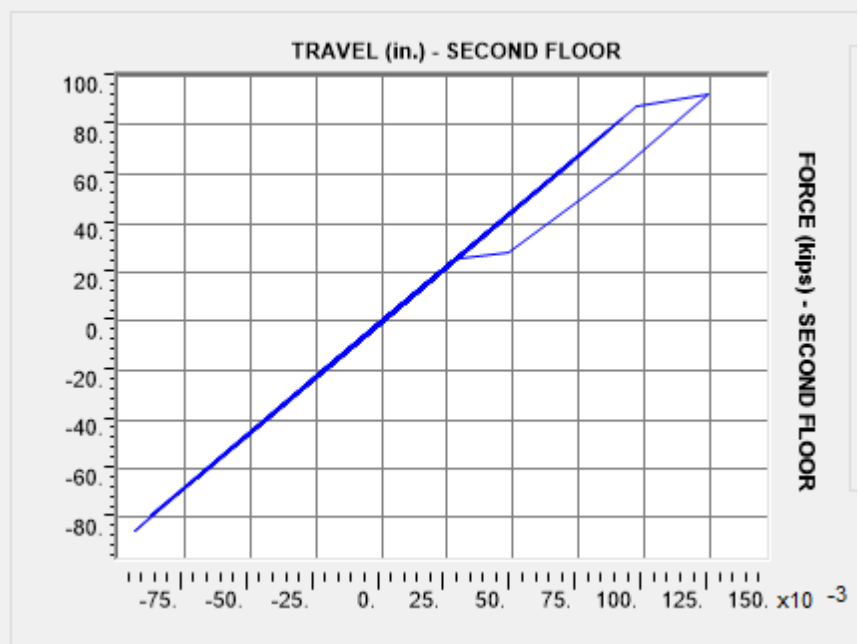

Figure 195: Force-Travel Two-Story Upper FSD Northridge 100%

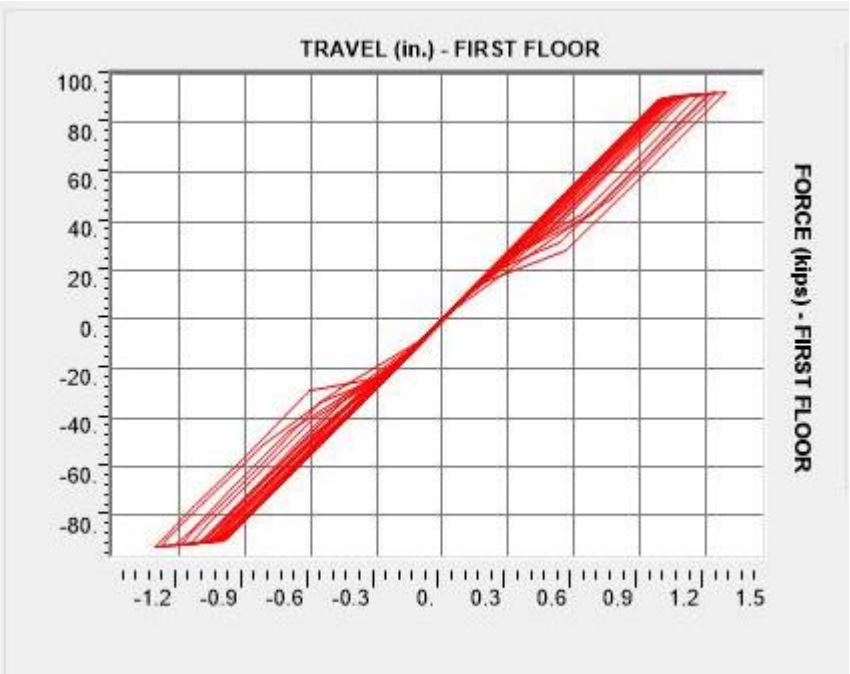

Figure 196: Force-Travel Two-Story Lower FSD El Centro 10%

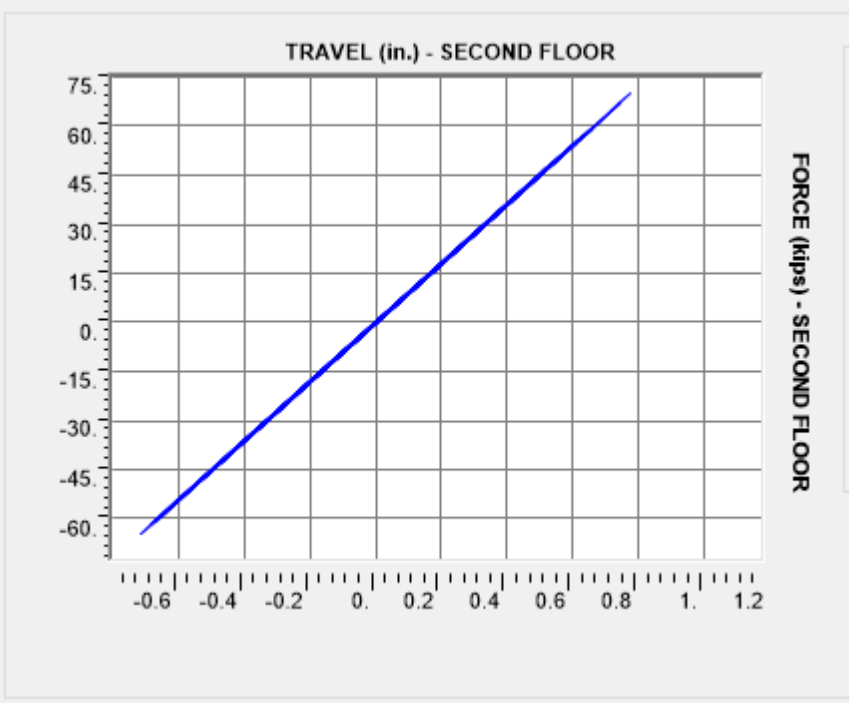

Figure 197: Force-Travel Two-Story Upper FSD El Centro 10%

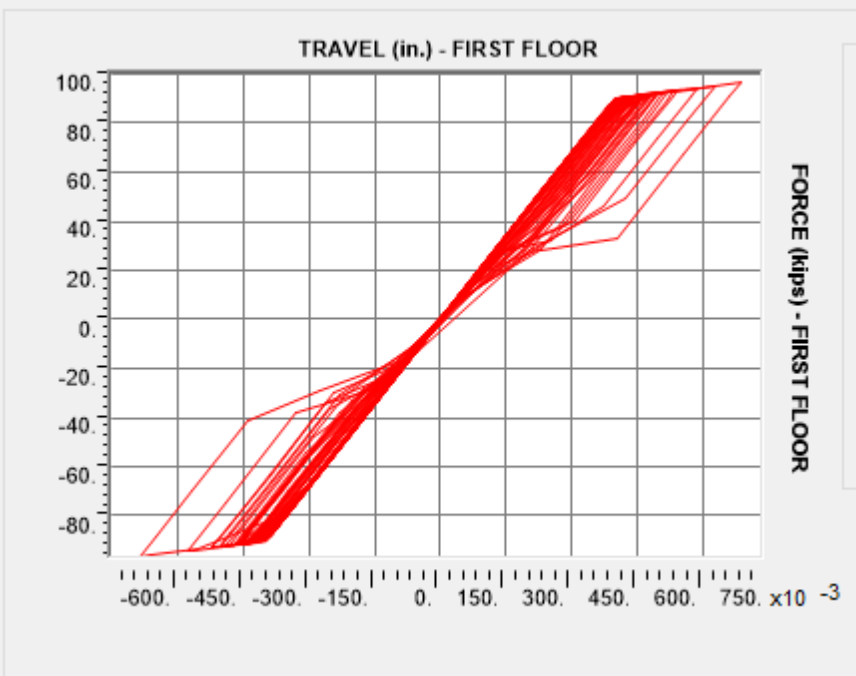

Figure 198: Force-Travel Two-Story Lower FSD El Centro 25%

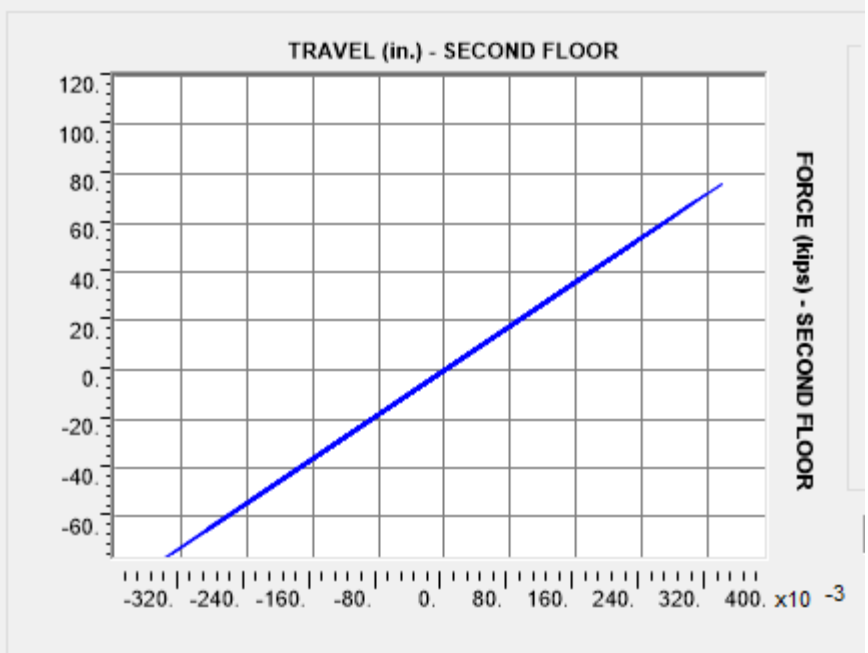

Figure 199: Force-Travel Two-Story Upper FSD El Centro 25%

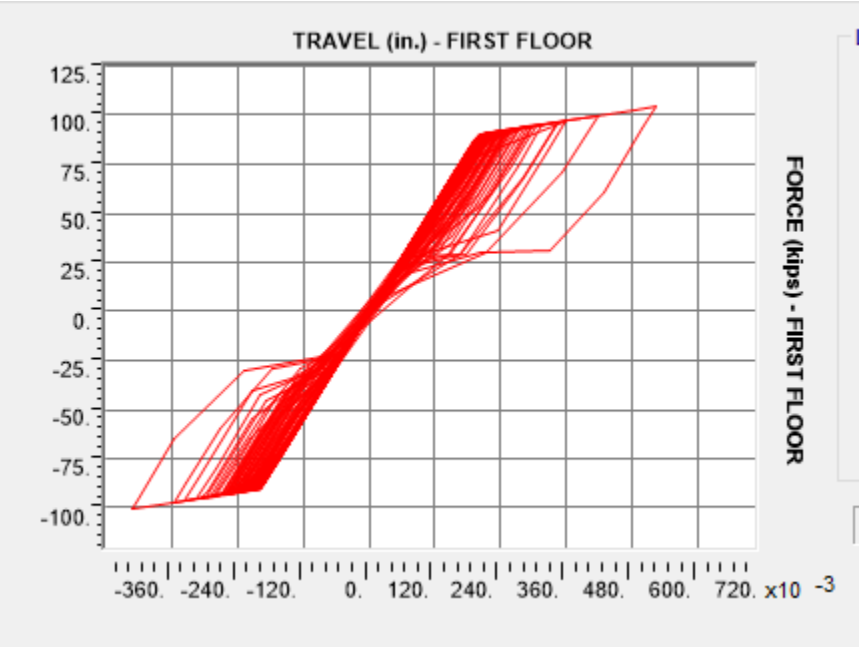

Figure 200: Force-Travel Two-Story Lower FSD El Centro 50%

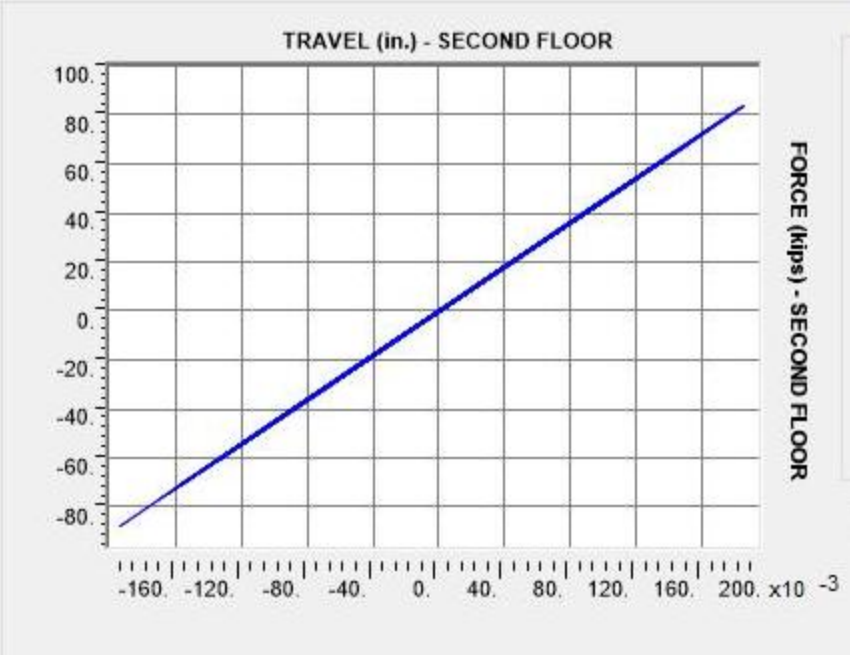

Figure 201: Force-Travel Two-Story Upper FSD El Centro 50%

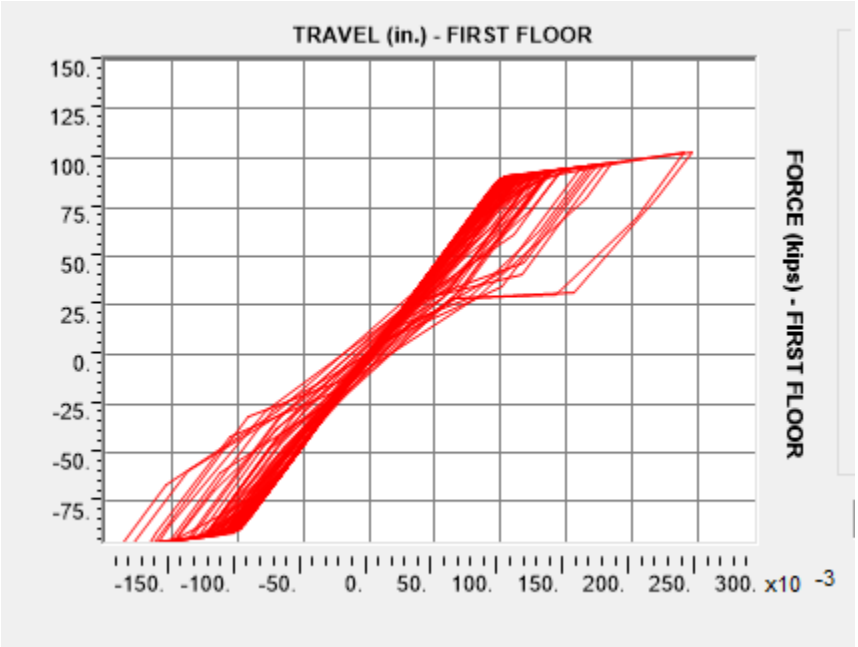

Figure 202: Force-Travel Two-Story Lower FSD El Centro 100%

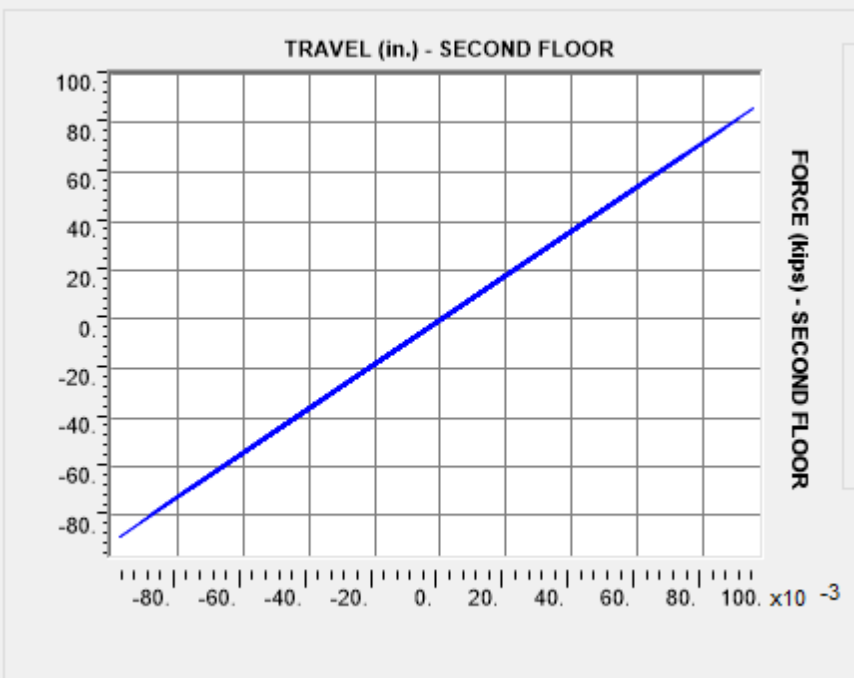

Figure 203: Force-Travel Two-Story Upper FSD El Centro 100%

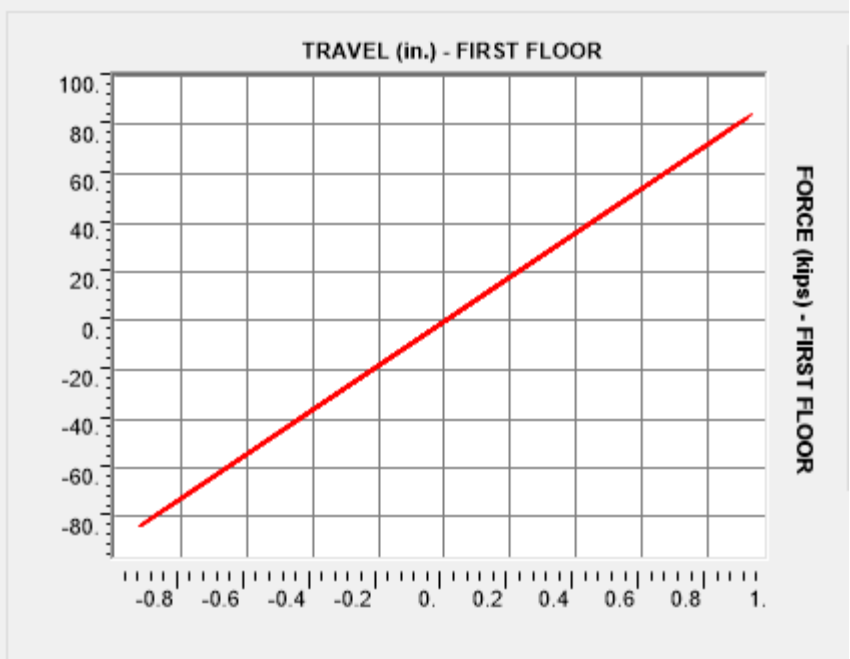

Figure 204: Force-Travel Two-Story Lower FSD Kern 10%

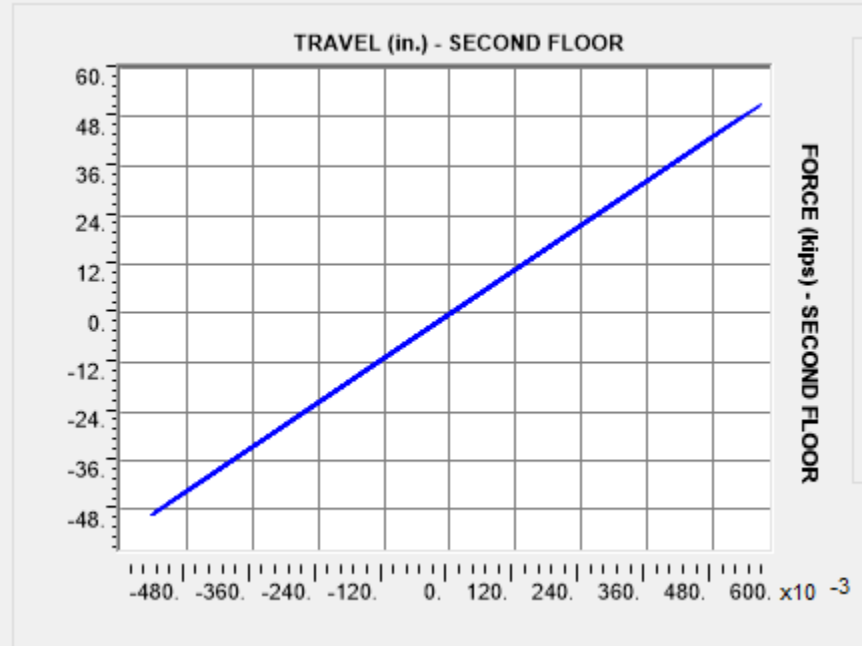

Figure 205: Force-Travel Two-Story Upper FSD Kern 10%

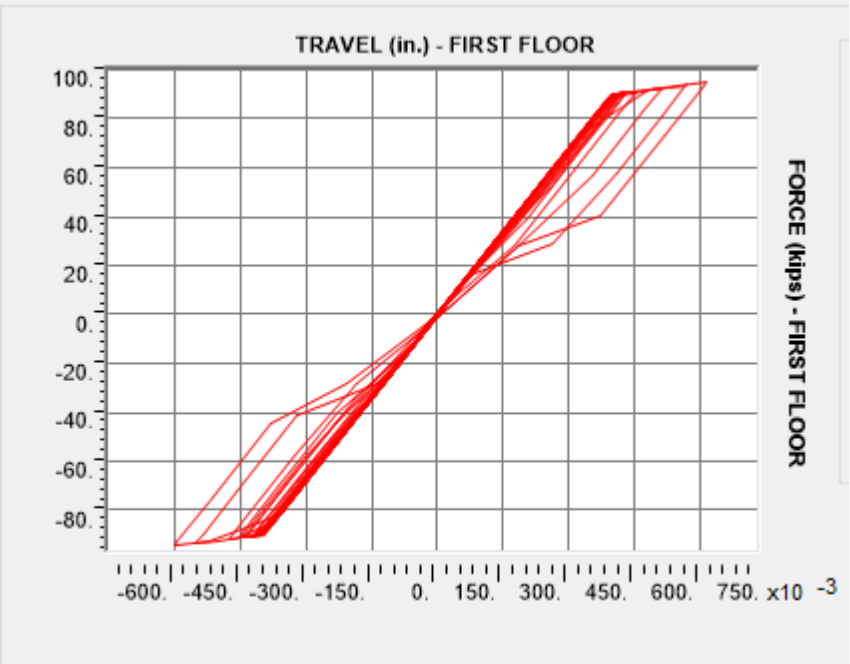

Figure 206: Force-Travel Two-Story Lower FSD Kern 25%

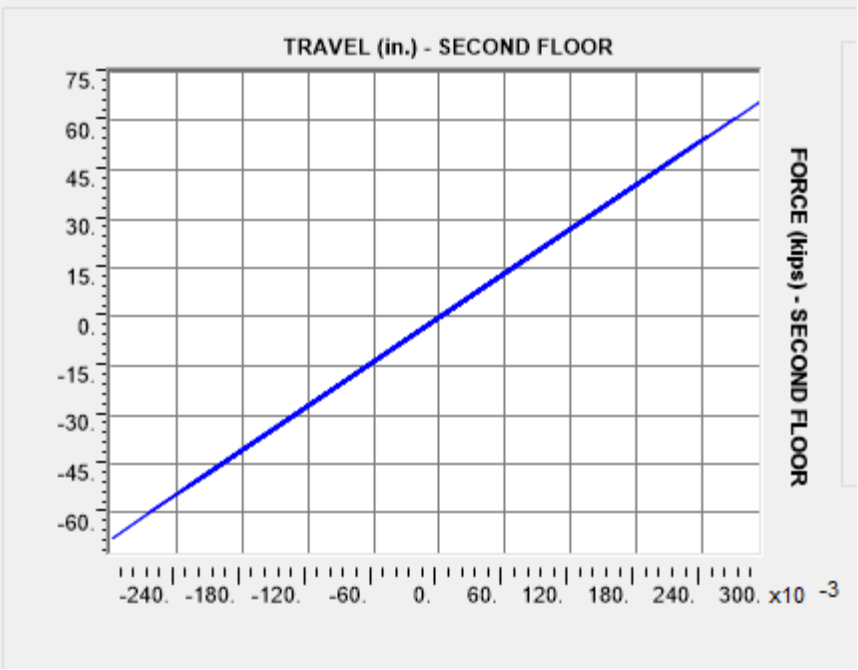

Figure 207: Force-Travel Two-Story Upper FSD Kern 25%

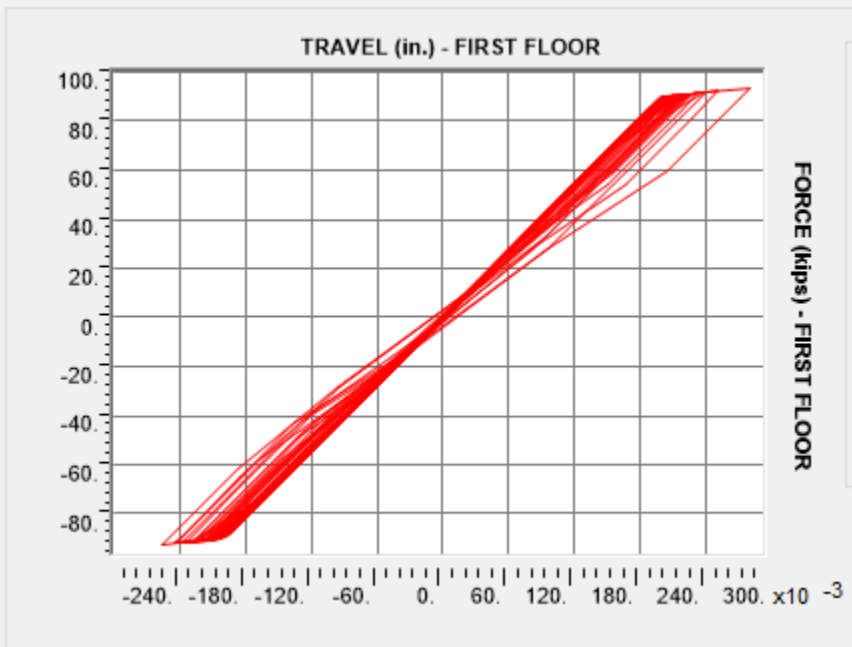

Figure 208: Force-Travel Two-Story Lower FSD Kern 50%

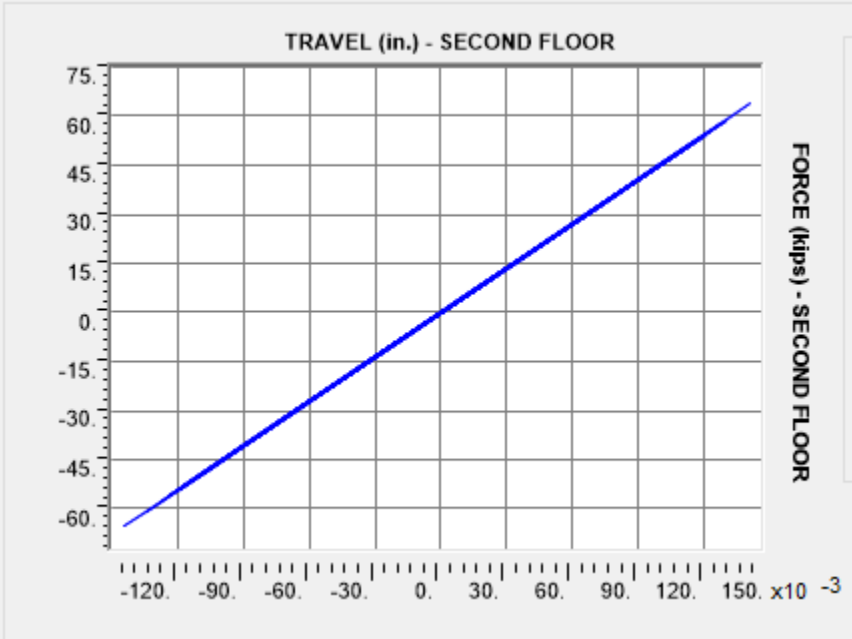

Figure 209: Force-Travel Two-Story Upper FSD Kern 50%

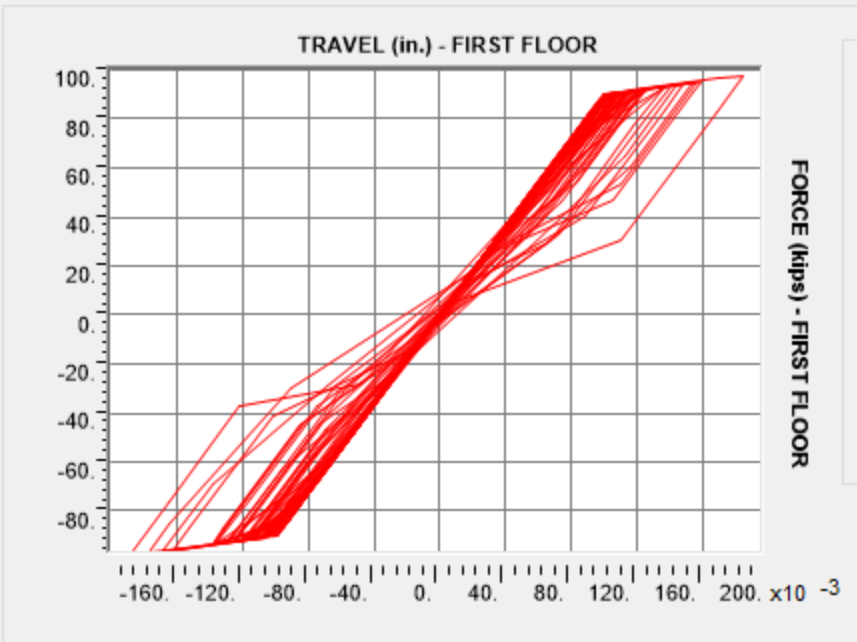

Figure 210: Force-Travel Two-Story Lower FSD Kern 100%

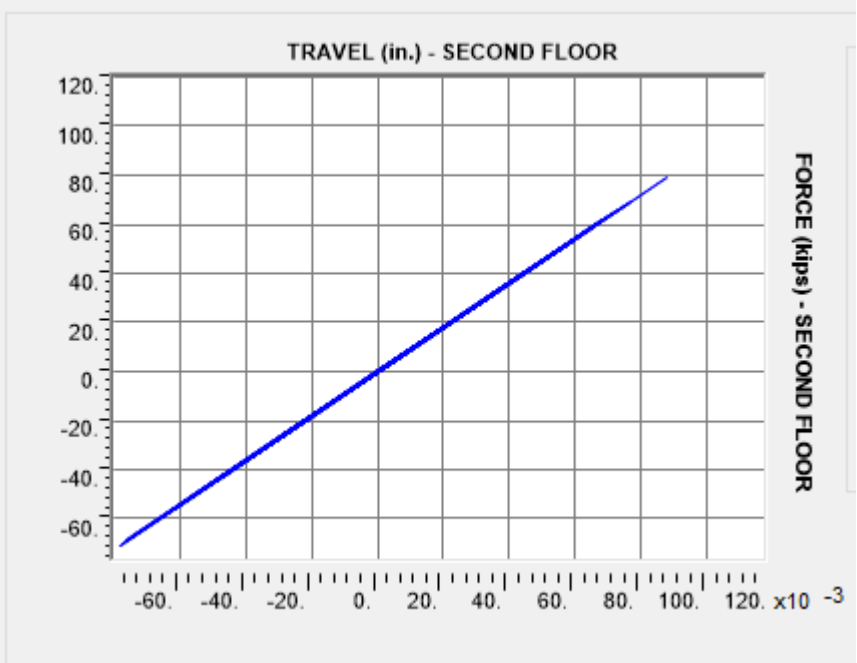

Figure 211: Force-Travel Two-Story Lower FSD Kern 100%

Appendix Z: Three-Story FSD Force-Travel Diagrams

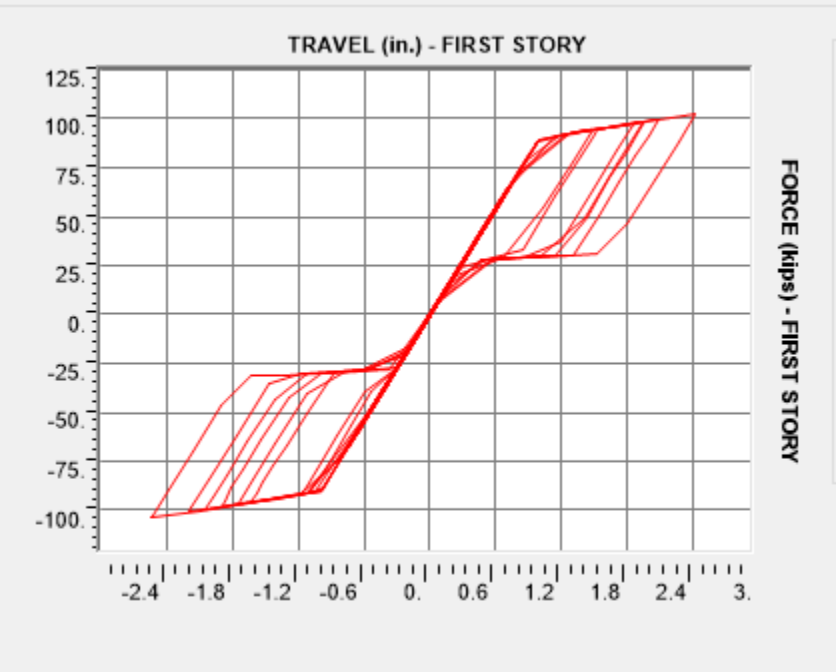

Figure 212: Force-Travel Three-Story Lower FSD Loma 10%

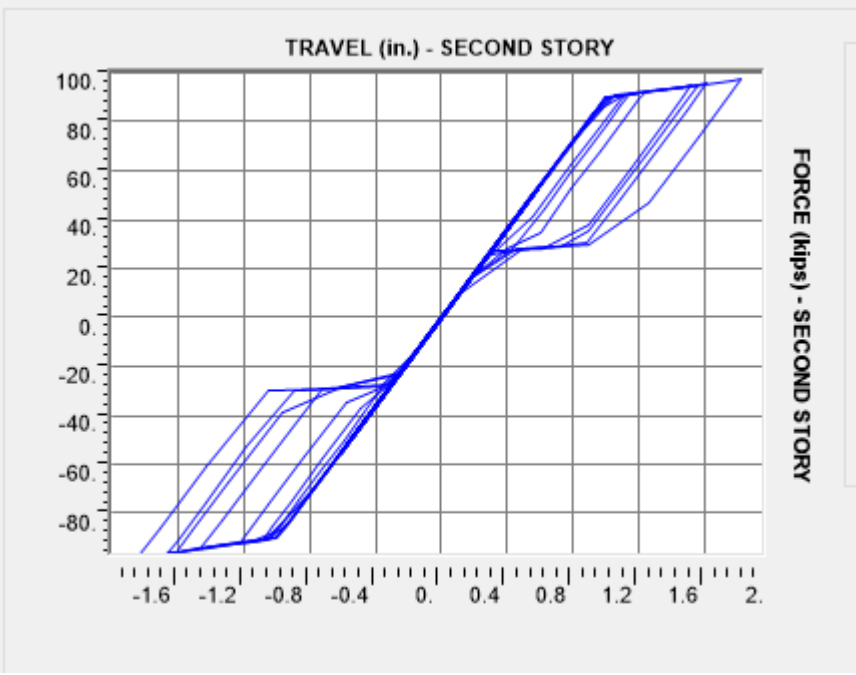

Figure 213: Force-Travel Three-Story Middle FSD Loma 10%

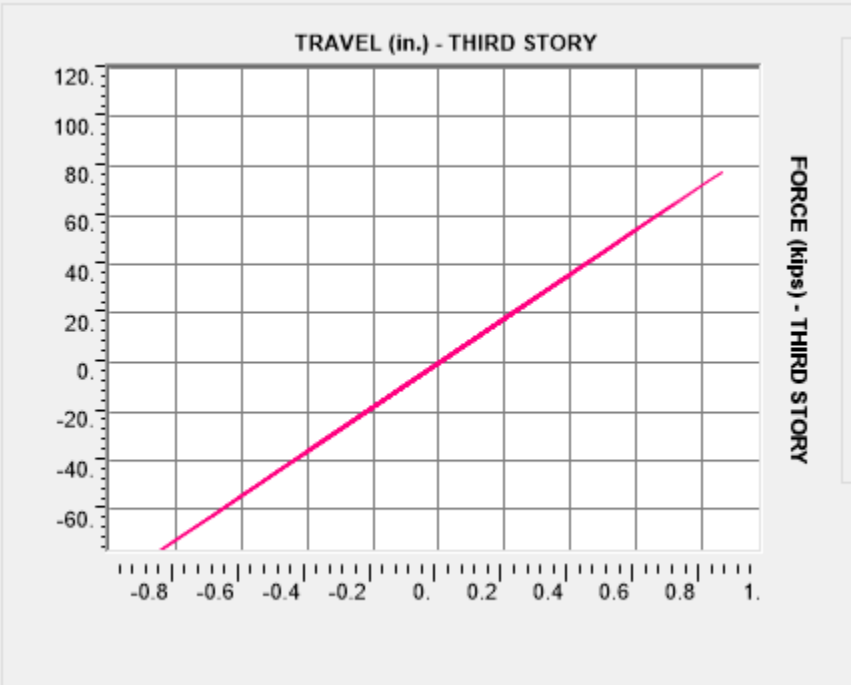

Figure 214: Force-Travel Three-Story Upper FSD Loma 10%

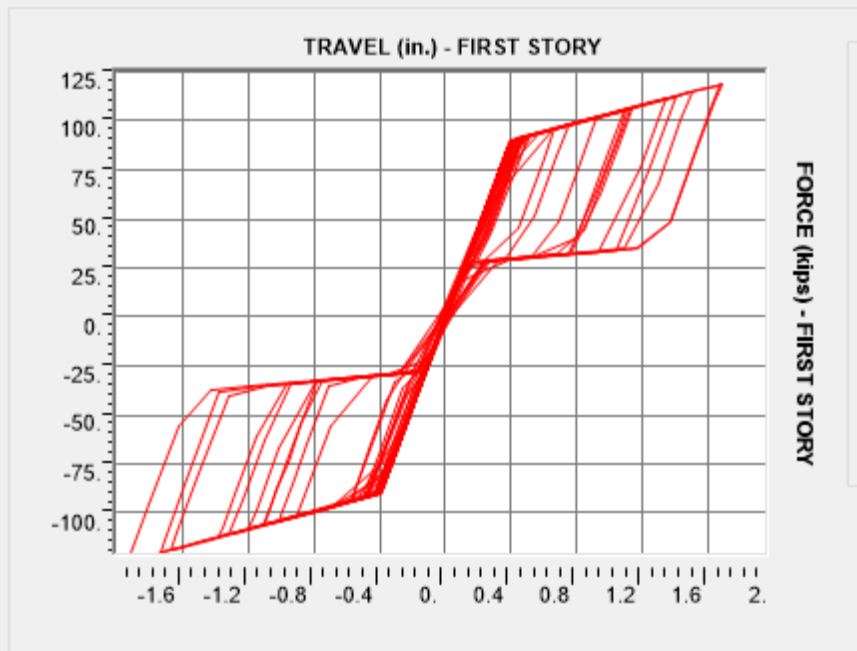

Figure 215: Force-Travel Three-Story Lower FSD Loma 25%

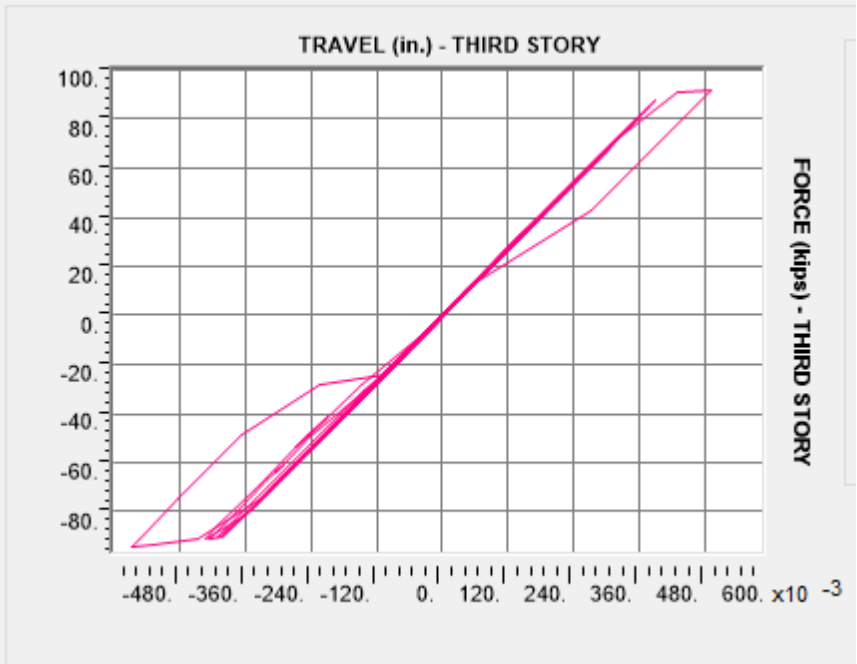

Figure 216: Force-Travel Three-Story Upper FSD Loma 25%

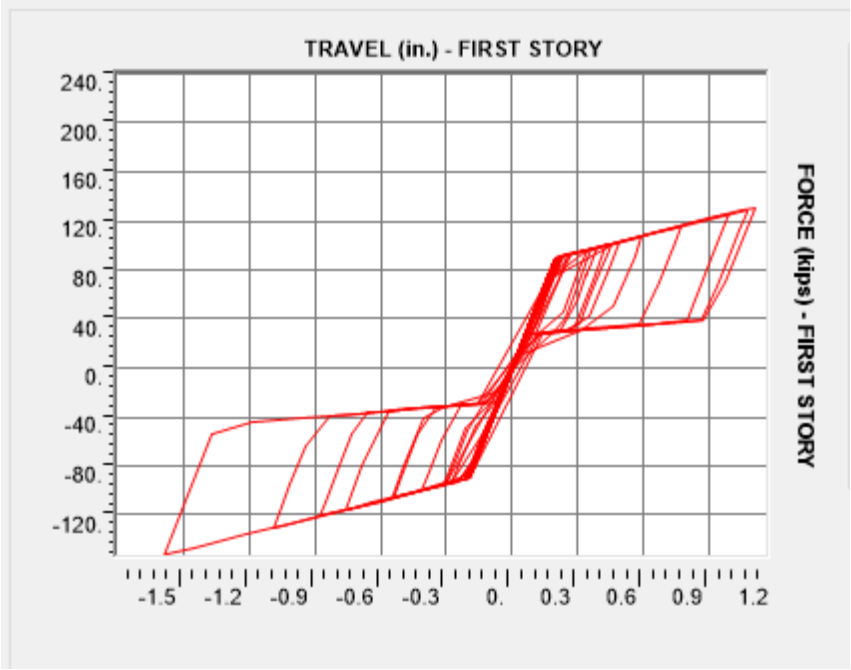

Figure 217: Force-Travel Three-Story Lower FSD Loma 50%

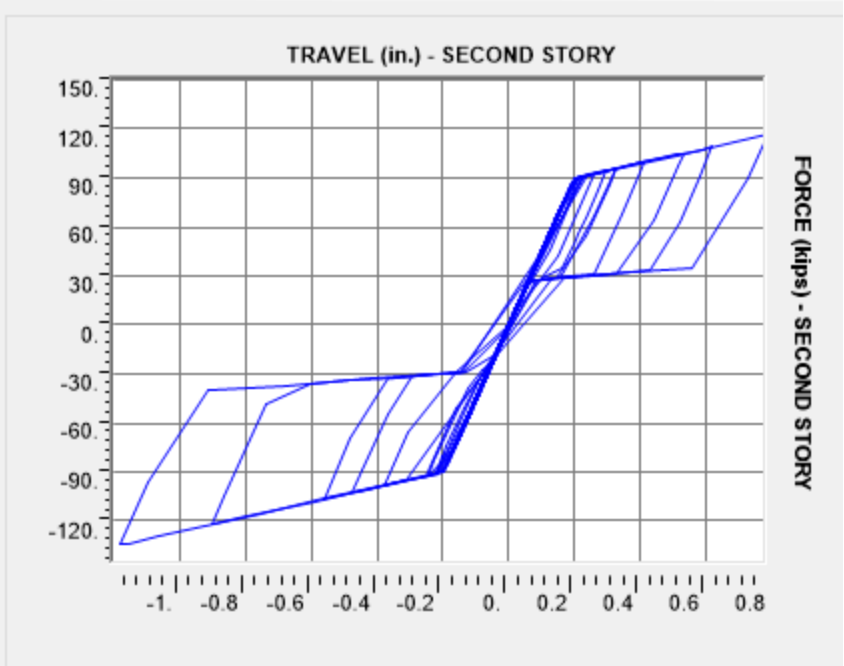

Figure 218: Force-Travel Three-Story Middle FSD Loma 50%

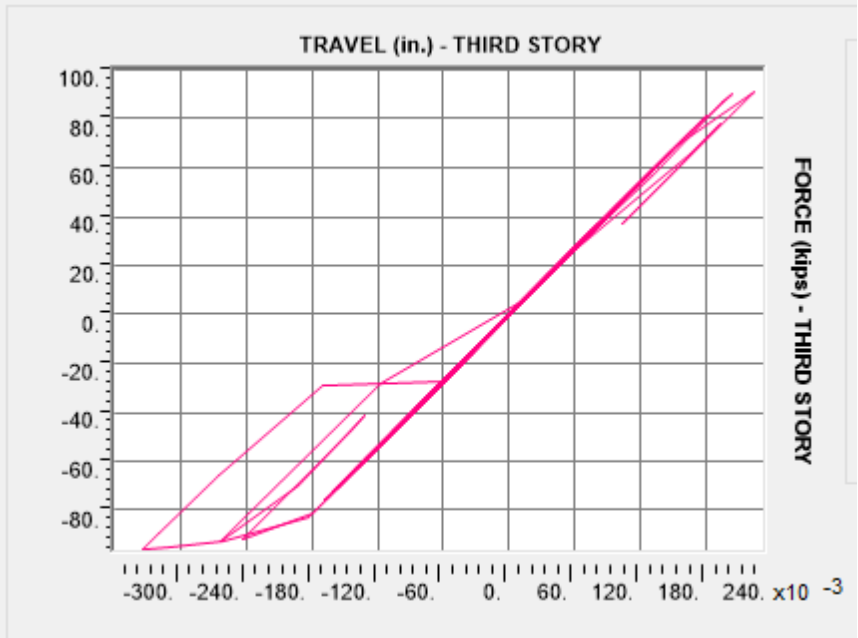

Figure 219: Force-Travel Three-Story Upper FSD Loma 50%

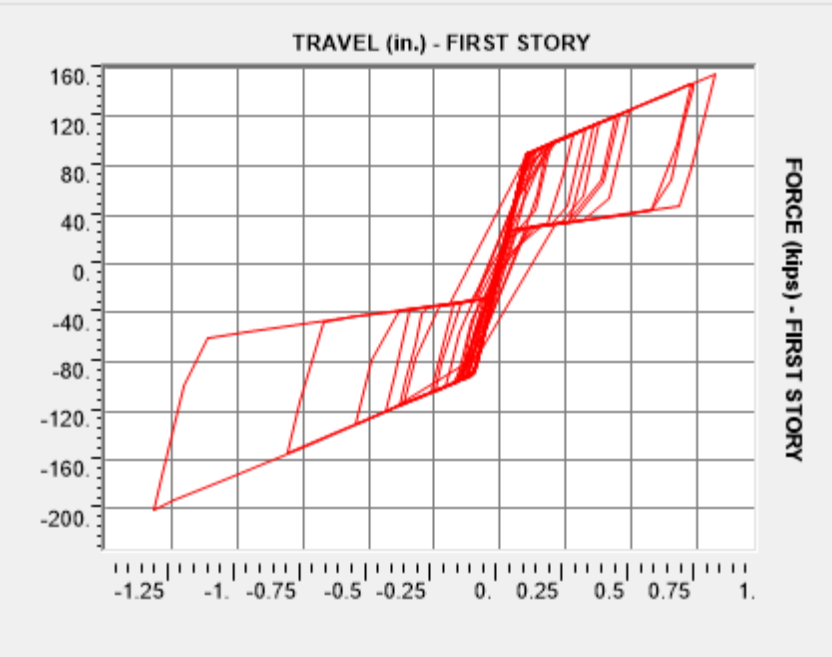

Figure 220: Force-Travel Three-Story Lower FSD Loma 100%

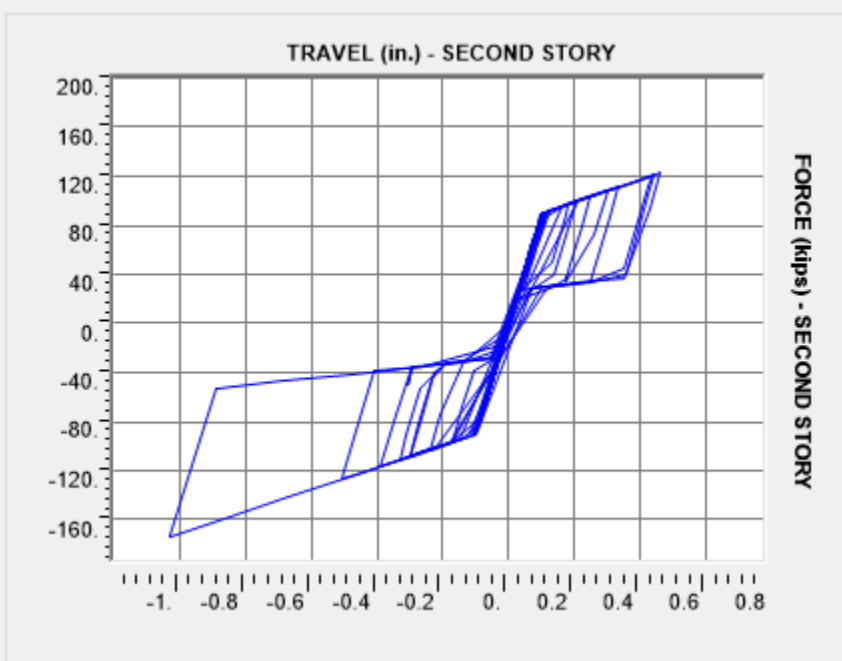

Figure 221: Force-Travel Three-Story Middle FSD Loma 100%

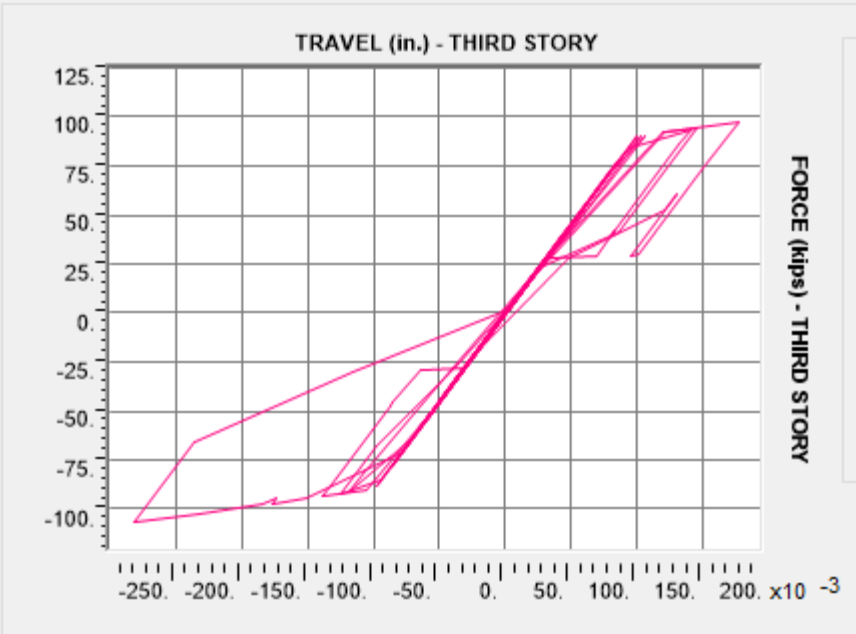

Figure 222: Force-Travel Three-Story Upper FSD Loma 100%

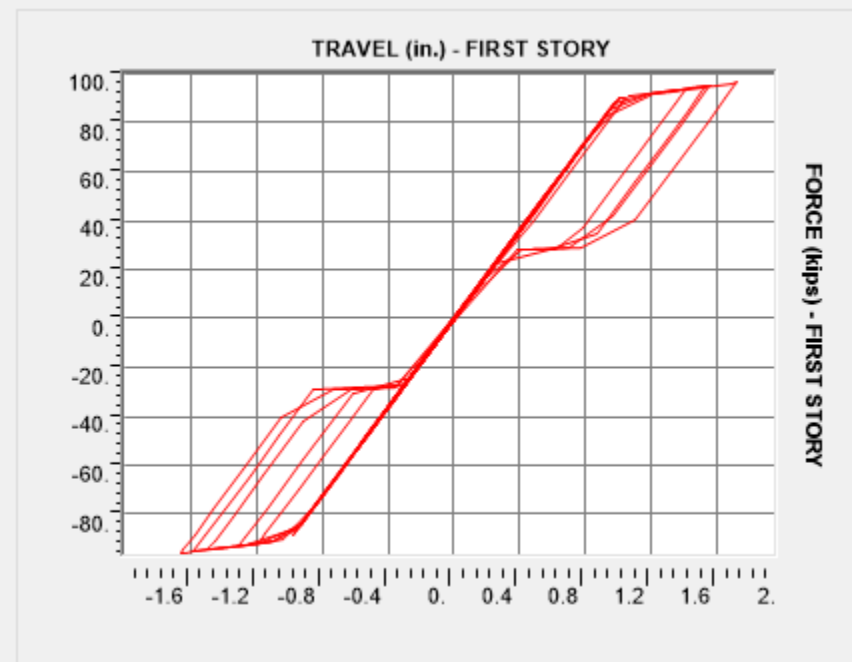

Figure 223: Force-Travel Three-Story Lower FSD Northridge 10%

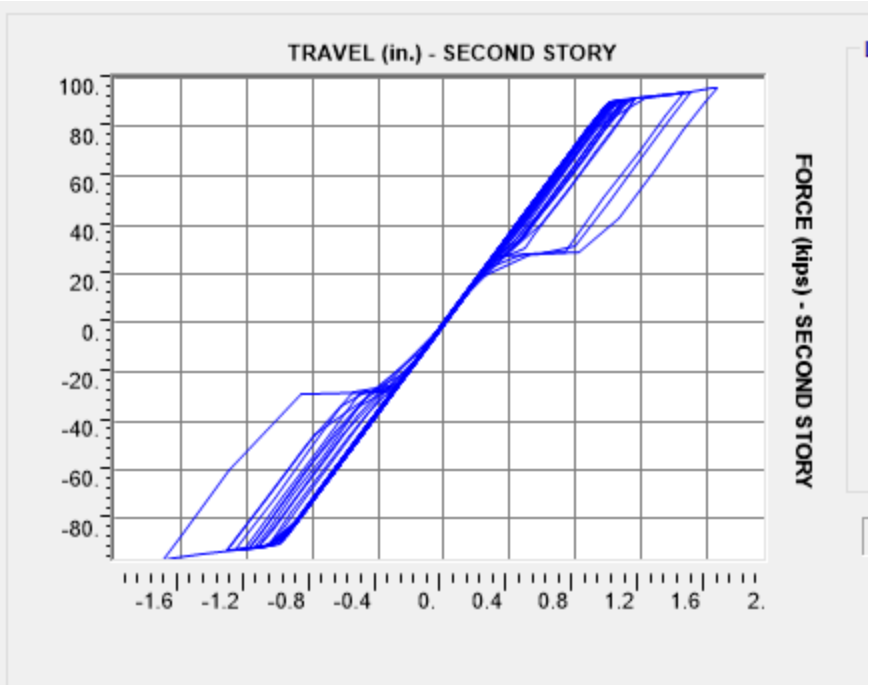

Figure 224: Force-Travel Three-Story Middle FSD Northridge 10%

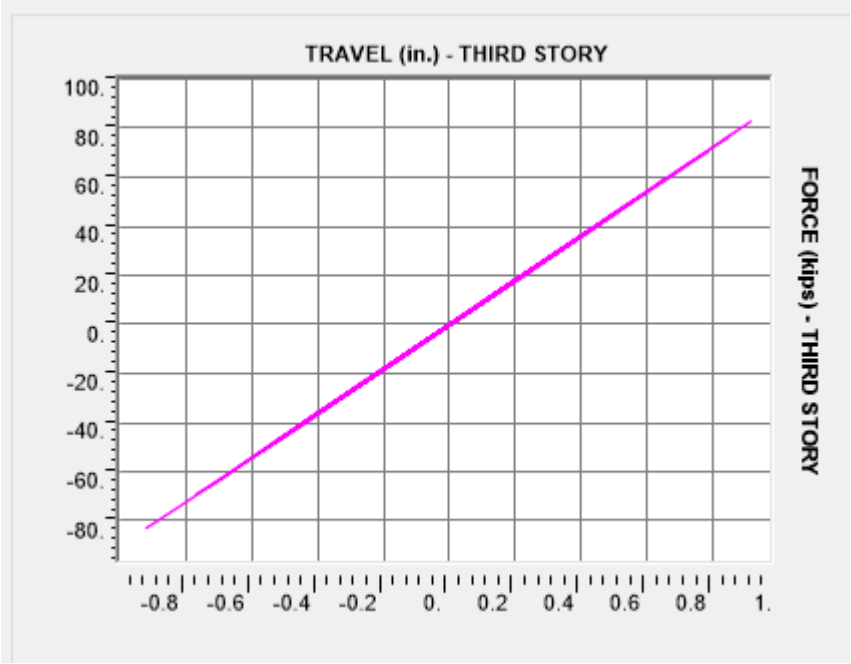

Figure 225: Force-Travel Three-Story Upper FSD Northridge 10%

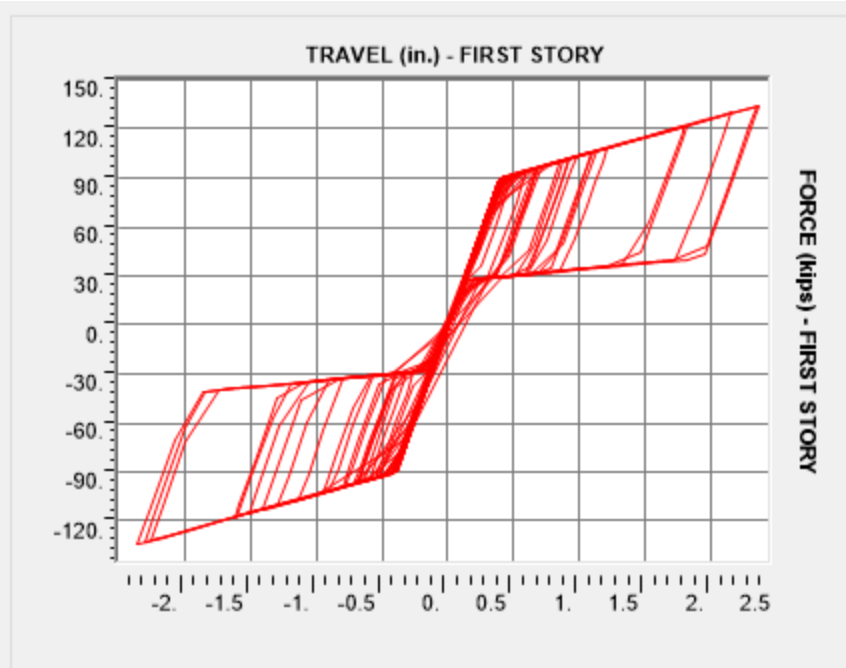

Figure 226: Force-Travel Three-Story Lower FSD Northridge 25%

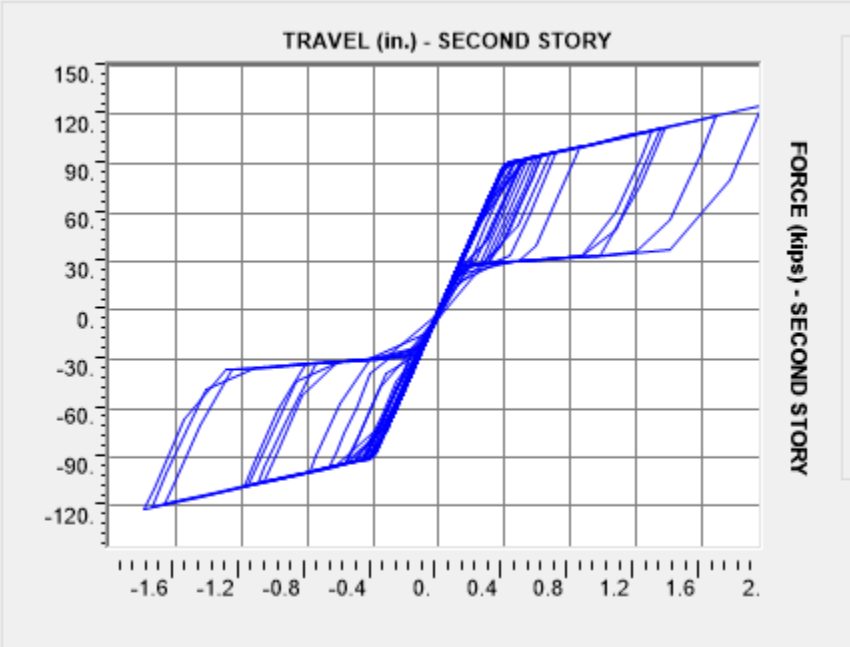

Figure 227: Force-Travel Three-Story Middle FSD Northridge 25%

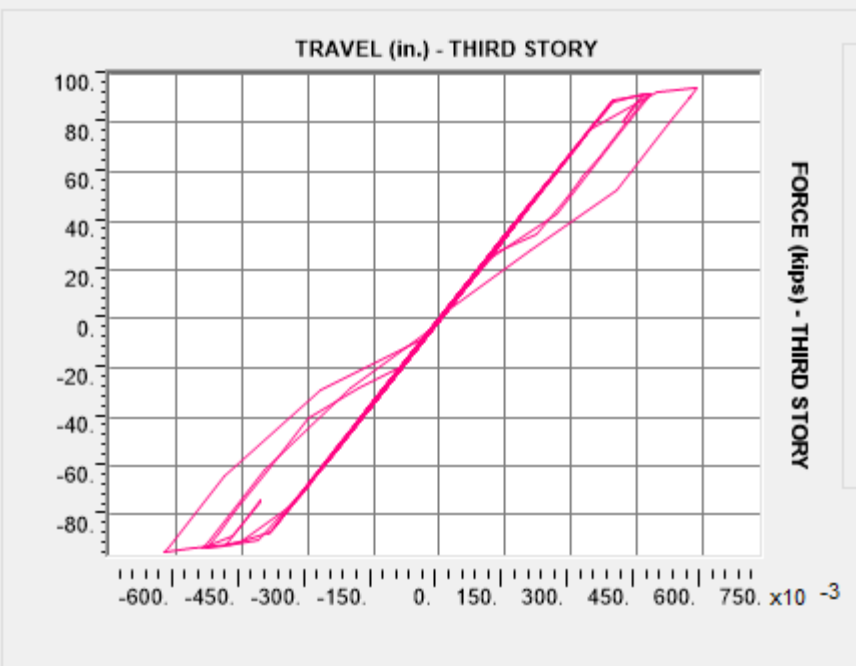

Figure 228: Force-Travel Three-Story Upper FSD Northridge 25%

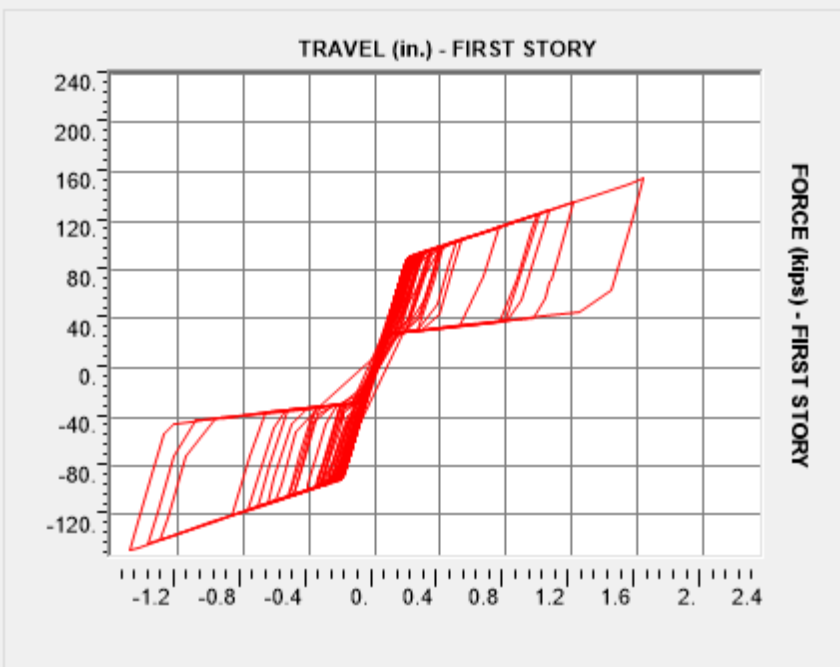

Figure 229: Force-Travel Three-Story Lower FSD Northridge 50%

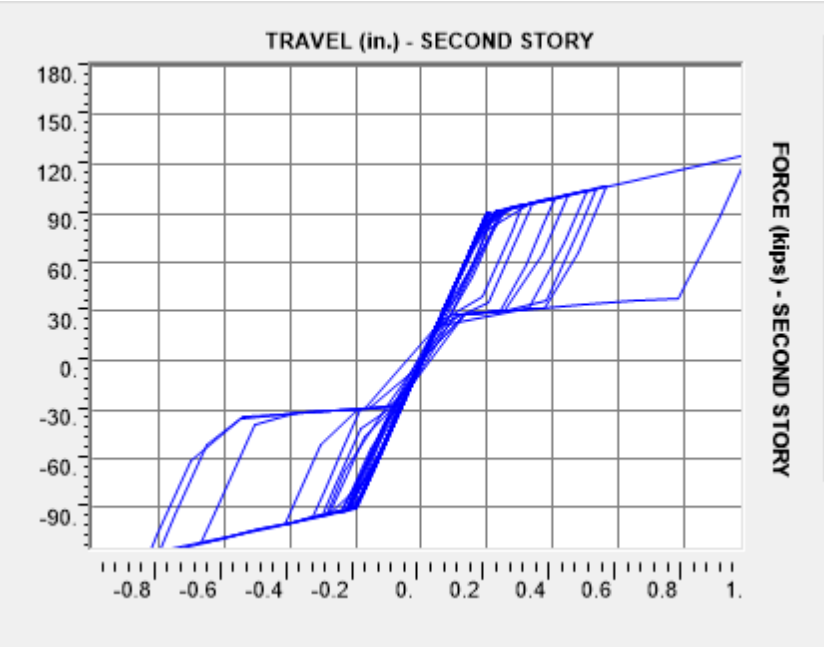

Figure 230: Force-Travel Three-Story Middle FSD Northridge 50%

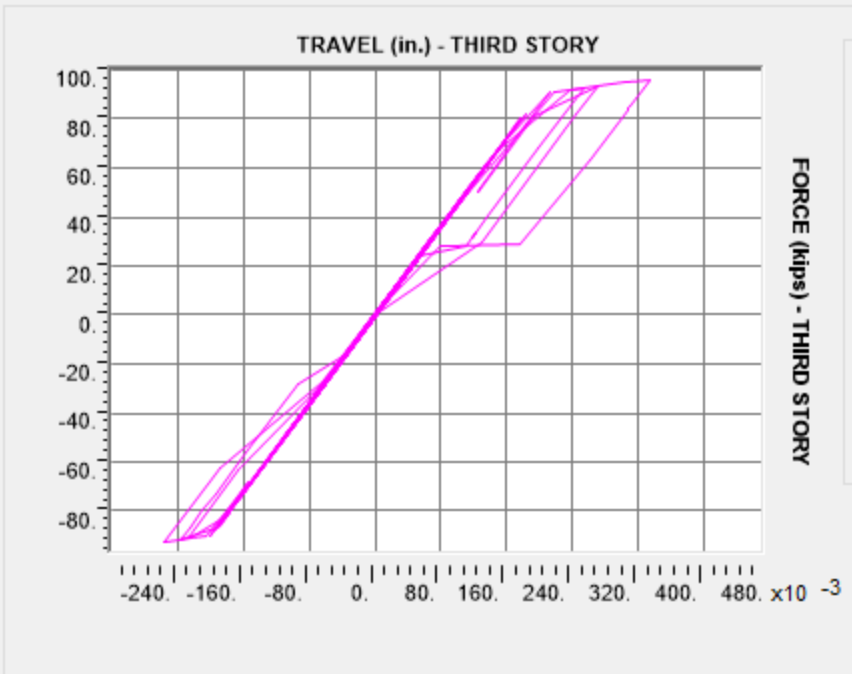

Figure 231: Force-Travel Three-Story Upper FSD Northridge 50%

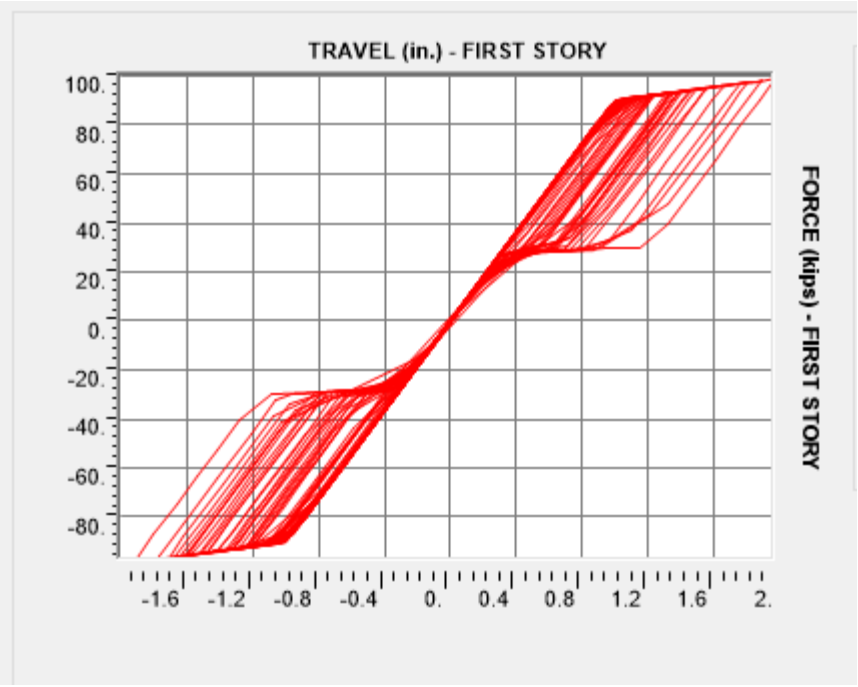

Figure 232: Force-Travel Three-Story Lower FSD Northridge 100%

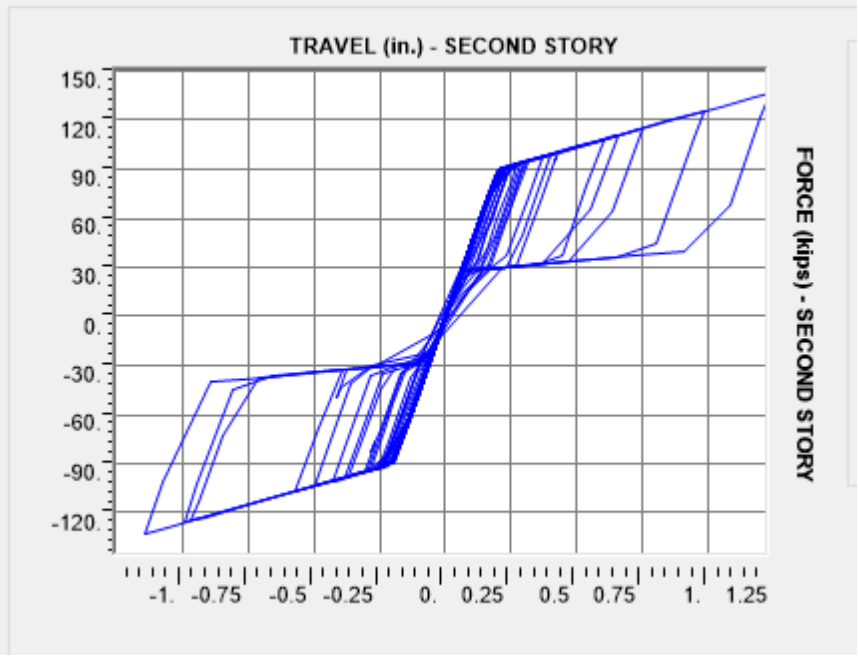

Figure 233: Force-Travel Three-Story Middle FSD Northridge 100%

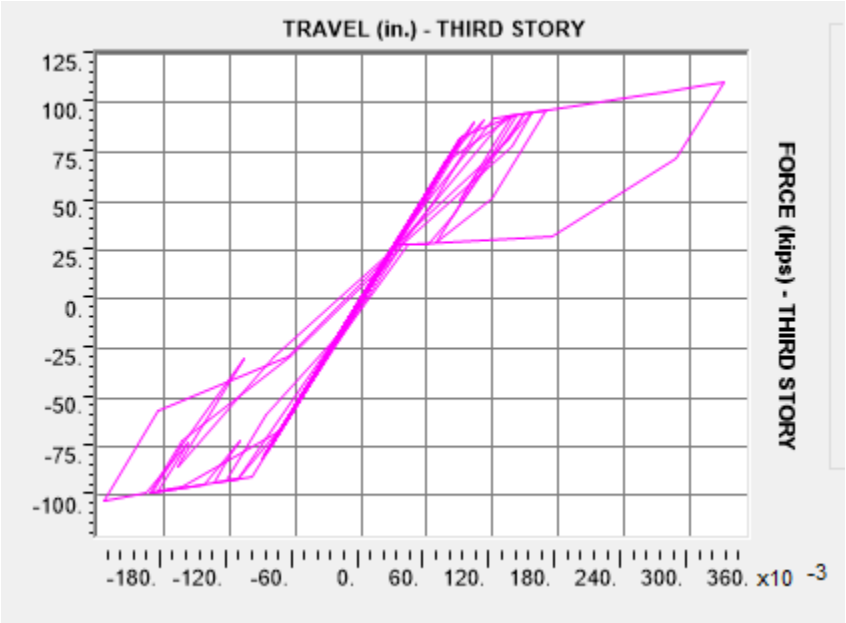

Figure 234: Force-Travel Three-Story Upper FSD Northridge 100%

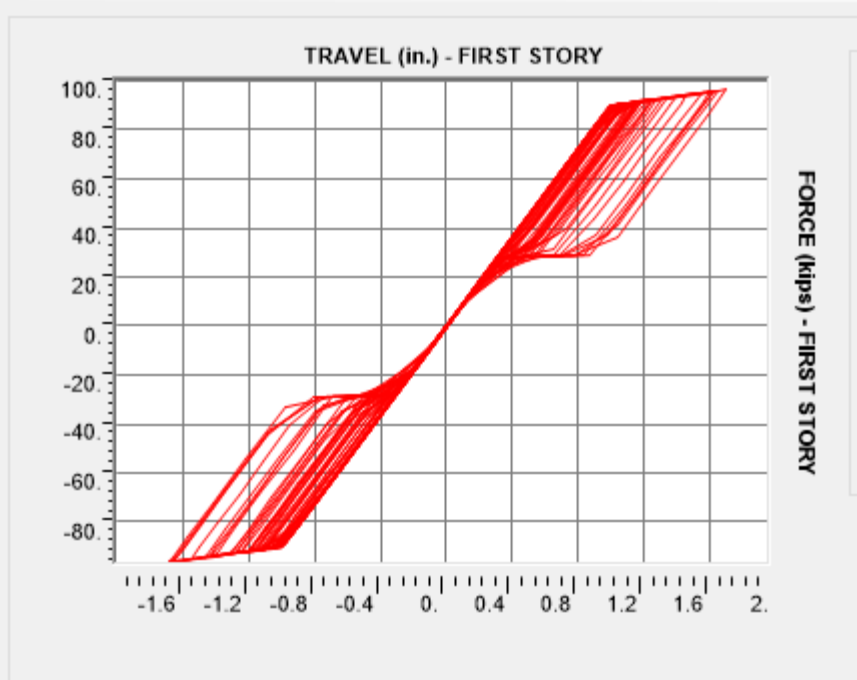

Figure 235: Force-Travel Three-Story Lower FSD El Centro 10%

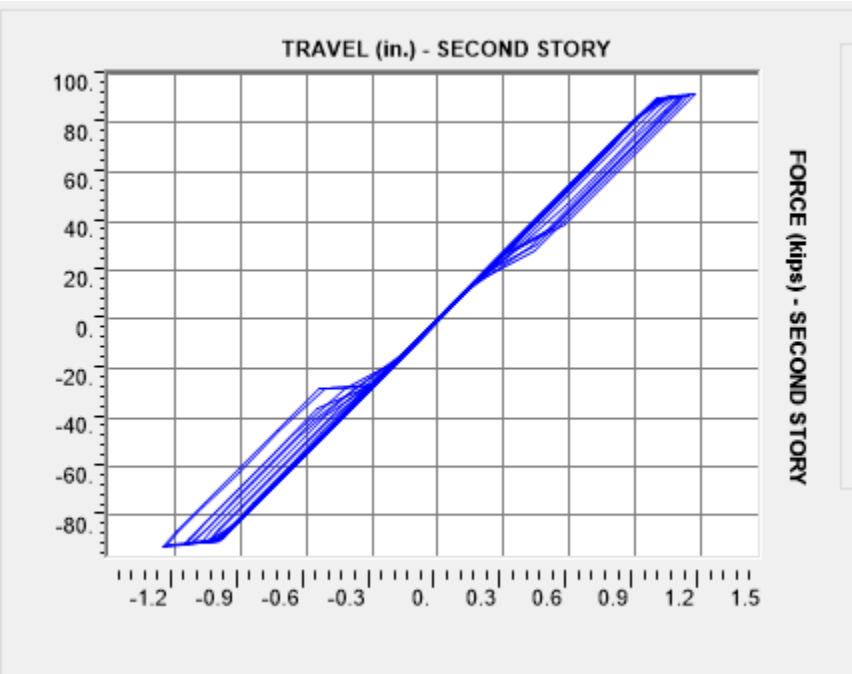

Figure 236: Force-Travel Three-Story Middle FSD El Centro 10%

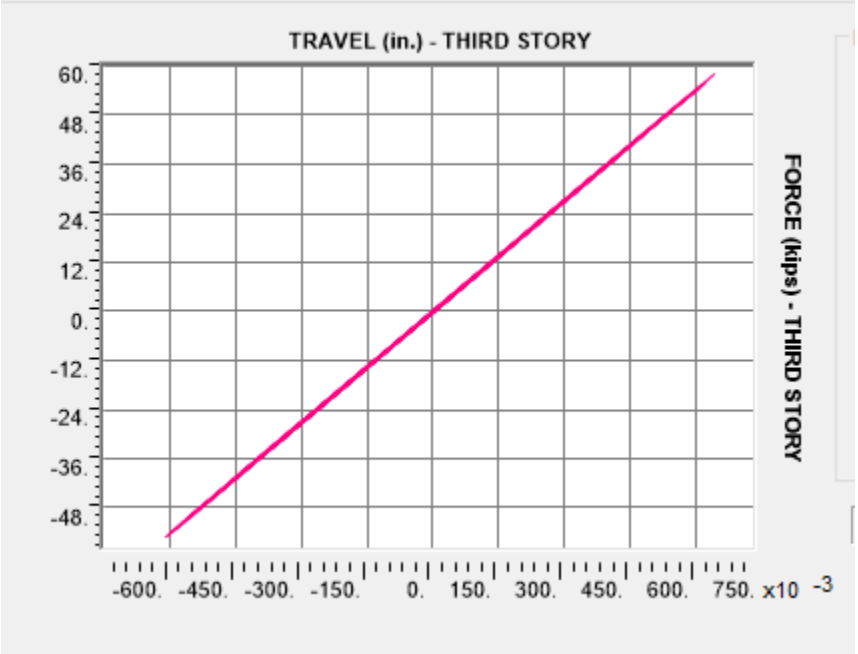

Figure 237: Force-Travel Three-Story Upper FSD El Centro 10%

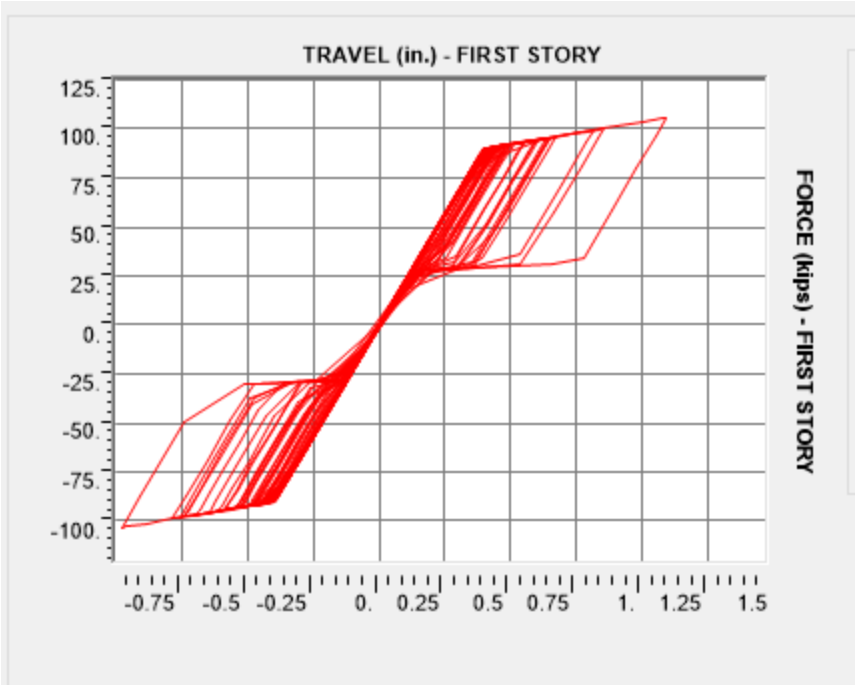

Figure 238: Force-Travel Three-Story Lower FSD El Centro 25%

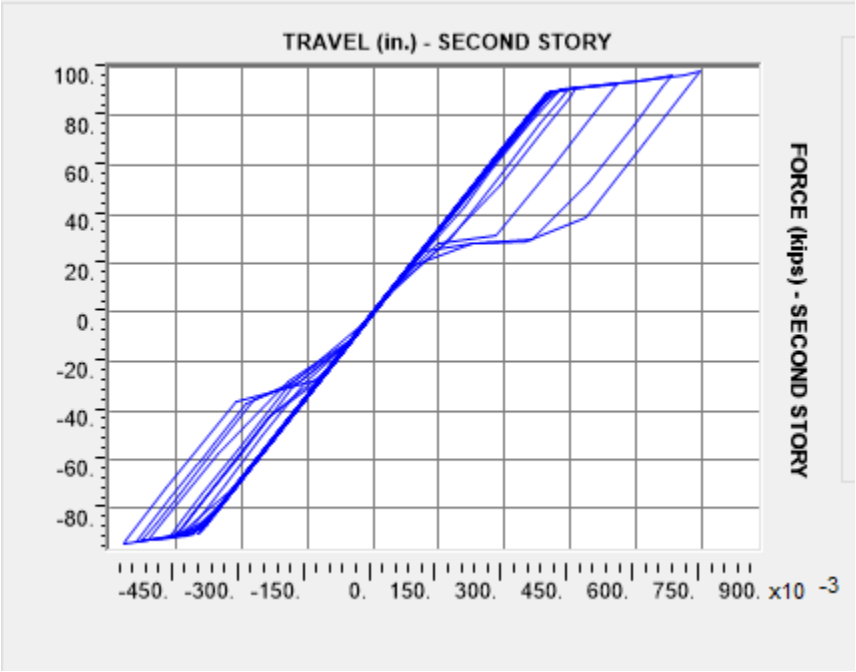

Figure 239: Force-Travel Three-Story Middle FSD El Centro 25%

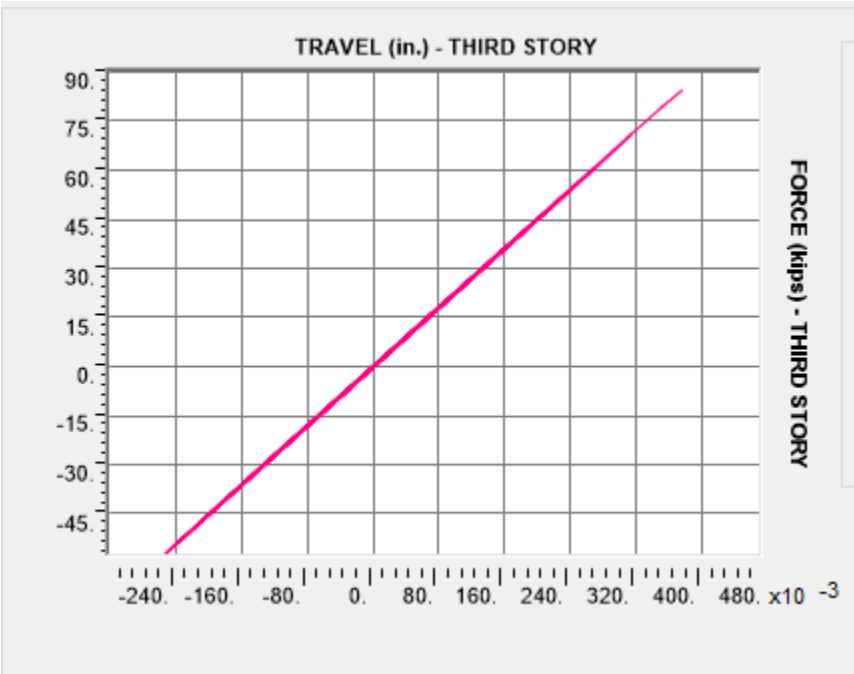

Figure 240: Force-Travel Three-Story Upper FSD El Centro 25%

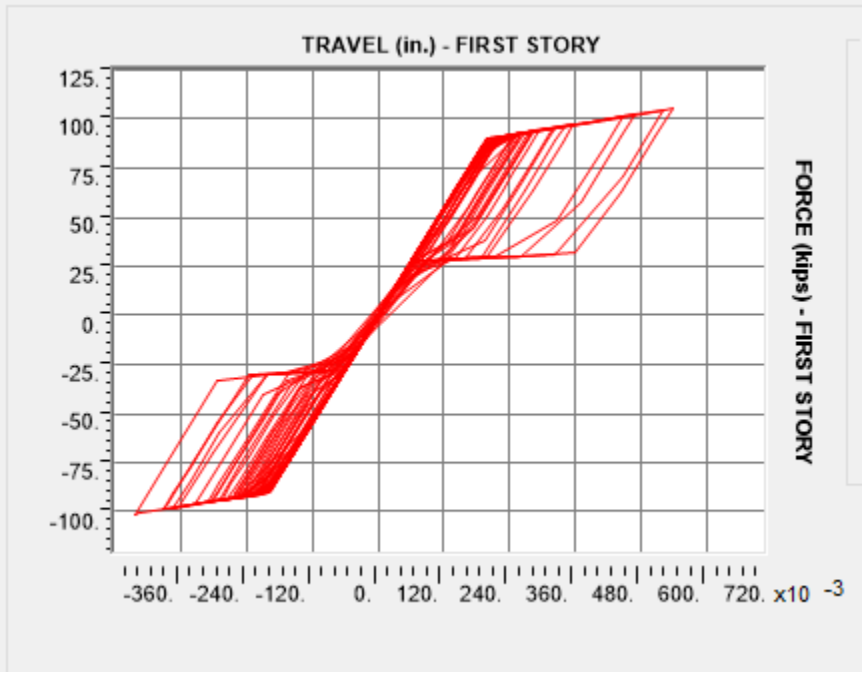

Figure 241: Force-Travel Three-Story Lower FSD El Centro 50%

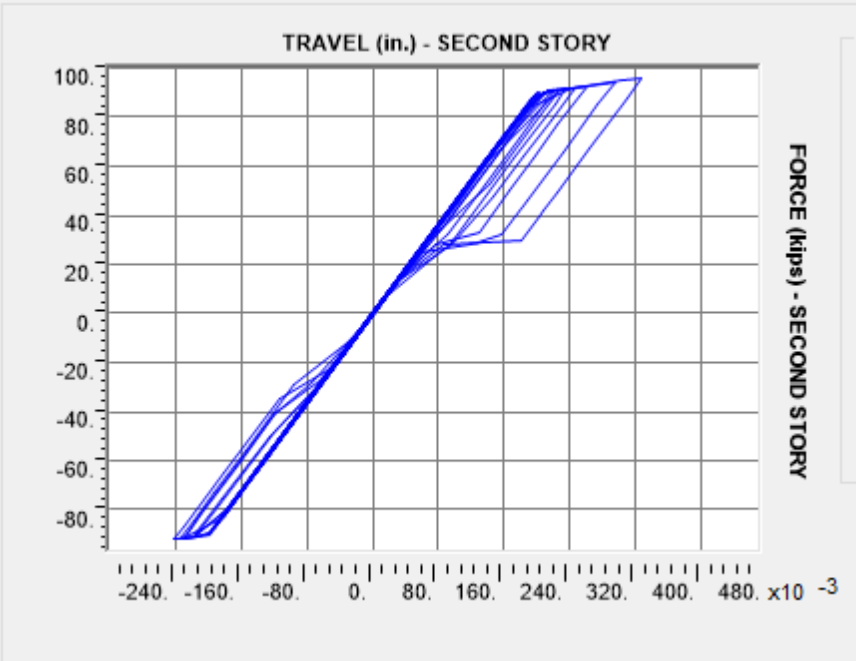

Figure 242: Force-Travel Three-Story Middle FSD El Centro 50%

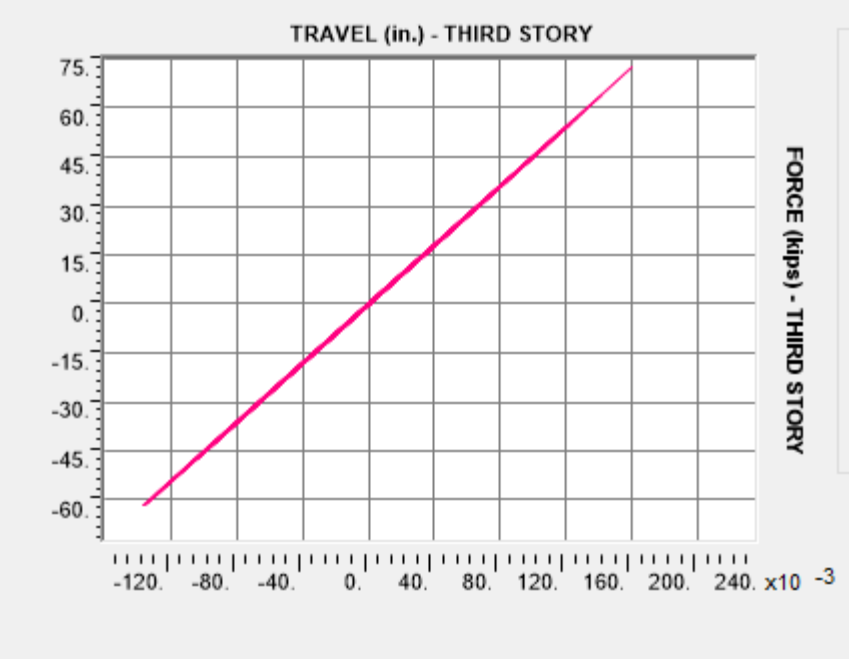

Figure 243: Force-Travel Three-Story Upper FSD El Centro 50%

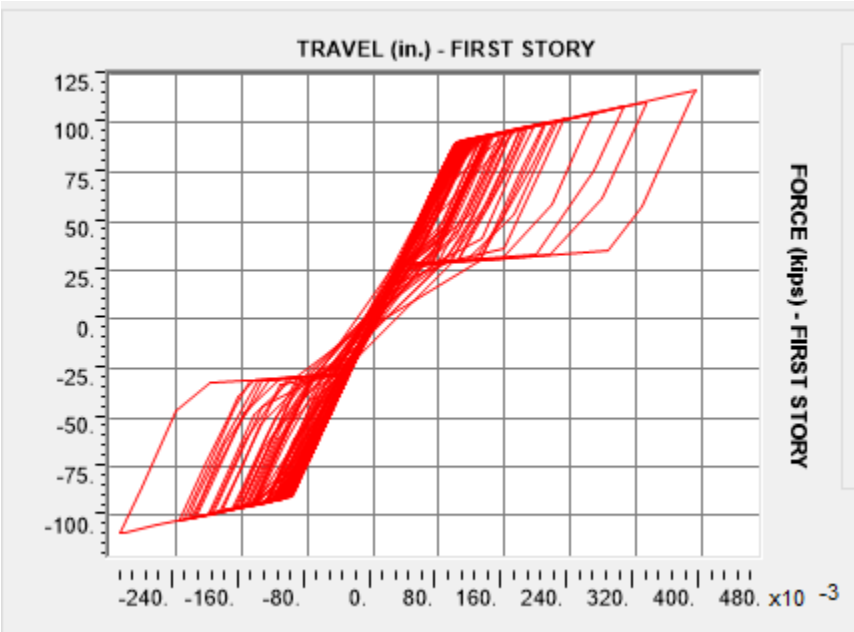

Figure 244: Force-Travel Three-Story Lower FSD El Centro 100%

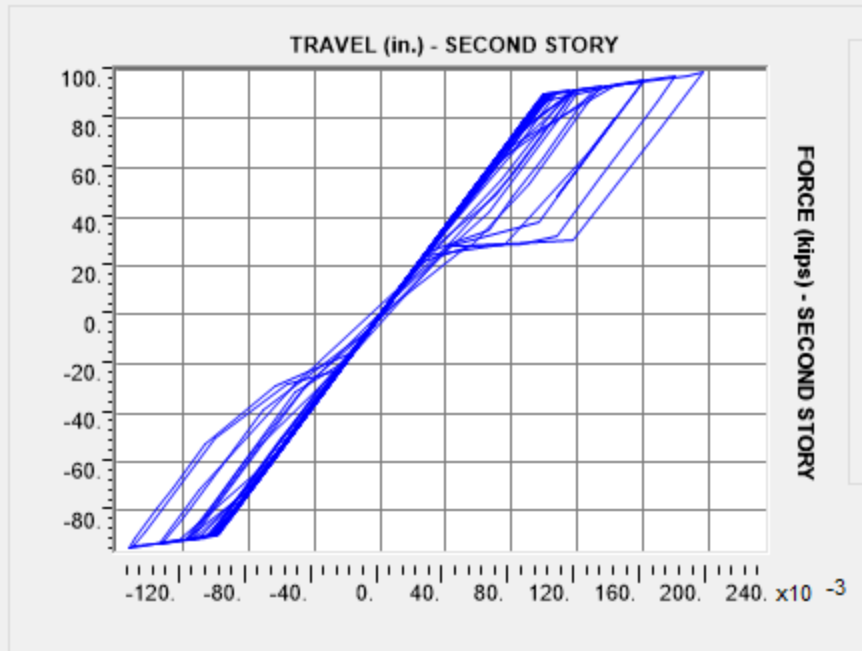

Figure 245: Force-Travel Three-Story Middle FSD El Centro 100%

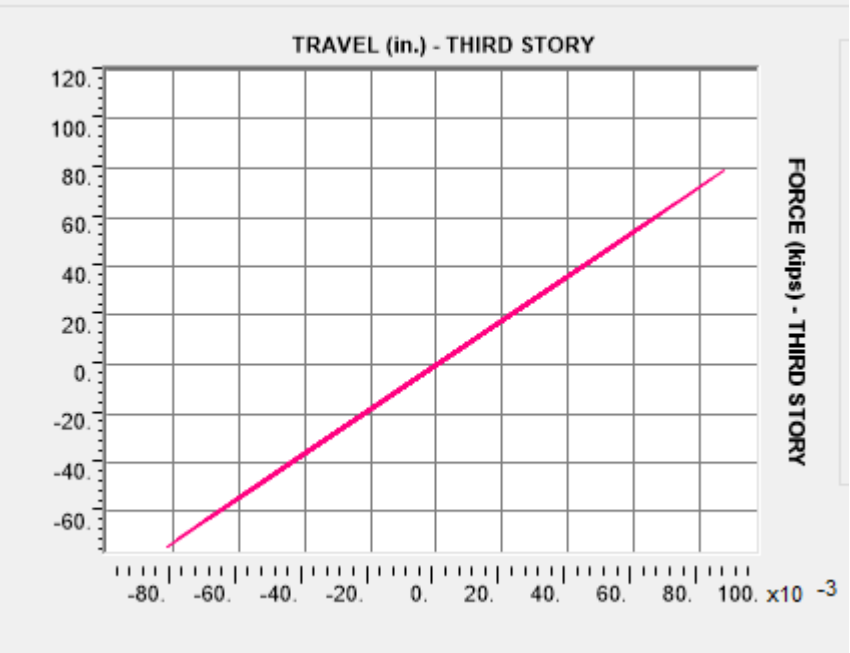

Figure 246: Force-Travel Three-Story Upper FSD El Centro 100%

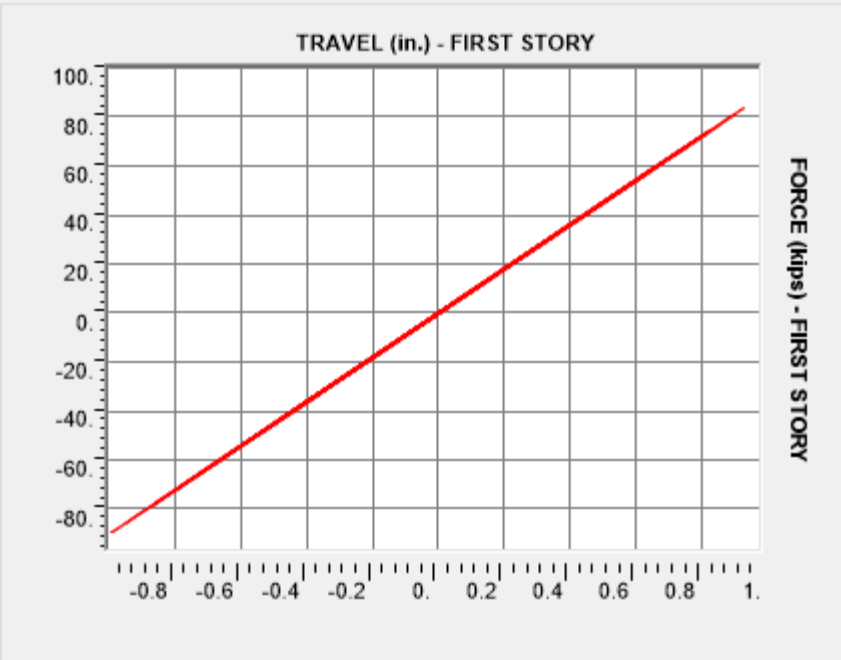

Figure 247: Force-Travel Three-Story Lower FSD Kern 10%

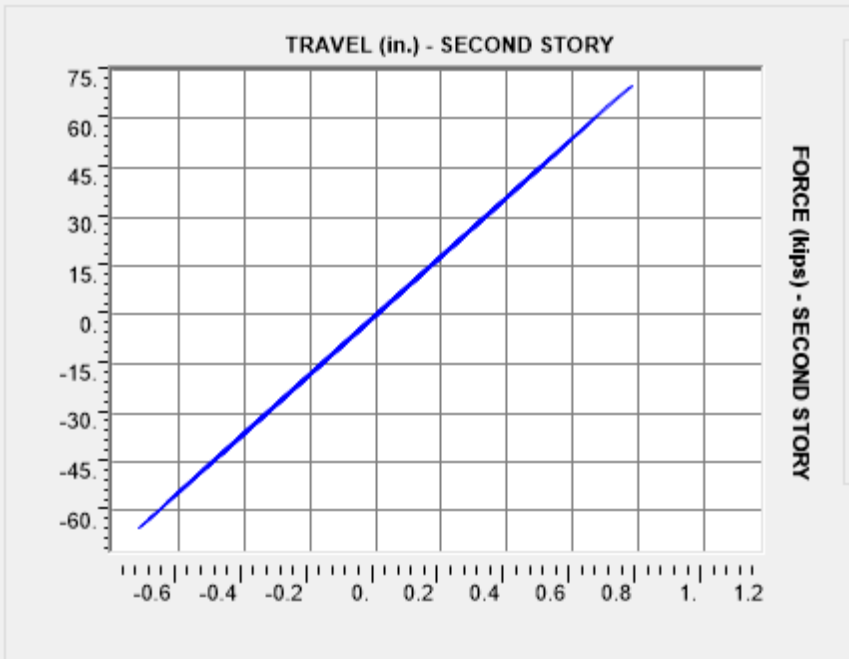

Figure 248: Force-Travel Three-Story Middle FSD Kern 10%

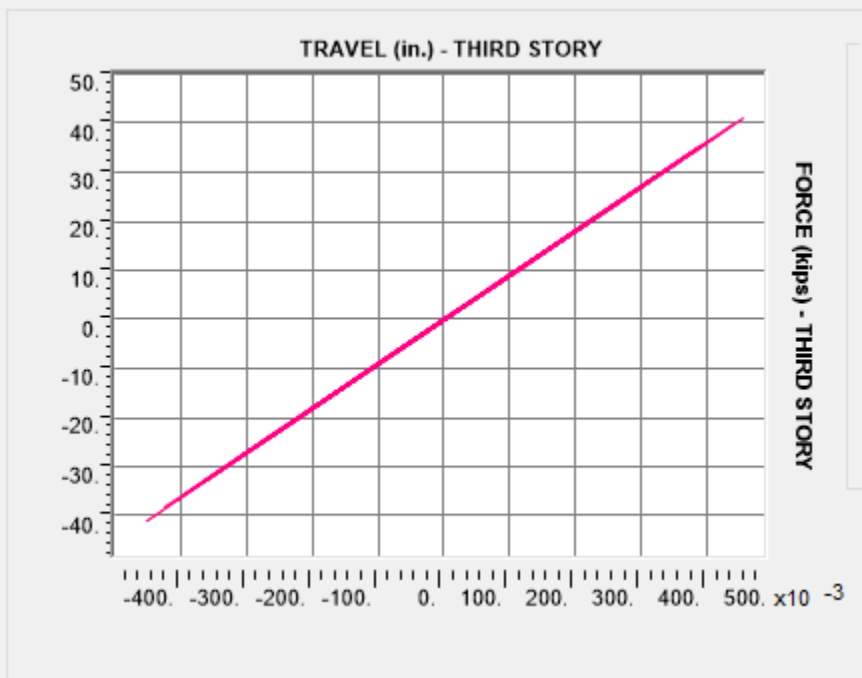

Figure 249: Force-Travel Three-Story Upper FSD Kern 10%

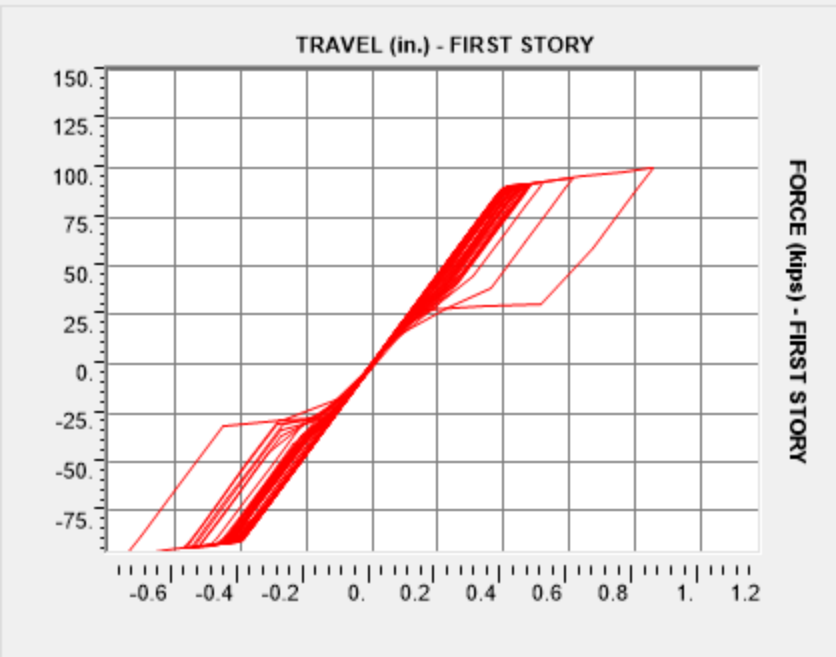

Figure 250: Force-Travel Three-Story Lower FSD Kern 25%

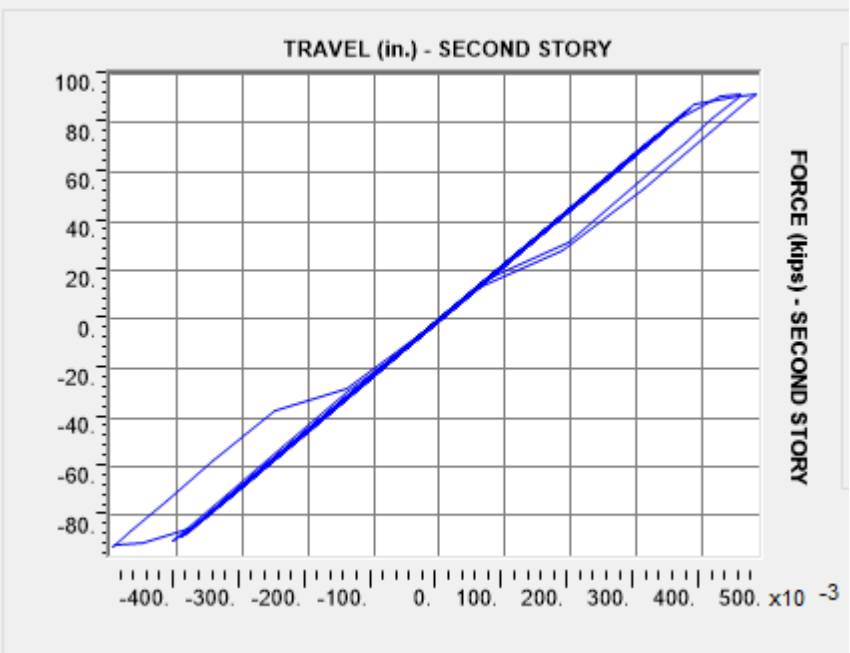

Figure 251: Force-Travel Three-Story Middle FSD Kern 25%

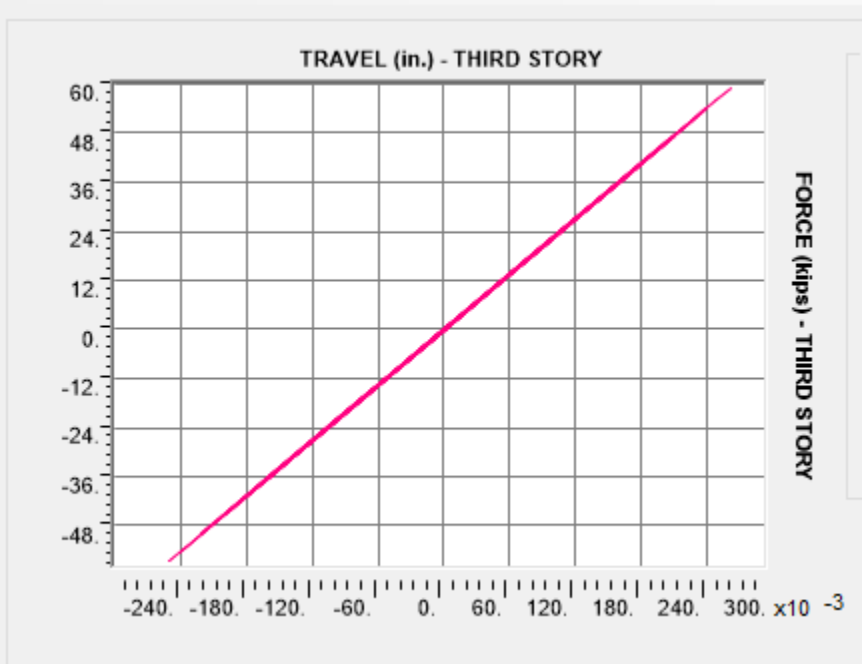

Figure 252: Force-Travel Three-Story Upper FSD Kern 25%

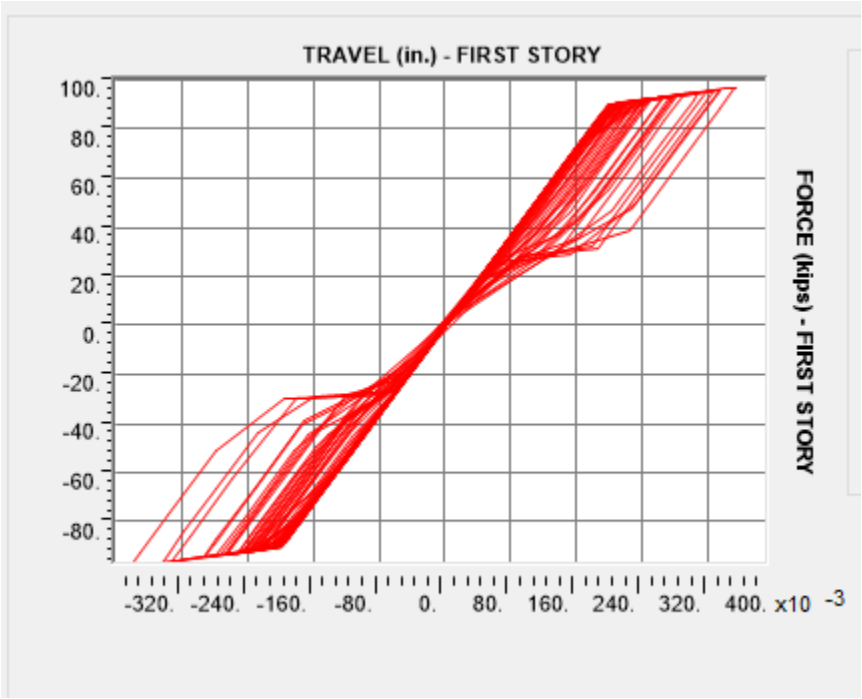

Figure 253: Force-Travel Three-Story Lower FSD Kern 50%

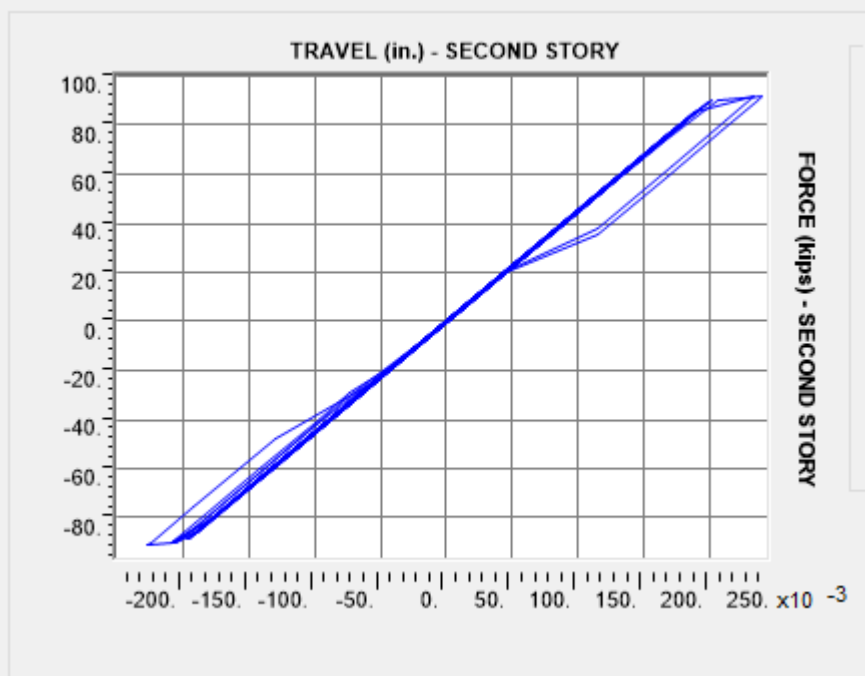

Figure 254: Force-Travel Three-Story Middle FSD Kern 50%

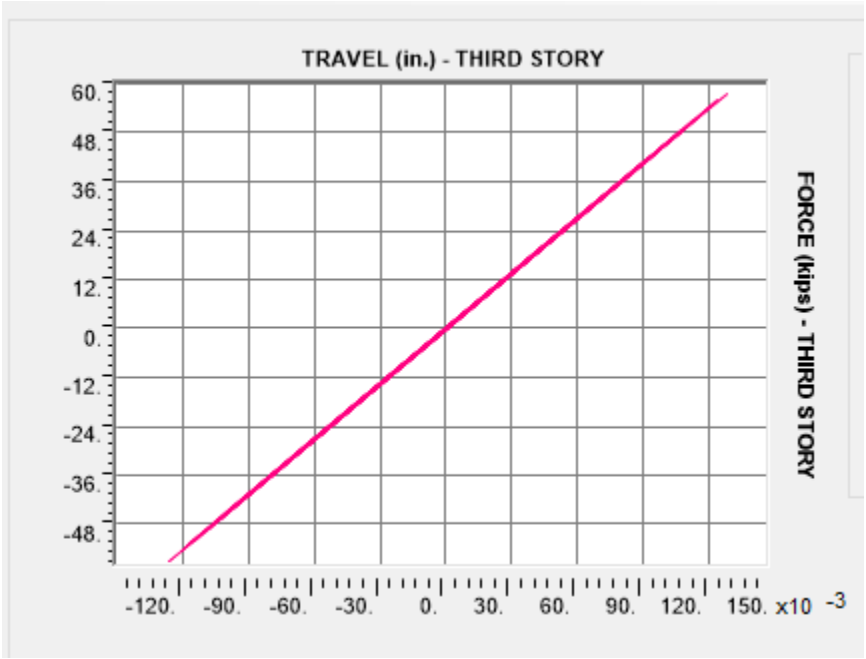

Figure 255: Force-Travel Three-Story Upper FSD Kern 50%

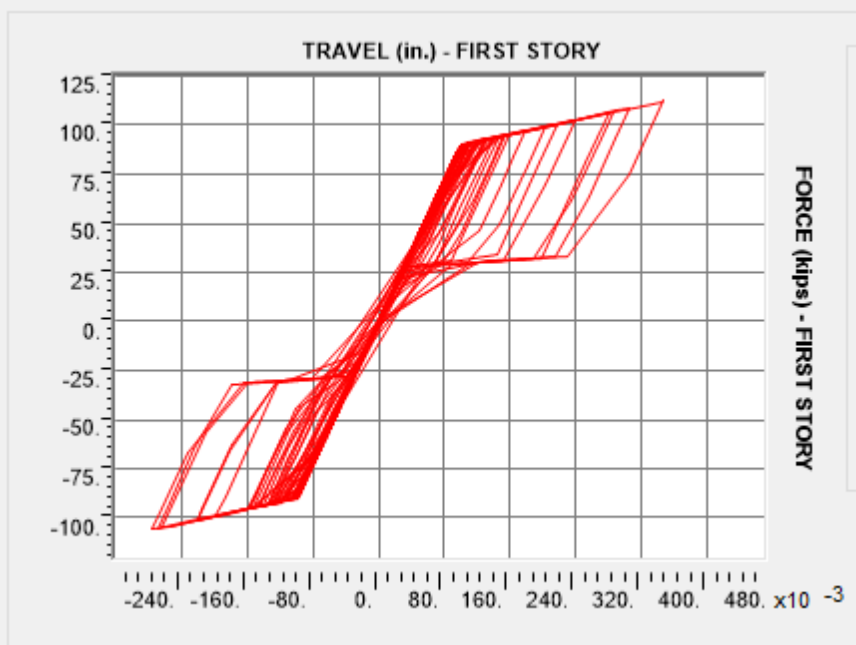

Figure 256: Force-Travel Three-Story Lower FSD Kern 100%

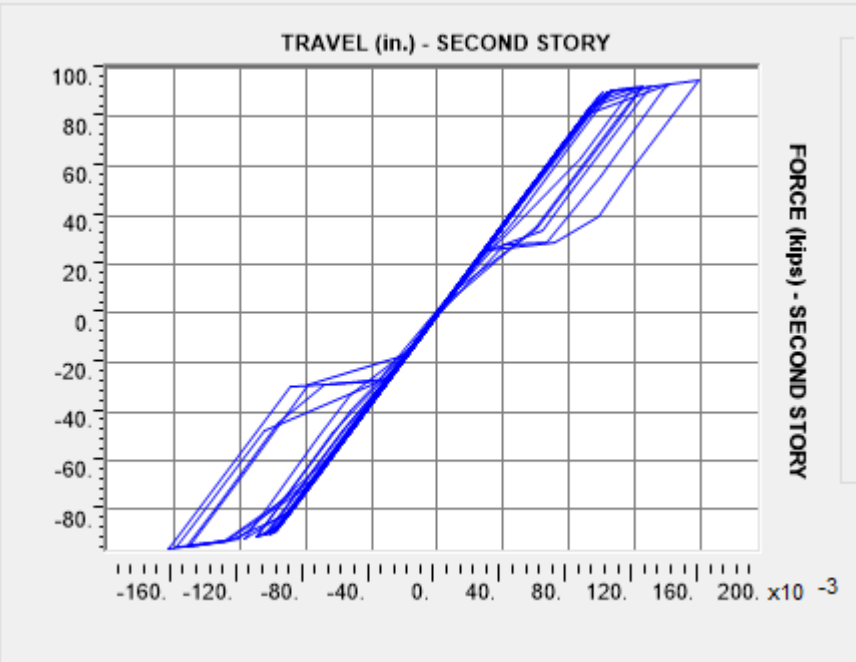

Figure 257: Force-Travel Three-Story Middle FSD Kern 100%

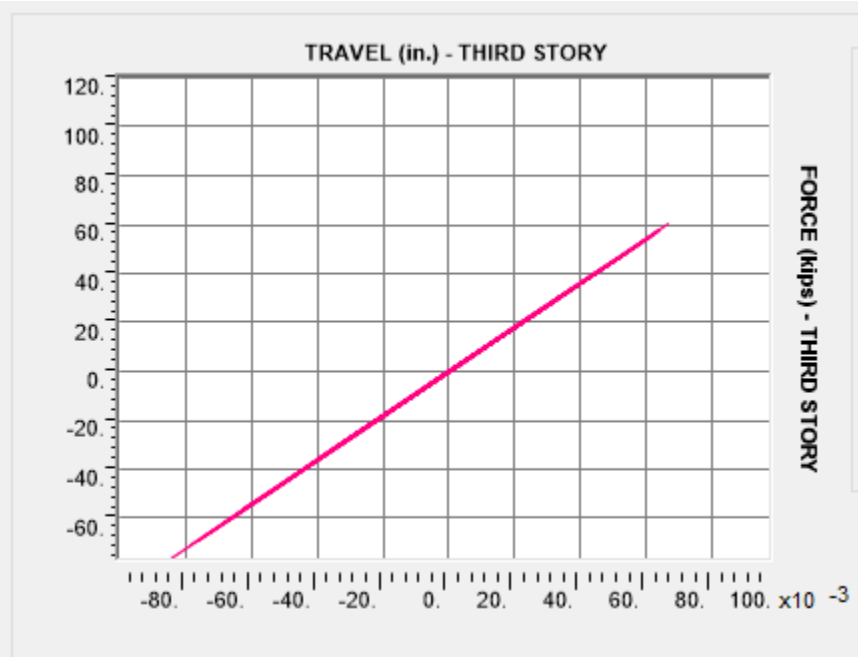

Figure 258: Force-Travel Diagram Upper FSD Kern 100%